THE ATLAS INNER TRACKER

AND

THE DETECTION OF LIGHT SUPER-SYMMETRIC HIGGS BOSONS

PROEFSCHRIFT

ter verkrijging van
de graad van doctor aan de Universiteit Twente,
op gezag van de rector magnificus,
prof. dr. F.A. van Vught,
volgens besluit van het College voor Promoties
in het openbaar te verdedigen
op woensdag 1 oktober 2003 om 15.00 uur

door

Marcel André Vos
geboren op 7 oktober 1972
te Doorn

Dit proefschrift is goedgekeurd door:

prof. dr. ing. B. van Eijk (promotor) en
dr. J.A. Fuster (assistent-promotor)

Voor Vincent

The work reported in this thesis has been possible thanks to the financial suppo rt of the Spanish research council CSIC. The research was carried out at the Ins tituto de Física Corpuscular (IFIC) in Valencia, Spain.

The ATLAS inner tracker and the detection of light SuperSymmetric Higgs bosons. Marcel Vos, 2003.

ISBN 90-365-1947-0

Contents

Introduction

This thesis reflects over four years of experimental physics within the ATLAS collaboration. It forms a representative cross section of the different aspects to the preparation of a modern-day high energy physics experiment. An important effort is dedicated to the development and testing of specialised detector elements. The detector layout is optimised using a detailed Monte Carlo simulation of the design and the relevant energy loss processes. The experiment's discovery potential for signatures of new theoretical proposals is evaluated.

In chapter 1 the Standard Model - in a sense the synthesis of the great theoretical advances of the last century: relativity, quantum mechanics and field theory - is briefly introduced. Two subjects with special importance for this work, the Higgs mechanism and the theory of the strong interaction (Quantum Chromodynamics or QCD) are highlighted.

We will see that, although the Standard Model is extremely successful in describing the laws that govern the smallest particles, many questions still remain. Some of these are addressed by new theories. Among the most promising ideas is the introduction of a new symmetry (*super-symmetry* or *SUSY*). The phenomenological implications of the simplest nontrivial super-symmetric extension of the standard model (the *Minimal Super-symmetric Standard Model* or *MSSM*) are briefly discussed in this chapter.

It is now up to experimental physicists to verify the Standard Model or encounter *new*, non-standard physics. To this end, the 'Centre Européen de Physique Nucléaire' (CERN) is building the Large Hadron Collider (LHC). It is to accelerate two proton beams in opposite directions, to an unprecedented energy of 7 TeV. The two beams collide in four interaction points.

Large experimental facilities are built in each interaction point. The ATLAS collaboration is building a general-purpose detector that is sensitive to a wide range of signatures from non-standard physics. The detection of the Higgs boson and super-symmetric particles occupy a prominent place in the ATLAS physics program. In chapter 2 the proposed detector layout is discussed.

The inner tracker is designed to accurately reconstruct the trajectories and production vertices of charged particles produced in the collision. It will consist of a pixel vertex detector close to the interaction point, a multiple-layer semiconductor tracker (SCT), and a transition radiation tracker (TRT) in the outermost layers. The silicon micro-strip detectors employed in the SCT are the subject of chapter 3. The operational principles of silicon detectors are introduced and the design of the SCT detector *modules* is discussed.

During the research and development phase of the experiment, the performance of prototype detectors is studied by submitting them to a beam of particles from an accelerator. In chapter 4, the experimental setup, off-line preprocessing and analysis steps of the SCT *beam*

tests are described. An overview of results for recent, final-design module prototypes is given.

The *vertexing* capability of the inner tracker offers the possibility to detect displaced secondary production vertices due to the decay of long-lived particles. A good vertex resolution allows to identify jets of particles that stem from the fragmentation of a bottom quark. To efficiently *tag* b-jets, however, requires an excellent vertex resolution. In chapter 5 the tracking and vertexing performance of the inner tracker is studied using detailed Monte Carlo simulations. A prediction for the ATLAS b-tagging performance is presented.

In the final chapter, the possibility to discover the two lightest Higgs bosons predicted by the MSSM through their decay to muons is discussed. Associated production with b-quarks ($gg \to b\bar{b}h^0/A^0$) is strongly enhanced for certain combinations of MSSM parameters.

Efficient b-tagging allows a significant reduction of the background from standard model processes. The expected production cross sections for signal and background processes are discussed, as well as the simulation of the event and detector effects. The discovery potential of the ATLAS experiment for this channel is presented.

Chapter 1

Theoretical background

In this chapter, a brief introduction to the "physics of the LHC" is given. A global, detailed review of the theory is beyond the scope of this work. The discussion is limited to a few issues with special relevance for this thesis.

The theoretical model of the fundamental forces and particles, known as the Standard Model, is briefly introduced in section 1.1. The Higgs mechanism by which the fundamental particles of the standard model acquire masses is the subject of section 1.1.2. Some aspects of the standard model description of the strong interaction, Quantum-Chromo-Dynamic or QCD, are discussed as well.

Despite the success of the Standard Model, many physicists believe it is not the final answer. The principle of super-symmetry is one of the most promising theoretical developments beyond the Standard Model. Its theoretical advantages are discussed in section 1.3, as well as possible experimental signatures to prove or refute super-symmetric models.

Finally, in section 1.3.2 the Minimal Super-Symmetric extension of the Standard Model (MSSM) is introduced. The MSSM is the simplest super-symmetric theory that reproduces the results of the Standard Model. The Higgs sector of the MSSM is discussed in some detail. In chapter 6 the potential of the ATLAS detector for the discovery of two of the MSSM Higgs bosons is studied.

1.1 The Standard Model

1.1.1 Introduction

The Standard Model is the only existing mathematically consistent description of fundamental particles and their interactions. It has been enormously successful in explaining and predicting the results of many high energy physics experiments.

The Standard Model has three main components, associated with three fundamental interactions. Quantum Electro-Dynamics (QED) describes the electromagnetic interaction. The Glashow-Weinberg-Salam model merges QED with a description of the weak nuclear interaction. Finally, Quantum Chromo-Dynamics (QCD) is the quantum field theory of the strong nuclear interaction. At present, a satisfactory description of the fourth fundamental interaction, gravity, is still missing.

The Standard Model describes the constituents of matter and their interactions in terms of fundamental point-like particles. An important property of the fundamental particles of the theory is their internal angular momentum or "spin". Matter is made of fermions; particles with spin $s = 1/2$. Interactions between matter particles are described by the exchange of messenger particles or gauge bosons that have integer spin.

All known fermions are listed in table 1.1.

quarks	mass (GeV)	Q (q_e)	leptons	mass (GeV)	Q (q_e)
d	0.0061 ± 0.0006	-1/3	e	0.000511	-1
u	0.0034 ± 0.0006	+2/3	ν_e	~ 0	0
s	0.105 ± 0.020	-1/3	μ	0.106	-1
c	1.19 ± 0.11	+2/3	ν_μ	~ 0	0
b	4.24 ± 0.11	-1/3	τ	1.8	-1
t	165 ± 5	+2/3	ν_τ	~ 0	0

Table 1.1: *The fundamental spin-1/2 particles of the Standard Model. The masses of the charged leptons are very accurately known. The listed values do not represent the full experimental precision. See for example [1]. The* running *quark masses are evaluated in the $\bar{M}S$ scheme; the light quarks (*u,d,s*) at a scale of 2 GeV, the* c, b *and* t *quark at a scale equal to their mass $m_q(m_q)$. The values are from [2] and references therein.*

The fermions are classified according to whether or not they are sensitive to the strong interaction. Fermions that do, i.e. those that carry colour charge, are called quarks. They are also sensitive to the electromagnetic and weak interactions. Six quark types or *flavours* have been demonstrated to exist: up, down, strange, charm, bottom and top. Ordinary matter consists of u and d type quarks. The combination of two u and one d quark gives the proton, while the neutron consists of two d and one u quark. The heavier quarks (s,c,b and t) and leptons (μ, τ and their neutrinos) are only formed in accelerator experiments and processes involving high-energy cosmic radiation. Quarks cannot be observed as free particles, but their existence is inferred from strong experimental evidence. The theory that describes the strong interaction, QCD, is the subject of 1.2.

The remaining fermions only interact through the electromagnetic and weak interaction. These are called leptons. The electron, muon and tau carry both electrical charge and weak isospin (the charge associated to the weak interaction). Only the electron is found in ordinary matter. The corresponding neutrinos are electrically neutral and interact only weakly. The electron neutrino ν_e was originally discovered in radioactive neutron decay: $n \rightarrow p + e^- + \nu_e$. The fact that neutrinos have small non-zero masses was discovered only recently and only imprecise limits on their individual masses are available [3, 4, 5].

The Standard Model fermions are classified in three families. Strict lower limits have been set on the mass of 4^{th} generation quarks and leptons. Analyses of the Z partial decay widths into hadrons, leptons and neutrinos at LEP1 [6, 7, 8] indicate that there are exactly three families of light neutrinos (assuming lepton universality). The family structure and the different masses of the fermions form one of the outstanding questions of the Standard

Model.

The matter particles of table 1.1 interact with each other by exchanging messenger particles (gauge bosons). Each of the known interactions is associated with an integer-spin particle (or particles) of table 1.2.

The gauge bosons of the electromagnetic and weak interactions are experimentally very well established. The carrier of the electromagnetic interaction, the photon, is observed daily in the form of light. The photon is believed to be massless (the experimental upper limit is $m_\gamma < 10^{-16}\ eV$). The gauge bosons of the weak interaction, the W and Z bosons, have been observed in accelerator experiments. Their properties (masses, widths) are known to good accuracy.

The negative results of searches for additional charged or neutral vector gauge bosons within the Standard Model [1] yield lower limits on their masses: $m_{W'}, m_{Z'} > 650\ GeV$.

The gluons responsible for the strong nuclear interaction cannot be observed as free particles. There are, however, strong reasons to believe they exist. The theory of the strong interactions, QCD, is discussed in section 1.2.

To date it has not been possible to incorporate gravity into the Standard Model. Still, the name for its messenger particle, the graviton, has already been chosen.

interaction	name	symbol	spin	mass (GeV/c^2)	Q q_e
electromagnetic	photon	γ	1	0	0
weak nuclear		Z	1	91.187 ± 0.007	0
interaction		$W^\pm$	1	80.417 ± 0.10	± 1
strong	gluons	g	1	0	0
gravity	graviton	G	2	0	0
	Higgs	H	0	$114 < m_H < 200$	0

Table 1.2: *The bosons of the Standard Model. These integer spin particles are responsible for the three (four) fundamental interactions. The masses of the gauge bosons are from [1]. The limits on the mass of the Standard Model Higgs boson are discussed in section 1.1.2.*

The Higgs boson is not associated with a fundamental interaction and is listed in table 1.2 for completeness. The Higgs mechanism, proposed to provide masses to the fermions and gauge bosons of the Standard Model [9], is discussed in the next section.

1.1.2 The Higgs Mechanism

In the Standard Model, the gauge bosons and fermions acquire non-zero masses through the Higgs mechanism. For a detailed discussion the reader is referred to references [9, 10, 11, 12]. Reports of experimental Higgs searches can be found in the references given at the end of this section. Here, only a superficial introduction to the subject is given.

A central concept in the Higgs mechanism is spontaneous symmetry breaking. It implies that the Lagrangian of the system retains its invariance under the symmetry group, while the vacuum state (ground state of the system) no longer exhibits the invariance.

As an example, consider the case of a single complex scalar field and the $U(1)$ invariant Lagrangian under phase rotations:

$$L(\phi, \phi^\dagger, \partial_\mu\phi, \partial_\mu\phi^\dagger) = \partial_\mu\phi^\dagger\partial^\mu\phi - \mu^2|\phi|^2 + \Lambda|\phi|^4 \tag{1.1}$$

Choosing a negative value for the mass-squared term μ^2 the conventional vacuum solution is converted into the famous "Mexican hat" potential, with an infinite number of degenerate states of minimum energy. The vacuum state has (spontaneously) broken the symmetry and thus acquires a non-zero expectation value.

The unphysical negative mass is taken care of by a redefinition of the field ϕ and an expansion around the vacuum expectation value in terms of real fields $\rho(x)$ and $\xi(x)$. The Lagrangian then becomes:

$$L(\phi, \phi^\dagger, \partial_\mu\phi, \partial_\mu\phi^\dagger = \frac{1}{2}\partial_\mu\rho\partial^\mu\rho + \frac{1}{2}\frac{(\rho+v)^2}{v^2}\partial_\mu\xi\partial^\mu\xi + \mu^2\rho^2 - \Lambda v\rho^3 - \frac{\Lambda}{4}\rho^4 - \frac{\mu^2v^2}{4} \tag{1.2}$$

This now is the Lagrangian for two physical, real scalar fields. Even though the Lagrangian does not explicitly exhibit the original $U(1)$ invariance, it still possesses the underlying internal symmetry of the gauge group. Moreover, while $\rho(x)$ has a positive mass, the Nambu-Goldstone boson $\xi(x)$ is massless.

The Higgs mechanism [9] couples spontaneous symmetry breaking to a local gauge symmetry. In this case, the theory acquires a massive vector gauge field, as well as a massive scalar. The vector gauge field has become massive by absorbing the Nambu-Goldstone boson.

Applying this mechanism to the Standard Model, the vector gauge bosons of the weak interaction acquire masses:

$$m^2_{W^\pm} = \frac{g_2^2v^2}{4}, m_{Z^0} = (g_1^2+g_2^2)\frac{v^2}{4} = \frac{m_W^2}{\cos^2\theta_W} \tag{1.3}$$

where g_1 and g_2 are coupling constants and the masses of W and Z bosons are related by the Weinberg weak mixing angle θ_W. The Higgs mechanism moreover allows to introduce Yukawa-like terms of the form $\frac{1}{\sqrt{2}}g_f v(\bar{f}_L f_R + \bar{f}_R f_L)$, yielding fermion masses $g_f v/\sqrt{2}$.

Thus, the spontaneous breaking of the local gauge symmetry provides a mechanism by which the gauge boson and fermions of the theory acquire non-zero masses. Nowadays, most physicists believe that the Higgs mechanism is the key to understanding particle masses.

A physical state is associated with the Higgs field: the Higgs boson. The Standard Model Higgs mechanism does not predict its mass. However, some constraints on the mass may be derived from theoretical requirements. The requirement of unitarity for elastic W^+W^- scattering yields an upper bound on the renormalised Higgs mass of $\sim 1\ TeV$ [13]. The triviality bound follows from the requirement that the Standard Model should reduce to a trivial theory at infinite scale and yields a slightly inferior limit of $\sim 640\ GeV$ [14].

Indirect experimental evidence also points to a Standard Model Higgs mass well below $1\ TeV$. Precision measurements at LEP are sensitive to the logarithm of the Higgs mass through radiative corrections. Global fits of LEP2 electroweak results favour a light Higgs. An upper bound of $\sim 200\ GeV$ is derived at 95 % confidence level [15]. A lower bound is inferred from the absence of a Higgs signal in direct searches of $e^+e^- \to ZH$ at LEP2: $m_H >$

114 GeV [16]. Note that both the theoretical bounds and experimental limits are strictly valid only for a standard model Higgs boson.

If the Standard Model Higgs mechanism is responsible for the generation of gauge boson and fermion masses a physical state is likely to exist in the energy range up to 1 TeV [11]. Hadron colliders like the Tevatron and LHC may bring the Higgs boson within experimental reach in the next ten years [17].

1.2 QCD

Within the Standard Model, the strong nuclear interaction is described by a model known as Quantum Chromo-Dynamics (QCD). Some key concepts of QCD are introduced in the following sections.

1.2.1 The parton model

The *parton* model is a central part of QCD. It was originally proposed to describe the results of $e^- p$ scattering experiments, like the collision shown in figure 1.1. These experiments probe the internal structure of the proton, a compound object of finite size ($\sim 1\ fm$).

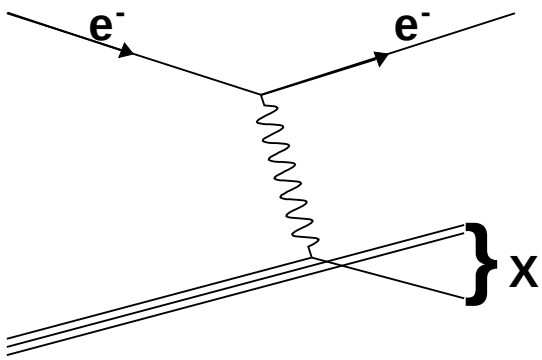

Figure 1.1: *Diagram for deep inelastic scattering of an electron off the proton. The proton is represented as three independent quark lines (for the valence quarks).*

The inelastic electron-proton scattering cross-section $\sigma(e^- p \to e^- X)$ in the one-photon approximation can be written as [18, 19]:

$$\frac{d\sigma}{dQ^2 d\nu} = \frac{\pi\alpha^2 \cos\theta/2^2}{4E^2 \sin\theta/2^4 EE'}\{\frac{1}{\nu}F_2(x,Q^2) + \frac{1}{M_p}F_1(x,Q^2)\tan\theta/2^2\}$$

where E and E' are the energy of the electron before and after the collision and θ is the scattering angle. Q^2, ν and x are kinematic variables: $Q^2 \equiv -q^2$ is given by the momentum

transfer of the intermediate photon, $\nu \equiv \frac{P\cdot q}{M_p} = E - E'$ and $x = \frac{Q^2}{Q^2+P_X^2-M_p^2}$ with P_X the momentum of all hadronic products of the collision. F_1 and F_2 are the *structure functions* of the proton.

In the *naive* parton model the proton is assumed to consist of a number of free, point-like fermions. Each of these *partons* carries a fraction ξ_i of the proton momentum $p_i^\mu = \xi_i P^\mu$. The transverse momenta and masses of the partons are neglected[1].

The parton model gives the following prediction:

$$2xF_1(x,Q^2) = F_2(x,Q^2) = \sum_i e_i^2 x f_i(x) + \mathcal{O}(\alpha_s(Q))$$

where the $f_i(x)$ are the parton densities that express the probability to find a parton of type i with momentum fraction x and e_i is the charge of the parton. To first order, the structure functions $F_1$and F_2 are independent of Q^2, a property known as Bjorken scaling. The Q-dependence appears in higher order corrections. The parton model offers a surprisingly good description of the structure of the proton.

Electron-proton scattering is only sensitive to the electrically charged constituents of the proton. Experimentally, it is found that these carry only about half of the proton momentum. Processes like the rate of large transverse momentum jets and heavy quark production in hadron collisions probe the electrically neutral particle content of the proton. The electrically charged partons are readily identified with the u and d valence quarks and a sea of light $q\bar{q}$ pairs. The momentum fraction carried by neutral particles is attributed to gluons.

1.2.2 Renormalisation

In the Standard Model, a problem arises in the calculation of higher order Feynmann diagrams: loop diagrams lead to divergent integrals. This is known as ultraviolet divergence. Fortunately, a solution exists that is proven to be valid for all gauge theories. Renormalisation plays a fundamental role in all gauge theories of the Standard Model. It becomes especially important in QCD due to its large coupling constant.

As an example consider the gluon self-energy diagram of figure 1.2. From the Feynmann prescription for this diagram one obtains the following integral:

$$\int \frac{d^4k}{(2\pi)^4} \frac{k^\alpha (k-q)^\beta}{k^2(k-q)^2} \tag{1.4}$$

which clearly yields infinity.

First, the infinite part of the integral is isolated from the physically meaningful part. In dimensional regularisation, instead of performing the integral in 4 dimensions, it is calculated in $D = 4 + 2\epsilon$ dimensions:

$$\int \frac{d^Dk}{(2\pi)^D} \frac{k^\alpha (k-q)^\beta}{k^2(k-q)^2} = \frac{-i}{6(4\pi)^2} \left(\frac{-q^2}{4\pi}\right)^\epsilon \Gamma(-\epsilon)\left(1-\frac{5}{3}\epsilon\right) \frac{q^2 g^{\alpha\beta}}{2(1+\epsilon)+q^\alpha q^\beta} \tag{1.5}$$

[1]This approximation is correct in the infinite momentum frame of the proton

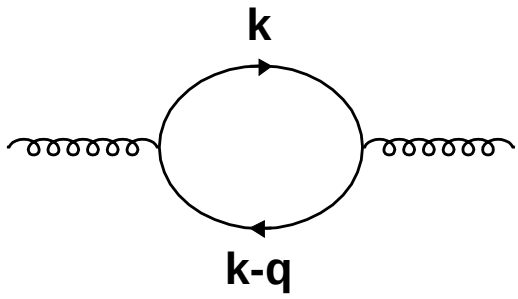

Figure 1.2: *Gluon self-energy diagram.*

where the Γ-function is given by

$$\Gamma(-\epsilon) = -\frac{1}{\epsilon} + \gamma_E + \mathcal{O}(\epsilon^{\in}) \tag{1.6}$$

and $\gamma_E = 0.577215$ a constant. The divergence is now localised in the $1/\epsilon$ term of the Γ-function. It is convenient to introduce an arbitrary scale μ_R with the dimension of energy (the renormalisation scale):

$$\mu^{2\epsilon}(\frac{-q^2}{4\pi\mu_R^2})^{\epsilon}\Gamma(-\epsilon) = \mu_R^{2\epsilon}(\frac{1}{\epsilon} + \gamma_E - \ln 4\pi + \ln -q^2/\mu_R^2 + \mathcal{O}(\epsilon^{\in})) \tag{1.7}$$

Thus, the divergent result is split into a term containing the divergence and a finite q^2 dependent term. There is an arbitrariness in this separation concerning which part of the finite contribution is absorbed in the couplings. Several renormalisation *schemes* exist: the most commonly used is the modified minimal subtraction ($\bar{MS}$) scheme, where the $1/\epsilon + \gamma_E - ln4\pi$ term is subtracted.

At this point the theory can be renormalised: the divergence can be absorbed by a redefinition of the fields, couplings and masses of the theory. Through this redefinition, the couplings and masses acquire a dependence on the renormalisation scale μ_R. The coupling constants and masses of renormalised theories are *running* constants.

Of course any physical observable should be independent of the arbitrary scale μ_R. This requirement can be expressed as:

$$\mu_R^2\frac{d}{d\mu_R^2}R(-q^2/\mu_R^2, \alpha_s(\mu_R), m(\mu_R)/Q) = (\mu_R^2\frac{\partial}{\partial\mu_R^2} + \beta(\alpha_s)\frac{\partial}{\partial\alpha_s} - \gamma(\alpha_s)m\frac{\partial}{\partial m})R = 0 \tag{1.8}$$

i.e. the observable R is required to be invariant under a change of variables $\mu \to \mu'$. The requirement 1.8 yields the renormalisation group equations:

$$Q^2\frac{\partial\alpha}{\partial Q^2} = \beta(\alpha) \tag{1.9}$$

and

$$Q^2 \frac{\partial m}{\partial Q^2} = -\gamma(\alpha_s) m(Q^2) \tag{1.10}$$

that govern the running of the coupling constant and the masses of the theory.

In QCD, the gauge bosons that mediate the interaction - the gluons - carry colour charge themselves. Therefore, gluon-gluon interactions are possible. Technically, it is the result of the non-Abelian nature of the SU(3) group.

The self-coupling of the gluons has vast phenomenological consequences. In a perturbative expansion of the β function:

$$\beta(\alpha_s) = -\beta_0 \alpha_s^2 - \beta_1 \alpha_s^3 - \beta_2 \alpha_s^4 + \mathrm{O}(\alpha_s^5) \tag{1.11}$$

the first term has the form:

$$\beta_0 = \frac{1}{4\pi}(11 - \frac{2}{3} n_f) \tag{1.12}$$

The constant positive term is due to the gluon contribution while the negative term arises from the quarks: n_f is the number of active flavours.

Provided $n_f < 16$, β_0 is positive. This implies that the QCD coupling constant α_s decreases with increasing Q^2. At short distances (large Q^2) quarks and gluons behave like free particles: a property known as asymptotic freedom[2]. For low values of Q^2 the strength of the coupling increases. Therefore, quarks and gluons are confined inside colour singlet states.

In practice this means that quarks and gluons cannot be observed as free particles, but are always found in combinations that have no net colour charge. Combinations of three quarks give rise to baryons, like the proton (uud) and the neutron (ddu). Another possibility to form colour singlets is the combination of a quark and an anti-quark into a meson (for example $\pi^+ = u\bar{d}$, $K_0 = d\bar{s}$, $B^0 = d\bar{b}$). Thus, the five lightest quarks give rise to a broad spectrum of hadronic states. The top quark is special due to its large mass; its weak decay $t \to W^+ b$ with a lifetime of $\sim 10^{-25}$ s prevents the formation of hadronic states.

1.2.3 Factorisation

QCD incorporates the naive parton model of section 1.2.1 in quantum field theory. The parton density functions are rigorously defined.

In the naive parton model, the parton transverse momenta are restricted to be small. The inclusion of the gluon emission diagrams of figures 1.3 removes this restriction. Quarks in the proton can acquire sizeable transverse momenta through the emission of gluons. Conversely, gluons can acquire transverse momentum through the process $\gamma^* g \to q\bar{q}$.

As a first consequence, Bjorken scaling is broken by higher order terms $\alpha_s \ln Q^2$. Moreover, the inclusion of gluon emission diagrams like those of figures 1.3 leads to a singularity for collinear emission of the gluon (i.e. when the transverse momentum of the gluon vanishes $k_T = 0$). This is known as collinear divergence.

[2]The concept of asymptotic freedom is experimentally tested in relativistic heavy-ion collisions. In the dense environment created in the collisions a short lived *plasma* of free quarks and gluons is expected to be formed. So far no conclusive evidence has been found.

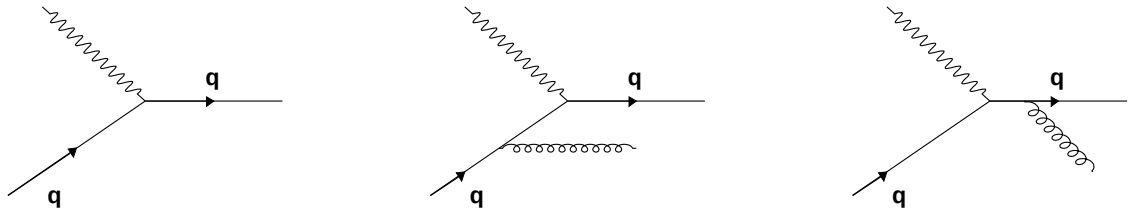

Figure 1.3: *Diagram for the scattering of a photon of a quark. The central and rightmost diagrams include a gluon emitted from the quark line.*

As for the ultra-violet divergence (see section 1.2.2), dimensional regularisation allows to separate (factorise) the divergent part from the part where perturbation theory is applicable. Exactly as for the renormalisation of the coupling constant, the collinearly divergent factor is absorbed into an unmeasurable *bare* parton density distribution q_0 at a factorisation scale μ_F.

The factorisation of the structure functions into a non-perturbative and a perturbative contribution is possible to all orders in perturbation theory. Several *factorisation schemes* are available, depending on which fraction of the finite part is absorbed into the bare parton density.

The introduction of the arbitrary factorisation scale μ_F should not affect the value of the physical observables of the theory. This requirement yields the Dokshitzer-Gribov-Lipatov-Altarelli-Parisi (DGLAP) equations [20] that describe the evolution of the parton density functions with the scale Q^2. Once the parton density function at a certain scale Q^2 is known, the DGLAP equation allows to evolve the PDF to any other scale. For a derivation, see for instance reference [18].

The parton densities $q(x, Q^2)$ cannot be calculated in perturbation theory, but can be measured at any scale from their relation to the deep inelastic scattering structure functions. A large body of experimental data at different scales is available. QCD fits using the DGLAP equations to evolve the parton density to different scales are used to constrain the parton density functions. The resulting u, d, s-quark and gluon densities at a scale $Q^2 = 10\ GeV^2$ are shown in figure 1.4.

The parton densities of the heavier quarks: charm, bottom and top are an important theoretical issue. The theoretical prediction for heavy-quark production in hadron collisions differs significantly from the experimental results [22, 23, 24]. For bottom quark production at the Tevatron, the next-to-leading-order contributions lead to a duplication of the cross-section compared to the leading-order calculation [25].

On the one hand this is attributed to difficulties in extending the factorisation to a situation with multiple scales (in DIS: the energy scale Q^2 of the scattering photon and the heavy quark mass scale [26]). On the other hand, an important unresolved theoretical issue is the possible existence of an *intrinsic* heavy quark content in the proton in addition to the *perturbative* content from gluon splitting ($g \to Q\bar{Q}$).

Parametrisations of the parton densities [27, 28, 29], including the heavy quarks, are

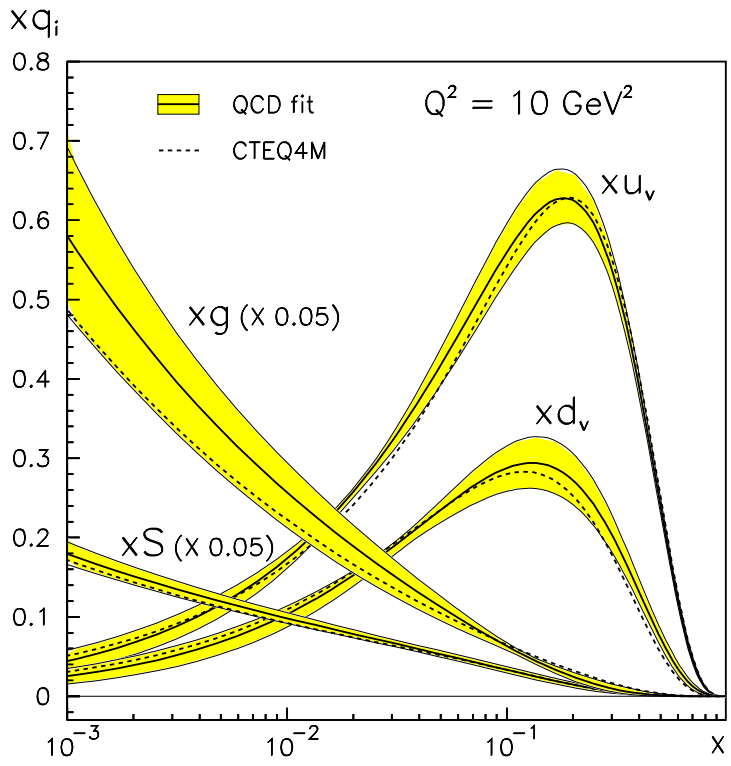

Figure 1.4: *Parton density functions (multiplied by x) of the valence quarks. The strange quark and the gluon contributions have been scaled down by a factor 20. The continuous and dashed lines represent two different QCD fits to Deep Inelastic Scattering data. The filled bands are error estimates. Figure taken from [21]*

publicly available in electronic libraries [30].

1.2.4 Hadroproduction

The general QCD prescription for the calculation of cross sections for collisions of two hadrons is given by the perturbative expression:

$$\sigma = \sum_{i,j} \int dx_1 dx_2 f_i(x_1, \mu_F^2) f_j(x_2, \mu_F^2) \sum_{m=0}^{n} (\alpha_s(\mu_R^2))^{m+k} \sigma_{ij}^{(m)}(p_1, p_2, \frac{Q^2}{\mu_F^2}, \frac{Q^2}{\mu_R^2}) \qquad (1.13)$$

where k is the power of α_s of the lowest-order diagram, x_1 and x_2 are the momentum fractions of the two hadrons carried by the parton: $p_1 = x_1 P_1$ and $p_2 = x_2 P_2$. The $f_i(x, \mu_F^2)$ represent the QCD quark and gluon density functions, evaluated at a factorisation scale μ_F. The amplitude of the hard scattering process at order m is given by $\sigma_{ij}^{(m)}$.

Two arbitrary scales appear in equation 1.13. The renormalisation scale μ_R is the result of the renormalisation of the ultra-violet divergence, as discussed in section 1.2.2. The fac-

torisation scale μ_F is due to the factorisation of the collinear divergence. The physical picture is that the couplings and PDFs absorb those effects that cannot be described perturbatively, see sections 1.2.2 and 1.2.3.

The physical cross section cannot depend on these arbitrary scales: as the scales are varied, the results of each order in α_s change in such a way as to keep the total cross section independent of μ_R and μ_F. In practice, the calculation of all orders in perturbation theory is not feasible: for many processes, the calculation of even the first orders is a tedious task. In general, the result of the (truncated) calculation shows a dependence on the renormalisation scale μ that becomes less important with each order that is calculated. In fact, the dependence of the result on the scale μ within some bounds is often taken as an indication of the stability of the result.

1.2.5 Jet formation

Quarks and gluons are confined in colour singlet states and cannot be observed as free particles. Scattering process ($qq \to qq$ for the LHC) and the decay of heavy objects (eg. $H \to b\bar{b}$) give rise to quarks in the final state of the event. Real gluons with sizeable momenta can be radiated off quarks. For these quark and gluon final states, jets of colour-neutral particles are observed.

Jets are formed through a cascade of gluon radiation and the creation of quark-anti-quark pairs (gluon splitting). In some cases, the transverse momentum of the emitted gluon is large enough to form a separate, experimentally distinguishable, jet. In the initial phase of the cascade the energy of the partons is sufficiently large that their behaviour is described by perturbative QCD.

In principle, matrix elements for the processes can be explicitly calculated order by order, thus taking into account the exact kinematics. However, in practice, calculations after $\mathcal{O}(\alpha_s^2)$ become extremely difficult.

In the parton shower approach, the parton cascade develops analogous to that of electromagnetic showers. The probabilities of each of the branchings of one to two partons: $q \to qg$, $g \to gg$ and $g \to q\bar{q}$ are given by (DGLAP or Altarelli-Parisi) splitting kernels. This implies a simplification of the kinematics, but allows the calculation to be carried out to an (in principle) arbitrary number of partons.

While the parton shower picture provides a good description of the jet structure, it is not able to predict the rate of sufficiently energetic gluons that form a well-separated jet. Therefore, often combinations of the two approaches are applied: for the first, relatively hard branchings, matrix element calculations are used; the subsequent branchings are described by the parton shower formalism.

In any case, the perturbative calculation of the cascade is stopped when the parton energy is of the order of 1 GeV. At that point α_s becomes of order 1 and perturbation theory is no longer applicable.

The partons produced in the cascade transform into hadrons. Hadronisation cannot be described in perturbative QCD. Instead, phenomenological models are used: the Lund string model (in the PYTHIA event generator [31]) and the cluster model (in HERWIG [32]) are the most popular.

1.3 Super-Symmetry

Even though the standard model is extremely successful, many physicists believe it is not the final answer. The most obvious shortcoming is the failure to incorporate gravity in the field theory formalism. Moreover, the standard model does not offer an explanation for the complex family structure and the masses of the fundamental fermions.

Many theories have been formulated that go beyond the Standard Model. In this section the advantages of introducing yet another symmetry - super-symmetry - are discussed. After a brief introduction, the simplest super-symmetric theory that embeds the standard model - the minimal super-symmetric extension of the standard model (MSSM) - is presented. Special emphasis is given to the Higgs sector. Possible experimental signatures in future (and past) experiments are discussed.

1.3.1 Introduction

One of the principal problems of the Standard Model is related to radiative corrections to the Higgs mass due to fermion and boson loops on the Higgs propagator. After introducing a cut-off scale to regulate the ultra-violet divergence of the loop integrals, these loop diagrams contribute mass-squared terms with a quadratic dependence on a high-energy cut-off scale Λ_{UV}. A miraculous cancellation of terms of the order of the Planck scale is required for the Higgs to have a mass of the order of 100 GeV. The so-called *hierarchy problem* is one of the main incentives to search for extensions to the Standard Model.

Super-symmetry (or SUSY) offers a solution to the hierarchy problem. The key is in the opposite sign of the Λ_{UV}^2 radiative corrections to the Higgs mass from fermions and bosons. To achieve a systematic cancellation of (scalar) boson and fermion contributions to the Higgs mass, a new symmetry is postulated that explicitly links the bosonic and fermionic worlds. Thus, for each each fermionic degree of freedom a bosonic degree of freedom must exist and the divergences in the Higgs mass cancel in a natural way.

Formally, super-symmetry generator operators are introduced that change the spin of a particle by $\pm 1/2$, converting a boson into a fermion and vice versa. In principle, this idea can be taken to an arbitrary level of complexity by adding more instances of the super-symmetry generator operators. However, theories with ≥ 2 copies of the generator often lead to phenomenological difficulties. Therefore, most studies are limited to the simplest (N=1) case.

The physical consequence of the introduction of super-symmetry is the creation of a (or more than one) super-partner for each known particle. In a world where super-symmetry exactly holds the super-partners are the mirror image of the original particle in all quantum numbers[3] except, of course, spin; super-partners should have equal mass, electric charge, weak isospin and colour.

The fact that none of the super-partners has been discovered indicates that super-symmetry, if it exists, is a broken symmetry. The breaking of the symmetry allows super-partners to acquire much larger masses (of the order of 1 TeV) than those of their standard model counterparts and thus escape detection. A discussion of the many super-symmetry

[3]The mass and gauge transformation operators commute with the super-symmetry generator operators

breaking mechanisms that have been proposed is beyond the scope of this thesis. The interested reader is referred to references [33, 34, 35].

An interesting question is whether or not baryon- and lepton-number violating processes, forbidden in the standard model, are allowed in our super-symmetric theory. These processes, among which proton decay to a positron and a pion, are experimentally strongly constrained. In super-symmetry, conservation of baryon and lepton number can be imposed by introducing R-parity symmetry:

$$R_P = (-1)^{3B+L+2s} \tag{1.14}$$

where s is the spin of the particle and B and L stand for baryon and lepton number. The combination of quantum numbers is chosen so that Standard Model particles necessarily have $R_P = +1$, while their super-partners have $R_P = -1$.

In addition to the regained stability of the proton, the (ad hoc) introduction of R-parity has considerable phenomenological advantages. Super-partners to the standard model particles can only be produced in pairs and the decay chain ends with the lightest super-symmetric particle (LSP), that is necessarily stable. A stable, weakly interacting LSP is an interesting dark matter candidate.

Further support for super-symmetry derives from the observation that the introduction of super-symmetry improves the unification of the running gauge couplings of QCD and electroweak interaction theory. In the framework of grand unifying theories the three interactions are expected to merge into a single super-interaction close to the Planck scale. The observed values for the couplings are extrapolated, over many orders of magnitude, using the renormalisation group equations of each interaction. With an appropriate choice for their masses, the new particles introduced by super-symmetry lead to an improved convergence.

Super-symmetry is part of many attempts to include gravity into a super-standard model, most notably in string theory. Finally, the choice of additional symmetries that can be incorporated in the Standard Model is severely restricted by the Coleman-Mandula theorem [36].

Experimental searches for super-symmetric signatures have been carried out in the LEP and Tevatron experiments and form an important section of the physics program of the LHC experiments. One of the most promising experimental signatures for R-parity conserving models is the energy carried out of the detector by non-interacting SUSY particles. This is experimentally observable as the presence of unbalanced transverse momentum (missing p_T) of the event. So far, searches for SUSY signatures have yielded results in agreement with the Standard Model, i.e. no evidence for the existence of super-symmetry is found [37, 38, 39, 40].

1.3.2 The MSSM

With the introduction of the super-partners the particle content of the theory is at least doubled[4]. The super-symmetric theory with the smallest particle content that embeds the standard model is known as the super-symmetric extension to the standard model (MSSM). In this section, the most important properties of the MSSM are presented.

Single particle states of a super-symmetric theory form so-called super-multiplets. These contain the super-partners: fermion and boson states linked by the generator operators.

[4]The known fermions and bosons are not believed to be each others super-partners

For the fermions (with two helicity states) in the Standard Model two real scalars form the simplest possible super-partner. The combination of spin-1/2 fermions with 2 real scalars is called the chiral or matter super-multiplet. Super-partners to the standard model fermions are named by prepending a "s" to the name of the standard model particle: squark, slepton, selectron, etc.

The spin-1 vector bosons are most simply linked with spin-1/2 fermions in the gauge or vector super-multiplet. The names of super-partners of gluons, W and B bosons[5] are gluinos, winos and binos.

As in the Standard Model, the MSSM particles acquire mass through the Higgs mechanism [41]. The scalar Higgs bosons and the corresponding fermionic higgsinos form a chiral super-multiplet. However, two such doublets of opposite hyper-charge are needed to give mass to the two families of quarks. This is a result of the structure of the super-symmetric Lagrangian. Contrary to the Standard Model it does not allow complex conjugates (they would cause the symmetry to be broken in an uncontrolled way). Therefore, two Higgs doublets are needed to give mass to *up* and *down*-type quarks.

The vacuum expectation values v_u and v_d of the Higgs doublets with hyper-charge +1/2 and -1/2 are related by the angle β:

$$\tan\beta = v_u/v_d \tag{1.15}$$

Top, charm and up quarks couple to the Higgs field as $v_u = v\sin\beta$, while the bottom strange and down quark, as well as charged lepton have masses proportional to $v_d = v\cos\beta$. The value of $\tan\beta$ is not predicted by super-symmetry.

The two doublets yield a complex Higgs sector with five physical Higgs bosons. Three neutral bosons exist: the CP-odd scalars h^0 and H^0 and the CP-even pseudo-scalar A^0, and two charged scalar Higgs bosons: H^+ and H^-. The Higgs sector is completed by the five super-partners to the Higgs bosons, the higgsinos.

At tree level, all Higgs boson masses and couplings can be expressed in terms of two free parameters. Choosing the ratio of the vacuum expectation values $\tan\beta$ and m_A the masses of the Higgs bosons become (see for example [42, 43]):

$$m^2_{H,h} = \frac{1}{2}[m^2_A + m^2_Z \pm \sqrt{(m^2_A + m^2_Z)^2 - 4m^2_A m^2_Z \cos 2\beta^2}]$$

$$m^2_{H^\pm} = m^2_W + m^2_A$$

The couplings of the Higgs bosons to fermions can now be expressed in terms of β and α [42, 43], where

$$\cos 2\alpha = -\cos 2\beta \frac{m^2_A - m^2_Z}{m^2_H - m^2_h}$$

Tree-level formulae are listed in table 1.3.

For a SUSY breaking scale of $\mathcal{O}\,(1\,TeV)$ the tree-level mass of the lightest Higgs is bound to be light: $m_h < m_Z$. However, the tree-level masses and couplings are subject to sizeable radiative corrections from loop diagrams of (s)top and (s)bottom quarks [44, 45]. Two-loop calculations are available [46, 47]. The radiatively corrected masses show a significant

[5]The Z and W bosons are mixed states of W_1, W_2, W_3 and a B boson

MSSM	h	H	A
down quarks and leptons	$-\sin\alpha/\cos\beta$	$\cos\alpha/\cos\beta$	$-i\gamma_5\tan\beta$
up quarks	$\cos\alpha/\sin\beta$	$\sin\alpha/\sin\beta$	$-i\gamma_5\cot\beta$

Table 1.3: *Tree-level correction factors to the Standard Model Higgs-fermion coupling* $-\frac{ig m_f}{2m_W}$.

dependence on the top mass and the trilinear gauge coupling A_t. In practice, most analyses concentrate on one or a few benchmark scenarios that reduce the complexity by choosing *reasonable* values for most parameters.

In this work, the maximal mixing scenario [48, 49] (also known as maximal m_h scenario) is chosen. This choice implies heavy super-partners, i.e. $M_{SUSY} \sim 1\ TeV$. The mixing in the scalar top sector is chosen so as to yield the largest possible mass for the lightest Higgs boson h^0. This is achieved by setting the Higgs mixing parameter μ to a value of 200 GeV and $X_t^{\bar{M}S} = A_t - \mu/\tan\beta = \sqrt{6}M_{SUSY}$, where A_t is the trilinear Higgs-stop coupling (Renormalisation Group calculations [48, 49]). This yields a much larger upper limit on the mass of the lightest Higgs boson: $m_h < 130\ GeV$.

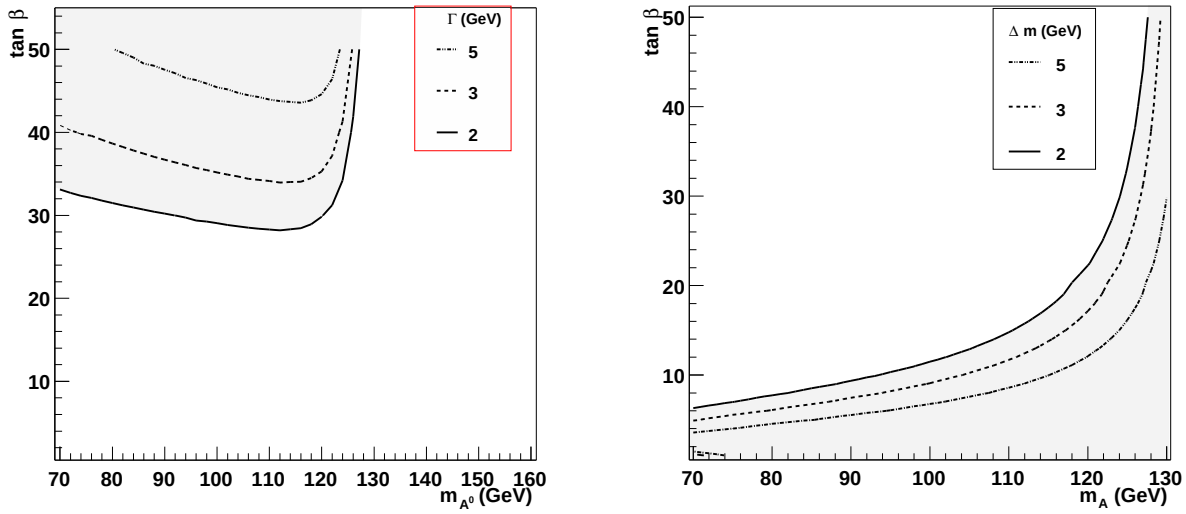

Figure 1.5: *Contours on* m_A, $\tan\beta$ *space of the total width of the h boson (leftmost figure) and mass difference (rightmost figure) of the A and h boson of the MSSM (maximal mixing scenario)*

Within the benchmark scenario only two free parameters are left: m_A and $\tan\beta$. Variation of either of these has enormous consequences for the phenomenology of the MSSM Higgs sector. In the following the effect of these two parameters on the production cross section, mass and width of the Higgs bosons is discussed.

The total widths of the Higgs bosons show a strong dependence on the ratio of the vacuum expectation values of both Higgs doublets. In the leftmost figure of 1.5 the total width of

the h^0 boson is shown in the form of contours on (m_A, $\tan\beta$) space. For $m_A < 120\ GeV$ and moderate values of $\tan\beta$ up to 20 the total width is small, less than 1-2 GeV. The shaded area indicates the region where the width becomes larger than the typical experimental resolution ($\Gamma > 2\ GeV$). The width increases rapidly to reach a width of around 6 GeV for $\tan\beta = 50$.

The masses of the Higgs bosons are determined by the value of the A mass and $\tan\beta$. Contours on m_A, $\tan\beta$ space for the mass difference between the h^0 and A^0 boson of the MSSM in the maximal mixing scenario are shown in the rightmost figure of 1.5. For small values of m_A the two lightest Higgs bosons are degenerate for nearly all values of $\tan\beta$ and their properties - width, production cross section and branching ratios - are very similar. When m_A approaches 130 GeV, the masses of the A^0 and h^0 bosons start to diverge. For even higher values of m_A the h^0 boson stays at its maximal mass of 130 GeV, while the mass of the H^0 is close to m_A. The exact behaviour during the transition depends on $\tan\beta$. The combinations of m_A and $\tan\beta$ where the mass difference becomes significant with respect to the typical experimental resolution is indicated as the region with the dark shading.

In hadron collisions, the MSSM Higgs bosons are produced directly (vua $q\bar{q} \to A^0/h^0$ and $gg \to A^0/h^0$) or in association with b-quarks ($gg \to A^0/h^0 b\bar{b}$ and $q\bar{q} \to A^0/h^0 b\bar{b}$). The coupling of the MSSM Higgs bosons to b-quarks is proportional to $\tan\beta$ ($\sin\alpha/\cos\beta$ for the h^0). Therefore, the cross-section for associated production with b-quarks is strongly enhanced for models with large values of $\tan\beta$. Associated production becomes the dominant production mechanism for $\tan\beta \sim 10$. This property makes models with large $\tan\beta$ very interesting for experimental searches. The production cross section of this channel is discussed in detail in section 6.1.2.

Many searches for the MSSM Higgs bosons have been performed. Direct searches of the channel $e^+e^- \to hA$ at LEP have yielded no excess signal over the Standard Model expectations. Due to the many degrees of freedom of the MSSM this observation yields a relatively soft lower limit on the mass of the MSSM Higgs bosons: $m_h > 90\ GeV$ [50, 51, 52]. Also, the low $\tan\beta$ region is disfavoured.

1.4 Summary

In this chapter, the Standard Model of particle physics is briefly introduced. The Standard Model provides a description of fundamental particles and their interactions. Three of the four known interactions - electromagnetism and the weak and strong nuclear interactions - are described in the framework of quantum field theory. The Standard Model particles acquire masses through the Higgs mechanism. A physical Higgs boson is predicted. Its mass is experimentally constrained by the negative results of Higgs searches at LEP, leading to a lower limit of $m_H > 114\ GeV$. Global fits of the electroweak precision data favour a light Higgs: $m_H < 200\ GeV$ at 95 % C.L.

In the Standard Model, the strong interactions are described by Quantum-Chromo-Dynamics (QCD). Fermions that feel the strong interactions are called quarks, while the gauge bosons of QCD are called gluons. Due to colour confinement, quarks and gluons cannot be observed as free particles. Whenever there are quarks or gluons in the final state of an event, jets of colour singlet particles are detected. However, high-energy (small-scale)

interactions are well described by a model, where the quarks and gluons are treated as free particles. This property is known as asymptotic freedom.

In field theory calculations, special techniques are needed to avoid infinite answers. The ultraviolet divergence is absorbed by a redefinition of the couplings and masses in the theory. It can be shown that any gauge theory is *renormalisable*. Similarly, the collinear divergence is absorbed in the parton density functions through a technique known as factorisation. In the process, arbitrary renormalisation and factorisation scales appear. Observables do not depend on these scales provided all orders of perturbation theory are calculated.

In many respects the Standard Model is an extremely good theory: its predictions have been confirmed in many experiments, often to great precision. It is, however, not expected to be the final answer. Its most obvious shortcoming is the failure to incorporate the gravitational interaction. Another issue is the hierarchy problem of the Higgs mechanism. To this latter problem an interesting solution has been proposed: the introduction of a fermion-boson symmetry, super-symmetry or SUSY, leads to a natural cancellation of the quadratic divergences in the radiative corrections to the Higgs boson mass.

The simplest super-symmetric model that embeds the results of the Standard Model is known as the minimal super-symmetric extension of the Standard Model (MSSM). In the MSSM, all Standard Model fermions have a bosonic super-partner and vice versa.

Like in the Standard Model, particles in the MSSM acquire masses through the Higgs mechanism. The MSSM Higgs sector consists of two doublets, that yield five physical Higgs bosons: two neutral scalars h^0 and H^0, a pseudo-scalar A^0 and two charged Higgs bosons $H^{\pm}$. The lightest MSSM Higgs boson h^0 is expected to be light: $m_h < 130\ GeV$. For certain combinations of the MSSM parameters, associated production of the Higgs bosons with b-quarks is strongly enhanced. The negative result of searches for MSSM Higgs bosons at LEP leads to a lower limit on the h^0 and A^0 mass of 90 GeV.

Chapter 2

LHC & ATLAS

The Large Hadron Collider (LHC) is currently being built in the former LEP tunnel at the 'Centre Européen de Physique Nucléaire' (CERN) in Geneva, Switzerland. It will accelerate protons to an unprecedented energy of 7 TeV. Two beams of opposite orientation will be made to collide at four interaction points, each of which will be equipped with a large experimental apparatus: ATLAS, CMS, LHC-B and ALICE.

In section 2.1 the Large Hadron Collider is briefly introduced. The physics program defined by the ATLAS collaboration is outlined in section 2.2 together with the proposed layout of the ATLAS detector. The following sections are devoted to the different subsystems that compose the detector. Finally, in the concluding section 2.7 the chapter is summarised.

2.1 The Large Hadron Collider

The LHC is to collide protons at an unprecedented center-of-mass energy of 14 TeV. The collision of (heavy) protons allows to reach much higher energy than electron-positron storage rings (such as the LEP collider, previously operated at CERN) as a much smaller fraction of the beam energy is lost due to synchrotron radiation. As protons are compound objects, the hard collision does not involve the full momentum of the protons: the partons (quarks and gluons) that make up the proton each carry a fraction of the proton momentum. Effectively, the maximum energy that becomes available in the collision is therefore $\sqrt{x_1 x_2 s}$, where x_1 and x_2 are the momentum fraction carried by both partons. Thus, the LHC will be able to explore the energy regime up to several TeV.

Contrary to LEP (where electrons and positrons were collided) and the Tevatron at Fermilab (that collides beams of protons and anti-protons) in the LHC both beams will consist of the same particle. The use of protons in both beams, rather than a proton and an anti-proton, offers important advantages with respect to the beam lifetime. However, it requires separate channels for both beams, complicating the design of the accelerator elements.

The 14 TeV center-of-mass energy presents a great challenge for accelerator technology. As shown in figure 2.1, CERN's existing accelerators, the Proton Synchrotron and Super Proton Synchrotron, are used to accelerate protons up to 450 GeV. After injection into the

LHC, the two beams are accelerated to an energy of 7 TeV.

To bend the 7 TeV proton beams around the 27 km circumference, extremely large magnetic fields are needed. Specially designed super-conducting dipoles provide an 8.36 T magnetic field for both beams using a single yoke and cryostat. To reach the required current of 15 kA, the coils are made of special materials, copper-clad Niobium-titanium. A sophisticated cryogenics system using super-fluid Helium is used to refrigerate the coils to 1.9^o K. Apart from 1296 dipoles, a large number of steering magnets and focusing quadrupoles are needed.

For the accelerator to be an effective probe into the new energy range, a large number of *interesting* events has to be accumulated. The LHC combines a bunch crossing frequency of 40 MHz with the highest luminosity achieved up to date. The accelerator is intended to ramp up from initial "low" luminosity $\mathcal{L} \sim 10^{33} s^{-1} cm^{-2}$ to the design luminosity of $\mathcal{L} = 10^{34} s^{-1} cm^{-2}$ in the first years.

To reach the design luminosity, the LHC must be filled with nearly 3000 bunches, each containing 10^{11} protons. The beams are to be stored in the LHC for periods of $\sim$ 10 hours. The high beam current of 0.5 A leads to unprecedented levels of the beam-beam effect and strong wake fields. A careful design is needed to avoid beam losses. This is especially important in the super-conducting magnets: the heat generated by a beam particle incident on a super-conducting magnet can lead to a loss of super-conductivity (quenching). Therefore, the sensitive regions are protected by a collimation system.

The two beams are collided in four designated interaction points. In each of these, a large experimental apparatus is to be installed. The ATLAS detector, one of the two general-purpose experiments, is discussed in the following sections.

Prototypes of the LHC magnets have been tested exhaustively. The accelerator is currently being assembled at CERN.

2.2 The ATLAS detector

To fully benefit from the LHC potential, the ATLAS detector design is optimised to be sensitive to a wide range of physics signatures. The most important design considerations are briefly discussed in this section.

A central place in the physics program is occupied by the mechanism of electroweak symmetry breaking. If the standard model Higgs boson exists (and is not detected before the LHC starts running), the ATLAS experiment will be able to discover the Higgs boson irrespective of its mass (provided it is below 1 TeV). Throughout the energy range from 100 GeV to 1 TeV the standard model Higgs is expected to be produced directly via gluon and vector boson fusion: $gg \to H$ and $WW \to H$ with minor contributions from $q\bar{q} \to H$ and $ZZ \to H$; or in association with gauge bosons (WH and ZH) or quark anti-quark pairs $gg \to t\bar{t}H$. The ATLAS collaboration requires good efficiency and resolution for the most important decay channels: $H \to \gamma\gamma$ for the lowest mass range and $H \to b\bar{b}$ and $H \to ZZ^{(*)} \to 4l$ for intermediate and high masses.

Important design considerations come from the search for super-symmetry. A promising experimental signature is the missing momentum carried out of the detector by the weakly

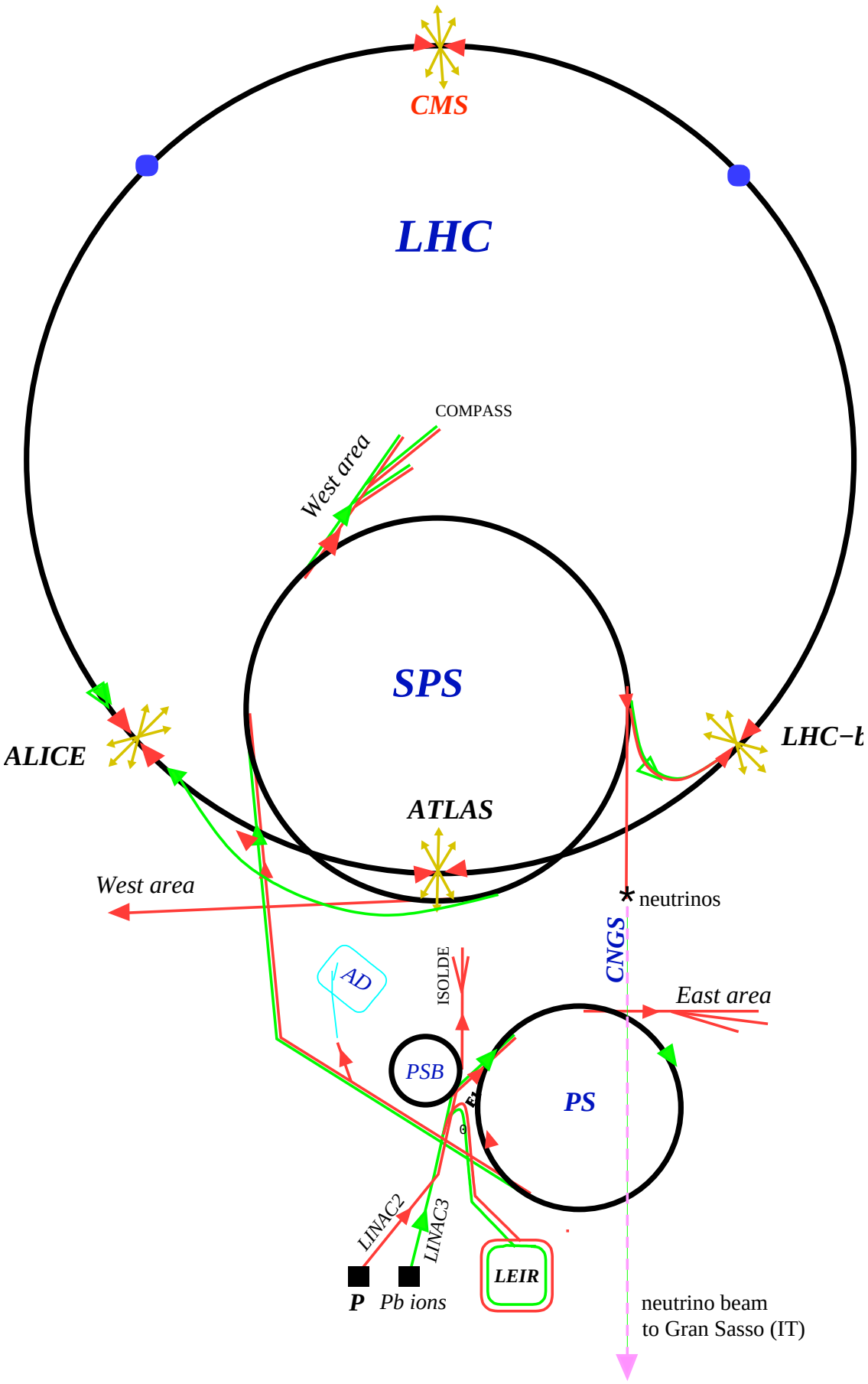

Figure 2.1: *Overview of the CERN accelerator complex.*

interacting sparticles. For SUSY theories with a Higgs mechanism, detection of several of the Higgs bosons should be possible for most viable combinations of parameters.

The potential of the ATLAS detector to discover signatures of so-called little Higgs models [53] is currently being studied. Interesting signatures include a range of decay channels of the heavy gauge bosons Z', for example to lepton pairs, b-quarks, or Zh.

Models with large extra dimensions may be experimentally testable in ATLAS through their missing p_T signature [54, 55].

The LHC could also produce *new* physics not related to the electroweak symmetry breaking: extra neutral or charged gauge bosons (Z', W') with higher masses than those of the Z and W boson, or as of yet undiscovered heavy quarks, leptons or neutrinos.

The high luminosity and high bunch crossing frequency make the LHC a true factory for many known particles:

- a new energy regime of QCD is opened up by the LHC. The theory will be tested with high statistics measurements up to momentum transfers (Q^2) of a few 100 GeV and fractional momenta of the proton carried by the parton down to $x = 10^{-5}$. The study of the production of gauge bosons, direct photons and high p_T jets allows the determination of the parton density functions. Moreover, a good description of the QCD (background) processes is essential in many searches for *new physics*.

- approximately 300 million single W's are to be produced per year. The statistical error on the W mass will thus be reduced to $\sim 2\ MeV$.

The LHC rate of production of *heavy flavour* is comparable to many dedicated experiments (b-factories):

- 10^{12} $b\bar{b}$ pairs are expected to be produced per year at the initial *low* luminosity of $10^{33} cm^{-2} s^{-1}$: the final statistics available for b-physics is limited by the rate the data can be recorded. Measurement of CP violation in the B-sector, B_s^0-mixing and rare decays of B-mesons allow to over-constrain the Cabbibo-Kobayashi-Maskawa matrix.

- eight million $t\bar{t}$-pairs are expected for an accumulated luminosity of 10 fb^{-1}. This amount of statistics allows a determination of the top mass with an error of $\sim 2\ GeV$.

To meet the physics goals the ATLAS experiment is to measure all products of the collision that have a sufficiently long lifetime to be detected. Of all particles, the energy-momentum four-vector is to be determined with great precision. Where possible, the particle type should be determined with high efficiency. The proposed detector is to consist of a number of specialised sub-detectors, as shown in figure 2.2.

The innermost detector layers around the interaction point are occupied by the inner tracker. It is to provide precise *tracking* and *vertexing* of charged particles. The momentum of charged particles is determined from the curvature of the trajectory in the 2 T magnetic field in the inner detector cavity. The inner detector plays an important role in the detection of Higgs decays to leptons ($H \rightarrow Z^* Z \rightarrow l^+ l^- l^+ l^-$). The vertexing capability is essential for the Higgs decay channels into b- and τ-jets, searches for new physics and the top and B-physics programs.

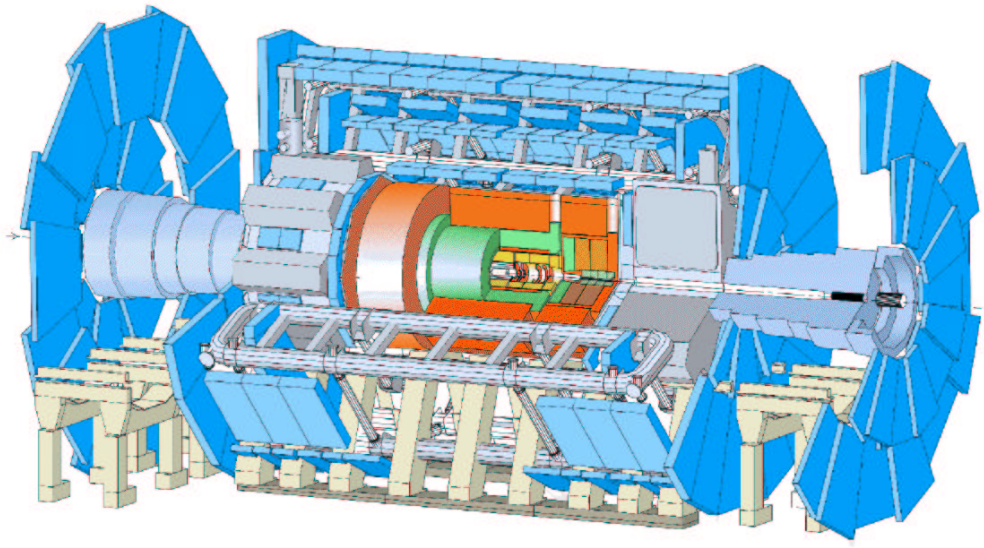

Figure 2.2: *Three dimensional view of the ATLAS detector*

The calorimetry system is situated between the inner and muon spectrometer. It is to accurately measure the energy of all collision products. The electromagnetic calorimeter - the first layer after the inner detector in figure 2.2 - measures the energy of the shower produced by photons, electrons and positrons traversing dense material. The $H \to \gamma\gamma$ channel imposes a special constraint on the photon identification performance of the ATLAS detector. Combining the information from the electromagnetic calorimeter and the inner detector ATLAS expects to be able to identify over 85 % of photons with a rejection for electrons of more than a factor 500 and a π^0 rejection of 3.

The shower created by hadrons is contained in the hadronic calorimeter. The calorimeters provide an energy measurement for jets of particles. The hermetic coverage allows the identification of events where weakly interacting particles left the detector undetected through a determination of the missing transverse momentum.

The muon spectrometer forms the outer layer of the ATLAS experiment. Muons that have sufficient energy to traverse the entire detector are identified. Multiple position measurements in a 0.6 Tesla field allow a precise determination of the momentum of high-p_T muons. Muons form an important signal. The golden channel for detection of a heavy standard model Higgs can have up to 4 muons in the final state. The detection of MSSM Higgs bosons through their muon decay is discussed in chapter 6. Finally, muons play a crucial role in the event selection (trigger).

ATLAS is a 2π detector, typical of colliding beams experiments, i.e. it has approximate cylindrical symmetry. Therefore, a cylindrical coordinate system is most appropriate. In the following, space points are identified using the position along the beam axis z, the transverse

radius R and the azimuthal angle ϕ. In hadron colliders the colliding partons each carry a fraction x_i of the proton momentum. Thus, the center-of-mass frame of the collision is generally not the laboratory frame. Two variables that have favourable properties under Lorentz transformations[1] are widely used: the momentum of the particle in the R direction or transverse momentum p_T and the rapidity $y = 1/2 \log (E + p_z)/(E - p_z)$. In the relativistic limit, the particle mass has a small effect and the pseudo-rapidity $\eta = -\log \tan \theta/2$, where θ is the polar angle (between the particle trajectory and the beam axis), is a good approximation.

The detector has a barrel + end-cap geometry. In the region around the interaction point the detector layers form cylindrical surfaces parallel to the beam axis. The end-caps are made up of wheels in the $R\phi$ plane perpendicular to the beam axis. The coverage in rapidity for precision physics thus extends to $|\eta| < 2.5$. The calorimeters cover a much larger rapidity range, up to $|\eta| = 5$.

The subsystems of the ATLAS detector are briefly introduced in the following sections.

2.3 The Inner Detector

The inner tracker consists of several layers of position sensitive detectors of three different technologies, as shown in figure 2.3. Pixel detectors occupy the radii between 5 and 15 cm from the interaction point, micro-strip detectors cover the intermediate layers (at radial distances of 30 to 50 cm) and a straw detector (TRT) occupies the outer layers.

For all tracks with a transverse momentum of more than 0.5 GeV^2 the inner detector geometry is optimised to provide:

- 3 high resolution 3D space point measurements in the pixel detector
- 4 3D space points with good resolution in the bending plane and reasonable resolution in the second coordinate in the semiconductor tracker (SCT)
- a large number (~ 36) of measurements in the transition radiation tracker (TRT).

The required coverage is obtained with a combination of cylindrical barrels in the central region and vertical wheels in the end-caps.

Using the space-point measurements of the different inner tracker layers, the helicoidal trajectory of the track is reconstructed. Simulations of the inner tracker response to minimum-ionising-particles (muons) yield the following parametrisations in terms of the track transverse momentum and polar angle θ for the five helix parameters [56]:

$$\sigma(\frac{1}{p_T}) \approx 0.36 \oplus \frac{13}{p_T \sqrt{\sin \theta}} (TeV^{-1})$$

$$\sigma(\phi) \approx 0.075 \oplus \frac{1.8}{p_T \sqrt{\sin \theta}} (mrad)$$

[1] Rapidity *differences* and the transverse momentum are invariant under boosts along the z-axis

[2] Particles with $p_T < 0.4$ GeV form *loopers*, i.e. the radius of curvature in the 2 T magnetic field becomes smaller than the size of the inner detector.

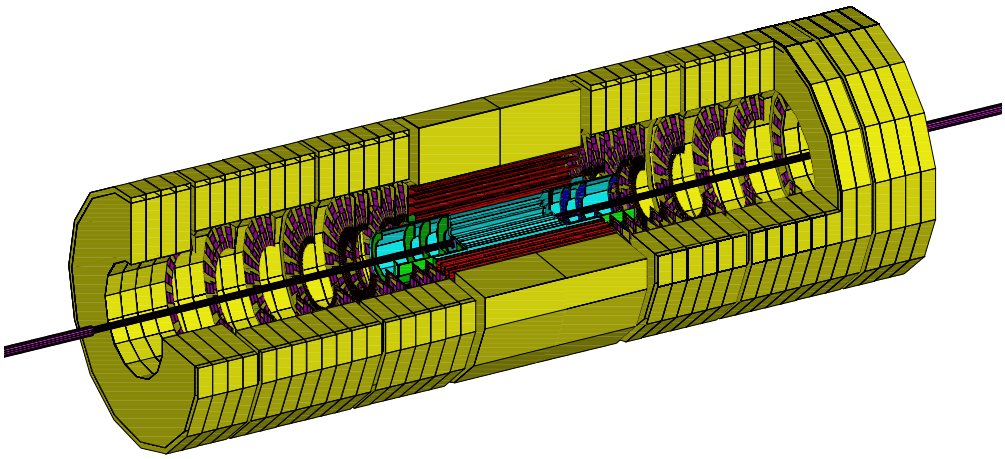

Figure 2.3: *Three-dimensional view of the ATLAS inner detector.*

$$\sigma(\cot\theta) \approx 0.70 \cdot 10^{-3} \oplus \frac{2.0 \cdot 10^{-3}}{p_T\sqrt{\sin^3\theta}}$$

$$\sigma(d_0) \approx 11 \oplus \frac{73}{p_T\sqrt{\sin\theta}}(\mu m)$$

$$\sigma(z_0) \approx 87 \oplus \frac{115}{p_T\sqrt{\sin^3\theta}}(\mu m)$$

where the transverse momentum p_T is given in GeV. The track direction close to the interaction point is given by the azimuthal and polar angle ϕ and θ. The last two helix parameters, d_0 and z_0, denote the impact parameter - the shortest distance to the interaction point - in the $R\phi$ and Rz planes, respectively.

The vertex resolution of the inner detector gives the possibility to detect (displaced) production vertices of particles. Thus, jets originating in the decay of particles with relatively long lifetimes such as b-quarks and the τ lepton may be efficiently identified (tagged). The ATLAS b-tagging performance is discussed in detail in chapter 5.

Good transverse momentum resolution is required even for high-p_T particles: 30 % for 500 GeV charged particles with $|\eta| < 2.0$, at least 50 % for very forward particles.

In addition to a good resolution, high tracking efficiency is one of the primary goals of the inner detector. In the acceptance for high precision physics, $|\eta| < 2.5$, 95 % of the minimum-ionising particles with $p_T > 5$ GeV are expected to be reconstructed. The probability to reconstruct fake tracks should be less than 1 %. These requirements are relaxed slightly in the vicinity of high p_T candidates. Muons loose nearly all of their energy due to ionisation. The performance for other particle types may deteriorate slightly due to nuclear interactions (for hadrons) or bremsstrahlung (for electrons).

In the following sections the magnet and the three detector subsystems are briefly introduced. Further sections discuss the levels of radiation that the detector is expected to receive during the lifetime of the experiment and the material budget that the inner tracker design represents.

2.3.1 The inner detector solenoid

The magnetic field in the inner detector cavity is produced by a super-conducting solenoid. The magnet encloses the complete inner detector. It is 2.5 meters in diameter and 5.3 meters long. The location of the solenoid, in front of the electromagnetic calorimeter places strict requirements on the amount of material. The thickness of the solenoid is only 45 mm. This is achieved using a single layer NbTi/Cu coil wound around a support structure. The coil is cooled to 4.5 Kelvin to reach super-conduction. The thermal enclosure and cryostat are shared between the solenoid and the cryogenic liquid argon calorimeter to save material.

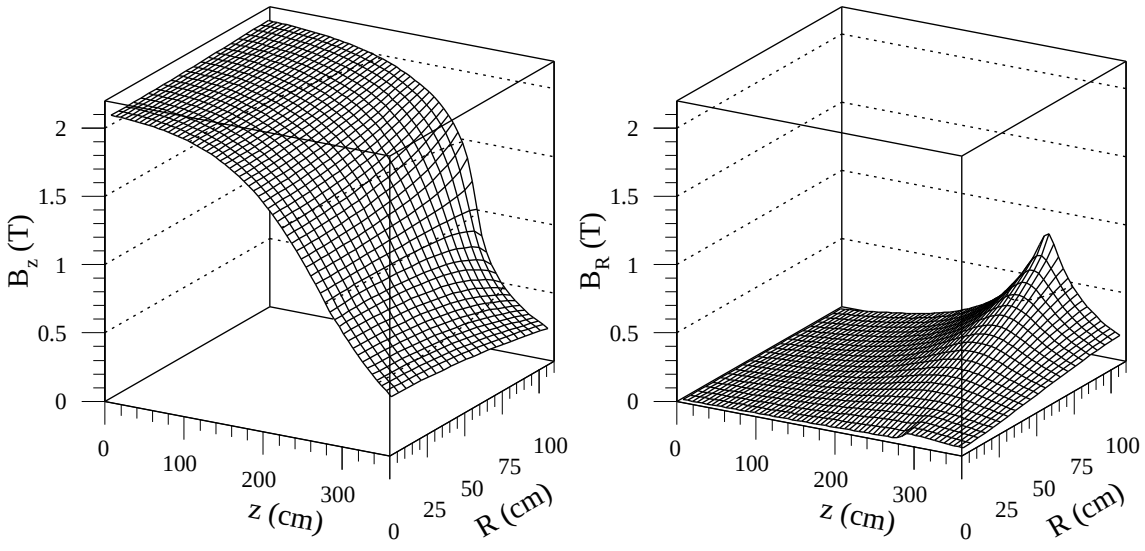

Figure 2.4: *Field maps: the field strength versus longitudinal and radial distance from the interaction point of the longitudinal (leftmost figure) and radial (rightmost figure) component of the magnetic field in the inner detector volume. Figure taken from [56].*

The solenoid yields a 2 T field parallel to the beam axis. The length of the solenoid is less than that of the inner detector tracking volume. Therefore, the deviations from a homogeneous field are quite large. In figures 2.4 the field maps are shown for the longitudinal (B_z) and radial (B_R) components of the field. The longitudinal field component drops rapidly towards large longitudinal distances from the interaction point: $|z| > 1m$, while a significant radial component develops. Provided that a good description of the field is available, the effect on the track reconstruction accuracy is limited. However, the need to utilise realistic field maps presents an additional complication to simulation and reconstruction algorithms.

2.3.2 The PIXEL detector

The pixel detectors provide three high resolution three-dimensional space points close to the interaction point. High granularity and unambiguous determination of the two coordinates are vital in the high occupancy environment at small radii.

The layer at lowest radius (called the B-layer because of its prominent role in B-physics) cover the full rapidity range $|\eta| < 2.5$. Barrel layer two and three cover pseudo-rapities

$|\eta| < 1.7$. Three end-cap disks are used to provide additional space points in the forward regions $1.7 < |\eta| < 2.5$.

Each layer is equipped with detectors consisting of a silicon diode segmented in small rectangular *pixels*. Charged particles traversing the diode deposit a small signal through ionisation. Applying a reverse bias voltage the liberated carriers drift to the segmented readout plane of the detector[3].

Each pixel is bump-bonded to a readout channel in the front-end chips that are mounted on the diode. The readout electronics amplifies and shapes the detector signal. The pixel readout is *binary*. A discriminator on the readout chip reduces the analog signal to one bit (hit/no hit) of digital information, thus limiting the amount of data from the ~ 100 million channels.

The pixel size is $50 \times 400\ \mu m^2$. The narrow side of the pixels is oriented in the $R\phi$ plane. Thus the pixel detector yields a good resolution in the bending plane of the solenoidal magnetic field, essential to the transverse momentum measurement. The position along the beam axis is measured with slightly less precision. A high granularity in this coordinate is important to assure a good two-track resolution.

Irradiated pixel sensor prototypes have been submitted to extensive beam tests [57, 58, 59]. Even after an integrated fluence equivalent to $1.1 \cdot 10^{15}$ neutrons per cm^2, the pixel detectors recover a large fraction of the deposited signal, provided a reverse bias voltage of 600 V is supplied. The tracking efficiency is approximately 98 %. The spatial resolution of prototype pixel detectors for particles incident under an angle of 10 degrees is found to be better than 10 μm in the bending plane.

2.3.3 The Semi-Conductor Tracker

The semiconductor tracker (SCT) is to provide four precision space points in the intermediate radii (from 30 to 56 cm) of the inner detector. Silicon micro-strip detectors allow to cover the large area ($60m^2$) while maintaining a reasonable number of readout channels (~ 6 million).

Four cylindrical barrels cover the pseudo-rapidity range $|\eta| < 1.4$, whereas two end-caps with nine wheels each extend the acceptance to $|\eta| < 2.5$. The inner radius of the SCT is 30 cm from the interaction point, the outermost layer is at 56 cm. The barrel extends to a distance along the beam of 80 cm in both directions. Nine wheels with different inner radii provide measurements in the region from $z = 80$ to $z = 270$ cm. This layout yields four measurements irrespective of the rapidity of the particle, while optimizing the material distribution (see section 2.3.5).

Silicon micro-strip detectors, like pixel detectors, are based on a depleted diode. In this case, however, the readout plane is segmented in narrow bands or strips. Thus, a single sided silicon micro-strip detector measures a single coordinate of the position of the track. As for the pixels, the SCT readout is binary.

In the SCT two single-sided detectors are glued back-to-back under a small stereo angle of 40 $mrad$. Combination of the two measurements allows the determination of a two-dimensional space point. Each SCT layer is thus expected to provide a spatial resolution of $\sim 17\ \mu m$ in the $R\phi$ plane. The resolution of the second coordinate is of the order of 570 μm.

[3] A detailed discussion of the silicon junction is postponed to section 3.1.1

The second coordinate is essential to resolve ambiguities in the pattern recognition, i.e. to assign hits to tracks in the dense tracking environment.

The semiconductor tracker design is discussed in detail in chapter 3. Results from beam tests of SCT prototypes are reported in chapter 4.

2.3.4 The Transition Radiation Tracker

The Transition Radiation Tracker occupies the outermost region of the inner detector cavity. It is described in detail in [60]. More recent results on the tracking and particle identification performance in beam tests can be found in references [61, 62]. Here, only a very brief summary of the operating principles and the role of the TRT in the ATLAS inner detector is given.

Transition radiation is produced when a relativistic particle traverses an inhomogeneous medium, in particular the boundary between materials of different electrical properties. The intensity of transition radiation is roughly proportional to the particle energy $I = m/\sqrt{1-\beta^2}$, where m is the mass and $\beta = v/c$ is the velocity of the particle. Thus transition radiation allows the identification of highly relativistic particles. Electron/hadron discrimination is possible for momenta from $\sim 1\ GeV$ upwards. Transition radiation is emitted in the X-ray regime, i.e. between 10 and 30 keV. The photons are rather well collimated in the forward direction.

In the TRT multiple polyethylene foils act as radiators. Interleaved with the radiator are layers of straws filled with a gas mixture. These have a dual functionality; the same straw measures the passage of charged particles through the ionisation of the gas and the transition radiation X-rays that are absorbed by the gas molecules.

A large number of straws and radiator layers is stacked in the volume. Each track traverses on average 36 straws. Thus, the number of transition radiation emissions along the track forms a powerful variable for electron pion separation. On the other hand the large number of measurements allows the use of a straw detector with relatively large active elements (the straw diameter is 4 mm and the maximum length is 144 cm) in the high rate environment of the LHC.

The straws are made of conductive Kapton film and filled with a gas mixture of Xenon, Carbon Fluoride CF_4 and Carbon Dioxide in proportion 70:20:10. The Xenon content of the gas ensures efficient X-ray absorption. The addition of fast CF_4 minimises the pile-up of signals from consecutive bunch crossings. Each straw is equipped with a gold-plated tungsten anode wire of 50 μm diameter. When a high voltage is applied between the anode wire and the walls of the straw signals are amplified through an avalanche in the gas.

The straws are read out on both sides by a Transition Radiation Detector Analogue integrated circuit. After the amplification and shaping stages two thresholds are applied. The low-level threshold is used to detect the signal from ionisation. The Drift-Time Measuring Readout Chip uses the low-level signal to determine the drift time with a resolution of 3.125 ns. The drift time in the straw is used to determine the distance of the track to the anode wire. The high-level threshold is roughly a factor 30 higher and detects the absorption of transition radiation photons that produces larger signals.

Beam tests of prototype TRT sectors [61, 62] have demonstrated a single straw spatial

resolution of the order of 150-200 microns. The transverse momentum resolution of the TRT prototype was found to vary between 0.8 % to 2.4 % for 20-100 GeV pions in a 1.56 Tesla magnetic field. The hit efficiency is around 95 %. For an electron identification efficiency of 90 % the pion rejection is close to 100.

2.3.5 Material budget

The material in the inner detector affects the resolution of the track reconstruction and adds to the *dead* material in front of the calorimeter. Excessive material causes a deterioration of the detector performance through a number of effects:

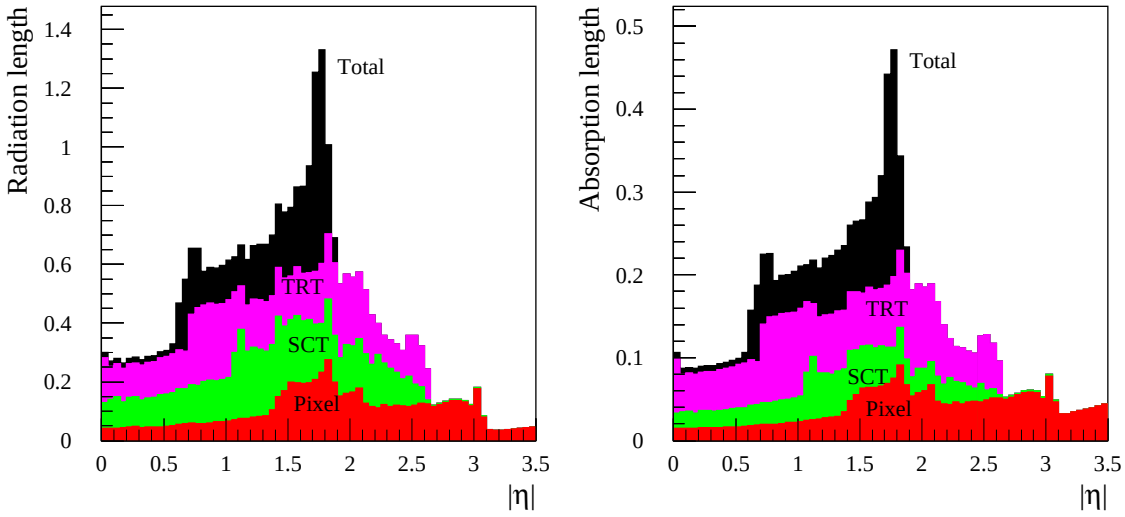

Figure 2.5: *The expected inner detector material at the time of the inner detector technical design report (1999). Material expressed in terms of radiation length X_0 (leftmost figure) and interaction lengths λ_{abs} (rightmost figure). Figures taken from [60].*

- low energy particles can be absorbed in the material, leading to a loss of efficiency
- multiple Coulomb scattering dominates the resolution of the track reconstruction for low momentum tracks
- electron bremsstrahlung affects the resolution of the EM calorimeter and the tracker
- photon conversion ($\gamma \rightarrow e^+e^-$) leads to a reduction of the important $H \rightarrow \gamma\gamma$ signal[4]

In the design of the inner detector the material distribution was therefore carefully taken into account. The silicon detectors are made as thin as the signal-to-noise requirement allows. Cables and support structures are made of light-weight low-Z materials, i.e. aluminium and carbon fiber, respectively.

[4]The photon conversions can partly be recovered, provided the electron and positron produced in the conversion are identified as such in the inner tracker.

The expected distribution of material in terms of radiation length X_0 for electrons and photons and absorption lengths for hadrons is shown in figures 2.5. The amount of material increases steadily in the barrel region from central rapidity to $|\eta| \sim 1.4$ due to the longer path length of incident particles through the detector. A peak is observed around $|\eta| = 1.5 - 2.0$. These reflect the services of the inner detector (cables) being taken out of the detector. In the histogram labeled "total" the inner detector material is included that is outside the tracking volume, but still in front of the EM calorimeter.

The effect of the inner detector material on the tracking performance is studied in chapter 5.

2.3.6 Radiation levels

The LHC will produce unprecedented particle fluxes. One of the major design challenges of the ATLAS detector is the development of detector components that are able to stand the radiation over the ten years of operation of the LHC.

Detailed Monte Carlo models are used to predict the fluxes for different types of particles. The damage to the detector components is classified according to energy loss mechanisms. Damage in the silicon detectors scales roughly with the non-ionising energy loss. Therefore, radiation levels are expressed as an equivalent fluence of 1 MeV neutrons. In figure 2.6 the expected equivalent yearly fluence of neutrons in the inner detector cavity is shown. The origin of the coordinate system represents the interaction point. The longitudinal (along the beam axis) and radial distance to the origin are shown on the horizontal and vertical axes respectively.

Many electronic circuits, on the other hand, are sensitive to damage by ionisation due to charged particles. The ionising dose is expressed in Grays or the number of charged hadrons. The expected yearly charged particle fluence is shown in figure 2.7.

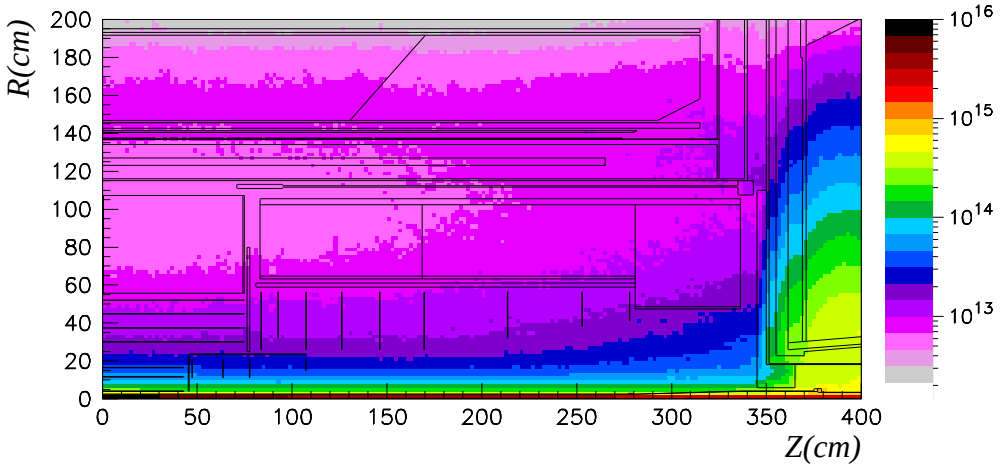

Figure 2.6: *Expected neutral fluence in the inner detector cavity in units of equivalent 1 MeV neutrons per square centimeter per year. The figure shows a cross-section of one quadrant of the inner layers of the ATLAS detector. The inner detector elements are drawn in the figure. The origin corresponds to the interaction point. The* z *coordinate is the distance along the beam axis, R represents the radial distance. Figure taken from [60].*

Figures 2.6 and 2.7 show quite large fluences at small distances from the interaction point. Both fluences decrease by several orders of magnitude at a radial distance of 10-20 cm from the interaction point.

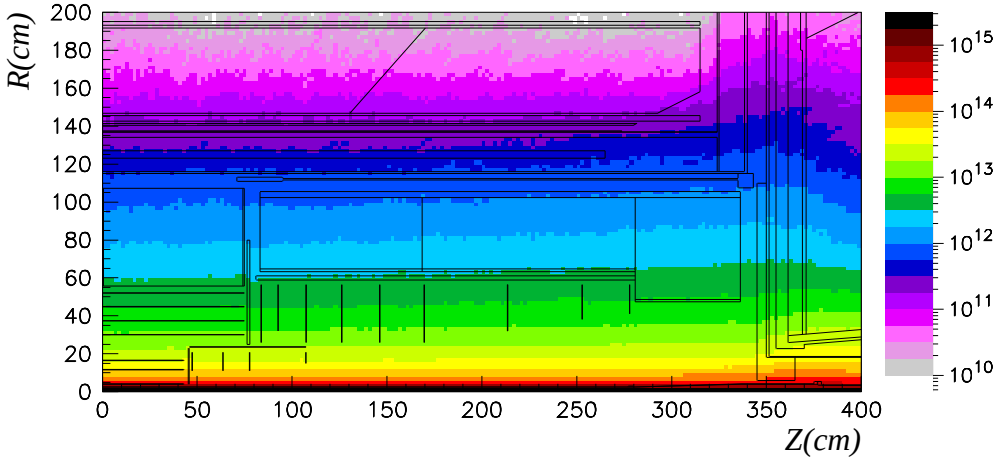

Figure 2.7: *Expected charged particle fluence per square centimeter per year. The coordinate system is identical to that of figure 2.6. Figure taken from [60].*

Expectations for the integrated fluence of charged and neutral particles over the lifetime of the ATLAS experiment are listed in table 2.1. For each sub-detector typical and maximum values for the equivalent 1 MeV neutron fluence and the ionising dose are given.

	Non-ionising dose ($10^{13} n_{eq} cm^{-2} y^{-1}$)		**Ionising dose** (**kGy/y**)	
sub-detector	typical	maximum	typical	maximum
PIXEL	5	50	30	300
SCT	1.5	2	4	10
TRT	0.7	1	2	6

Table 2.1: *Annual dose of non-ionising and ionising radiation in the inner detector. The results refer to operation of the LHC at the design luminosity of* $10^{34} cm^{-2} s^{-1}$. *The values are taken from [60].*

Using the results of table 2.1 and an assumption on the luminosity of the LHC over the ten years of envisaged operation, an expected integrated dose can be established. All detector components are designed to be radiation-tolerant up to this dose. Tests on irradiated prototypes are routinely performed. PIXEL detector prototypes are irradiated to a fluence equivalent to 10^{15} neutrons per cm^2 and an ionising dose of 600 kGy. The reference fluence for the SCT is $3 \cdot 10^{14}$ 24 GeV protons/cm^2. Extensive tests are done to cross-check the results of the standard tests with other particle types and energies, dose rates, etc.

2.4 Calorimetry

The ATLAS calorimeter system is to measure the energy (and $\theta - \phi$ direction) of all particles and jets formed in the collision. The energy measurement of calorimeters is based on the formation of a shower, a cascade of particles, when relativistic particles traverse dense matter.

Electrons and photons create a shower through pair production, $\gamma \rightarrow e^+e^-$ and bremsstrahlung ($e \rightarrow e\gamma$) in the electric field of the nucleus. The energy loss for a given material is characterised by the radiation length X_0. The lateral development of the shower is determined by the Moliere radius.

Hadrons produce a cascade of hadron-nucleus interactions. The longitudinal development of the shower is determined by the interaction length of the material. Hadronic showers contain a variable electromagnetic component from radiation of photons (bremsstrahlung) and π^0 decays. The shower shape of hadronic showers is more irregular than in pure electromagnetic showers.

The radiation and interaction length are material dependent. Generally, for dense materials, the interaction length is up to an order of magnitude longer than the radiation length. This property is used in the ATLAS calorimeters to separate the electromagnetic and hadronic showers.

Some particles do not (generally) create a shower. Energetic muons loose energy through ionisation. The relatively small energy loss presents a challenging signal for the detector resolution and noise. The weakly interacting neutrinos, and some non-interacting particles like super-partners or the gravitino, leave no measurable signal in the detector and thus escape direct detection. However, their presence can be inferred from an unbalanced transverse momentum in the event, the so-called missing p_T, provided the detector hermetically covers a large geometrical acceptance.

The inner layer of the ATLAS calorimeter system consists of a compact, dense electromagnetic calorimeter. In figure 2.8 it is drawn with a light grey fill colour. It closely follows the outer envelope of the inner detector. While the EM calorimeter represents ~ 25 radiation lengths to EM showers, its material only amounts to ~ 1.2 interaction lengths.

The electromagnetic calorimeter is followed by a hadronic calorimeter. The different technologies, tile calorimeter in the barrel region, liquid argon in the end-caps, are shown in figure 2.8. The hadronic calorimeter presents ~ 8 interaction lengths over the rapidity range $|\eta| < 3.2$. Together with the material of the EM calorimeter these are intended to contain the hadronic showers. In the very forward regions ($3.2 < |\eta| < 3.9$) the liquid argon forward calorimeter (FCAL)

The design and expected performance of the electromagnetic and hadronic calorimeters are briefly discussed in the following sections.

2.4.1 The Electromagnetic Calorimeter

The electromagnetic calorimeter is involved in many measurements in ATLAS. The main physics goal is the detection of the standard model Higgs boson through its decay to photons; $H \rightarrow \gamma\gamma$. This decay is the most promising channel in case the Higgs boson is light, close to the LEP limit of 114 GeV. An excellent invariant mass resolution is needed to disentangle

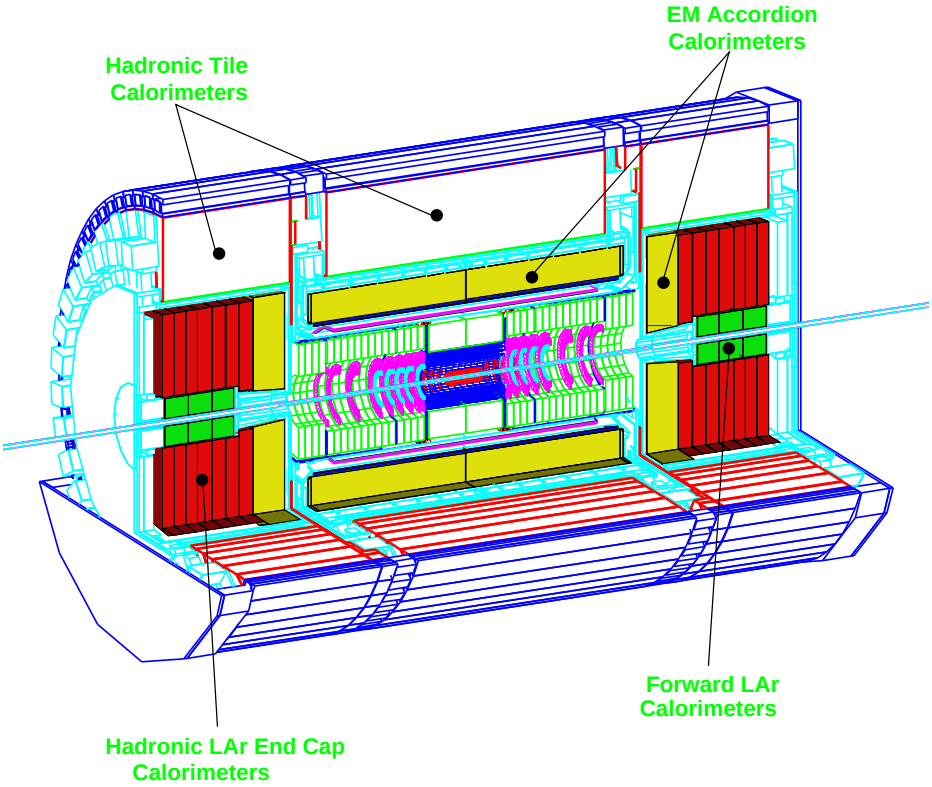

Figure 2.8: *Layout of the ATLAS calorimeters. In the center of the figure a cross section of the inner detector is drawn. The next layer is formed by the electromagnetic calorimeter. The tile barrel and liquid Argon end-caps of the hadronic calorimeter form the outer layer. Figure taken from [56].*

the signal from the irreducible continuum $\gamma\gamma$ background. For a 1 % mass resolution the energy resolution requirement for the sampling and constant terms becomes:

$$\sigma(E) \sim 10\%/\sqrt{E} \oplus 1\%$$

where the energy is expressed in GeV. The $H \to \gamma\gamma$ channel also poses strict requirements on the energy scale precision and the linearity of the response. It further requires a measurement of the photon direction in θ with a resolution of $\sigma(\theta) \sim 50mrad/\sqrt{E}$ (The energy E in GeV), to avoid deterioration of the invariant mass resolution due to the spread of the z-coordinate of the interaction point ($\sigma_z^{PV} \sim 5.6\ cm$).

A reducible background to the photon decay of the Higgs boson is formed by γ-jet and jet-jet events, where the jets mimic a photon signal. A rejection by a factor 5000 for jets, maintaining a photon efficiency of 80 %, is needed to reduce these events to below the irreducible background.

τ-jets are important in the Minimal Super-Symmetric extension of the standard model.

In a large fraction of parameter space the decay of MSSM Higgs boson to τ-leptons is observable in ATLAS, provided hadronic τ decays can be separated from QCD jets. Fine-grained shower shape information from the EM calorimeter, together with information from the inner detector and the hadronic calorimeter, are needed to achieve a separation of ~ 400 for a τ-efficiency of 30 %.

Another important goal is the search for heavy partners of the Z and W gauge bosons. ATLAS is sensitive to the Z' and W' up to 5-6 TeV. For decays of these heavy objects into electrons ($Z' \to e^+e^-$, $W' \to e\nu$) the mass resolution of the EM calorimeter is expected to be competitive with the precision of the muon spectrometer for $Z' \to \mu^+\mu^-$ or $W' \to \mu\nu$.

ATLAS will have a dense, high-granularity Liquid Argon calorimeter to measure the energy of photons and electrons [63, 64]. The electromagnetic shower develops in lead absorber plates. The thickness of the absorber plates is 1.5 mm in the barrel section and 1.7 mm and 2.2 mm in the first and second end-cap wheel. The absorbers are folded into an accordion shape and oriented along R (z in the end-caps) to provide complete ϕ symmetry without azimuthal cracks.

The energy measurement is based on the determination of the ionisation energy loss by the charged component of the shower (electrons and positrons) in thin (2-6 mm) gaps between absorber plates. To this end the gaps are filled with liquid argon and equipped with multiple electrodes. The electrodes are segmented into strips and pads, allowing a fine granularity. The response of a bipolar shaper with a shaping time of 30-40 ns[5] is sampled every 25 ns. The result is stored in an analog memory during the level-1 trigger latency. On receipt of a trigger, five samples (separated by 25 ns) are digitised and sent to the data acquisition system. A three-gain scale is used to cover the 16 bit dynamic range from 50 MeV to 3 TeV.

The full detector presents a total of 24 (26) radiation lengths in the barrel (end-cap) regions to reduce the error in the energy resolution due to longitudinal fluctuations of high energy ($E_T > 500\ GeV$) showers to an acceptable level. Particle identification (γ/jet, electron/jet and τ/jet separation) is achieved by laterally and longitudinally segmenting the calorimeter. High granularity is also needed to achieve good position resolution and control the noise contribution due to pile-up. The EM calorimeter is longitudinally segmented in three layers for most of the rapidity range. Each layer has a different granularity: $\delta\eta \times \delta\phi = 0.003 \times 0.1$, 0.025×0.025 and 0.05×0.025 for the first, second and third sampling respectively. The granularity becomes coarser in the most forward sections.

A fine-grained pre-shower layer (also known as the presampler) precedes the EM calorimeter for the rapidity range $|\eta| < 1.8$. It is intended to correct for the energy loss in the material in front of the EM calorimeter, which reaches 2 to 3 X_0 in this rapidity range. The presampler is made of a 1.1 cm thick liquid Argon layer with a granularity of a few mm ($\delta\eta \times \delta\phi = 0.025 \times 0.1$).

Extensive simulations of the electromagnetic calorimeter indicate that the geometry and technology proposed by the ATLAS collaboration meet the strict requirements for the energy and position resolution posed by the physics program [65]. A slight deterioration of the

[5]The noise contribution from pile-up depends on the location (rapidity) in the detector. The peaking time has been optimised for each region to obtain the best quadratic sum of the electronics and pile-up noise contributions.

performance is expected in the barrel to end-cap transition region about $|\eta| = 1.5$. Beam tests of prototype modules with ATLAS-like electronics confirm the simulation results [66].

2.4.2 The hadronic calorimeter

The hadronic calorimeter will measure the energy and direction of *jets* of particles formed by the hadronisation of quarks or gluons, or from the hadronic decay of τ-leptons.

A good di-jet invariant mass resolution in the $H \rightarrow b\bar{b}$ channel is vital for the detection of the standard model Higgs boson in the low and intermediate mass range. The jet energy resolution is required to be measured with a precision given by:

$$\frac{\Delta E}{E} = \frac{50\%}{\sqrt{E}} \oplus 3\%, |\eta| < 3 \tag{2.1}$$

$$\frac{\Delta E_T}{E_T} = \frac{100\%}{\sqrt{E}} \oplus 10\%, 3 < |\eta| < 5 \tag{2.2}$$

where the energy E is expressed in GeV.

A hermetic hadronic calorimeter with a large rapidity coverage is crucial to the measurement of missing transverse momentum (p_T^{miss}), the missing transverse momentum of the event.

The total thickness of the electromagnetic + hadronic calorimeters is required to be over 10 interaction lengths, both to fully contain the shower and to minimise leakage into the muon spectrometers.

In the barrel region, a tile calorimeter will measure the energy of the hadronic shower. A central barrel and two extensions (extended barrels) yield a total pseudo-rapidity coverage of $|\eta| < 1.6$. Three longitudinal sections present 1.4, 3.9 and 1.8 interaction lengths to incoming hadronic particles. The total thickness, summing the 1.2λ in the electromagnetic calorimeter and the extra material in the support structure, reaches 11 λ. The tiles and absorber plates are oriented perpendicular to the beam axis and staggered in depth.

The thickness of one period is 17 mm (3 mm scintillator tile + 14 mm absorber). Each tile is read out on both sides by wavelength shifting fibres and two separate photo-multiplier tubes. Readout cells are formed by joining groups of tiles. The groups are chosen so that cells are pseudo-projective to the interaction point. Thus, a granularity of $\delta\eta \times \delta\phi = 0.1 \times 0.1$ (0.2×0.1 in the third sampling) is achieved, with a total number of channels of the order of 10000.

In the forward region, a Liquid Argon Hadronic Calorimeter is preferred because of its radiation-tolerance. The liquid Argon hadronic end-cap calorimeter covers the pseudo-rapidity interval from $|\eta| = 1.5$ to $|\eta| = 3.2$. The absorber material is provided by 25 and 50 mm copper plates arranged in a parallel-plate geometry. The 8.5 mm gap between the plates is filled with liquid Argon and equipped with 3 electrodes.

The rapidity range from $3.2 < |\eta| < 3.9$ is covered by the high-density forward calorimeter. The FCAL is made of rod electrodes in a metal (copper/tungsten) matrix with regularly spaced longitudinal channels filled with liquid Argon. The forward hadronic calorimeters share the end-cap cryostat with the electromagnetic calorimeter.

The ATLAS calorimeter performance technical design reports [65, 64, 67] present the results of detailed simulation studies of the hadronic calorimeters. The energy resolution requirements of equations 2.1 and 2.2 are found to be met by the current design. This conclusion is corroborated by experimental results obtained in beam tests of prototype modules [68, 69]. From a detailed study a mass resolution of about 16 GeV is expected for two important benchmark channels: the decay of a standard model Higgs to a $b\bar{b}$ pair and the detection of the super-symmetric neutral Higgs boson A^0 and H^0 through their decay to $\tau^+\tau^-$.

2.5 The muon spectrometer

Many of the physics processes of interest involve the production of muons. Therefore, the identification of muons provide an important signature for the event selection (trigger) of the experiment. Also, the accurate determination of the momenta of muon pairs allows the precise reconstruction of short-lived particles that decay into muons. A good example is the detection of a super-symmetric Higgs boson through its muon decay channel investigated in chapter 6.

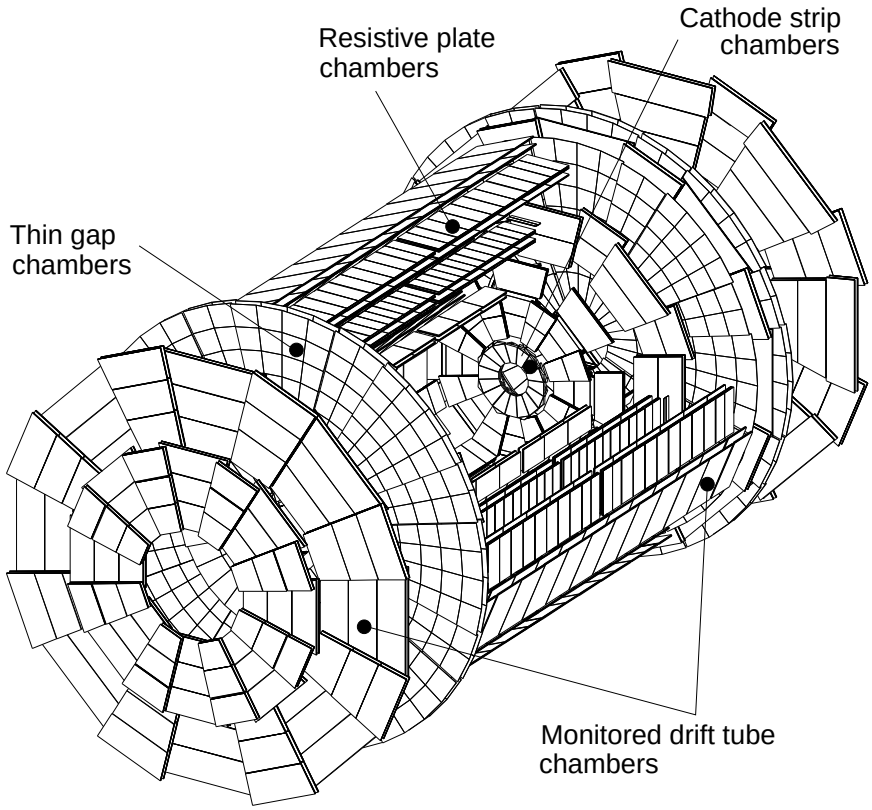

Figure 2.9: *Layout of the ATLAS muon system. Figure taken from [56].*

The magnetic field in the muon spectrometer is provided by a large (26 meter long by an outer diameter of 20 meter) octagonal structure of air-core toroids, producing an approximately cylindrical field. The barrel toroid covers the pseudo-rapidity range $|\eta| < 1.0$, while two end-cap toroids cover the forward region $1.4 < |\eta| < 2.7$. In the transition regions the field is a combination of barrel and end-cap fields.

Muons do not feel the strong interactions and are relatively heavy. The dominant energy loss mechanism in matter is ionisation. These properties allow muons to traverse the entire inner detector and calorimeter. The muon spectrometer forms the outermost layer of the ATLAS detector. It provides efficient identification (> 90 %) of all muons with $p_T > 6\ GeV$ and pseudo-rapidity $|\eta| < 2.7$. Position measurements in three layers in the 0.6 Tesla field of the air-core toroids yield a very precise measurement of the transverse momentum of high-p_T muons. Combining the measurements of the muon spectrometer and the inner detector, the momentum resolution of isolated muons is expected to be of the order of a few % over the p_T range from 6 GeV to several hundreds of GeV. The resulting invariant mass resolution for muon pairs originating from the decay of short-lived (Higgs, Z) bosons is of the order of 1.6 GeV for a mass of 130 GeV [56].

To achieve the momentum resolution and efficiency quoted above *and* provide a fast response for the trigger, a number of complementary techniques are used. Also, different technology choices are made to cope with the high rate in the end-cap regions. The location of the four different detector types is shown in figure 2.9.

The precision measurements of the muon momentum in the barrel region is based on the sagitta of three layers (stations) in the magnetic field. In each station multiple position measurements are made using monitored drift tubes (MDT). Each MDT consists of a 30 mm aluminium tube filled with a gas mixture of Argon (93 %) and Carbon-dioxide (7 %) at a pressure of 3 bar. The signal is read on a central W-Re wire. The track position with respect to the wire is determined from the drift time measurement with a resolution of ~ 80 μm.

In the end-caps no stations can be placed in the field volume. The momentum is determined from a point angle measurement using the four vertical stations of the end-cap. The stations are equipped with cathode strip chambers. These are multi-wire proportional chambers filled with a 30 % Argon, 50 % CO_2, 20 % CF_4 mixture. The avalanche in the gas induces a signal on the cathode. The segmentation of the cathode yields a position measurement with a resolution of ~ 60 μm. A second cathode measures the coordinate perpendicular to the bending direction, thus providing robust pattern recognition.

The muon trigger is based on a number of dedicated, fast detectors. Resistive plate chambers consist of a narrow gas ($C_2H_2F_4$) gap between resistive Bakelite plates covered with readout strips at a pitch of 30-39 mm. These RPCs combine an adequate spatial resolution of 1 cm with an excellent time resolution of 1 ns. The use of two perpendicular orientations allows the measurement of the η and ϕ coordinate.

Again, in the end-caps a different choice is made as a result of the high rate. Thin Gap Chambers are multi-wire proportional chambers filled with a highly quenching gas mixture of 55 % CO_2 and 55 % n-pentane. This allows operation of the chambers in saturated mode. The distance between cathode and anode is kept very small (2.8 mm) to assure a short drift time.

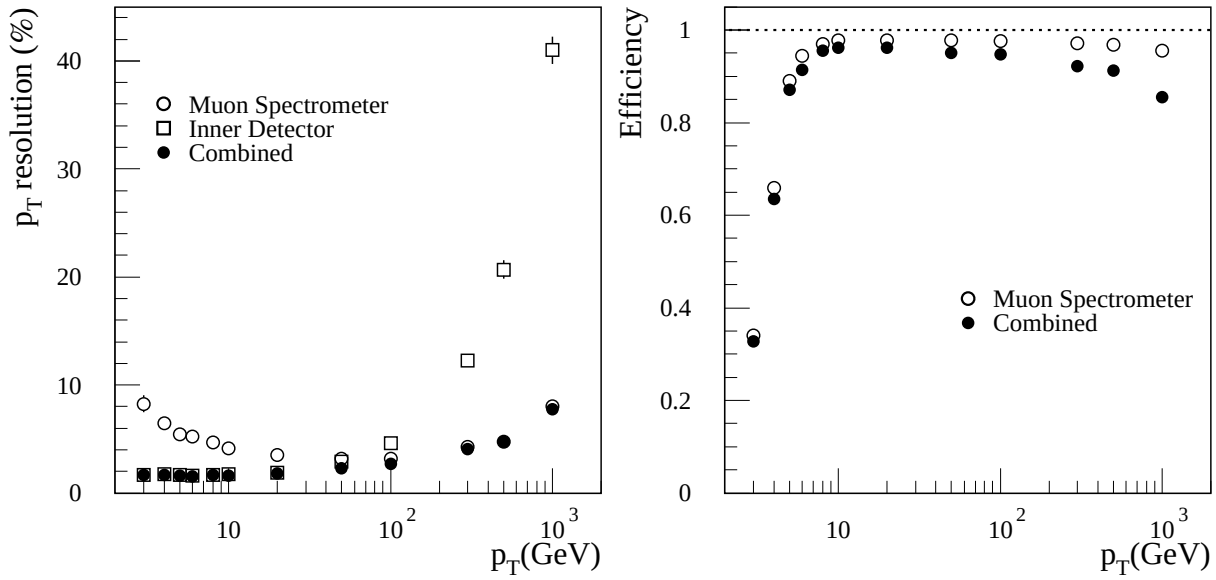

Figure 2.10: *Muon reconstruction performance of the muon spectrometer (open circles), the inner detector (open squares) and the combination of both (filled circles). Transverse momentum resolution ($\sigma(p_T)/p_T$) (leftmost figure) and reconstruction efficiency (rightmost figure) versus muon transverse momentum. Figures taken from [56].*

Simulation studies [56, 70] and beam tests [71] indicate that the muon spectrometer is capable of providing an efficient trigger for events where muons with a transverse momentum over 6 GeV are produced. The final ATLAS muon reconstruction uses the combined information from the high resolution measurements in the muon spectrometer and the inner detector. Figures 2.10 show the complementarity of the performance of the inner detector and the muon spectrometer yield a good performance over a large p_T range: $\sigma(p_T) < 2\%$ for $6 < p_T < 100\ GeV$, slightly deteriorating to about 5 % for 1 TeV muons. Moreover, the reconstruction efficiency is over 90 % throughout the momentum range ($p_T > 6\ GeV$).

2.6 The trigger

The high design luminosity of $10^{34}/cm^2s$ of the LHC will lead to over 20 interactions per bunch crossing. Thus, each second close to 10^9 interactions occur. Most of these interactions are minimum bias events that have a limited interest. The detector consists of very complex systems producing large amounts of data. The SCT and PIXEL detectors read out $\sim$ 6 million and $\sim$ 100 million channels respectively. Current data storage technology limits the amount of data that can be stored to the order of 100 MB/s. This corresponds to a maximum trigger rate of $\sim$ 100 Hz.

The trigger system is designed to bridge this gap, maintaining nearly all interesting physics events, while efficiently rejecting the minimum bias background. The system is to be capable of a fast reconstruction of (part of) the data from the different detectors to look for signatures of interesting physics. This decision making process is divided into a number

of stages or trigger levels, see figure 2.11, that are discussed separately.

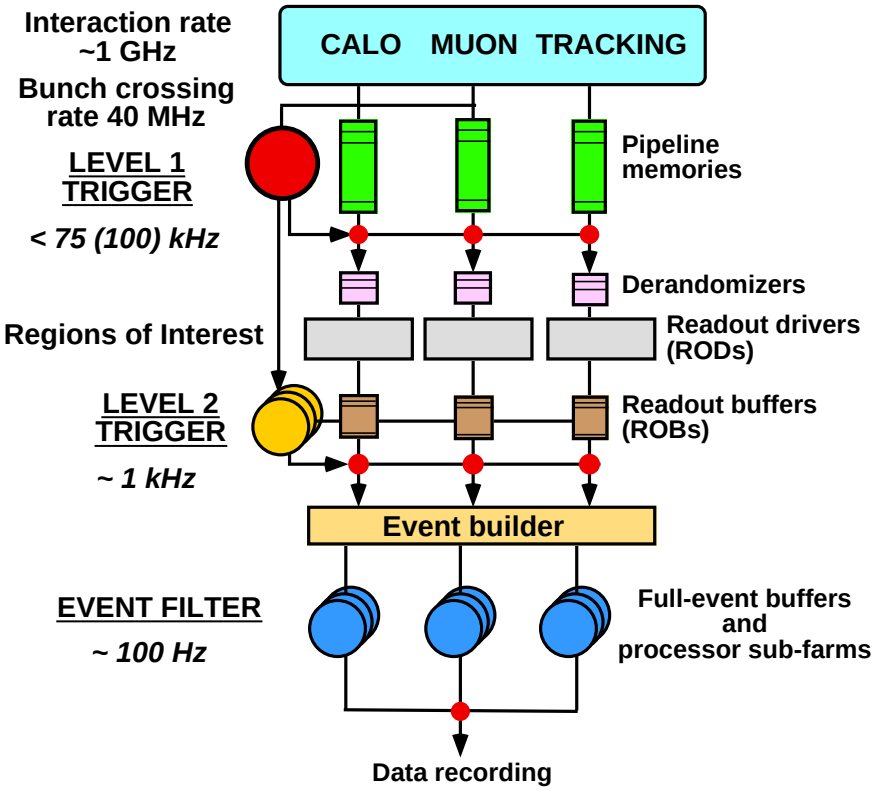

Figure 2.11: *Schematic view of the ATLAS trigger. Figure taken from [56].*

One of the most challenging aspects of the trigger design is the need to keep an open design to unknown physics channels. The criteria used to classify the events should be as simple and general as possible to avoid biases.

A detailed description of the trigger and data acquisition systems is to be found in the ATLAS technical design report and specific proposals and progress reports from the trigger community [56, 72, 73, 74, 75]. An interesting introduction can be found in reference [76]. The technical design report for the high level trigger will be presented in summer 2003.

2.6.1 The Level-1 trigger

This is the lowest trigger level: it has to deal with the high bunch crossing frequency of 40 MHz. The time to reach the level-1 decision is only $\sim 3\ \mu s$.

During the trigger latency the data from the detector is stored in a pipeline. To achieve a fast turn-back time, the Level-1 trigger uses information from a relatively small number of detectors through a special data channel, i.e. it acts before the full data is collected by the Read Out Drivers. At this level, the trigger decision is entirely based on an analysis of the data from the dedicated, fast muon stations (Thin Gap Chambers and Resistive Plate Chambers) and the calorimeter data with a reduced granularity. As indicated in figure 2.11, no information from the inner detector is available at this level.

The algorithms are implemented in hardware to cope with the high rate and the short latency. The use of Field Programmable Gate Arrays allows for the fast adaptation of the threshold levels as a reaction to changes in the luminosity or the measurement of more precise cross-sections.

The physics events of interest are characterised by the relative high transverse momentum of the collision products. The Level-1 trigger considers the presence of muons or electromagnetic, hadronic or jet clusters with relatively high transverse momentum as evidence for interesting physics.

The maximum output rate of the first trigger level is limited to 100 kHz. For the events that pass the level-1 selection, the results are used to determine detector regions of interest (ROIs) that are to be analysed more carefully in the higher levels.

2.6.2 The High Level Trigger

The high level trigger comprises the Level-2 trigger and a third level that is labeled as the event filter in figure 2.11. In these two steps the 100 kHz event rate is further reduced to about 1 kHz and 100 Hz, respectively.

The second level trigger reconstructs the data in the regions of interest defined by the level-1 trigger. Thus, in the majority of events only a fraction of the total data has to be reconstructed. The muon or electron candidates are extrapolated back to the inner detector. The requirement of consistency of the level-1 hypothesis with the inner detector data yields an efficient rejection of background events.

A wide range of physics signatures are translated into trigger menus. Examples are the presence of isolated particles with high transverse momentum: electrons with $p_T > 25\ GeV$, photons with $p_T > 20\ GeV$ or muons with $p_T > 20\ GeV$. Also pairs of isolated electrons or muons with slightly lower momentum are accepted. A number of additional menus is based on the presence of a single jet with very high transverse momentum ($p_T > 360\ GeV$) or triplets or quadruplets of jets with a more moderate p_T threshold. Finally, the presence of missing transverse energy combined with at least one jet is taken to be a signature.

The third stage, the event filter, is placed after the event builder. At this point detailed alignment and calibration data are available. The definition of an abstract event data model allows the use of off-line algorithms in the event filter.

The high level trigger is entirely implemented in software and is to be executed on farms of commercially available processing units. This allows a flexible adaptation of algorithms, known as steering.

B-physics dominates the trigger rate during the initial years when the LHC is run with lower luminosity. The B-trigger is dominated by the low p_T muons returned at high rates by the level-1 trigger. The rate is reduced by reconstructing the decay products of the B-meson using the full information of the inner detector.

2.7 Summary

The Large Hadron Collider (LHC) is currently being built in the former LEP tunnel at the 'Centre Européen de Physique Nucléaire' in Geneva, Switzerland. It will collide protons at

an unprecedented center-of-mass energy of 14 TeV.

The bunch crossing frequency of 40 MHz allows to reach the highest luminosity ever achieved: from the initial "low" luminosity $\mathcal{L} \sim 10^{33} s^{-1} cm^{-2}$ the accelerator is to ramp up in the first years to $\mathcal{L} = 10^{34} s^{-1} cm^{-2}$.

The combination of high energy and high luminosity allows to study the energy range from $\sim$ 100 GeV to a few TeV. Several theoretical predictions may thus be tested. If the standard model or its minimal super-symmetric extension is correct, the elusive Higgs boson is expected to be produced in sufficient quantities at the LHC. Many *new physics* scenarios predict observable features below 1 TeV: for example the lightest stable super-partner of super-symmetric models.

Also, the high luminosity yields high rates of many standard model processes. The LHC will be a b, t, Z and W-factory. The study of their decay channels allows precision measurements of many standard model parameters.

The ATLAS detector is to be installed in one of the four bunch-crossing areas of the LHC. It is one of the two general-purpose experiments. To fully benefit from the LHC physics potential the ATLAS experiment is to consist of three sub-systems:

- the inner detector is to provide precise tracking and vertexing in the innermost layers around the interaction point
- the calorimeters are to precisely measure the energy and direction of all interacting particles
- the outer layers of the detector are occupied by muon chambers that are to yield a precise measurement of the muon momenta

The design of prototypes satisfying the strict requirements posed by the physics program has been successfully completed. Production of the detector elements is proceeding in high-energy physics institutes and industries all over the world.

Chapter 3

The Semi-Conductor Tracker

The semiconductor tracker (SCT) collaboration has designed silicon micro strip detector modules to cover the intermediate radii of the ATLAS inner detector. In this chapter these modules are discussed in detail.

The first section provides some background information on the operating principles of silicon micro-strip detectors. In section 3.2 the effect of radiation on the properties of the detector and front-end electronics is discussed. The findings are illustrated by a Monte Carlo model for the detector signal before and after irradiation. In section 3.3 the SCT module design is presented. The detectors and read-out electronics are discussed in detail. Finally, section 3.4 summarises the most important findings.

3.1 Introduction to Silicon Micro-strip Detectors

In this section the operating principles of silicon micro-strip detectors are described. The first section is devoted to the reverse biased silicon *pn* junction. Then, the main mechanism by which energy is deposited in the detector - ionisation - is discussed briefly, together with the drift of the charge carriers that allows to collect the deposited energy on one (or both) of the sides of the junction.

3.1.1 The reverse biased *pn*-junction

The basis of semi-conductor micro-strip detectors is formed by a reverse biased semi-conductor junction. Here, the case of a silicon *pn* junction - the choice of the SCT - is discussed.

A *diode* is created by joining *p*-type semiconductor material, doped with elements from group III (acceptors), with *n*-type material, doped with elements from group V (donors). In the contact region between materials with both types of dopants, a depleted region forms through the diffusion of charge carriers. This region can be made to extend further into the material by applying a negative reverse bias voltage V_A. With some assumptions, known as the depletion approximation, the width w of the depleted region can be calculated in one

dimension perpendicular to the contact area (see for example [77]):

$$w_n = \sqrt{\frac{2K_S\epsilon_0}{q}(-V_A)\frac{N_A}{N_D(N_A+N_D)}} \tag{3.1}$$

for the n side and:

$$w_p = \sqrt{\frac{2K_S\epsilon_0}{q}(-V_A)\frac{N_D}{N_A(N_A+N_D)}} \tag{3.2}$$

for the depleted region on the p side. The dielectric constant $K_s\epsilon_0$ is a material constant and q is the charge of the electron. The relative widths of the depleted regions on both sides of the junction is seen to depend solely on the dopant concentrations: N_A is the acceptor concentration of the p-type material and N_D the donor concentration of the n-type material. This relation can be expressed as:

$$N_A w_p = N_D w_n \tag{3.3}$$

By choosing the acceptor concentration much larger than the donor concentration the depleted region can be made to extend much further into the n-type material than in the p direction. Thus, a large thickness of n-bulk can be depleted using a thin layer of heavily doped p-type material. Junctions with heavier doping of the p-type material are denoted as p^+n. Typical dopant concentrations in detector applications are of the order of 10^{12} for the bulk n-type material and up to 10^{14} for the p^+ implants.

The reverse bias voltage where the full thickness of n-type bulk is depleted - the full depletion voltage - is given by:

$$V_{FD} = \frac{qd^2}{2K_S\epsilon_0}\frac{N_D(N_A+N_D)}{N_A} = \frac{qd^2}{2K_S\epsilon_0}|N_{eff}| \tag{3.4}$$

where d is the detector thickness and the effective dopant concentration is related to the specific resistivity and the carrier mobility by the relation $N_{eff} = 1/(q\mu\rho)$. In typical detectors depleted regions of several hundreds of microns are obtained with bias voltages of less than 100 V.

The reverse bias voltage gives rise to a leakage current in the diode. In reference [77] the leakage current is calculated for an ideal diode taking into account two contributions: the diffusion current is generated in the non-depleted silicon and reaches the depleted region by diffusion; the generation current is due to thermally generated carriers in the depleted region. The sum of both contributions gives the total leakage current:

$$I \sim -I_0 - qA\frac{n_i w_n}{2\tau_0} \tag{3.5}$$

where n_i is the intrinsic carrier concentration, A is the detector surface and τ_0 is the effective carrier lifetime $\tau_0 = \frac{\tau_p+\tau_n}{2}$. The diffusion current I_0 is generally small in silicon. The proportionality of the generation current to the depletion width W leads to a dependence on the bias voltage $I \propto \sqrt{V_A}$ for $V_A < V_{FD}$. The intrinsic carrier concentration depends strongly on the temperature:

$$n_i \propto e^{-E_g/kT} \tag{3.6}$$

where E_g is the band gap, 1.12 eV in silicon. Therefore, the sensor temperature is an important parameter to control the leakage current.

At a certain reverse bias voltage the drift field is so high that carriers may become energetic enough to ionise an atom in the lattice. The created electron-hole pair is accelerated and releases more carriers. The avalanche thus created is responsible for an abrupt rise of the leakage current. This mechanism is called avalanche break-down and the voltage at which it occurs is known as the break-down voltage.

Progress in the semi-conductor industry makes possible the creation of large area detectors: out of a single 4" wafer, $6 \times 6cm^2$ silicon detector can be made; 6"' wafers allow even large areas. Detectors can be made to stand high voltages, up to 500 V with a very small leakage current (several μA at room temperature).

3.1.2 Ionisation

Passage of a charged particle through matter results in the ionisation of the medium, i.e. electrons are liberated from the atoms. In solids this leads to the creation of an electron-hole pair. The mean rate of energy loss for relativistic heavy charged particles [1] in a medium is given by the Bethe-Bloch equation, see for example [1]:

$$- < \frac{dE}{dx} >= Kz^2 \frac{Z}{A} \frac{1}{\beta^2} [\frac{1}{2} \log \frac{2m_e c^2 \beta^2 \gamma^2 T_{max}}{I^2} - \beta^2 - \frac{\delta}{2}] \tag{3.7}$$

where β and γ are given by the velocity of the particle: $\beta = v/c$ and $\gamma = \sqrt{1-\beta^2}$. The path length dx is expressed as mass per unit area, thus taking into account the energy loss dependence on the density of the material. The maximum energy that can be transferred in a collision, is given by:

$$T_{max} = \frac{2m_e c^2 \beta^2 \gamma^2}{1 + 2\gamma m_e/M + (me/M)^2} \tag{3.8}$$

where M is the mass of the incoming particle. The variables that appear in the formulae are listed in table 3.1. For material constants the numerical value for silicon at room temperature is given.

The term $\delta/2$ is due to the density effect: the electric field of the incoming particle polarises atoms along its path, which in turn shield the electric field. The effect - a reduction of the energy loss - becomes significant for highly relativistic particles in dense media.

$$\delta/2 \rightarrow \log \hbar\omega_p/I + \log \beta\gamma - 1/2 \tag{3.9}$$

The mean energy loss reaches a minimum and is nearly independent of particle type for $\beta\gamma \sim 1$, corresponding to a momentum of of the order of a GeV for pions, protons and muons. The energy loss rises very slowly with increasing momentum. Therefore, relativistic particles (other than electrons or positrons) are often treated like Minimum Ionising Particles (MIPs).

[1] The adjective "heavy" excludes electrons and positrons. Their energy loss is not well described by the Bethe-Bloch expression of equation 3.7

Property	*Symbol*	*Value*	*Units*
mean excitation energy	I	173	eV
atomic number of the medium	Z	14	
atomic mass of the medium	A	28.09	
density of the medium	ρ	2.33	g/cm^3
Ionisation potential		3.62	eV
charge of incident particle	z	± 1	
Plasma energy	$\hbar\omega_p$	$28.816\sqrt{\rho < Z/A >}$	eV
electron charge	e	$-1.6 \cdot 10^{-19}$	C
electron mass	$m_e c^2$	0.511	MeV
Euler's constant	C	0.577	

Table 3.1: *A list of some important properties of Silicon at room temperature, their symbol, numerical value and units. Values taken from [78] and [1]*

In some collisions the energy transfer is substantial and the emitted electron can travel significant distances, of the order of 15 μm in silicon. These so-called δ-electrons (or δ-rays or knock-on electrons), in their turn, ionise atoms along their trajectory, resulting in a displacement of the center of the charge distribution of several μm.

The energy loss *distribution* for a thin absorber is given by Landau's theory [79]. Formally, the requirement that the absorber should be thin can be expressed as: $\overline{\Delta}/T_{max} < 0.01$, that is the average energy loss $\overline{\Delta}$ in the absorber should be small compared to the maximum energy loss T_{max} in a single collision. In Landau theory it is then assumed that the maximum energy transfer is infinite, the electrons can be treated as free and the incident particle has a constant velocity to reach the following energy distribution [79, 78]:

$$f(x,\Delta) = \phi(\lambda)/\xi \tag{3.10}$$

$$\phi(\lambda) = \frac{1}{\pi}\int_0^\infty e^{-u\ln u - u\lambda}\sin(\pi u)du \tag{3.11}$$

$$\lambda = \frac{1}{\xi}[\Delta - \xi(\ln\xi - \ln\frac{(1-\beta^2)I^2}{2mc^2\beta^2} + \beta^2 + 1 - C)] \tag{3.12}$$

The number of created electron-hole pairs is obtained by dividing the deposited energy by the ionisation potential of the material (3.62 eV for silicon at room temperature). In the following the signal is assumed to be equal to the charge of all carriers of one type [2].

For 180 GeV pions normally incident on a 285 μm thick silicon wafer, Landau theory predicts that approximately 22,300 electron-hole pairs are created. Landau theory ignores atomic binding effects. Also, direct collisions giving rise to δ-electrons are not taken into account. Nevertheless, the most probable energy loss predicted by Landau theory is found to be rather accurate. The experimentally observed energy *distributions*, however, are generally

[2] This is obviously a simplification. Although the signal is predominantly due to one type of carriers that drifts towards the readout plane, the drifting carriers of the other type also contribute. The simulation in section 3.2.3 includes both contributions

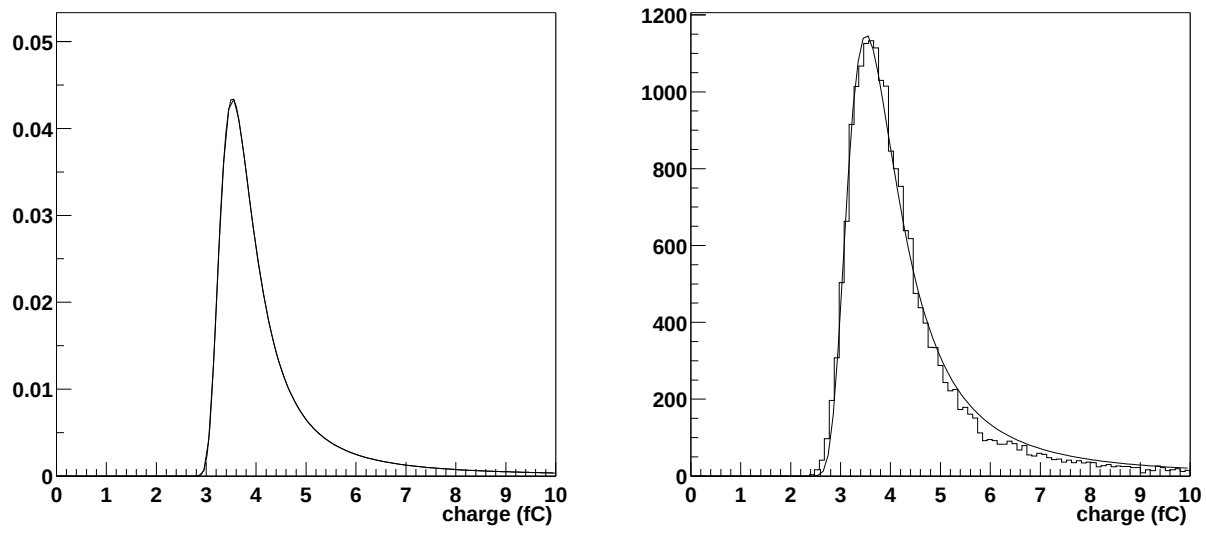

Figure 3.1: *Distribution of charge depositions by 180 GeV pions perpendicularly incident on a Silicon wafer. The smooth line superposed on the histogram represents a fit with a Landau distribution with variable height, most probable value and width. Leftmost figure: calculation according to the Landau formalism; fit results: MPV = 3.58 fC, width/MPV = 6.3 %. Rightmost figure: simulation using the GEANT4 [80] package (courtesy of Pavel Reznicek); fit results: MPV = 3.58 fC, width/MPV = 9.2 %.*

significantly broader than the Landau prediction [81, 82]. Various semi-phenomenological models exist that provide a good description of the observed distributions [81, 80, 82]. Figures 3.1 compare the charge distributions for 180 GeV pions in 285 μm of silicon. The leftmost figure corresponds to the theoretical Landau distribution, the rightmost figure to a Monte Carlo calculation in GEANT4 [83].

The peak of the charge distribution is $\sim$ 3.6 fC. In binary systems, with on-chip discrimination, it is easier to determine the median charge than the peak of the charge distribution. The expected median charge is 3.9 fC from Landau theory and 4.0 fC from simulations using GEANT4.

3.1.3 Charge collection

From the discussion in previous sections it has become clear that charged particles produce a small signal when passing through silicon. In a reverse biased pn junction the created holes and electrons drift to the anode and cathode sides of the device, respectively.

The drift time for a carrier released at a distance z_0 from the readout side is to first order proportional to the drift field and the mobility. If a uniform field is assumed the charge collection time becomes a simple function of device thickness d and bias voltage V:

$$t \approx \frac{z_0}{\mu E_{drift}} \approx \frac{z_0 d}{\mu V} \tag{3.13}$$

where z_0 is the distance from the readout plane where the charge carriers were created. The mobility μ is nearly three times larger for electrons than for holes. Therefore, collection of the signal due to electrons is much faster. A detailed simulation of charge collection, taking into account a realistic electric field and saturation of the carrier velocity, is presented in section 3.2.3.

The initial ionisation is limited to a cylinder of radius $\sim$ 1 μm around the particle's trajectory. The spatial distribution of the cloud of drifting carriers is dominated by diffusion. The contribution due to the repulsion between carriers of the same type is insignificant. For carriers released at time t=0 at z=0, the spatial distribution evolves with time according to:

$$\frac{dN}{N} = \frac{1}{\sqrt{4\pi Dt}} e^{\frac{-z^2}{4Dt}} dz \tag{3.14}$$

forming a Gaussian distribution of width $\sigma = \sqrt{2Dt}$. The diffusion constant D is related to the carrier mobility: $D = \frac{kT}{q}\mu$ where k is Boltzmann's constant, T is the temperature and q is the electron charge. Using the approximation in equation 3.13, the dependence of the drift time and the diffusion constant on the mobility (and thus carrier type) cancel and the spatial distribution of the drifting carriers is the same for electrons and holes.

Electron-hole pairs due to ionisation are produced uniformly along the particle trajectory. The spatial distribution of the charge reaching the readout plane is the integral of equation 3.14 over the position along the track z_0 where the bounds are given by the thickness of the detector. The resulting width of the spatial distribution for a typical device close to room temperature is quite small. Belau et al. [84] have measured the FWHM in a 280 μm thick device at room temperature to be around 10 μm at 50 V and 5 μm at 200 V.

Silicon detectors take advantage of the narrow spatial distribution of the charge to create a position sensitive detector. The sensitivity to the position of the particle is obtained by segmenting the dopant material on the readout side[3]. Using the advanced photo-lithographic techniques of semiconductor industry, micro-strips of the order of 10 μm wide at a pitch down to 20 μm are obtained[4].

Even if the full deposited charge is collected on a single readout strip, a signal of typically 4 fC is very small. External amplification is in general needed before further processing of the signal. Long cables between the readout strip and the electronics would imply a large input capacitance for the amplifier, with the corresponding loss of noise performance, and are not practical in large systems with of the order of a million channels. The electronics is therefore located very close to the silicon sensors. Its presence in the tracking volume leads to strict requirements on the power consumption, the amount of material used and the radiation hardness of the electronics design. Modern integrated components are able to meet these requirements.

[3]Double-sided strip detectors take advantage of the fact that both types of carriers drift in opposite directions by segmenting both sides of the detector in micro-strips

[4]Pixel detectors use the same technology, but instead of strips the surface of the junction is subdivided in small rectangular areas. Detection of signal on one of the pixels provides an unambiguous measurement of two spatial coordinates. This makes pixel detectors extremely suitable for environments with a high track density, like the region nearest to the interaction point in the ATLAS experiment

3.2 Radiation damage

In section 2.3.6 it was estimated that the inner layers of the SCT must resist large fluences of charged particles and non-ionising radiation throughout the lifetime of the ATLAS experiment. High doses of radiation seriously alter the properties of detector devices. In this section a brief overview is given of what is known about the effects of radiation on the properties of detectors and electronics.

In the description of the effects of radiation on devices, two mechanisms should be distinguished:

- ionisation damage is caused by charged particles that ionise the Silicon atoms, liberating charge carriers.
- displacement damage occurs when incident particles displace a Silicon atom from its position in the crystal lattice.

The effects of both types of radiation damage are quite distinct in bulk silicon like the detectors, or very complex, sensitive circuits like the electronics. Therefore, the effects of radiation is discussed separately for the detectors and the read-out electronics.

3.2.1 Detectors

Ionisation is the dominant energy loss mechanism in Silicon - it is this mechanism that allows to use of silicon devices as tracking detectors. Generally it does not cause persistent damage in the bulk of the silicon. Charge carriers due to ionisation can, however, be trapped in the oxide or poly-silicon layers that are used to isolate certain peripheral structures - guard rings, bias circuit - in the detectors. Holes trapped in an oxide layer attract high densities of electrons that may form conducting channels. A careful design of the insulating structures of the detectors is needed to avoid this type of problems.

Although non-ionising events are relatively rare, they are the dominant source of damage for bulk silicon in the detectors. Displacement damage occurs when a non-ionising interaction removes silicon atoms from their lattice site. The probability depends on the radiation type and energy, but usually scales rather well with the non ionising energy loss (NIEL). Displacement damage is commonly expressed in the equivalent fluence of 1 MeV neutrons. Displacement damage has been studied extensively, for example by the ROSE collaboration [85, 86].

Whenever an atom is displaced from its lattice site, two lattice defects are created immediately: an interstitial atom and a vacancy. The recoiling silicon atom can in its turn displace atoms creating a defect cluster. Defects can be quite mobile and thus combine with other defects or impurities in the Silicon (Oxygen, Carbon), giving rise to a complex spectrum of (multiple) defects.

The lattice defects created by radiation predominantly act as acceptors in the bulk Silicon [87, 85]. As the irradiation proceeds the effective doping of the material changes. At some point the concentration of acceptors due to defects exceeds the initial doping; the n-type silicon of the bulk has undergone *type inversion*. The evolution of the effective dopant

concentration with fluence is described by [88]:

$$N_{eff}(\Phi) = -N_0 e^{-c\Phi} + g_c\Phi + g_s\Phi e^{t/\tau(T)} + N_Y(\Phi, t, T) \tag{3.15}$$

The first term accounts for donor removal, hence the dependence on the initial dopant concentration N_0. The second term reflects the creation of new acceptor states. The rate of both processes, i.e. the constants c and g_c, depends on particle type and energy. The third and fourth time-dependent terms represent the annealing of the damage: the radiation-induced defects are not stable, but evolve with time. Different types of defects can combine to create new states or recombine. The third term corresponds to the processes that lead to reduction of the acceptor states, so-called beneficial annealing. The fourth term describes anti-annealing: processes leading to an increase in acceptor states. The fluence, time and temperature dependences of anti-annealing can be parametrised as [88]:

$$N_Y(\Phi, t, T) = g_Y\Phi[1 - \frac{1}{1 + g_Y\Phi \cdot k_0 e^{-E_a/k_BT} \cdot t} \tag{3.16}$$

Operation at a low temperature can slow down the anti-annealing and extend the lifetime of the detector, but constrains the number and duration of the accesses to the detector.

Figure 3.2 shows the evolution of the effective dopant concentration of equation 3.15 for two different values of the initial dopant concentration. The constants are taken from [88] and correspond to irradiation with high energy protons. Note that the irradiation is supposed to be sufficiently fast, or the temperature kept sufficiently low, that annealing plays no role. It is clear that any gain obtained by using high dopant concentrations becomes insignificant for high fluences. For the inner layers of the SCT, where the total expected fluence is equivalent to $2 - 3 \cdot 10^{14}$ protons/cm^2, type inversion is expected to occur after a few years of operation of the ATLAS detector.

The change in effective dopant concentration leads to a range of changes in the properties of the detector. After type inversion the pn junction forms at the backplane. This means that in partially depleted operation a dead zone occupies the region between the depleted bulk and the readout strips, stopping the carriers before reaching the readout strips. A signal can still be induced across the dead region, but the relatively large distance results in a signal attenuation.

The depletion voltage is linked to the dopant concentration (see equation 3.4) and therefore evolves with irradiation, as well. In n-type material, the depletion voltage first decreases. After type inversion the depletion voltage starts to rise again. In hard radiation environments, the increase in depletion voltage will eventually limit the lifetime of the detectors. In the case of SCT prototypes irradiated to the full dose of $3 \cdot 10^{14}$ protons/cm^2, depletion voltages of the order of 200-300 V have been estimated.

Some defects can form mid-gap states. These may act as stepping stones in the thermal generation of carriers and thus increase the leakage current. Reference [85] finds a linear increase of the leakage current with fluence: $I = \alpha\Phi_{eq}V$, where the proportionality constant α is about 4 A/cm. A high leakage current can lead to a significant noise contribution[5]. Moreover, when the detector is not sufficiently cooled the interplay between temperature

[5]The different noise sources of the electronics are discussed in section 3.3.2

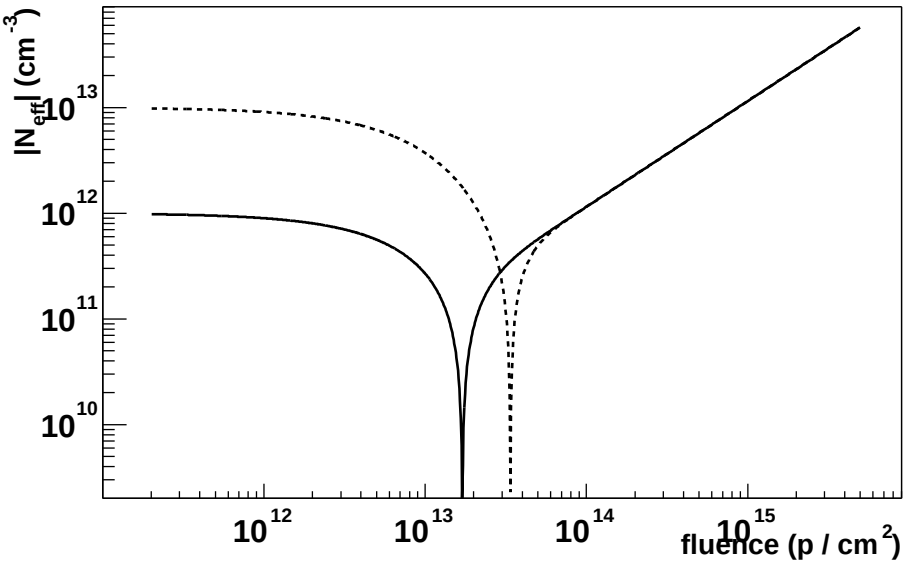

Figure 3.2: *Calculation of the effective dopant concentration in an n-type silicon wafer as a function of the fluence of high energy protons, according to equation 3.15. The solid and dashed lines correspond to wafers with an initial dopant concentration of* $10^{12}/cm^3$ *and* $10^{13}/cm^3$*, respectively.*

and leakage current can lead to thermal runaway [89]. The increase in leakage current can be countered by operating the detector at low temperature (see relation 3.6).

Some types of lattice defects act as traps for the charge carriers. Generally, release times are long compared to the integration time of the electronics. Therefore, trapping reduces the collected charge. As the trapping probability depends on the drift velocity of the carriers, over-depleting the detector helps to reduce the effect of trapping (see reference [90] for a detailed model).

The capacitance between neighbouring readout strips has been reported to increase after irradiation to high doses [91]. This is a concern as the load capacitance is an important factor in the electronics noise (see equation 3.19). The effect, however, has been found to predominantly occur at low frequencies. At the high frequencies relevant for the high speed electronics in silicon detectors for the LHC the increase in inter-strip capacitance is small [92].

Finally, the defects may affect the mobility of the carriers in silicon. Most recent measurements [93] are consistent with no change. Still, the high depletion voltage and the field configuration in type-inverted detectors affect the charge collection time. Figure 3.3 shows the result of a parameterisation of measurements in [93] of the collection time for holes in a non-irradiated 285 μm thick wafer and a similar wafer, irradiated to $2.4 \cdot 10^{14} p/cm^2$.

The ROSE collaboration found that the effect of displacement damage by charged hadrons in silicon diodes can be mitigated by diffusing a large ($\sim 10^{17} cm^{-3}$) concentration of oxygen into the Silicon [85]. The oxygen impurities are thought to combine with vacancies thus avoiding the creation of the more harmful di-vacancy states. Typical oxygenated diodes show an increase of the effective dopant concentration (and thus the bias voltage) with the fluence that is about half that of the standard material. In large area detectors the beneficial

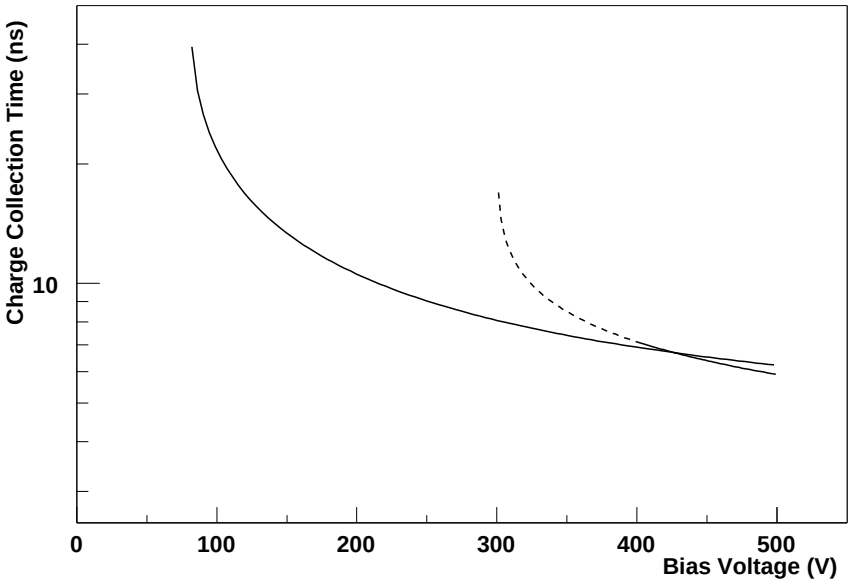

Figure 3.3: *Charge collection time as a function of bias voltage. Parameterisation of measurements on a non-irradiated wafer (continuous line) and a wafer irradiated to* $2.4 \cdot 10^{14} p/cm^2$ *(dashed line) in reference [93]*

effect is slightly less pronounced [94, 90].

To summarise the intricate combination of effects: irradiated detectors have large depletion voltages (up to 300 V). The signal in under-depleted operation of p^+n detectors is severely attenuated. Moreover, some over-depletion is necessary to ensure fast charge collection and to avoid charge losses due to trapping. The leakage current increases roughly linearly with fluence, but sufficient cooling of the detector can avoid a negative impact.

3.2.2 Electronics

The proximity of the readout electronics to the detectors implies the need for the design of Integrated Circuits that are tolerant to high doses of radiation. Different types of circuits present different sensitivities to ionisation and displacement damage. In the following, the effect of both mechanisms on a number of key structures is discussed.

The high dopant concentrations in the structures of modern Integrated Circuits (dopant concentrations are of the order of 10^{16} - 10^{20} cm^{-3} in typical transistors, compared to $\sim 10^{12} cm^{-3}$ in the bulk of a silicon detector) render the front-end electronics relatively insensitive to changes in the effective dopant concentration.

However, significant displacement damage may occur due to the creation of mid-gap states. The front-end electronics makes an extensive use of bipolar transistors. Creation of mid-gap states in the forward-biased base-emitter junctions enhances the recombination probability over the generation probability, leading to a loss of carriers. The practical im-

plication of carrier loss is a decreased DC current gain, leading to a degradation of the noise performance of the amplifier circuit. The noise of the front-end electronics is discussed in detail in section 3.3.2.

The carrier loss due to the creation of mid-gap states depends on the relative concentrations of carriers and defects. This implies that the negative effects can be minimised by reducing the size of the structure. The development of deep sub-μm IC technology, even though not originally designed to be radiation-hard, offers great advantages in the production of more radiation-tolerant electronics.

Charge carriers liberated by ionising charged particles can get trapped in oxide layers and oxide-silicon interfaces. The charge concentrations that are thus built up give rise to parasitic fields that alter the electrical characteristics of the device.

In bipolar devices the parasitic fields in the oxides lead to a loss of the current gain β.

Metal Oxide Semiconductor Field Effect Transistors (MOSFETs) are currently the most extensively used element in digital circuitry. The use of oxide layers in the gates makes these devices very sensitive to ionisation damage. Ionisation damage can seriously alter the threshold voltage of such devices and thus the timing characteristics of the digital circuit. A careful design is needed to ensure that the speed of the circuit is maintained after irradiation.

Finally, a sudden dose of charge left by an ionising particle can cause the state of a logical register to alter (bit-flip). These are called Single Event Upsets (SEUs). If the SEU occurs in a crucial register, for example the configuration register of a chip, the functioning of the device may become incorrect. The probability of SEUs can be reduced by isolating the registers from the surrounding bulk, but no device is completely immune. Therefore, unless all registers are triplicated, regular resets and reconfigurations are necessary in high radiation environments.

3.2.3 Signal simulation

It is instructive at this point to study some of the properties of the detector signal and how they change after irradiation. In this section, a Monte Carlo algorithm [95] for the deposition, drift and collection of the signal is described briefly.

The charge deposition by MIPs is simulated by generating a random charge according to a Landau distribution, convoluted with a Gaussian to account for the broader distribution [81], in small intervals along the particle's track.

To simulate the drift of the charge carriers inside the Silicon, a detailed map of the field set up in the reverse biased pn junction is needed. Here, a discrete map of the electrical field in the Silicon is obtained by solving Poisson's equation,

$$\nabla^2 V = \frac{-\rho}{\epsilon_0 \epsilon_{Si}} \tag{3.17}$$

on a mesh. For the depleted region, a fixed charge density ρ is assumed. In practice, its value is calculated from the depletion voltage V_{FD} and the detector thickness d:

$$V_{FD} = \frac{ed^2|\rho|}{2\epsilon_0 \epsilon_{Si}} \tag{3.18}$$

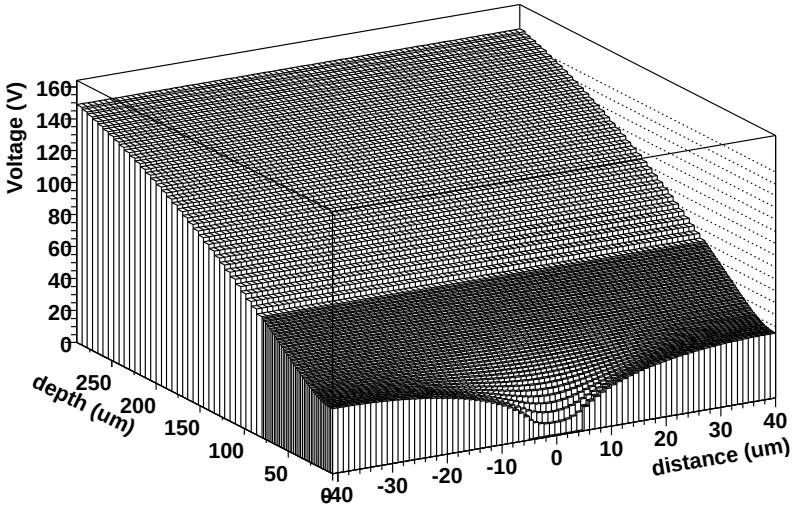

Figure 3.4: *Voltage throughout the Silicon for an applied voltage of 150 V.*

The resulting field map for a p^+n detector is shown in figure 3.4 for a bias voltage of 150 V. The depletion voltage is set to 65 V in non-irradiated detectors.

When the bias voltage is lower than the depletion voltage, the depleted region covers a fraction $w = \sqrt{V_{bias}/V_{dep}}$, where the charge density is assumed to vanish. In the partially depleted detector the region near the backplane has essentially zero field. In this situation carriers are likely to recombine before drifting a considerable distance. Therefore, charge deposited in the undepleted region does not contribute to the total detector signal.

The drift of the charge carriers through the field is simulated according to a parametrisation by Muller and Kamins [96]. They describe the drift velocity of the carriers as a function of electrical field, carrier type and temperature. The model takes into account saturation of the drift velocity.

The signal is induced on the strips by the moving charges. For a detailed discussion for example [97]. The induced signal is proportional to the amount of charge and the drift velocity of the carriers. The dependence of the signal on the distance to the strip is described by a weighting field, found by solving the Laplace equation (see figure 3.5). The weighting field is a steep function of distance to the strip. Therefore, only moving charges close to the strip contribute significantly to the signal.

The total signal is the sum of the currents induced by moving electrons and holes. Figure 3.6 shows the relative contribution of both carrier types. The curves are the average over 1000 charge depositions over the range of incidence positions from $-p/2$ to $p/2$, where p is the readout pitch. Only the signal on the closest readout strip is considered.

In the field of figure 3.4, electrons are swept away towards the backplane. As the weighting field rapidly becomes negligible with distance to the strip, only the electrons deposited close to the strip induce a considerable current. The detector signal therefore has a fast component due to electrons, represented by the dotted curves in the figures 3.6.

The main component of the signal is formed by holes. Holes drift across the entire thick-

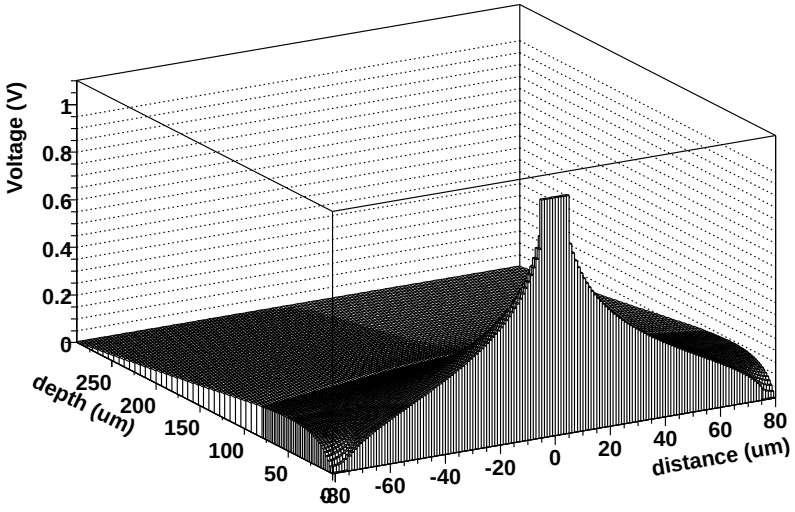

Figure 3.5: *Weighting field*

ness of the detector to induce most of the signal in the large field gradient close to the strip. Therefore, holes induce a signal over a much longer time interval. The front-end electronics for the LHC experiments needs to be very fast to deal with the bunch crossing frequency. Typical integration windows are of the order of 20 ns. Up to biases of approximately 100 V, the detector pulse is relatively long and some charge is likely to be lost.

In the case of irradiated detectors there are more uncertainties. The model described here does not take into account charge trapping, possible effects related to the carrier mobility, etc. Therefore, the simulation is not expected to provide a full description.

Again, a discrete field map is generated by solving Poisson's equation, but now the bulk has inverted to p-type. Therefore, the pn junction forms near the backplane. The depletion voltage is set to 200 V. Figure 3.7 shows how the field across the silicon changes for a type-inverted detector. The resulting induced signal is shown for two bias voltages in figure 3.8.

When type-inverted detectors are operated partially depleted, an undepleted, "zero-field" region forms on the readout side of the detector. Carriers drift in the direction of the strips until they stop in this dead region. The weighting field (figure 3.5) is only large close to the strips, or equivalently, the induced signal is strongly attenuated with increasing distance to the readout strips. Therefore, in under-depleted operation the signal is strongly suppressed.

Figures 3.8 show the time resolved currents induced on the readout strip for two different detector bias voltages. All conditions are kept fixed with respect to the simulation of the non-irradiated detectors, except the silicon type, the depletion and bias voltages and the silicon temperature.

From the simulation of the simplified field configuration, relatively fast charge collection is expected in severely damaged detectors, provided the detectors are operated with sufficient over-depletion. To correctly interpret this results, it should be noted that a number of effects have not been taken into account; the evidence of complex field configurations in type-inverted detectors (double junction) is neglected and trapping of carriers is not taken

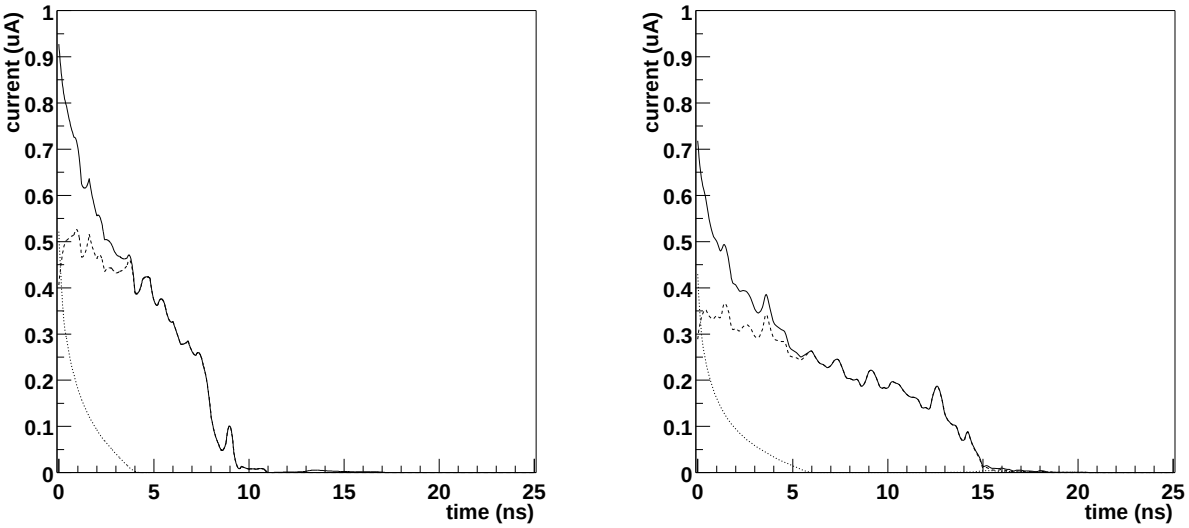

Figure 3.6: *Detector signal due to holes (dashed line), holes (dashed line) and the sum of both signals (continuous line). The simulated detector bias voltages are 275 V (leftmost figure) and 150 V (rightmost figure).*

into account.

3.3 The SCT module design

In this section, the detectors designed by the SCT collaboration are discussed in some detail. After a detailed discussion of the design of the silicon sensors and the readout electronics, the building blocks of the SCT - the barrel and end-cap modules - are presented. The mechanical precision and the thermal performance are also discussed.

3.3.1 The SCT detectors

Good descriptions of the SCT detectors and their electrical performance exist, see for example reference [60]. In this section only some properties that are essential to the remaining chapters are briefly discussed.

The geometrical constraints on detectors for the barrel and end-cap regions are very different: whereas in the barrel region the detectors are arranged parallel to the beam axis, in the end-caps the modules are placed on wheels perpendicular to the beam axis. Therefore, different sensors have been designed: a single rectangular barrel detector with parallel strips and five flavours of wedge-shaped detectors for the end-cap modules. Apart from these geometrical considerations the detectors have very similar properties.

All detectors in the SCT are made by introducing p^+ strips in n-type bulk of $< 111 >$ orientation. The thickness of the detectors is 285 ± 15 μm for all detector types. The resistivity of the substrate is specified to be between 3 and 8 $k\Omega/cm$.

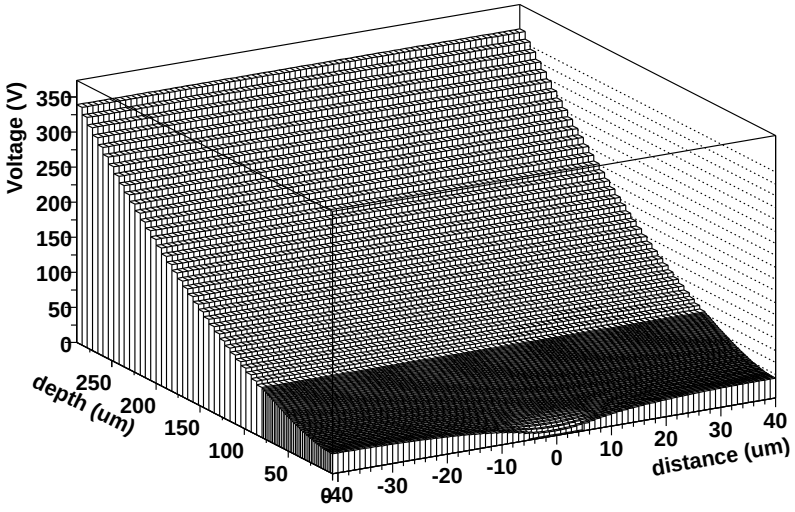

Figure 3.7: *Voltage throughout the type-inverted Silicon for an applied voltage of 350 V*

The detectors are designed to stand high bias voltages. Guard rings are used to step down the voltage towards the edge of the detector.

Leakage currents generated in the detector may represent a quite heavy DC load on the electronics. This is avoided by implementing an AC coupling between the strips and the electronics. In the SCT detectors the coupling capacitor is integrated in the detector design. This is achieved by implementing an insulating silicon oxide layer between the strip implants and the surface strip metallisations. The sensitivity to photo-lithographic faults (pin-holes, punch-through), that could lead to shorts between implant and metallisation, are avoided by the addition of a second layer of a different material (Si_3N_4). In the sample of detectors produced for the SCT the number of defect channels due to this type of defects is very rare, well below the required 1 %.

A simplified electrical schematic of three strips is depicted in figure 3.9. The coupling capacitance to the readout electronics is denoted C_c. The specification for the coupling capacitance is $> 20\ pF/cm$. Two further capacitances, the capacitances to the back plane and neighbouring strips, are drawn explicitly. These make up the load capacitance on the amplifier and are a determining factor in the noise performance (see section 3.3.2). Moreover, the coupling between neighbouring strips leads to signal loss in the binary readout scheme. The value for the inter-strip capacitance depends essentially on the width of the metallisation layer. The inter-strip and strip-to-backplane capacitance are measured routinely on all detectors, yielding values of $\sim 1\ pF/cm$ and $1.3/768\ nF$, respectively.

In order to keep the strip implants at a defined potential (ground in this case), they are connected to a common ground rail through a poly-silicon bias resistance. The implementation of a large resistance, $1.25 \pm 0.75\ M\Omega$, ensures that the contribution to the noise related to the bias resistance is negligible.

The metal strips present a resistance that leads to an additional noise contribution (see equation 3.19). With the specified aluminum strip resistance for the SCT detectors of less

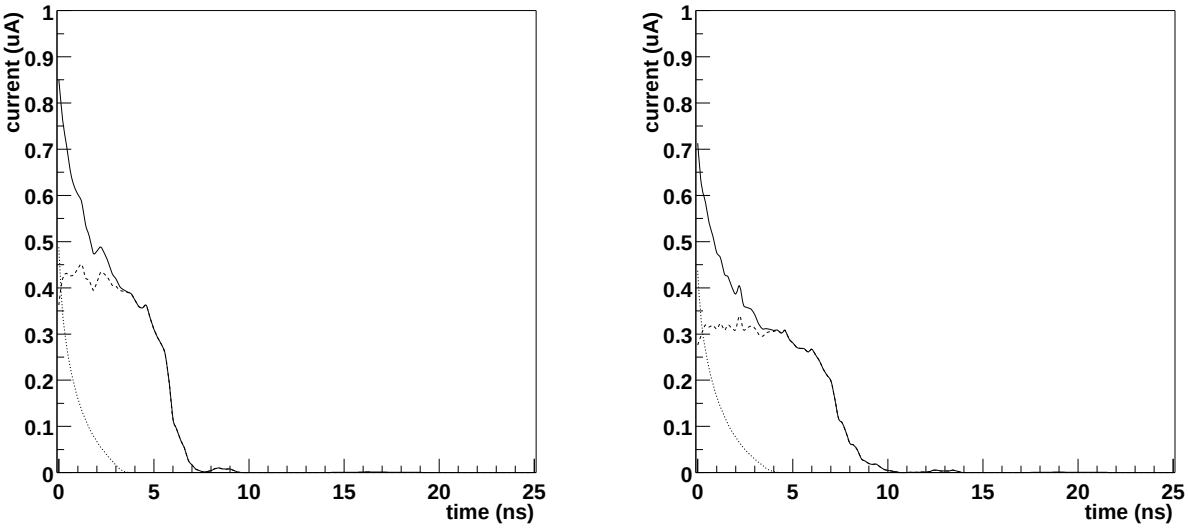

Figure 3.8: *Detector signal due to holes (dashed line), electrons (dotted line) and the sum of both signals (continuous line). The simulated detector bias voltages are 500 V (leftmost figure) and 350 V (rightmost figure).*

than 15 Ω/cm this contribution is small.

The electrical integrity of all detectors delivered to the SCT is tested extensively. Standard tests in the Quality Assurance cycle include IV scans: the leakage current is monitored while the detector bias voltage is stepped up to 500 V. Two specifications are set: the current measured at a temperature of 20^o C is to be inferior to 6 μA when the detector is biased to 150 V and to 20 μA at a bias voltage of 350 V. In case the current at one of these voltages exceeds the specification or a breakdown is observed below 350 V the detector is discarded. Further specifications are set on the depletion voltage (< 150 V), the long term stability of the leakage current and the number of defective strips.

For a fraction of the detectors, a more extensive set of tests is performed. For each of the 768 strips the capacitance to its immediate neighbours is measured. Measurements of the coupling capacitance and bias resistance of single strips allows the detection of defects like implant breaks and shorts between strips. Defects in the dielectric between the strip implant and metallisation are found by applying a voltage between the bias ring and the readout pad. Also, the resistivity of the metallisation is measured.

The effect of radiation on the electrical performance of SCT detectors has been studied extensively. For the wafers to be used in the SCT, type inversion is found to occur after some $0.5 \cdot 10^{14}$ NIEL equivalent neutrons/cm^2. After a fluence of $3 \cdot 10^{14}$ protons/cm^2 the depletion voltage is found to be of the order of 200-300 V.

Measurements of the leakage current after irradiation to $3 \cdot 10^{14} p/cm^2$ and an annealing period of 7 days at 25^o find 150 μA at a bias voltage of 350 V and a temperature of -18^o C. Measurements under the same conditions before irradiation showed a current of 0.1 μA. Even though the leakage current increases a factor 10000, the leakage current remains within the specification.

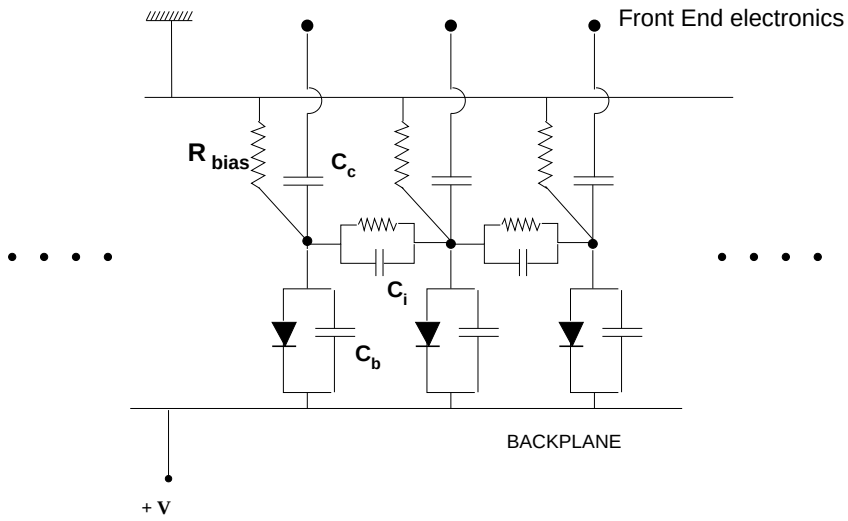

Figure 3.9: *Equivalent diagram of three strips with their capacitive connections to the front-end electronics, the neighbouring strips and the backplane.*

Property	*Symbol*	*unit*	*Specification*	*Conditions*
Leakage current	I_{leak}	μA	< 6	$V_{bias} = 150\ V$
Leakage current	I_{leak}	μA	< 20	$V_{bias} = 350\ V$
Current stability	ΔI_{leak}	μA	< 2	$V_{bias} = 150\ V$, 24 hours
Depletion voltage	V_{FD}	V	< 150	
Substrate resistivity	ρ	$K\Omega/cm$	$3 < \rho < 8$	
Metal strip resistance	R_{ms}	Ω/cm	< 15	
Bias resistance	R_{bias}	$M\Omega$	1.25 ± 0.75	
Inter-strip capacitance	C_{inter}	pF/cm	< 1.1	$V_{bias} = 150\ V$, 100 kHz
Coupling capacitance	C_c	pF/cm	≥ 20	1kHZ

Table 3.2: *The most relevant specifications for the SCT detectors.*

The most relevant SCT detector specifications are summarised in table 3.2. Production of the detectors in industry has succesfully been completed. Detailed tests in the SCT institutes retain a large fraction of the detectors; the rejection rate is below the 1 % level.

3.3.2 Front-end electronics

The baseline SCT readout is binary, i.e. the amplified analog signals are discriminated on the module, so that of each channel only one bit of information remains.

The SCT front-end is developed in the bipolar, radiation hard DMILL technology. DMILL (Durci Mixte sur Isolant Logico-Lineaire) [98, 99, 100, 101] is a radiation-hard standard for the design of BiCMOS Integrated Circuits. DMILL offers MOS transistors, fast *npn* bipolar transistors and large resistances.

The strong point of the DMILL technology is the possibility to integrate fast, low-noise

analog circuits and digital functions in a single chip. The analog functionality required for the front-end can be implemented in bipolar devices, while the digital part can profit from fast CMOS devices. The implementation of ASICs in DMILL is described in references [102, 103].

The relatively large structure size, 0.8 μm, renders the DMILL technology inherently less tolerant to large doses of radiation than the emerging deep sub-μm technology, with structure dimensions of $0.25\mu m$. The maximum radiation levels expected in the SCT are at the upper limit of the DMILL radiation tolerance specifications.

The ABCD [104, 105, 106, 107, 108, 109] readout chip integrates the analog and digital functionality in a single chip. Figure 3.10 shows a block diagram of the chip with the analog - amplification and shaping - and the digital functionality - pipeline and event buffers.

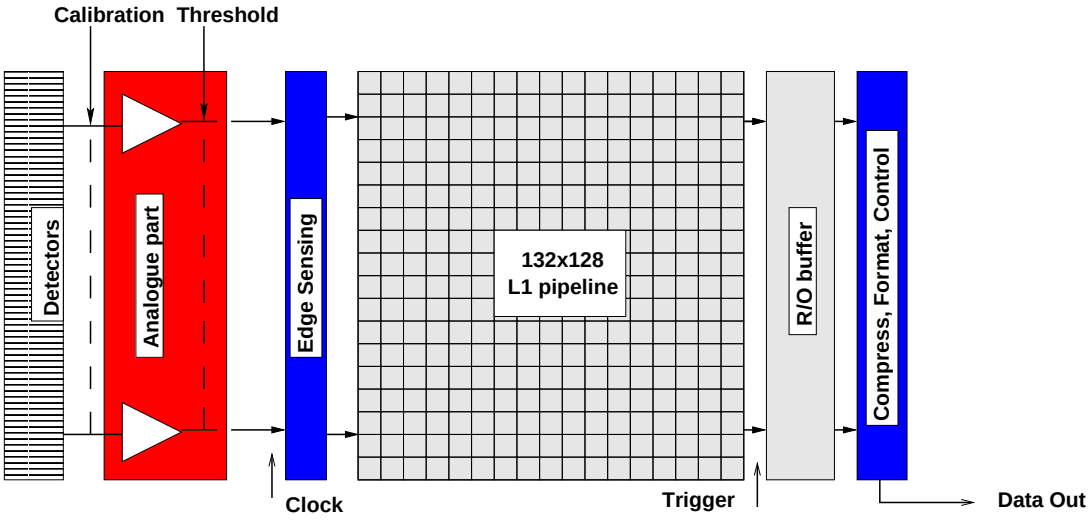

Figure 3.10: *Block diagram indicating the functionality of the ABCD chip.*

The analog functionality of the ABCD chip includes pulse shaping, amplification and discrimination for 128 readout strips. The schematic of a single channel is shown in figure 3.11. The front-end circuit is based on a trans-impedance amplifier with a bipolar transistor followed by an integrator, providing fast semi-Gaussian shaping.

The noise performance of the amplification stage is very important for the overall performance of the detector. In general, the noise of a front-end system can be written as the quadratic sum of two contributions: thermal noise due to variations in the velocities of the charge carriers and shot noise as a result of the fact that the current consists of discrete quanta of charge.

For a front-end system based on *npn* bipolar transistors the equivalent noise charge (ENC) due to thermal and shot noise can be written in the following form, see for example [110]. For the thermal noise charge:

$$ENC = \sqrt{\frac{4kTC_{load}^2}{\tau}(r_{bb'} + R_{ms} + \frac{kT}{2qI_c})} \tag{3.19}$$

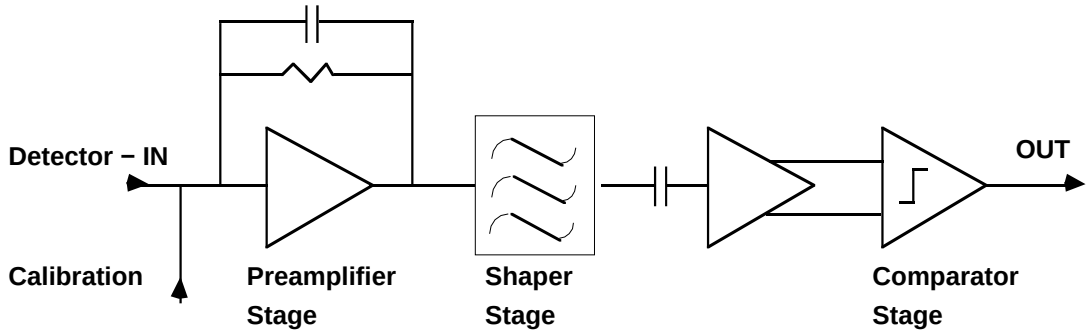

Figure 3.11: *Schematic diagram of the analog stages of a single channel as implemented in the ABCD chip.*

where $r_{bb'}$ and I_c are the base spread resistance and the collector current of the input transistor, respectively. The thermal noise charge is proportional to the load capacitance C_{load} and inversely proportional to the square root of the peaking time τ. The contribution from the metal strip resistance of the detector R_{ms} is normally small, unless extremely long ladders of silicon detectors are assembled.

The shot noise is independent of the load capacitance:

$$ENC = \sqrt{2q\tau(\frac{I_c}{3\beta} + I_d + \frac{2kT}{q}(\frac{1}{R_{FB}} + \frac{1}{R_b}))} \tag{3.20}$$

where β is the DC current gain of the input transistor. I_d is the detector leakage current. The last term accounts for the shot noise of the feedback and bias resistors R_{FB} and R_b.

The dependence on the amplifier peaking time τ and the collector current of the input transistor are opposite for the thermal and shot noise contributions. Therefore, for a given design of peaking time, gain and capacitative load, the collector current should be chosen to minimise the noise charge. From equations 3.19 and 3.20 a proportionality (to first order) of the noise charge with the square root of the temperature may be expected.

In the previous section, the load on the amplifier was identified to come from the inter-strip capacitance of the detector and to a lesser extent the strip-to-backplane capacitance. For the full 12 cm of 2 ganged SCT detectors the total load is $\sim$ 12 pF and the thermal noise contribution is dominant. Due to the short peaking time of the ABCD shaper/amplifier shot noise due to the detector leakage current is not significant for leakage currents up to 2-3 mA [111].

A shaper optimises the signal to noise ratio of the front-end. The transfer function of an ideal $CR(RC)^3$ is:

$$h(t) = (\frac{t}{\tau})^3 e^{-t/\tau} \tag{3.21}$$

where τ^3 is the shaping time. The design peaking time of the shaper is 20 ns. The response of the shaper to a certain input is obtained by convoluting the time resolved input pulse with the transfer function h(t) of equation 3.21. A more realistic description of the action

of the ABCD shaper is obtained by taking into account an extra differentiation step with an RC time of 150 ns. The result of this extra step is an undershoot of the pulse, leading to a faster fall-off of the tail.

In the binary readout scheme the pulse obtained by amplification and shaping of the signal is reduced to one bit of digital information on the chip by comparing with a preset threshold. The discrimination threshold is set in the chip configuration register and is the same for all 128 channels. Small non-uniformities in the response of the amplifiers across the channels are corrected by adjusting the 4 bit trimDAC of each channel. The range of all trimDACs on a chip is chosen by setting two bits in the configuration register. Thus, fine matching can be obtained before irradiation, while no channels drift out of the trimmable range when the irradiation causes increasing non-uniformity at a later stage of the experiment.

An important feature of the ABCD is that the discriminator can be operated in two modes: in level sensing mode the discriminator returns a digital 1 whenever the signal is higher than the threshold, whereas in edge sensing mode a 1 is returned only when a low to high transition occurs. Operating the discriminator in edge sensing reduces the tail of the (shaped) signal, and thus the probability that ghost hits appear in the consecutive beam crossing.

The discriminator output of each channel remains in a digital pipeline during the trigger latency. The three last cells of the pipeline, corresponding to the binary hit information of three clock cycles, are duplicated in the event buffer. On arrival of a level 1 trigger, the information in the event buffer is compressed and made available to the off-detector electronics.

The compression algorithm compares the three-bit hit pattern to a compression pattern. If the hit pattern satisfies the requirement the hit pattern of the channel is added to the data stream. Three compression modes are available:

- ANYHIT compression $1XX|X1X|XX1$
- LEVEL compression $X1X$
- EDGE compression $01X$

In ANYHIT compression the channel is read out if the signal was over threshold in any of the three clock cycles. This mode is useful when the trigger and readout cannot be synchronised. In the ATLAS experiment the timing of the modules is carefully tuned. Particles from a particular bunch crossing create hits in the central, triggered clock cycle. The LEVEL and EDGE compression modes use this information to provide an additional noise rejection.

An integrated calibration circuit allows a fast and accurate characterisation of the analog stages of the channel. A Digital to Analog Converter (DAC) and a chopper circuit generate a voltage step of settable height. This voltage step is applied to a 100 fF calibration capacitor, thus creating a fast (less than a few ns) charge pulse that is injected into the input of the preamplifier. By scanning the threshold voltage over a large range and registering the binary response, the S-curve - counts over threshold versus threshold voltage - can be reconstructed. The S-curve for a fixed charge and Gaussian noise is described by a complementary error function. The threshold where 50 % efficiency is obtained (VT50) is

the threshold corresponding to that input charge. The width of the S-curve is a measure of the output noise.

The relation between input charge and threshold voltage (the response curve) is determined by repeating the above procedure for a number of input charges in the range of interest (0.5 - 10 fC). Note that the charge-threshold relation is determined for the chip as a whole

The gain of the analog stage of the chip is obtained as the derivative of the response curve. The typical value for ABCD chips is 50-60 mV/fC. After irradiation to $\sim 3 \cdot 10^{14}$ protons/cm^2, the gain is nearly halved. The equivalent noise charge at the input of the amplifier (in fC) is obtained by dividing the output noise (measured in units of threshold voltage, mV) by the gain (in mV/fC). The input noise value shows a slight dependence on input charge due to the non-linearity of the response curve at high charges and of the calibration circuit at low charges. For purposes of comparison the equivalent input noise charge obtained when injecting a test charge of 2 fC is quoted.

For ABCD chips with the full load of 12 cm long readout strips the equivalent noise charge is found to be around 1500 electrons. Inner detector modules with a single 6 cm wafer yield $\sim$ 1100 electrons. After irradiation to a fluence of $\sim 3 \cdot 10^{14}$ protons/cm^2, the noise charge increases to about 1800 electrons. The input noise is found to depend on the temperature. Typically, the input noise increases roughly 7 ENC/degree [112], slightly more for irradiated modules.

Some important specifications on the front-end performance are listed in table 3.3.

Property	*Unit*	*Specification*	*Conditions*
Gain	mV/fC	50	$I_{shaper} = 20\ \mu A$
Linearity		$< 5\%$	$Q \in [0, 4]\ fC$
ENC	e^-	< 1500	
ENC	e^-	< 1800	after $3 \cdot 10^{13} p/cm^2$
Threshold variation		$< 2.5\ \%$	1 fC, trim-range 00
Threshold accuracy		$< 1\ \%$	
Peaking time (τ_p)	ns	20	
Time-walk at $Q_{thr} = 1\ fC$	ns	< 16	$Q \in [1.25, 10]\ fC$
Double pulse resolution	ns	< 50	for two 3.5 fC pulses
Large pulse recovery	μs	< 1	for a 80 fC pulse

Table 3.3: *The most relevant specifications for the SCT front-end electronics. For a more complete list see reference [104].*

The calibration capacitor has a nominal value of 100 fF. Variations in the production process have a relatively large effect on these small capacitances. The ABCD project specification [104] requires a 3 σ spread of less than 20 % over the full production and 2 % within a single chip. Measurements of the thickness of the oxide of test structures on each wafer of ABCD chips yield a correction factor for the calibration capacitance of the chips from that wafer. Application of these correction factors greatly improves the uniformity in gain, noise and signal measurements between different modules.

The height of the voltage step shows some variations between chips. Probing of the

voltage step of different chips from the same wafer has yielded a spread of 2 %. The variation between the voltage steps of different chips on a module irradiated to a fluence of $3 \cdot 10^{14}$ protons/cm^2 is found to be twice as large: 4 % [113]. The DAC output further shows a small temperature dependence. For typical temperature variations within a cooled setup this effect can be ignored, but special care is needed when comparing measurements obtained in different set-ups.

3.3.3 The barrel module

The four cylindrical barrels in the central rapidity region are equipped with nearly 2000 rectangular barrel modules. The modules are placed under a $\sim 7^o$ tilt angle, to ensure overlaps between neighbouring modules.

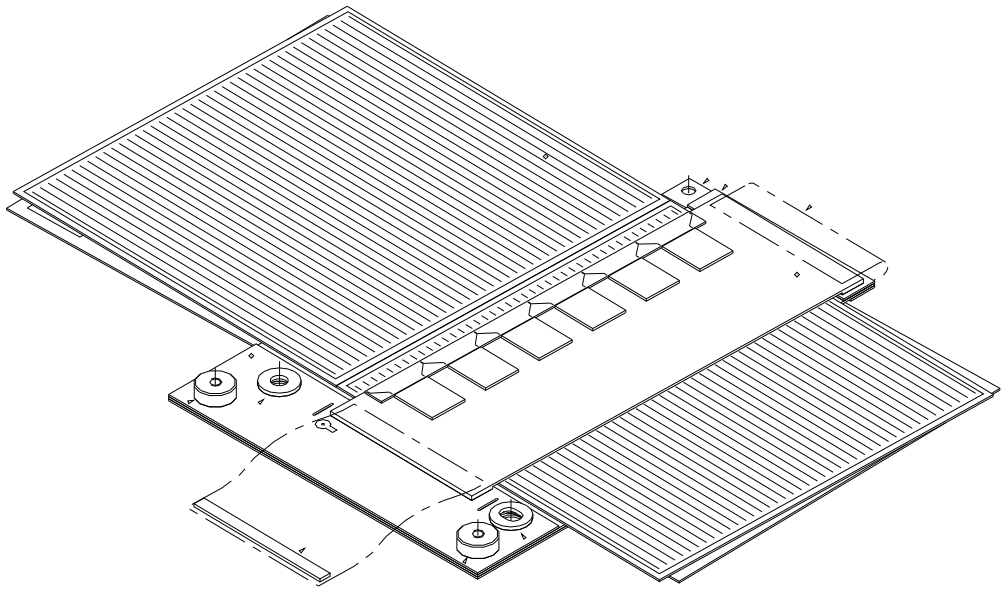

Figure 3.12: *Top view of a barrel module.*

A single module design, shown in figure 3.12, is intended to populate the four barrels. The barrel modules have a 6 by 12 *cm* rectangular active area. The 12 *cm* long strips are obtained by ganging together two wafers using micro-bonds. The parallel strips are implanted at a 80 μm pitch.

For the barrel region the solenoidal magnetic field deflects the particle trajectories in the $R\phi$ plane. To yield a good resolution in the bending plane, the strips of the barrel modules are approximately aligned with the beam axis.

A second set of detectors on the back of the module is rotated by a stereo angle of 40 *mrad*. The stereo angle allows the measurement of three-dimensional space points. The momentum

measurement requires a good spatial resolution in the bending plane. The measurement of the z-coordinate is essential to be able to assign hits to tracks in the dense tracking environment of the inner detector. However, in the non-bending plane, the resolution requirement is less stringent.

The relative resolutions in both planes are determined by the choice of the stereo angle. In the next chapter, it will be shown that a small stereo angle of $40mrad$ leads to the required spatial resolution. A small stereo angle has the additional advantage of reducing the ambiguities in the assignment of hits on both sides of the module to space points.

The two sets of wafers are glued on a base-board made out of beryllia and a pyrolytic graphite (TPG) piece that provide a mechanically rigid base for the module and good thermal conductivity. In the barrel module the front-end electronics is connected to the detector strips in the center of the module (center-tap readout).

The readout chips are mounted on a hybrid that forms a bridge across the surface of the detectors. The hybrids are produced as a single object that is folded around the detectors to provide a support for the readout chips on the front and back of the module.

The adaptation of the detector and chip pitch is achieved through fan-in vias. In the barrel modules, these are incorporated into the hybrid.

3.3.4 End-cap modules

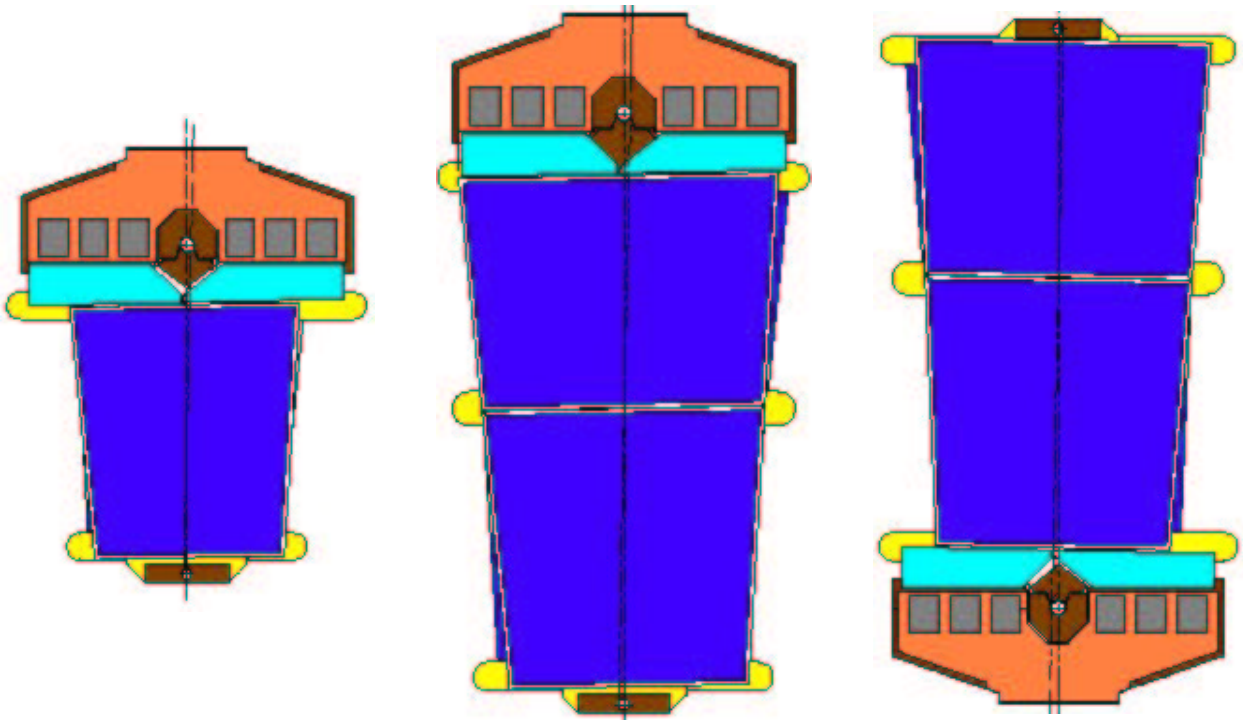

Figure 3.13: *Top view of an end-cap inner, middle and outer module (in that order from left to right).*

In the end-caps three module types, shown in figure 3.13, have been designed to equip the wheels. The outer and middle rings are to be equipped with modules consisting of four silicon wafers yielding an active area similar to that of barrel modules. The inner ring module has only two back-to-back wafers.

In order to achieve a precise determination of the $R\phi$ coordinate in the vertical end-caps the strips are oriented radially. The angle between two consecutive strips is 0.207 $mrad$ for middle and inner detectors and 0.1615 $mrad$ for the outer detectors. This implies a variation of the readout pitch along the module's long axis. The smallest pitch is 54.4 μm on the narrow edge of the inner modules and the maximum pitch is 94.8 μm on the broad edge of the middle module. Again, the central symmetry axes of two sets of wafers form a stereo angle of 40 $mrad$. Thus, while the $R\phi$ measurement is very precise, the R coordinate is measured with less precision.

In the end-cap module design the mechanical rigidity and thermal conductivity are provided by a TPG spine with aluminum nitride wings. The hybrid supporting the readout chips is located at the end of one of the wafers (end-tap readout). The hybrid is produced as a single piece using a technology similar to that of the barrel modules and wrapped around a carbon-carbon substrate with high thermal conductivity.

In the end-cap design the fan-ins are not incorporated into the hybrid to maintain a single hybrid design for the three geometrical module types. Instead, the vias are etched on separate pieces. The fan-ins are made out of low thermal conductivity glass, in order to maintain the thermal separation between detectors and hybrid.

The end-cap modules rest on two mounting blocks that act as precision locators and cooling points.

3.3.5 Alignment

As the SCT is to provide high-precision position measurements, a precise alignment of the modules is essential. Among the physics objectives, the measurement of the W mass implies an especially strict requirement on the alignment. To achieve a precision of 20 MeV, an alignment precision of $\sim$ 1 μm is required [114].

An initial X-ray survey of the assembled detector provides an alignment of reasonable precision $\sim$ 7-10 μm that is used as a starting point for the precision alignment using tracks produced in the p-p collisions. The relative alignment of a module to its neighbours is obtained using the signal of muon tracks in the overlap between modules. The relative alignment of the different layers is achieved using a sample of high p_T muons from $Z \rightarrow \mu^+\mu^-$ and $W \rightarrow \mu\nu$ decays. The trigger rates for isolated low and high p_T muons are sufficient to achieve an alignment with a statistical precision of the order of 1 μm in the $R\phi$ direction using the data of a single day [114]. Dynamical deformations on a short time scale - thermal effects and vibrations - are expected to dominate the alignment precision. Deformations are monitored using an interferometric length measurement technique (Frequency Scan Interferometry) on a geodetic network of retro-reflectors (jewels) mounted in strategic positions on the inner detector. A straightness monitor based on laser beams and amorphous silicon sensors complements this measurement.

The SCT module is a compound object consisting of four wafers. In the alignment

process the module can be treated as a rigid, perfectly aligned object provided that the error introduced by misalignment of the wafers does not significantly affect the resolution. The total error budget determined from these considerations is listed in table 3.4 for the barrel and end-cap sectors. The error budget includes wafer-to-wafer misalignments, but also the error introduced by the mounting of the module on the support structure. The module assembly error is required to be small compared to the total budget.

	total error budget (μm)		module error (μm)	
coordinate	*barrel*	*end-cap*	*barrel*	*end-cap*
R	100	50	15	17
ϕ	12	12	3	4
z	50	200	17	66

Table 3.4: *The error budget for misalignments in the R, ϕ and z coordinate for barrel and end-cap modules. The second pair of columns lists the error budget reserved for wafer-to-wafer alignment.*

In the barrels, the tilt angle leads to a mixing of the R and ϕ coordinates. Therefore, the in-plane flatness requirement (RMS < 15 μm) is far more severe than the corresponding requirement in the end-caps (RMS < 66 μm).

Based on the maximum RMS errors in table 3.4, engineering tolerances have been defined: all wafers in one plane should not deviate more than $\pm$ 5 μm from the ideal position, for the front-to-back alignment of both wafer pairs $\pm$ 10 μm is required and the stereo angle is to be within $\pm$ 0.5 $mrad$ of the design 40 $mrad$.

During assembly, the required in-plane alignment is achieved using optical pattern recognition on the fiducial marks on the wafers. Both wafers are brought into position on independent high-precision translation and rotation stages. The pair of wafers is aligned with respect to a coordinate system defined by transparent fiducials. As soon as the position is achieved the wafers are held with vacuum on a special jig. The second pair of wafers is aligned and held on a second identical jig. In the final step a sandwich is formed of the two pairs of wafers and the module support structure, i.e. the baseplate for barrel and the spine for end-cap modules[6].

As part of the quality assurance program, the robustness of the assembly under sudden temperature changes is tested in a series of thermal cycles. A precision metrology is performed on all assembled modules. The metrology results are stored in the SCT data base and are available to be used in the precision alignment of the SCT.

3.3.6 Thermal performance

The leakage current of the detectors depends strongly on the temperature (see equation 3.6). Moreover, the current at a given temperature rises strongly with radiation dose. At high temperature, (anti-) annealing takes place faster. A large leakage current leads to a noise penalty. Moreover, it brings about the risk of thermal runaway: the self-heating of the

[6]Different approaches are used across the module building sites. The explanation here intends to provide a summary of the method used by most sites

detector due to the leakage current leads to an increase of the current, which in turn leads to increased heat generation. The control of the sensor temperatures is an important design consideration.

All modules in the SCT are actively cooled. The cooling system is a two-phase refrigerator cycle. Cooling of the modules is achieved through the evaporation of C_3F_8 in the cooling pipes that run through the entire detector. Each module is brought into direct thermal contact with the pipes. The system is capable of providing cooling contact temperatures between -14^o and -30^oC in the absence of a heat load.

In the barrel region the pipes are equipped with cooling plates that make a sliding grease joint with a cooling contact area on the module. Contractions or extensions of the system are absorbed in the sliding joints. In the end-caps, cooling blocks are rigidly mounted on the carbon fiber wheels. Thermal distortions of the cooling pipe are absorbed in the *wiggles* in the pipe design. Middle and outer modules have a second cooling contact at end of the module furthest away from the electronics.

The cooling system is to take out the heat produced in the modules. The front-end electronics is an important heat source. Even though in the design of the electronics special care was taken to reduce the power consumption, a fully loaded hybrid with 12 ABCD readout chips dissipates a maximum power of 7 Watts. The heat load from the Nitrogen atmosphere is estimated to be about 0.2 W per silicon detector, i.e. 0.8 W for a barrel and outer and middle end-cap module [115].

The energy dissipated in the sensors themselves depends strongly on the temperature. In the end-cap design the sensors are to be kept below -7^o C to assure a negligible contribution to the total noise charge and avoid rapid annealing. Moreover, thermal runaway, should not occur whenever the power dissipated in the detector is below 240 $\mu W/mm^2$. The maximum sensor power that is considered safe, 240 $\mu W/mm^2$, corresponds to a total contribution of 3.5 W from the sensors; the power dissipation of the front-end is in all cases the dominant heat source.

Heat conductors sandwiched between the wafers provide a low-conductivity thermal path from the entire sensor surface to the cooling points. These are made of thermopyric graphite (TPG), that has a very good thermal conductivity. In the end-cap module, a long narrow strip - the spine - runs under the full length of the sensors. Barrel modules have a broad rectangular heat conductor that covers about half of the detector area.

To achieve the required low sensor temperature in the presence of a significant heat load from the electronics, the barrel and end-cap modules have a strict thermal split between thermal paths of the hybrid and the sensors. In the end-cap modules, the hybrid is located at the end of the detectors. In the barrel modules, the readout chips are mounted on a hybrid that forms a bridge across the surface of the detectors. The fan-ins that electrically link the readout strips and the electronics channels present a channel of low thermal conductivity. The mechanical joint of the hybrid and sensors is placed close to the cooling point so that not much heat can leak into the sensors. Thus, the design allows the electronics to run at a relatively high temperature ($\sim 2^o$ C), while the sensors are kept much cooler (below -7^o C.

Thorough tests have been performed of the thermal performance of barrel and end-cap modules under relevant loads. For a limited number of irradiated modules, tests have been performed on a prototype evaporative cooling system. These tests show that the SCT cooling

system is able of maintaining a sufficiently low sensor temperature.

3.4 Summary

In this chapter the necessary background information on silicon micro-strip detectors has been provided. Some of the technology choices for the ATLAS semiconductor tracker have been discussed.

It is found that a reverse biased pn junction can form a macroscopic volume of material free of charge carriers. Depletion depths of 285 μm are obtained with a bias voltage below 100 V. The electrons and holes created due to ionising charged particle drift towards opposite sides of the detector in the field created by the reverse bias voltage. For a wafer thickness of 285 μm the median signal that can thus be collected is about 4 fC. In single-sided micro-strip detectors, one side of the detector is segmented in narrow bands. Separations (pitches) of the order of several tens of microns can be achieved. Read-out of a single detector thus provides a precise measurement of spatial coordinate perpendicular to the strips.

The SCT collaboration has designed a silicon micro-strip detector for the intermediate layers of the ATLAS inner detector. The detectors are formed by p^+n diodes with 768 strip implanted at an 80 μm pitch.

The detectors are read out by binary electronics implemented in the radiation-tolerant ABCD chip. The analog functionality of the ABCD the fast amplification and shaping of the detector signal necessary. The front-end is sufficiently fast to work in the LHC 40 MHz bunch crossing frequency. The amplified signal is discriminated on the chip. The resulting single bit of hit information is stored in a digital pipeline during the latency of the level-1 trigger.

Four geometrical module types have been designed: three wedge shaped modules to equip the wheels in the end-cap region and a single module design to occupy the four cylindrical barrels. Two detectors are ganged together using micro-bonds to produce a 12 $\times$ 6 cm^2 sensitive area. Combination of the measurements of two pairs of wafers rotated by a small stereo angle yields a three-dimensional space point. With the 40 $mrad$ stereo angle of the SCT modules, an excellent resolution is obtained in the plane of deflection of the particles ($R\phi$). The second coordinate (z in the barrel, R in the end-cap) is measured with sufficient precision, to assign hits to tracks in the dense pattern recognition environment of the inner detector.

Numerous module prototypes of the four geometrical types have been produced. A number of these have been irradiated to $3 \cdot 10^{14}/cm^2$ of 24 GeV protons, expected to be equivalent to the fluence received over the 10 years of operation of the ATLAS detector. The detectors are found to resist this large dose, reaching a depletion voltage of 200-250 V. Efficient cooling of the detector is needed to control the leakage current. The maximum fluence in the SCT after 10 years of operation in ATLAS is at the upper limit of the radiation tolerance of the chip.

SCT modules have been submitted to severe thermo-mechanical and electrical tests. The design has passed a final design review. In system and beam tests the performance of a large multi-module assembly has been measured. The results of SCT beam tests are discussed in

detail in the next chapter. Production of barrel modules is proceeding. The end-cap module sites are currently qualifying to start module construction.

Chapter 4

SCT Beam tests

In this chapter the performance of the building block of the SCT - the module - is discussed. In beam tests the response of the module to particles from an accelerator is measured. Their main purpose is the study of the dependence of the single module performance on a series of external parameters - detector bias voltage, discriminator threshold, magnetic field, incidence angle of the particles, radiation history of the module, etc.

In recent years, prototype SCT modules have been tested repeatedly in the H8 beam line of the Super Proton Synchrotron (SPS) at CERN. In 1999 and 2000, additional tests were carried out in the $\pi 2$ beam line at KEK's 12 GeV Proton Synchrotron in Tsukuba (Japan). In this chapter, an overview of the most important results is given. Many of these have been published in internal notes and conference proceedings [116, 117, 118, 119, 120, 121, 122, 123]. A detailed write-up of early test beams can be found in [124, 125, 126, 127, 128, 129].

In the first section, the experimental setup used in recent years is described. In section 4.2, the off-line preprocessing steps of the raw data is outlined. In section 4.3 the most important measurements of the single-module performance - efficiency, noise occupancy, spatial resolution - are defined and an overview of results for recent SCT prototypes is given.

Two analyses are discussed in more detail. In section 4.5 a method to reconstruct the time-response of the binary Front End electronics is presented. The experimental results are compared to a detailed simulation of the charge collection. The implications of the findings for the operation of the SCT modules in the ATLAS environment are discussed. In section 4.6 the tracking performance of a multi-module system is evaluated. The results are compared to a simulation of the track reconstruction efficiency and resolution of the full SCT system. Finally, the results are summarised in section 4.7.

4.1 Setup

The H8 test area at CERN receives a secondary beam from the 450 GeV SPS. Several particle types and beam energies are available. The standard beam for tests of SCT modules consists of 180 GeV charged pions with a minor contamination of muons. The $\pi 2$ line at KEK delivers 4 GeV pions.

The test beam setup used in the last years is depicted in figure 4.1. The arrangement of module prototypes corresponds to the August 2002 beam test in the H8 beam line.

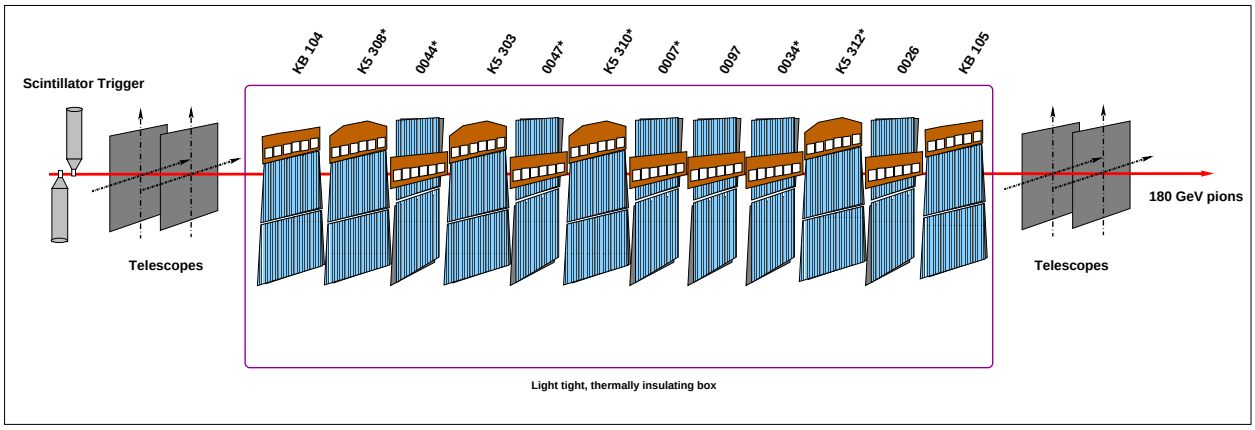

Figure 4.1: *Arrangement of the SCT prototype modules in the beam line during the August 2002 beam test.*

The complete test setup can be introduced in a 1.56 T magnetic field from the superconducting Morpurgo magnet. The magnetic field points vertically downward, i.e. parallel to the readout strips of the detectors in the standard module configuration.

The most important systems - binary readout and control, beam telescope, trigger and cooling - are discussed in the following sections.

4.1.1 Trigger

Two scintillator detectors read out by Photo Multiplier Tubes are used to detect the passage of beam particles and trigger the readout system. The response is sufficiently fast to control the jitter of the trigger signal to 1-2 nanoseconds.

In ATLAS the readout of the detectors is synchronised with the bunch crossings of the LHC. The system is to be carefully optimised to ensure that the signal is sampled at its peak. In beam tests, however, the beam and readout clock are not synchronised[1]. The beam particles, and the trigger, arrive with a random phase with respect to the 40 MHz readout clock. For LHC-speed electronics a 25 nanosecond variation of the timing has a severe effect on the apparent performance. Therefore, the trigger phase of each event is registered. In practice, the time between the raw trigger from the scintillators and the next rising edge of the clock is measured using a fast, high accuracy Time to Digital Converter (TDC). In the off-line analysis, the trigger phase information can be used to select events in a narrow time interval and evaluate the module performance in circumstances as close as possible to the LHC environment.

The acceptance of the scintillator detectors is typically $2 \times 2\ cm^2$, large enough to contain typical beam spots and comparable in size to the acceptance of the beam telescope. The SCT modules have a sensitive area of $6 \times 12\ cm^2$.

[1]In May 2000 SCT modules were tested in a beam from the SPS with an "LHC-like" bunch structure. In this special case the readout clock was synchronised to the accelerator

4.1.2 Beam telescope

The telescope is used to reconstruct the trajectories of incoming beam particles. Provided that the alignment of the system of telescope and modules is known, tracks can be interpolated to the plane of the modules under test. The alignment of the test beam system is discussed in section 4.2.

The telescope is composed of four modules mounted in pairs on either side of the thermal enclosure of the modules under test. The telescope and the modules are mounted on the same massive slab of granite to ensure the mechanical rigidity of the system.

Each of the four telescope modules consists of a two perpendicular Silicon Micro-Strip sensors with a strip pitch of 50 μm. The detectors are read out by VA2 analog multiplexed readout chips with 1 μs peaking time. The spatial resolution obtained is well below 5 μm.

IRAM VME modules are used to retrieve the charge information on each channel. A DSP on the IRAMs subtracts pedestals and applies a clustering algorithm, drastically reducing the data volume. The total dead time of the telescope, $\sim$ 13 ms, is the dominant factor in the event rate.

Routinely, one SCT module is read out as an anchor module. This means the module is left at a fixed threshold and bias voltage optimised for high efficiency and low noise. Thus, an extra measurement inside the setup is available. The requirement that at least one anchor plane is efficient effectively reduces residual inefficiencies due to readout glitches, badly reconstructed tracks and tracks with a large deflection due to multiple scattering in the setup.

In the KEK beam test, where the beam energy is much lower, multiple scattering is a serious problem. Therefore, the telescope and binary modules are interleaved. The intermediate telescope measurement removes tracks that suffer a large deflection rather efficiently.

4.1.3 Binary readout and control

The SCT prototypes are read out and controlled using a suite of custom VME modules.

The clock and control module (CLOAC) provides a central 40 MHz system clock that is distributed to all modules. It is also used to send short commands - resets and the L1 trigger - to the modules.

A slow command generator module (SLOG) assembles and sends slow commands. These are used to configure the readout chips on six binary modules and load the settings for the DACs that control the bias to the Front End circuit, the threshold and the trim DACs.

The MuSTARD module is capable of reading out both sides of six SCT modules through the spy connectors. This method is referred to as electrical readout, as opposed to the optical readout to be employed in the ATLAS experiment. In the beam test, each event is read-out and stored separately, i.e. the MuSTARD histogramming functionality is not used.

A full characterisation of the Front End is made prior to the beam test using the ABCD's on board calibration circuit(see section 3.3.2). The front-end settings are chosen for optimal performance. Generally, the non-irradiated modules are set to a front end bias current of 220 μA and a shaper bias current of 30 μA, whereas the irradiated modules were generally set to lower values of the front end bias current: $\sim$ 128 μA and shaper bias current: $\sim$ 24 μA.

The characterisation includes the trimming of all modules: the values of the trimDACs of all channels are set to minimise the threshold spread at an equivalent threshold of 1 fC.

An important step in the characterisation of the modules is the determination of the response curve; the relation between input charge and threshold voltage. Throughout the beam tests common thresholds (expressed in fC) are set on all modules, using a parametrisation of the response curve. Temperature and setup effects are avoided by running the calibration in-situ, immediately before data taking.

4.1.4 Cooling

The devices under test are held in a light-tight thermally insulating box. The box is flushed with cold nitrogen to ensure a dry atmosphere. Each of the modules is contained in its own aluminium test box: the "QMW box" [130] in case of the barrel modules and the "Valencia box" [131] for the forward modules. The module boxes are equipped with mounting points and cooling contacts similar to those to be employed in ATLAS. The modules are cooled individually by a water-ethanol (60:40) mixture at -15^o C flowing through a cooling pipe in the module box, immediately under the cooling point. The liquid flow from a commercial chiller is sufficient to remove the maximum power of 7 Watts dissipated by the front-end electronics.

The resulting hybrid temperatures, measured with a PT1000 or thermistor at the edge of the hybrid, are monitored continuously. Hybrid temperatures range between -5 and 5^o C. The differences between modules are small compared to the variation across the hybrid and should not lead to significant differences in electronics noise. The leakage current of irradiated detectors is in the range from 1 to 3 mA, depending on the bias voltage. The non-irradiated modules have tiny currents of the order of 1 μA.

4.2 Off-line Data Processing

During the beam test, data from all sub-systems - telescope modules, binary modules, TDC - are assembled into events and written to a binary data file. To facilitate the analysis, these raw data are processed off-line into summary files, named DSTs (for Data Summary Tape). The summary files present the data in an easily accessible n-tuple format. The off-line processing includes the internal alignment of telescope and module planes and the reconstruction of tracks using the measurements of the beam telescope.

4.2.1 Alignment

The beam telescope provides four very precise measurements in two perpendicular space coordinates. The reconstruction of the track and the interpolation to the plane of the prototype require a precise knowledge of the relative alignment of all detectors in the setup.

The positions of telescope and prototype modules are only approximately fixed by the mounting frames. A precision measurement of the relative alignment of all planes is obtained using the tracks in a large number ($\sim$ 10000) of events. For each track the measurements

of the prototypes and the telescope modules are compared. An iterative procedure minimises the residuals of a large number of tracks. Each detector plane measuring a separate coordinate - x and y for the telescope modules, u and v for the binary modules - is treated independently. The geometry and position of each plane are described by six parameters for barrel modules and eight for forward modules:

- d_0: the distance between strip 0 and the beam axis
- Z: the position along the beam axis
- ϕ: the angle of rotation around the beam axis
- η: the angle around the vertical axis (tilt angle)
- θ: the angle around the horizontal axis (dip angle)
- P: the strip pitch
- dP/dY: the variation of the strip pitch (end-cap only)
- Y_0: the offset in Y of the center of the module (end-cap only)

The pitch and pitch variation are kept fixed at their design values. The alignment procedure optimises the alignment error on a large sample of tracks by iteratively optimising the remaining parameters[2].

As a first step in the alignment procedure, the X and Y axes of the coordinate system are chosen to coincide with strip 0 of the two perpendicular planes of the most upstream telescope module. The Z axis is defined by the beam direction. In practice this is achieved by varying all but one (the Z position is fixed) parameters of the most downstream telescope module until the dX/dZ and dY/dZ of a large sample of tracks are minimised. Once the global system is defined, the remaining telescope planes are aligned by minimising the distance of their hits to tracks reconstructed from the outer two modules. At this stage only two space points are used to define a track. Ambiguities due to noise hits are avoided by requiring all four planes under consideration to have exactly one hit.

After the internal alignment of the telescope, the full telescope information can be used to reconstruct the tracks. The four space points provide an effective redundancy against "fake" tracks, i.e. tracks pointing to noise hits. Therefore, the earlier requirement can be dropped and the full statistics is used to align the SCT modules with respect to the global reference frame. The parameters of each individual plane are varied until the difference between the extrapolated track position and the measurement by the plane converges to a minimum.

In test beam runs where a magnetic field is applied, the assumption of straight tracks is no longer valid. However, applying the alignment procedure on data taken in the magnetic field yields good results, as the effect of the magnetic field is absorbed in the position of the planes.

The SCT modules are composed of four separate silicon wafers. Both stereo-planes of the module are aligned independently. Under the condition that the beam is contained in

[2]The position along the beam axis can be found due to the divergence/convergence of the beam

a single wafer, the alignment procedure is insensitive to the module assembly precision, i.e. the wafer-to-wafer and the front-to-back alignment.

The alignment procedure is repeated each time the setup is accessed and whenever the magnetic field is changed.

4.2.2 Track Reconstruction

The off-line pre-processing of the data includes the reconstruction of the tracks using the space points measured by the telescope[3].

The measurements on the two perpendicular planes of each telescope module are combined into three-dimensional space points. Track segments are constructed by combining all space point measurements on the most upstream and downstream telescope modules. Space points of the remaining two telescope modules are included to form a track candidate if the distance between the track segment and the space point is less than 50 microns. All tracks with at least three space points are stored.

A number of track quality indicators are available to select a sample of tracks with a predefined efficiency and purity. The most important are: the number of space points in the track fit, the χ^2 of the fit, the track gradients with respect to the beam axis and the efficiency of the anchor module. After applying these cuts, a large fraction of the track statistics remains, while the effect of fake tracks on the efficiency measurement is well below 1 %.

In the H8 beam tests, the position where the tracks are incident on each module is interpolated from the telescope hits with a precision of $\sim$ 5 μm. The dominant error is due to multiple scattering in the setup. In the KEK beam tests, with a much lower beam energy, track reconstruction precisions of better than 10 μm can be obtained for the central four modules without a great loss of statistics. For the modules located outside the beam telescope the track reconstruction precision deteriorates to approximately 20 - 30 microns.

4.2.3 Binary hits

In the beam tests the modules are read-out *electrically* through their spy connectors. In electrical read-out the sampling time cannot (easily) be fine-tuned for each module. During the beam test, the time information of each event is stored. The binary SCT modules are operated in the least severe (ANYHIT[4]) data compression mode. Thus, the full hit information from three consecutive clock cycles is stored. This procedure allows to select the optimum time window off-line, independently for each module.

The three-bit hit pattern is decoded off-line, disentangling the binary hit information of the three clock cycles. Clusters that include hits in consecutive strips and different time slots, are reclustered in each clock cycle. Thus, in the analysis phase the trigger phase measurement can be used to select binary hits from a single (optimum) clock cycle. This

[3]The cluster information from the telescope modules is available in the DST, so that custom track reconstructions are still possible

[4]See section 3.3.2 for a description of the data compression algorithms of the ABCD chip.

procedure is equivalent to operation of the modules in LEVEL compression, but the fine-tuning of the timing of the modules is done in the analysis stage.

Finally, the off-line provides some basic error flagging. The integrity of the binary data is checked and overflow of the DST buffers are detected. Data transmission errors leading to violations of the ABCD protocol are detected by MuSTARD. Events with one of these errors are stored in the DST with a special error flag.

4.3 Analysis & Results

A period of beam data with a fixed set of operating conditions is known as a *run*. Typically, a run contains 10.000 to 30.000 events and takes 15-30 minutes under normal beam conditions. Throughout the beam period a large number of runs are accumulated with different operating conditions. The most important parameters studied are discriminator threshold, bias voltage, incidence angle and magnetic field.

The first step in the analysis is the selection of the event sample. The selection cuts are described in section 4.3.1. In section 4.3.2 the most important benchmark observables that are be measured on a single run are discussed: efficiency and noise occupancy. The spatial resolution and a related quantity, the average cluster size, are discussed in section 4.3.3.

In the binary readout scheme the discriminator threshold is varied to recover the full charge distribution. The method to derive the median charge and the signal-to-noise ratio from a scan of the discriminator threshold through the charge distribution is presented in section 4.3.4. The results on recent prototype modules are compared to the theoretical energy loss in silicon. A number of charge collection effects are discussed.

In irradiated modules the performance depends strongly on the detector bias voltage. The dependence of module performance on bias voltage is the subject of section 4.3.5. Finally, in section 4.3.6 the effect of the incidence angle of the beam relative to the detector plane and of operation in a strong magnetic field are discussed.

4.3.1 Event selection

To select a sample of clean, unambiguous events, a number of event selection criteria are applied:

- **Single track events**. In a small fraction of events (depending on the beam intensity, generally of the order of 5 %) more than one track is reconstructed from the telescope information. As the integration time of the binary modules is much shorter than that of the telescope modules the second track is generally not detected in the binary system. To avoid ambiguities, events with more than one track are rejected from the analysis. Events where no track has been reconstructed are rejected as well.

- **Track quality**. From the remaining sample, only those events are accepted where the track satisfies the quality criteria. Most analyses require a minimum number of points in the track fit and set maximum values for the χ^2 of the fit and the slopes of the track with respect to the beam axis. In general, a hit close to the track in the

anchor module is required. This combination of cuts efficiently removes fake tracks and tracks suffering a large deflection due to multiple scattering inside the setup. The loss of statistics in this stage depends on the exact cut values, but is in general of the order of 10-30 %.

- **Masked channels**. During the characterisation of the modules a number of faulty channels is masked. Events where the track points to one of these "bad" channels or immediate neighbours are rejected from the analysis. In recent prototypes the fraction of masked channels is always below 1 %. The loss of statistics in this step is therefore small.

- **Time window**. A final cut removes those events where the trigger phase falls outside the optimum window. The window is optimised separately for each module. Only binary hits in one clock cycle are maintained. Thus, the data taken in ANYHIT compression is converted off-line into the equivalent of LEVEL compression. This cut is expensive in terms of statistics: for a 10 ns window only 40 % of the events are retained.

4.3.2 Efficiency and noise occupancy

The most important benchmark properties of the binary modules are efficiency and noise occupancy at the operating threshold, envisaged to be 1 fC. The efficiency is measured by comparing the prototype response to the *"real"* track position. The *"real"* position of the track on the module plane is interpolated from the telescope measurements. A detector plane is considered efficient if a binary cluster center is located within 100 μm of the *"real"* track position.

The noise hits are counted in noise events taken in the periods without beam between two spills of the accelerator. Thus, the noise events are taken in exactly the same operating conditions as the beam events. The occupancy is defined as the probability to find a hit due to noise on a channel in a given clock cycle.

Figure 4.2 shows the efficiency for a number of threshold settings around the envisaged operating threshold of 1 fC. The noise occupancy corresponding to each threshold is shown on the logarithmic axis on the right of the same figure. The results correspond to a non-irradiated barrel module and a module of the same type irradiated up to the reference fluence of $3 \cdot 10^{14}$ p/cm^2. All modules are operated in the same test beam reference conditions: the detector bias voltage is set to 150 V for the non-irradiated modules and to 450 V for the irradiated modules, the beam is incident perpendicularly on the modules and no magnetic field is applied.

When the modules are operated with sufficient over-depletion, the efficiency shows a long plateau where efficiencies over 99 % are obtained. The noise occupancy, on the other hand, is a rapidly falling, nearly Gaussian function of threshold, independent of bias voltage. The occupancies are found to coincide rather accurately with the expectation from the equivalent noise charges measured during the characterisation. After irradiation, the noise occupancy is considerably higher for a given threshold, in agreement with the increased noise charge.

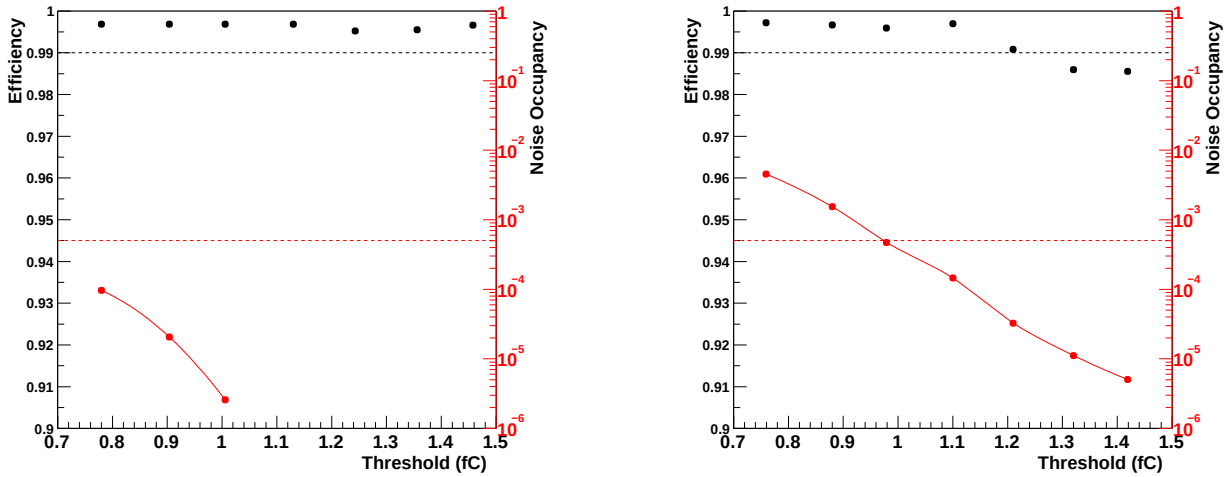

Figure 4.2: *Results under the reference conditions of the efficiency (left axis) and noise occupancy (right axis) versus corrected threshold in fC in the region near the nominal 1.0 fC operating point. The dashed lines indicate the module specifications for efficiency (99 %) and noise occupancy ($5 \cdot 10^{-4}$) at the nominal operating threshold. The leftmost figure corresponds to a non-irradiated barrel module, the rightmost figure to a module of the same type irradiated to the reference fluence of $3 \times 10^{14} p/cm^2$.*

Despite the higher bias voltage, the efficiency for irradiated modules is seen to fall off at a slightly lower threshold than for similar non-irradiated modules.

The SCT specifications require over 99 % tracking efficiency and a noise occupancy of less than $5 \cdot 10^{-4}$. Both requirements are indicated as dashed lines in the figure. The operating range is defined as the range in thresholds where the efficiency and noise occupancy specifications are both met. For non-irradiated modules of the four geometrical types, the operating range extends from $\sim$ 0.8 fC up to $\sim$ 1.5 fC. After irradiation, the operating range is significantly narrower on all modules. The lower limits range from 1.0 to 1.2 fC, whereas the upper limit is generally about 1.2 fC.

Silicon Micro-Strip detectors are discrete measuring devices. In detectors with analog readout the charge on multiple consecutive strips is measured and the position is determined from the properties of the cluster. The clustering procedure yields a quasi-continuous position measurement. In the binary readout scheme, however, the signal is over threshold on only one strip in most cases. Thus, only a discrete measurement is available. This could lead to non-uniformities in the response depending on the position of the track with respect to the two closest strips.

Figures 4.3 show the efficiency versus inter-strip position for perpendicularly incident tracks on an irradiated and a non-irradiated barrel module. The position is expressed in units of the read-out pitch: inter-strip position 0.5 corresponds to tracks crossing the detector at equal distances from the two strips and inter-strip positions of 0 and 1 correspond to tracks that are incident on the readout strip. In the central region diffusion of the charge carriers leads to increased charge sharing. The lower signal on each of the strips is reflected by the deteriorated efficiency at high threshold. However, no loss of efficiency is observed for the operating threshold. Note that the distribution is smeared by the uncertainty in the

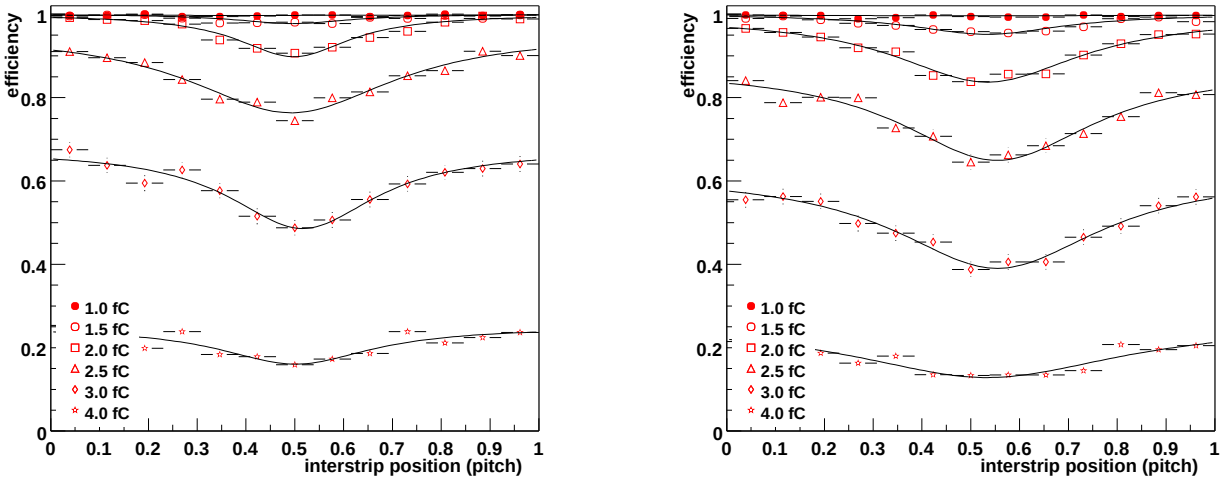

Figure 4.3: *Efficiency as a function of the inter-strip position of the incident particle. In the leftmost figure a non-irradiated module is shown. The module in the rightmost figures had been irradiated to the reference fluence of* $3 \times 10^{14} p/cm^2$.

position of the interpolated track that becomes significant at this level. The case for non-perpendicular incidence is discussed later on in this chapter.

4.3.3 Spatial resolution

The *residual* is defined as the difference between the position interpolated from the telescope measurement and the center of the cluster found in the binary module. For end-cap modules the residuals are projected on the line where the pitch is equal to that in the barrel modules (80 μm) to facilitate comparison. Typical residual distributions are shown in the upper two figures of 4.4. The empty histograms show the result using only single strip clusters: the residuals form a uniform distribution from $-p/2$ to $p/2$, where p is the readout pitch, characteristic for binary readout.

The spatial resolution is obtained as the width of the residual distribution. The spatial resolution due to single-strip clusters is given by the RMS of a uniform distribution with a width equal to the pitch: $\sigma = p/\sqrt{12} \sim 23\ \mu m$. The contribution from two-strip clusters is shown separately with dark fill colour. As the multi-strip clusters predominantly occur in a narrow region in the central region between two strips the resolution of the multi-strip clusters is better than that of single-strip clusters[5]. Note that the residuals are smeared by the error on the interpolation of the telescope tracks, of the order of 5 μm.

In normal operation the fraction of multi-strip clusters is small and the resolution is close to 23 μm, independently of the operating parameters. Also, no significant change is observed in the residuals at a threshold of 1 fC after irradiation. The effect of the bias voltage and the incidence angle on charge sharing are discussed in subsections 4.3.5 and 4.3.6, respectively.

The residual distribution of the upper figures of 4.4 is a measurement of the spatial resolution of a single detector plane. The stereo angle of 40 mrad between the two detector

[5]see the discussion in the next section

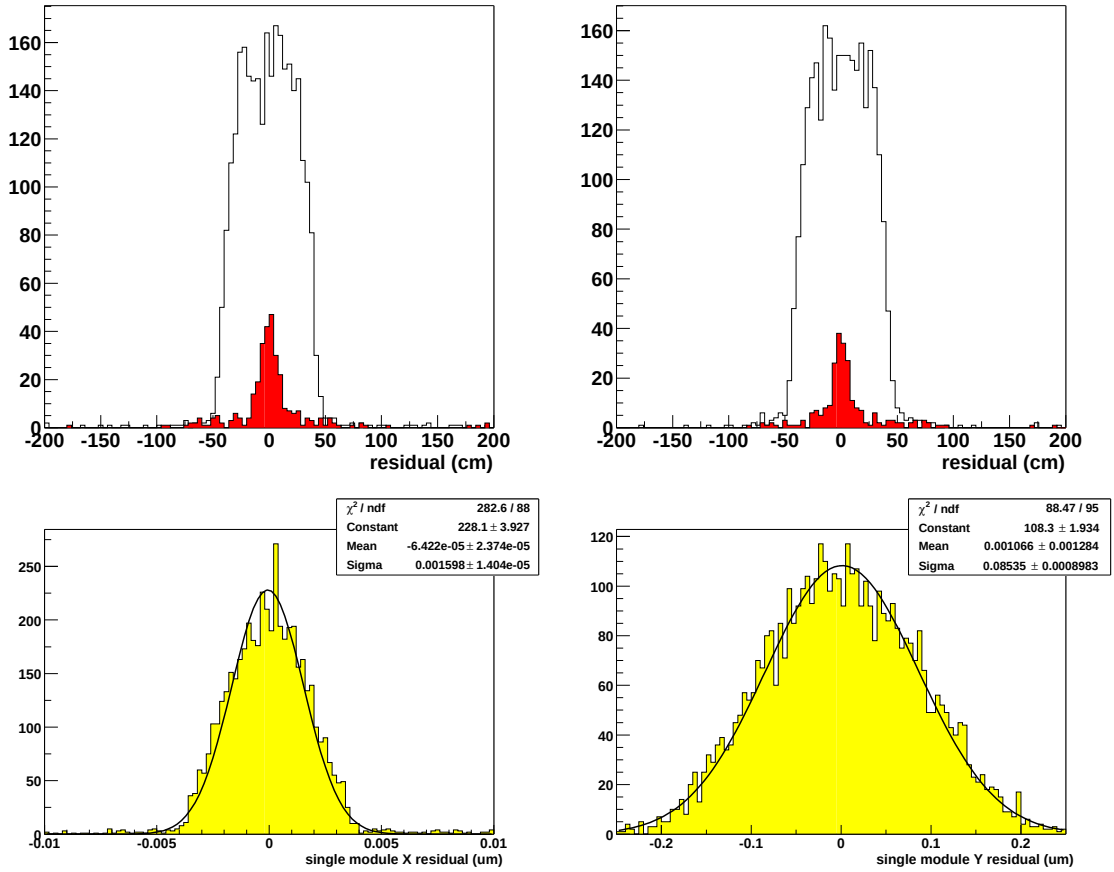

Figure 4.4: *Topmost figures: single plane residuals. Results are shown for an irradiated barrel module (leftmost figure) and an end-cap outer module (rightmost figure). For the end-cap module the residuals have been rescaled to a pitch of 80 μm. Bottom figures: residual of the space point measurement obtained by combining the two planes of the module. Leftmost figure: X-coordinate (perpendicular to the long axis of the module). Rightmost figure: Y-coordinate. The discriminator threshold is set to 1 fC.*

planes of the SCT module allows the determination of a two dimensional space point. The intersection of two 80 μm wide strips defines a rhomb with short axis $\frac{p}{\cos \alpha/2}$ and long axis $\frac{p}{\sin \alpha/2}$, where p is the readout pitch and α is the stereo angle. The short axis corresponds to the X axis of the global coordinate system in the test beam, while the long axis is identified with the Y axis. Projecting the uniform distribution in the rhomb on both axes yields triangular distributions with an RMS $\sim$ 17 μm in X and RMS $\sim$ 810 μm in Y, see figure 4.4. More detailed results on the single module resolution are reported in [118].

4.3.4 Median charge

In the binary readout scheme, a scan of the discriminator threshold through the charge distribution is performed to reconstruct the full signal distribution. The curve of efficiency as

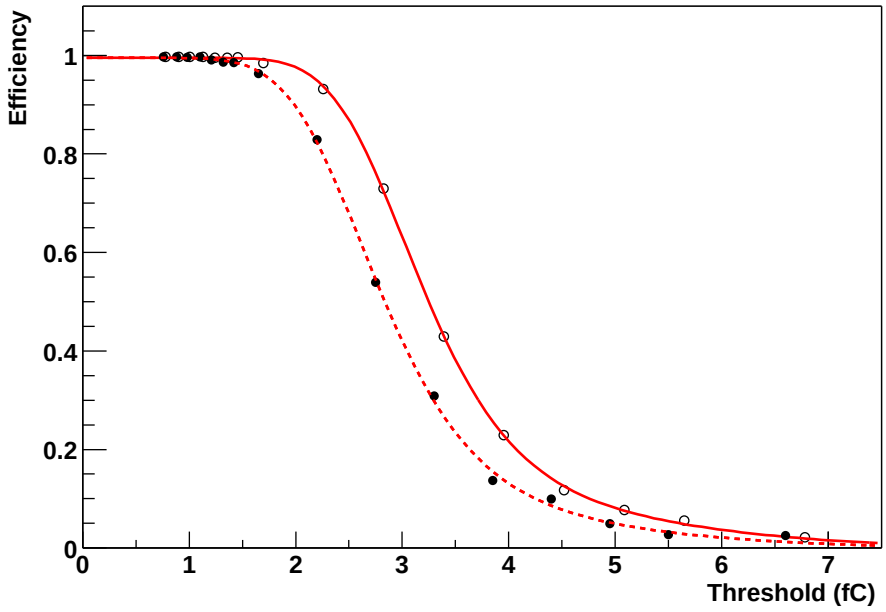

Figure 4.5: *Typical efficiency versus threshold* s-curves *results for a non-irradiated (solid line) and an irradiated (dashed line) module operated under reference conditions.*

a function of threshold (known as the S-curve) measures the integrated charge distribution. The *collected* charge distribution is described by the Landau distribution of the *deposited* charge convoluted with the Gaussian noise distribution and the effect of charge sharing between neighbouring strips. The median charge is measured as the charge corresponding to the threshold where 50 % efficiency is obtained. In practice, the threshold is expressed in equivalent charge and the value for the median charge is obtained directly from a fit with a skewed error function:

$$\epsilon = \epsilon_{max} f(x \cdot [1 + 0.6 \frac{e^{-\epsilon x} - e^{\epsilon x}}{e^{-\epsilon x} + e^{\epsilon x}}]) \tag{4.1}$$

where f denotes the complementary error function. The median charge μ, the width σ and the maximum efficiency ϵ_{max} are free parameters and $x = (thr - \mu)/\sigma^2$. This parameterisation describes the data quite accurately.

In figure 4.5 the S-curves of a non-irradiated and an irradiated module are shown for reference operating conditions. Each point corresponds to the efficiency measured on a single run of $\sim$ 15000 events. The lines represent the fit with the function of equation 4.1.

The error on the median charge is dominated by the uncertainties in the calibration. The variation of the calibration from one chip to the next is evaluated in the beam test by pointing the beam to areas of the detector read out by different chips and measuring the median charge of each chip separately. For non-irradiated modules the chip-to-chip spread in the median charge is of the order of 4%. After irradiation the spread increases to nearly 10% on some modules [132]. Correcting the charge of each chip by measurements of the calibration DAC output improves the uniformity, suggesting that the spread in median charges is due to variations in the components of the calibration circuit [113].

Therefore, the random error of a single median charge measurement is of the order of 0.1 fC for non-irradiated modules and 0.3 fC for irradiated modules. The median charge measured on a large number of recent barrel and end-cap (outer) modules is 3.5 $\pm$ 0.1 fC for a bias voltage of 300 V.

In practice, use of the signal-to-noise ratio removes most of the calibration dependence, greatly facilitating comparison between the different modules. Division of the median charge by the equivalent noise charge, measured as part of the electrical characterisation of the module, yields a signal-to-noise ratio of ~ 14. For inner modules the better noise performance yields a S/N ~ 20 as the 6 cm strips present a lower capacitive load on the amplifier.

From the calculation in section 3.1 a median *deposited* charge of 4.0 fC is expected. The observed median *collected* charge is clearly lower. Less than 0.1 fC can be attributed to the measurement procedure. Apparently, some of the deposited charge is not collected.

The binary readout scheme is essentially single-strip. The charge deposited on neighbouring readout strips cannot be recovered by reclustering the signal. In reference [117] three mechanisms that lead to signal leaking into the neighbouring strips are identified:

- **Diffusion** For tracks incident on the central region between two strips, diffusion of the charge carriers as they drift towards the read-out plane leads to significant charge sharing.

- **δ-electrons** In a fraction of the interactions a large momentum transfer takes place between the incident particle and an electron in the medium. Electrons with energies of several tens or hundreds of keV can travel significant distances ionising the medium along their trajectory.

- **Cross talk** The capacitative coupling of the strips - the inter-strip capacitance - leads to the induction of a signal on the neighbouring strips.

Multi-strip clusters due to diffusion of the charge carriers only occur when a track is incident on a narrow region exactly between read-out strips. This property is used to disentangle the diffusion component from the remaining two mechanisms. From a set of events two samples are formed: the first samples contains the full statistics, while in the second sample only tracks that are incident close to (within 20 microns of) a readout strip are accepted. The multi-strip cluster probability for the full sample - with contributions from the three mechanisms - and the reduced sample - diffusion no longer plays a role - is shown as a function of threshold in figure 4.6.

Charge sharing due to diffusion is found to lead to a significant increase in the multi-strip cluster probability only at low threshold. From the median charge obtained on both samples the charge loss due to diffusion of the carriers is estimated. For all module types the charge difference is found to be 0.13-0.16 fC.

The charge loss due to cross talk cannot be measured in the beam test. The fraction of the signal that is induced on neighbouring strips can be estimated from figure 3.9. Ignoring the impedance of the amplifier and assuming the capacitor on the hybrid that joins the detector backplane and HV ground is sufficiently large the following result is obtained for

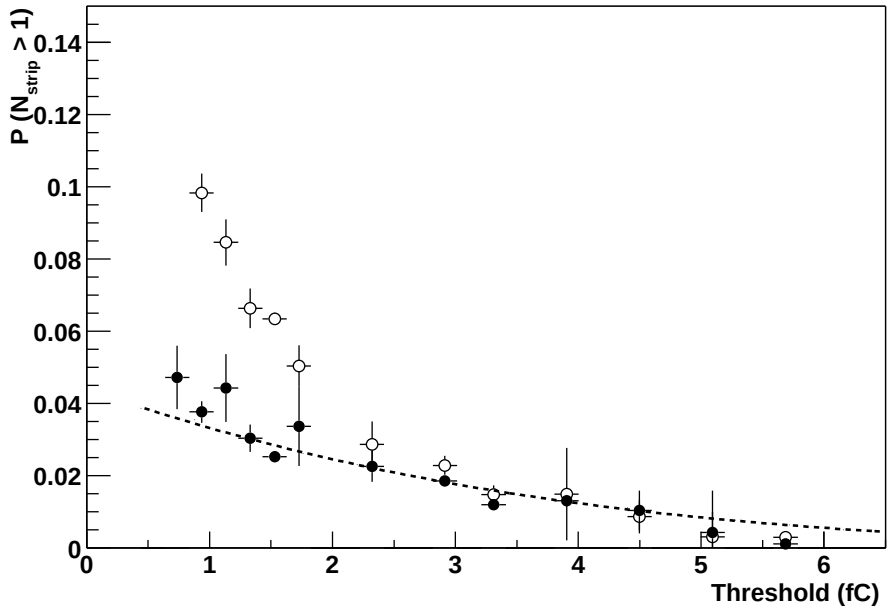

Figure 4.6: *Probability of multi-strip clusters close to the track. The open markers correspond to an analysis of all tracks, while for the curve with filled markers tracks in the central region between two strips are excluded. The dashed curve represents a calculation of the multi-strip probability for the latter case, using GEANT4.*

the signal induced on the neighbouring strips:

$$I_{neighbours} = \frac{I_s C_i}{C_c + C_i + C_b} \tag{4.2}$$

Using measured values for the coupling, inter-strip and strip-to-backplane capacitances of $C_c = 120\ pF$, $C_i = 6\ pF$ and $C_b = 1.7\ pF$, the charge loss due to cross talk is expected to be of the order of 6%, i.e. $\sim 0.26\ fC$.

The leakage of charge to neighbouring strips due to δ-electrons is found to dominate the multi-strip cluster probability at high thresholds. The effect on the median charge cannot be estimated from test beam data. Model (GEANT4) calculations show that even though the tail of the charge distribution becomes less pronounced as δ-electrons carry energy away from the central strip, the median of the distribution is not significantly affected.

The total charge loss due to the three charge sharing mechanisms is thus expected to be $\sim 0.4\ fC$. Signal loss due to charge sharing accounts for (most of) the discrepancy between the observed median charge ($3.5\ fC$) and the theoretical expectation ($4.0\ fC$).

4.3.5 Detector Bias Voltage

The bias voltage of the detector is an important operating parameter. For irradiated detectors the signal grows with increasing bias voltage. On the other hand, the maximum voltage is limited by the detector breakdown voltage (greater than $500\ V$ for SCT detectors), the

limit of the power supplies (450-500 V) and the limit posed by the cooling system. To find the best compromise, a good characterisation of the performance versus detector bias voltage is essential.

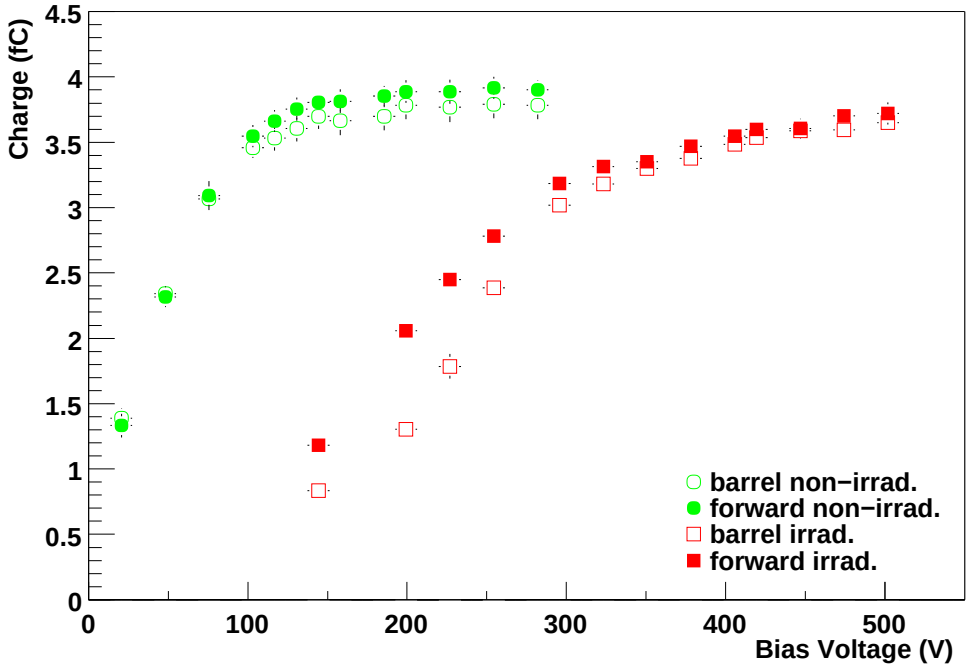

Figure 4.7: *Median charge as a function of bias voltage for barrel (open markers) and end-cap outer modules (filled markers). The square markers correspond to modules that had previously been irradiated to the reference fluence of* $3 \cdot 10^{14}$ *protons/cm*^{2}.

In the December 2000 beam test at KEK fine-grained, nested scans of detector bias voltage and threshold were performed. Even though the modules under test are of an old design, the bias voltage dependence is expected to be valid. The median charge measured at the reference voltage is $\sim 3.7\ fC$, larger than the more recent result presented in section 4.3.4. The difference is attributed to the absolute calibration of both batches of Front-End chips.

Figure 4.7 shows the dependence of the median collected charge on the detector bias voltage. Filled markers correspond to end-cap modules. Squares denote the irradiated modules. Each point has been obtained as the average over both sides of all modules of a given type. The error bars represent the variation (RMS) of the measurements used for the average.

For the non-irradiated modules the median charge is nearly constant from 150 V upwards. The charge difference between the reference voltage of 150 V and the highest voltage (300 V) is 0.15 fC. As the bias voltage approaches the depletion voltage (about 65 V in these modules) the median charge gradually decreases. This can be explained as a ballistic deficit of the shaper. The integration window of the front-end electronics is no longer large compared to the charge collection time of the detector, leading to charge loss. The discussion of drift time in section 3.1 indicates that the drift time of the holes becomes comparable to the peaking time of the shaper at a bias voltage of about 100 V. For a detailed discussion of

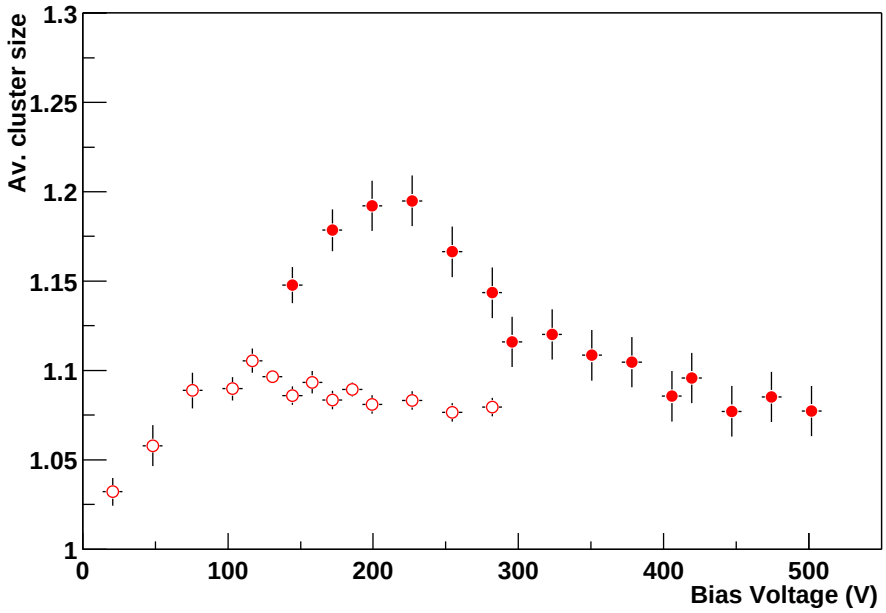

Figure 4.8: *Cluster size of the efficient clusters (close to the track) as a function of bias voltage. The discriminator threshold is 1 fC. Open markers represent non-irradiated modules whereas the filled markers correspond to a barrel module irradiated to the reference fluence.*

charge collection times, see references [93, 133, 134].

The collected charge decreases rapidly when the bias voltage is lowered below the depletion voltage (approximately 65 V). In under-depleted operation, only the charge deposited in the active, depleted region of the detector is being collected. As explained in section 3.1 the depleted region grows with the square root of the bias voltage.

The relation between signal and bias voltage for irradiated modules is more complicated. The collected charge does not saturate until the maximum available bias voltage in the beam test, 500 V, is reached. The depletion voltage is estimated to be about 250 V for these detectors. The maximum value of the charge (at 500 V) approximates the charge found in the non-irradiated modules. It should be noted that the uncertainty of the order of $\sim$ 10 % of the absolute calibration due to the effect of the irradiation on the calibration circuit is not reflected in the error bars.

Various possible explanations exist for the high over-depletion needed to reach full charge collection. Measurements by the ROSE collaboration [85] indicate that there is considerable charge loss due to trapping of the charge carriers in radiation-induced lattice defects. Assuming a constant trapping probability per unit time, the effect is bias voltage dependent (through the charge collection time). For small over-depletion, the different field distribution across the Silicon in type-inverted bulk material might lead to a ballistic deficit of the shaper.

In irradiated, type-inverted p^+n detectors the junction forms at the backplane, between the n^+ material of the backplane and the p-bulk. Thus, if the bias voltage is lower than the depletion voltage the depleted region does not reach the read-out side of the detector. Still, a small signal is induced on the strips across the dead region.

For modules irradiated to the reference fluence of $3 \cdot 10^{14} p/cm^2$ the combined effect of a moderate charge loss and a significant increase of the noise yields signal-to-noise ratios between 7 and 11 for a bias voltage of 470 V. The large variation in the results is not completely understood, although there are indications of a dependence on the production batch of the front-end chips and possibly module type. Also, the error on the fluence is of the order of 10-15 %.

The average cluster size provides a sensitive measure of the spatial distribution of the charge carriers as they reach the readout plane. Figure 4.8 shows the evolution of the cluster size with bias voltage. The dependence of cluster size on bias voltage is very moderate for the non-irradiated modules. The decrease below depletion voltage is due to the loss of collected charge. Raising the voltage from about 150 V to 275 V leads to a slight decrease of the average cluster size. In a high field the charge is collected faster and the effect of diffusion is less important.

Once more, in irradiated modules the behaviour is more complicated. The slight decrease of the average cluster size between 350 and 500 V is attributed to the decreasing collection time. The spatial distribution of the cloud of charge carriers becomes narrower as the carriers have less time to diffuse. The asymptotic cluster size at high bias voltage is similar for irradiated and non-irradiated modules, even though the plateau is reached at very different voltages. Approximately at the depletion voltage, the cluster size rises dramatically. This reflects the fact that for signals induced across relatively large distances, the charge is less localised. For the lowest voltages, the signal becomes very small and the cluster size decreases again.

4.3.6 Incidence angle & magnetic field

In the ATLAS detector the SCT modules will be subject to a 2 Tesla magnetic field. Also, tracks are in general not perpendicularly incident on the detector plane. Therefore, an important subject of study is the influence of the magnetic field and incidence angle on the performance of the modules.

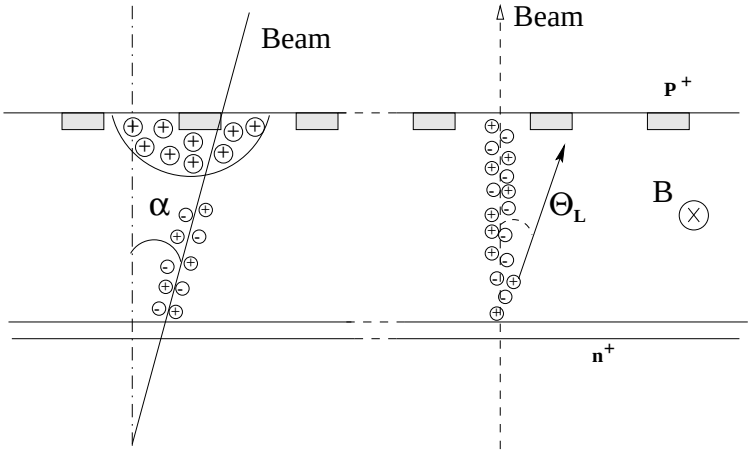

Figure 4.9: *Representation of the effect of the incidence angle and a magnetic field.*

In the August 2001 beam test [118] threshold scans were performed at various angles, both without magnetic field and in the 1.56 T field of the Morpurgo magnet. In this section the dependence of the most important parameters - efficiency at the operation threshold, median collected charge and spatial resolution - on the incidence angle and field is discussed.

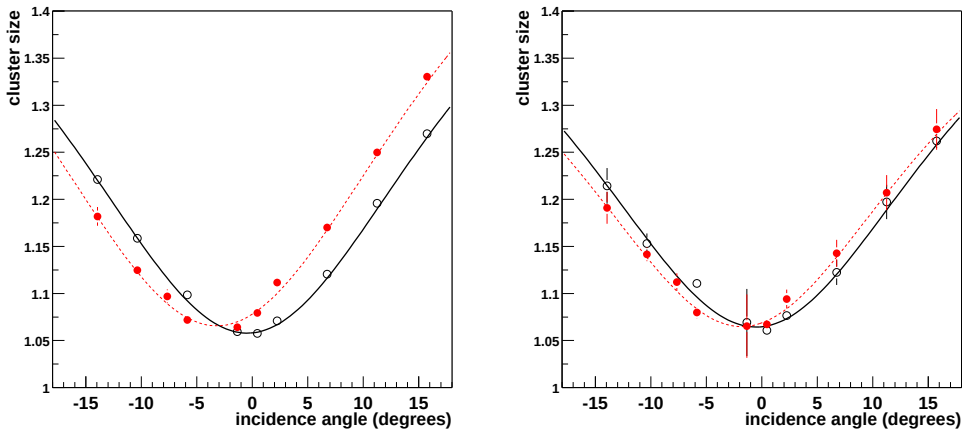

Figure 4.10: *Cluster size versus angle at a discriminator threshold of 1 fC (lower figures) versus incidence angle. Results are shown for non-irradiated (leftmost figure) and irradiated modules (rightmost figure). Filled marker are measurements in a 1.56 T magnetic field, open markers without field .*

Two orientations should be considered for the incidence angle in the inner detector. The angle in the detector R-z plane is determined by the detector barrel + end-caps geometry. It becomes quite large (68^o) for the outermost modules on the inner barrel. The longer path length through the silicon leads to a increase of the median charge with $1/\cos(\alpha)$. This simple geometric effect has been confirmed in beam tests up to angles of $\sim 16^o$ [118]. Recent tests extend this range to more than 30^o [132].

The incidence angle in the $R\phi$ plane depends on the deflection of particles in the solenoidal magnetic field. It is generally smaller: for a 1 GeV particle the incidence angle is of the order of $\sim 10^o$. The tilt angle of the barrel modules forms an offset of 7^o. The longer path length again leads to a small increase of the signal. But, in this orientation the projection of the particle trajectory on the readout plane is perpendicular to the read out strips. For large incidence angles the projected distance becomes significant compared to the pitch and charge sharing between neighbouring strips becomes important.

In a strong magnetic field the Lorentz force deviates the drifting carriers. Figure 4.9 shows how the Lorentz force is equivalent to a rotation by a small angle $\Theta_L = \mu^H B = r_H \mu B$, where μ^H the Hall mobility, the conduction mobility μ multiplied by the Hall scattering factor r_H [58].

In the August 2001 beam test the effect of incidence angle and magnetic field was studied in an orientation representative for barrel modules at $\eta = 0$. The detectors are biased to the nominal bias voltage: 150 V for non-irradiated modules, 350 V after receiving the full expected dose. The modules are naturally classified in two groups: irradiated and

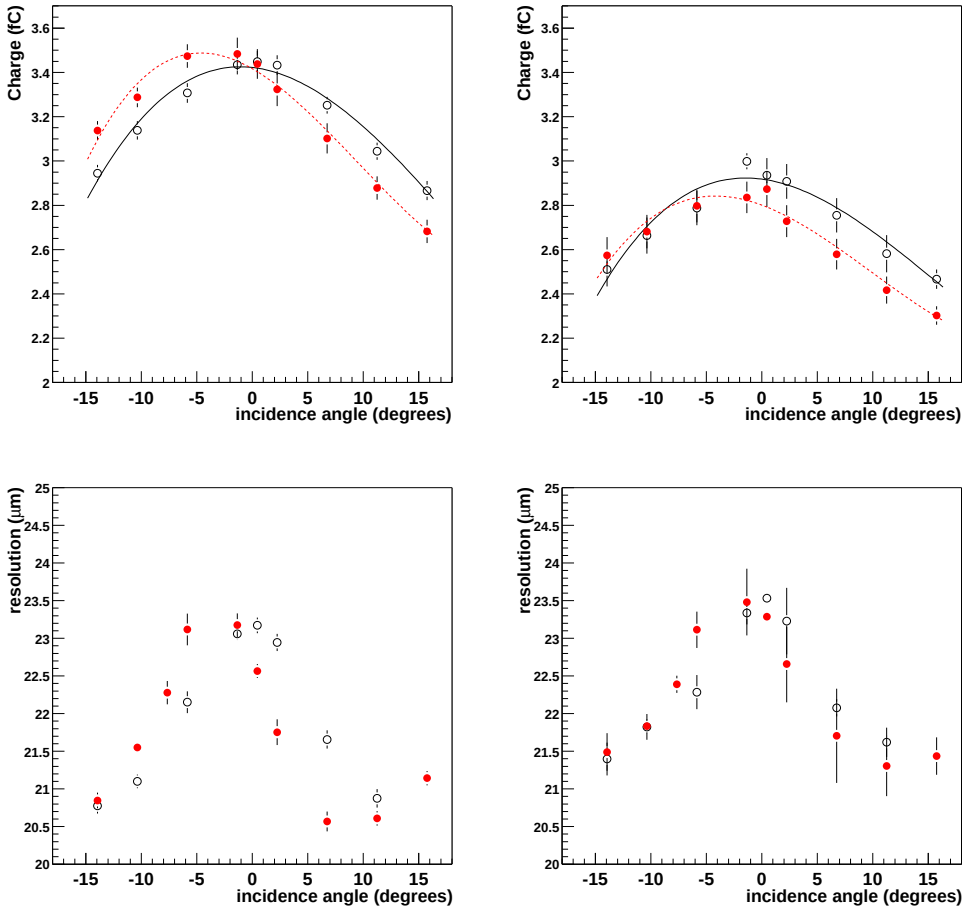

Figure 4.11: *Cluster size versus angle (upper figures) Median charge (central figures) and spatial resolution at a discriminator threshold of 1 fC (lower figures) versus incidence angle. Results are shown for non-irradiated (leftmost figure) and irradiated modules (rightmost figure). Filled marker are measurements in a 1.56 T magnetic field, open markers without field .*

non-irradiated modules. The results are presented as averages over all modules in a group. Statistical errors are calculated as the variation between the different modules in each group.

A sensitive measure of charge sharing is the average size of signal clusters. Noise clusters are excluded by requiring a maximal distance of 200 μm to the track position interpolated from the telescope measurement. Figure 4.10 shows the average cluster size as a function of incidence angle. Filled markers correspond to data taken without magnetic field, while the open markers show the same measurement in a 1.56 T magnetic field. The increase of cluster size with the incidence angle reflects the increased charge sharing.

The effect of the magnetic field is a shift of the distribution by a few degrees. The Lorentz angle is determined as the minimum of the cluster size versus angle curve. As a cross check, the fit results for data taken without magnetic field are calculated. The result $\Theta_0 = 0.4° \pm 0.2°$ reflects the overall uncertainty in the angle scale. The Lorentz angle obtained for both groups, non-irradiated and irradiated modules, is then:

$$\Theta_L(150V) = 3.3^\circ \pm 0.3^\circ \quad (4.3)$$

$$\Theta_L(350V) = 2.1^\circ \pm 0.4^\circ \quad (4.4)$$

As the irradiated modules are biased at a higher voltage, the observed difference could be due to an electric field dependence of the Lorentz angle or a change in the properties of the charge carriers due to irradiation. In the literature, the effect of proton irradiation on the mobility and thus Lorentz angle of holes is found to be compatible with no effect [93] [135] [136] or very small, of the order of 2% [133]. The difference in voltage, i.e. the electric field inside the detector, has an effect on Θ_L through the electric field dependence of the carrier mobility μ. Theoretical models [58, 135] applied to beam test conditions (silicon temperature $T = 261^o\ K$, thickness $d = 285\ \mu m$ and field $B = 1.56\ T$) predict values of $\Theta_L(150\text{V}) = 3.3^\circ$ and $\Theta_L(350\text{V}) = 2.4^\circ$. The predictions agree within errors with our measurements.

Figure 4.11 presents the median charge result for both groups of modules. The negative effect of charge sharing is stronger than the $(1/cos\alpha)$ increase due to the longer path length, so for non-perpendicular incidence the observed charge decreases. The effect is similar in non-irradiated and irradiated modules, although the absolute values of the charges are smaller for the irradiated modules. The effect of the magnetic field is a shift by the Lorentz angle with respect to the curves without magnetic field.

In the range of angles $[-14^o, 16^o]$ studied in the beam test no significant effect on the efficiency is observed at a threshold of 1 fC. For irradiated modules a small effect becomes visible when the discriminator threshold is raised to 1.2 fC. Still, the efficiency is over 97 % for all angles.

As discussed in section 4.3.3 the spatial resolution with binary readout depends on the number of strips in the cluster. An increase of multi-strip clusters is expected to lead to a better resolution. In figure 4.11 the effect of the incidence angle on the spatial resolution of non-irradiated (leftmost figure) and irradiated modules (rightmost figure) is shown. The difference between the worst (0°) and the best ($\pm 15^\circ$) resolution is about 2 μm. Again the magnetic field causes a shift.

4.4 Implications for ATLAS

In this section the beam test results are discussed in the light of their implications for the operation of the SCT in the ATLAS detector.

The current module design is found to meet the efficiency and noise occupancy specifications, even after a large fluence of irradiation. The envisaged operating detector bias voltage and discrimination threshold are found to satisfy the requirements for non-irradiated modules. The bias voltage is to be (gradually) increased during the lifetime of the experiment to ensure a good charge collection efficiency. The discriminator threshold is probably to be raised to 1.1 or 1.2 fC in order to control the noise occupancy.

And, importantly, the performance is - to a large extent - understood. The knowledge obtained in beam tests allows to improve the Monte Carlo simulation of the detector. Part of the beam test results have been incorporated into the *digitisation* step of the SCT module in the GEANT4 simulation of the the ATLAS detector [137]. A realistic description of the bias

voltage and incidence angle dependence of the response is implemented for non-irradiated modules. The model is currently being updated using more recent beam test data [138]. The effect of irradiation on the performance is to be implemented as well.

The deviation of the drifting carriers due to the Lorentz effect leads to a shift of the apparent position by several μm. A good description of the bias voltage dependence of the Lorentz angle allows for a precise correction of this effect.

4.5 Pulse shape reconstruction

In the analysis described in the previous section events from a narrow trigger phase window are selected to optimise the sampling time with respect to the charge deposition time and thus evaluate the module performance in an environment similar to the expected operation in ATLAS. An alternative approach, developed during the December 2000 test beam at KEK, is to explicitly reconstruct the dependence of collected charge on the charge deposition time. In this section the method is outlined. The results are compared to a detailed simulation of the charge collection in the detectors. A summary of this study was published in [120].

4.5.1 Method

The pulse shape reconstruction takes advantage of the fact that test beams are normally continuous, i.e. the sampling time varies randomly over the length of a clock cycle - 25 ns. The relative charge deposition time is measured as the delay between the raw trigger from the scintillators and the next rising edge of the 40 MHz system clock. The measured time range is extended to cover 75 ns using the hit information from the previous and next clock cycle provided by the ABCD.

Combining the efficiency versus time dependence for all runs of a threshold scan provides a 2-dimensional map of efficiency versus time and threshold. For each 1 ns time slice, the variation of efficiency with comparator threshold forms an S-curve. As in the previous analysis, the threshold is expressed as the equivalent charge injected to the front-end obtained from the response curve. The median charge for each time slice is found as the threshold where 50 % efficiency is obtained (VT50). The fit function of equation 4.1 is replaced by a complementary error function to ensure a robust fit of the out-of-time bins.

The resulting charge versus time curve represents the median time-resolved input of the discriminator. Thus, the response of the front-end to detector pulses can be studied.

In order to reduce the effect of charge sharing, only events where the track points to a position within 40 μm of a strip are accepted. This greatly facilitates the comparison with simulation.

In the KEK beam test six modules were tested: one irradiated and two non-irradiated modules of barrel and end-cap outer geometries. For each of the modules the pulse shape was reconstructed for a range of detector bias voltages.

The resulting pulse shapes are compared to a simulation of the detector and front-end electronics. To this end the time-resolved detector signals presented in section 3.2.3 are numerically convoluted with the transfer function of the ABCD amplifier/shaper of equation 3.21.

4.5.2 Results - comparison to simulation

In this section the pulse shapes reconstructed from the beam test data are compared to a simulation of the detector signal and the front-end response.

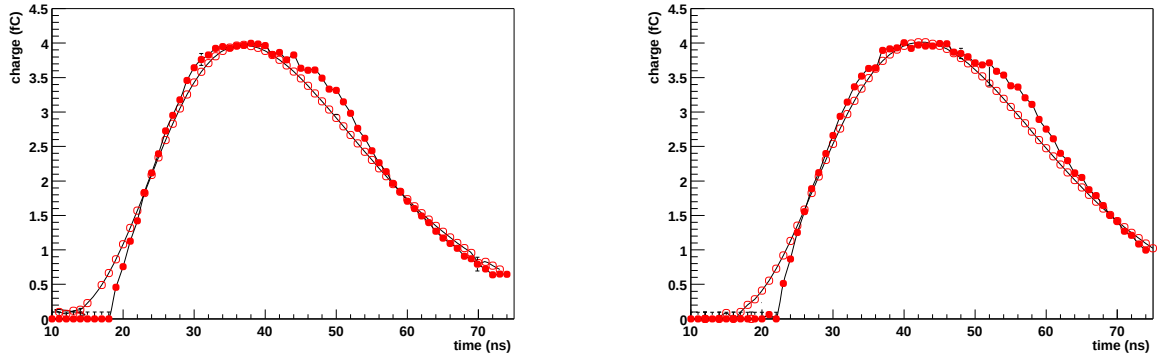

Figure 4.12: *Pulse shapes for non-irradiated modules. The leftmost figure shows the result for a barrel module, the rightmost figure for an end-cap module. The detector bias voltage is 150 V. The simulated pulse shapes are drawn with open markers in the same figure. The pulse heights are chosen to agree with the data.*

Figure 4.12 shows the pulse shape reconstructed for a non-irradiated barrel and end-cap module at a detector bias voltage of 150 V. The simulation result in the same figure corresponds to a peaking time of the shaper of 22 ns for the barrel module, close to the design value of 20 ns. In the case of the end-cap module a peaking time of 24 ns gives the best agreement with data. The results shown in figure 4.12 are representative for both geometrical module types in the KEK beam test. The significantly longer peaking time on the end-cap modules is most likely due to the high temperature of the end-cap hybrids in this beam tests. The effect is not observed on more recently produced end-cap modules.

The experimental results of both modules clearly deviate from the simulation: the experimental pulse shows a *shoulder* that is not present in the simulated curve. This shoulder persists up to the highest bias voltage in the beam test (275 V). Measurements of the pulse shape using the (fast) charge injection of the calibration circuit confirm the observation [118]. This suggests that the *shoulder* is not due to a detector effect, but a property of the front-end. A possible explanation is an extra delay[6] in the the discriminator for signals with a small over-drive (i.e. signals that are close to the threshold).

Figure 4.13 shows how the bias voltage changes the observed pulse shape. In the same figure the simulation results for the two bias voltages are drawn. Note that all parameters except the bias voltage are the same as in 4.12. The pulse shape hardly changes between 150 and 250 V, indicating that the detector signal is already fast with respect to the shaper peaking time at a bias of 150 V. The pulse height is virtually the same for both bias voltages: nearly the full signal is collected from 150 V upward.

[6]This delay is to be added on top of the time walk

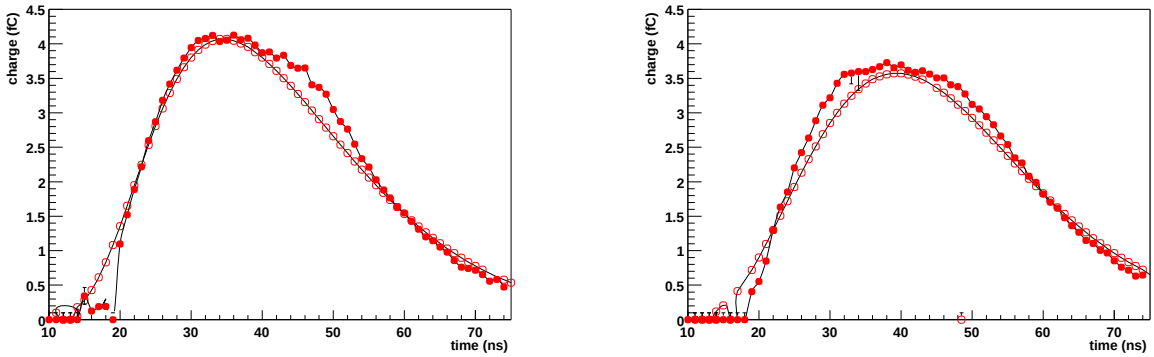

Figure 4.13: *Pulse shapes for a non-irradiated barrel barrel module at a detector bias voltage of 250 V (leftmost figure) and 100 V (rightmost figure). The simulation parameters are those of figure 4.12*

The pulse shape corresponding to 100 V is considerably lower and longer than at 150 V. The stretched pulse confirms that the charge loss between the depletion voltage ($\sim$ 65 V) and $\sim$ 150 V is dominated by ballistic deficit of the shaper: the detector signal becomes slow with respect to the integration time of the shaper leading to charge loss.

In figure 4.14 the test beam and simulation results are summarised. For each bias voltage, the pulse height is fitted using a parabola in a narrow range around the maximum. As a measure for the length of the pulse, the effective peaking time is plotted in figure 4.14. It is obtained from a fit of the pulse to a $CR(RC)^3$ shape. The dependence of both the length and height of the pulse on the bias voltage is described rather well by the simulation for depleted detectors (75 to 275 V), indicating that the charge collection model is adequate for non-irradiated modules. For under-depleted detectors the pulse height is predicted quite well, but the simulated pulse length is significantly lower than the measured values.

For the irradiated module of figure 4.15 the deviation of the pulse shape from the prediction by the model is much more pronounced. This is also observed in measurements with the calibration circuit. Radiation damage to the discriminator could explain the increased sensitivity to signals with a small over-drive.

The best fit of the simulation to the data is now obtained for a peaking time of 24 ns. The increase of the peaking time after irradiation is confirmed by time walk measurements using the charge injection circuit on many modules.

The pulse length dependence on bias voltage for over-depleted detectors is reproduced reasonably well in the simulation: virtually no dependence is seen down to 350 V, indicating that the detector signal is relatively fast for these bias voltages. For detectors operated with a small over-depletion voltage 250-350 V the effective peaking time is found to increase by up to 4 ns, indicating that ballistic deficit of the shaper becomes significant in this interval.

The pulse height behaviour is not reproduced by the simulation. While in the experimental result the pulse height gradually decreases when lowering the bias voltage from $\sim$ 500 V to the depletion voltage, the pulse height in the simulation is nearly constant in this range. This indicates that the charge loss in this region is due to an effect that is not taken

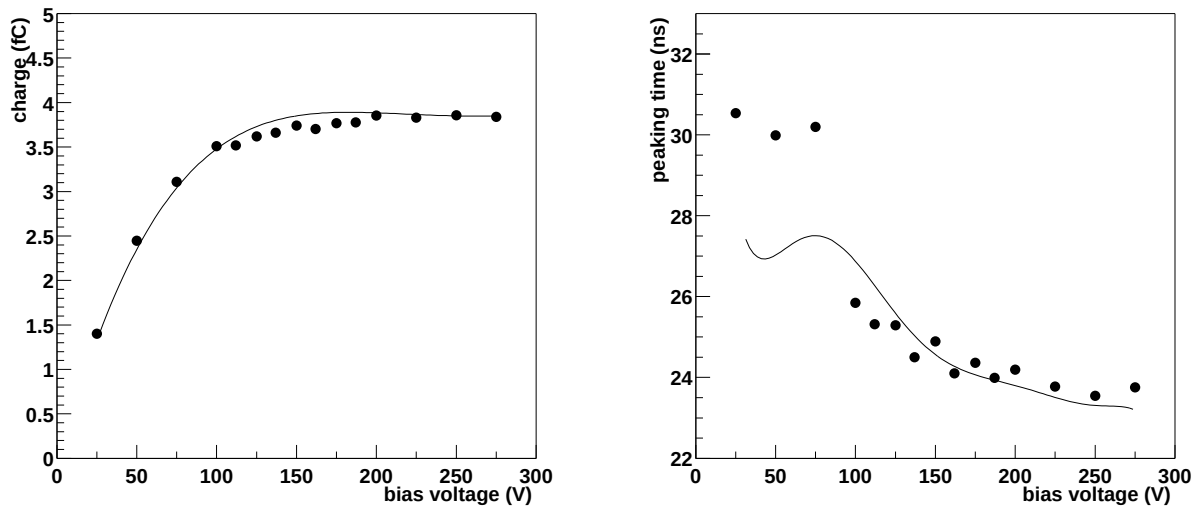

Figure 4.14: *Comparison of the experimental result (filled markers) and the simulation (continuous line) for the pulse height (leftmost figure) and the effective peaking time of the pulse (rightmost figure).*

into account in the simulation: the trapping of charge carriers in radiation induced lattice defects.

For under-depleted operation[7] a small signal is induced on the strip across the dead region. Qualitatively, this effect is predicted correctly by the simulation. The pulse length prediction, however, underestimates the experimental results significantly. This is not understood, but is not surprising given the complicated field properties in type inverted silicon detectors [133, 93].

4.5.3 ATLAS perspective

In the previous section a significant deterioration of the speed of the front-end circuit after irradiation is observed (see also [120, 119, 118, 132]). In this section the implications of this effect on the operation of the ATLAS detector are discussed.

In particular, inefficiencies due to out-of-time hits and the occupancy load of these hits in the consecutive event (ghost hits) are studied. The results are obtained from an analysis of prototype modules tested in the May and August 2002 data [132]. The results are compatible with those obtained in a beam with a 25 ns bunch structure in October 2001 [139].

The LHC bunch crossing frequency of 40 MHz requires the front-end electronics to react very rapidly to the signal. A too slow response leads to out-of-time hits that have the time-stamp of the consecutive bunch crossing. These so-called ghost hits cannot be assigned to the track and thus are a source of inefficiency. Moreover, they add to the occupancy of

[7] The SCT is not envisaged to be operated under-depleted. The measurement at low voltages were meant to indicate the depletion voltage

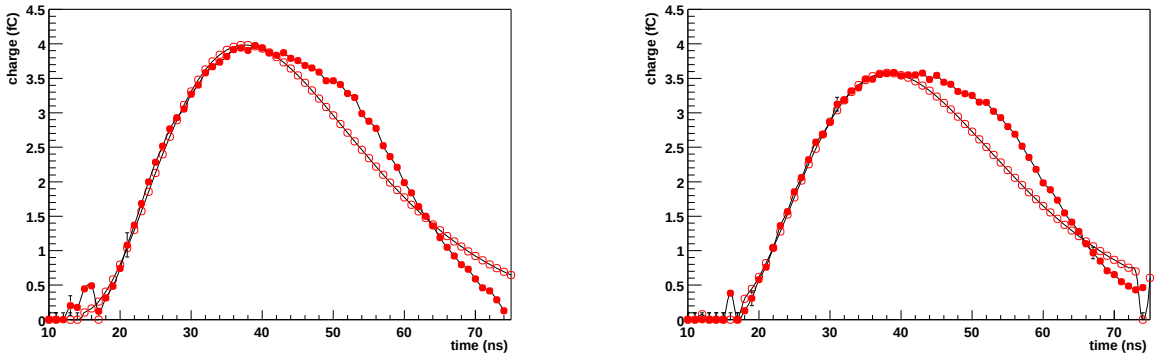

Figure 4.15: *Pulse shapes for an irradiated barrel operated at detector bias voltage of 500 V (leftmost figure) and 350 V (rightmost figure). The simulated pulse height is scaled to match the experimental results.*

the consecutive event. The ghost hit occupancy depends on the signal occupancy and the probability that a track leaves a ghost hit in the subsequent clock cycle. As the maximum signal occupancy is about 0.6 % [60], a ghost hit probability of the order of 1 % yields a maximum occupancy of $6 \cdot 10^{-5}$, insignificant compared to the allowed noise occupancy ($5 \cdot 10^{-4}$).

A special feature of the discriminator - the edge sensing circuit, see section 3.3.2 - effectively limits the signal to the time bin where the rising edge of the signal crosses the threshold. The leftmost figure of 4.16 shows the efficiency dependence on the arrival time of the particle in level-sensing discrimination. In level sensing mode (filled circles) hits are recorded over a time interval much longer than the 25 ns clock cycle. The effect of the edge sensing circuit is shown with open circles in the same figure: the range where the module is efficient is limited to 25 ns. Virtually no hits related to the track are found in the consecutive clock cycle.

The effect of irradiation on the timing characteristics is illustrated in the rightmost figure of 4.16. The irradiated module shows clearly slower rising and falling edges. As a consequence, the efficiency plateau is much narrower.

The edge sensing circuit effectively rejects ghost hits due to the tail of the signal induced on the strip. Some charge, however, is shared between two strips through dispersion of charge in the silicon or cross talk due to the inter-strip capacitance. Small charges due to charge sharing are likely to give a late discriminator response (time walk) and can thus appear in the clock cycle subsequent to the triggered cycle.

Efficiency versus time distributions similar to those in figures 4.16 have been reconstructed for a large number of modules and various bias voltages using data taken in the 2002 beam periods. To allow a quantitative comparison of the results a number of observables are defined. The time corresponding to the rising and falling edge is fitted as the 50 % efficiency point on both sides of the efficiency versus time distributions. The average of both values defines the center of the distribution t_c. Assuming that the clock and trigger jitter in ATLAS is of the order of 1 ns the efficiency for optimal timing is determined as the average in a

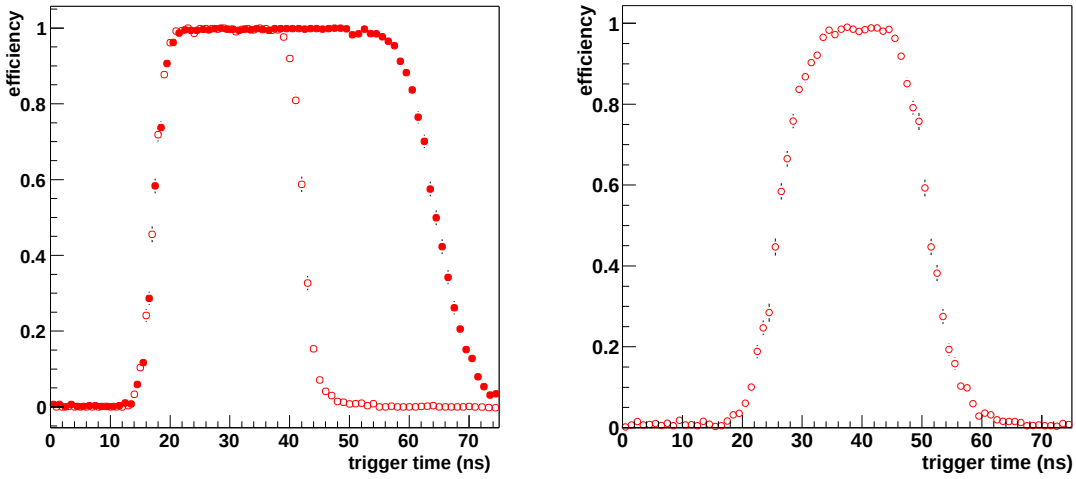

Figure 4.16: *Efficiency versus arrival time of the particle. Leftmost figure: a non-irradiated end-cap module at a detector bias of 250 V and a discriminator threshold of 1 fC. The discriminator is operated in level sensing (filled circles) and edge sensing mode (open circles). Rightmost figure: an irradiated end-cap module. The bias voltage and discriminator threshold are set to* $V_{bias} = 450$ *V and* $Q_{thr} = 1$ *fC.*

window $[t_c - 1.5, t_c + 1.5]$. The probability of a ghost hit in the subsequent bunch crossing is the "efficiency" in a similar window centered on $t_c + 25$ *ns*.

The maximum efficiency found with edge sensing discrimination is found to be well over 99 % for the non-irradiated modules and the irradiated barrel modules. The maximum efficiency and ghost hit rate are clearly anti-correlated. The ghost hit probability is found to be below 1 % for all modules.

The performance of two recent end-cap modules irradiated to a total fluence of $3.3 \cdot 10^{14} p/cm^2$, 10 % over the reference fluence, is clearly worse than that obtained on irradiated barrel modules. The ghost hit probability of these modules is 2-3 %. Operating one of these modules with an analog supply voltage to the chips of 3.8 *V* leads to an improved performance. The ghost hit probability is reduced efficiently by raising the threshold: at 1.2 *fC* the end-cap modules show a ghost hit rate close to or below 1 %, while still maintaining an efficiency compatible with 99 %.

The timing in ATLAS will be optimised module-by-module, i.e. it relies on the similarity of the response of all chips on the same module. As a measure for the variations in response between chips, the responses (rising edges of the signal) of two chips on the front and the back of the module are compared. For irradiated modules the average time difference between the rising edges of two randomly chosen chips on the front and back of the module is 2 ± 1 *ns*. Non-irradiated modules show much smaller differences in timing: 0.4 ± 0.3 *ns*.

The width of the distribution - the difference between the times corresponding to rising and falling edge - is found to be 25.1 ± 0.1 *ns* for all modules[8]. No systematic differences

[8]Measured at 1.2 *fC*. At 1.0 *fC* the distribution is slightly broader: 25.3 ± 0.1

are observed between modules.

4.6 Tracking

All results presented so far concern the performance of single modules. The tracking performance of the complete inner detector is extrapolated from the single module performance by Monte Carlo simulations [60]. In August 2002 an effort was made to study the performance of a system of several irradiated modules combined into a tracking array. The tracks reconstructed in the array of SCT modules are compared to the tracks found using the beam telescope. In this section the setup, analysis and results of this study are presented.

4.6.1 Setup

The setup for the tracking study is shown in figure 4.1. Some special arrangements for this study are briefly explained below.

Four irradiated barrel modules form a barrel tracking array. The separation between the modules was chosen to coincide as closely as possible with the distance between consecutive SCT barrels ($d = 90\ mm$ in H8 versus $\Delta R = 73\ mm$ in ATLAS).

The modules in this study were irradiated to a fluence of $\sim 3 \cdot 10^{14}$ protons/cm^2 prior to the beam test.

As discussed in section 4.1 the electrical readout scheme employed in H8 does not allow the fine-tuning of the timing of the modules. For a multi-module study the standard test beam approach does not work since it is not possible to match the time window of the different modules. To reduce the sensitivity to the timing of individual modules the logical OR of the hit pattern from the three time bins is taken as the binary result (ANYHIT data compression, see [104]). The discriminator is set to edge sensing mode throughout the tracking study as this is the envisaged operating mode for ATLAS.

The noise occupancy in this mode is nearly a factor three higher than in the LEVEL (X1X) or EDGE (01X) compression mode to be used in ATLAS. Therefore, throughout this section the noise occupancies are quoted together with the threshold. A threshold of $1.2 \pm 0.1\ fC$ is required to reach the specified noise occupancy of $5 \cdot 10^{-4}$ on all modules. The noise occupancy is a steep function of the threshold: for a threshold of $1.1\ fC$ the noise occupancy is $2 \cdot 10^{-3}$ and for $1.0\ fC$ the noise occupancy is $5 \cdot 10^{-3}$.

Runs of 25000 events were taken at a number of thresholds around the envisaged operating threshold of $1\ fC$ and at various bias voltages.

4.6.2 Tracking analysis

The event selection criteria were discussed in section 4.3.1. One additional requirement is added in this study: if more than 8 hits are found in the analog telescope the event is rejected. This cut is introduced to reduce the effect of interactions producing a second charged track in the setup. These are of course rather rare, but can mimic "fake" tracks at a rate of $\mathcal{O}(10^{-4})$.

For the selected events, a track finder algorithm reconstructs track candidates using only the binary information from the SCT modules. In a first step, the hits on both sides of each

module are combined into two-dimensional space points with associated errors. The residual distributions for the X and Y coordinates were presented in figure 4.4. The Z-coordinate is taken to be the center of the module thickness. Its numerical value is obtained from alignment.

The track finder creates track segments using all possible pairs of XY points on different modules. Each segment is extrapolated to the remaining module planes. The XY point closest to the track is included in the track fit. If the required number of space points is found, the segment becomes a track candidate. A track candidate is accepted if the χ^2 of the track fit is smaller than a predefined minimum value.

The accepted tracks are compared to the beam telescope track. The distance between two tracks is defined as the difference of the track parameters weighed by their errors:

$$d_{track} = \sum \frac{|a_i^{tel} - a_i^{bin}|}{\sigma_i} \tag{4.5}$$

where the a_i are the track parameters and the σ_i their errors.

A track is considered "good" if its distance to the telescope track d_{track} is smaller than 20 sigma. An event is labeled efficient if at least one "good" track is found. The remaining tracks are labeled as fakes. This definition of fake includes "spoiled" tracks, i.e. tracks where the track parameters are badly distorted due to the inclusion of incorrect hits.

As an example of the track reconstruction procedure, figure 4.17 shows a rare event, where an interaction occurs within the volume of the tracker. The collision of the beam pion knocks an electron out of its atom, creating a second (real) track. The left and right figure show an XZ and YZ view, where Z is the beam axis. The leftmost and rightmost rectangles represent the XY positions of combinations of hits in the X and Y plane of the upstream and downstream telescope modules. XY points on SCT modules are drawn as rectangles, where the size indicates the one sigma error on the position. The tracks reconstructed through the SCT points are shown as a continuous lines.

Whenever the outgoing tracks fall in the telescope acceptance these events can be identified by the extra hits in the telescope and discarded from the analysis. However, tracks that fall outside the telescope acceptance contribute to the measured fake rate. Their contribution is approximately $10^{-5} - 10^{-4}$, of the same order as the statistical error.

4.6.3 Results

In this section, efficiency and fake rate results are presented for a study using straight line fits.

The measurement of the tracking efficiency and the fake rate of depends on the choice of the track quality cut. A loose cut reduces the loss of efficiency, but will also lead to an unnecessarily high fake rate. The optimum value for the cut is a compromise between efficiency and fake rate. In the following a cut at $\chi^2 = 5$ is chosen.

At high threshold ($\sim 1.2\ fC$) the fake rate vanishes compared to the measurement error. For fake rates of the order of 10^{-4}, 95% confidence level upper limits are calculated. Lower limits are not calculated as at this level the rate is dominated by real tracks as in figures 4.17 in section 4.6.2.

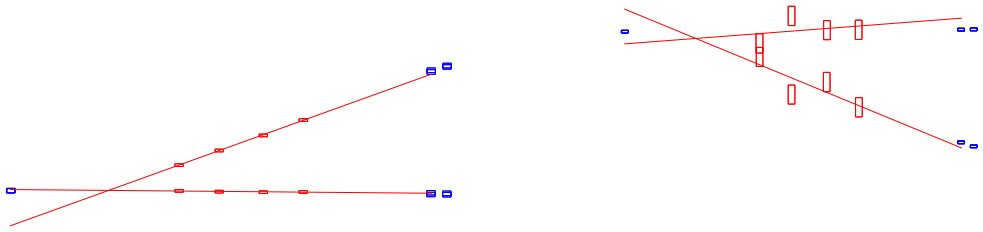

Figure 4.17: *Example of an event where a second track is due to a hard interaction in the tracking volume. In the leftmost figure an XZ view is shown, in the rightmost figure an YZ view.*

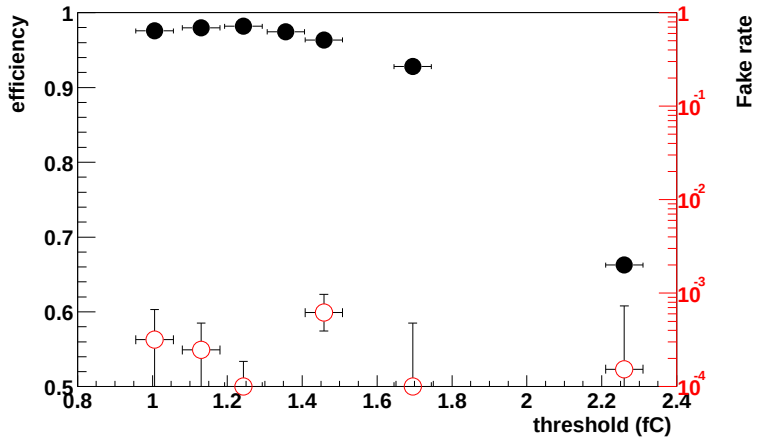

Figure 4.18: *Tracking efficiency and fake rate of a four-module tracking array versus (corrected) discriminator threshold. The tracks are fitted to a straight line. Detector bias is 500 V on the HV supply, resulting in 470-490 V on the detector.*

Figures 4.18 present the tracking efficiency and fake rate result for the optimised cut values. The maximum efficiency is over 97 %, obtained at a threshold of $\sim 1.2\ fC$.

The results of figure 4.18 correspond to a relatively high detector bias voltage of 470-490 V. Figures 4.19 show the tracking efficiency dependence on the supply bias voltage for a fixed threshold of 1.2 fC. Approximately 1-2 % of efficiency is lost when the detector bias is lowered to 370-390 V. No significant dependence of the fake rate on bias voltage is observed.

The behaviour of the tracking efficiency as a function of discriminator threshold and bias voltage is always within 1 % of the product of the efficiencies of the individual planes that make up the tracker: $\epsilon_{tracking} = \prod_{i=1}^{n} \epsilon_i$, where n is the number of detector planes, i.e. twice the number of modules, in the tracker and the ϵ_i are the plane efficiencies.

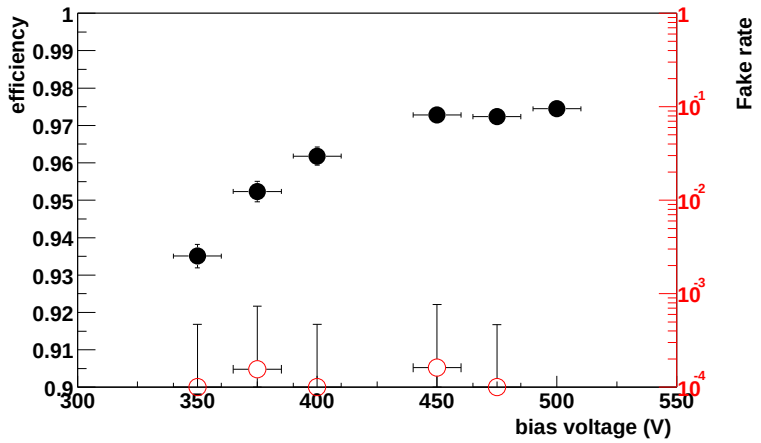

Figure 4.19: *Tracking efficiency and fake rate versus supply bias voltage for a four-module tracking array. The tracks are fitted to a straight line. The discriminator threshold is set so that the average noise occupancy is close to* $5 \cdot 10^{-4}$*: 1.2 fC.*

4.6.4 Helix fit - comparison with simulation

In this section, the straight line fit is replace by a helix fit. The linear fit in two dimensions has 4 free parameters. A helix fit has one more parameter that needs to be constrained. The effect of the extra degree of freedom is studied here. The experimental results are compared to a simulation of the SCT performance using the ATLAS simulation and reconstruction packages.

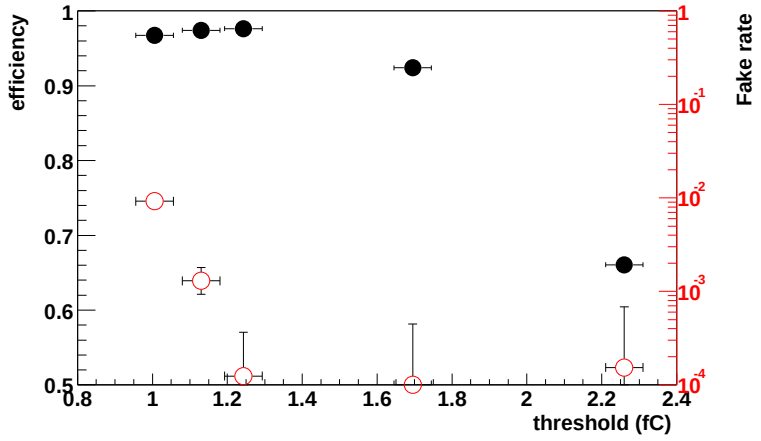

Figure 4.20: *Tracking efficiency and fake rate versus (corrected) discriminator threshold for a four-module tracking array. The tracks are fitted to a helix with a* p_T *cut-off of 2 GeV. The detector bias is 500 V on the HV supply, resulting in 470-490 V on the detector.*

The straight tracks of the beam test are fit as a helix with a very small curvature: i.e. the measured momentum becomes very large. But, this fit also allows for hits that do not form

a straight line to form a track as long as the resulting momentum is higher than a certain cut-off value. The fake rate depends strongly on this cut-off. For this study, a minimum momentum of 2 GeV is required.

Figure 4.20 shows the efficiency and fake rate versus discriminating threshold. As expected, the helix fit leads to a deterioration of the performance. The fake rate obtained at 97 % efficiency is ~ 1 % for a noise occupancy of $\sim 5 \cdot 10^{-3}$. Reducing the noise occupancy to $2 \cdot 10^{-3}$ by raising the threshold 0.1 fC leads to a reduction of the fake rate to $5 \cdot 10^{-4}$. A further 0.1 fC increase of the threshold yields a fake rate compatible with 0 within the statistical error, of the order of 10^{-4}.

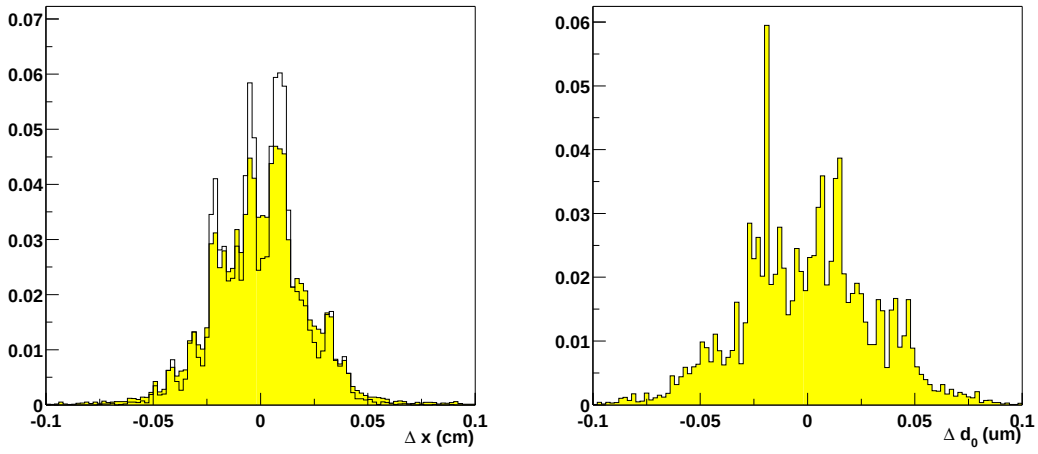

Figure 4.21: *Lefmost figure: the transverse impact parameter distribution obtained from the test beam analysis. The filled histogram corresponds to 1.0 fC, the empty histogram to 1.2 fC (V_{bias} = 500 V). Rightmost figure: the equivalent result from a simulation of the SCT.*

The track fit results yield an estimate the track parameter resolutions. A virtual interaction point is simulated from the track reconstructed in the beam telescope. The distance of the interaction point to the first module is taken to be the radius of the first SCT barrel, 21 cm. The transverse and longitudinal impact parameters are the shortest distance in the $R\phi$ and Rz planes between the track and the interaction point. The corresponding measurements in the test beam are the X and Y residual evaluated at the simulated interaction point. Similarly, the two angles of the ATLAS coordinate system ϕ and $\cot\theta$ at the point of closest approach to the interaction point are identified with the gradients dx/dz and dy/dz evaluated at the simulated interaction point.

Simulation results for conditions similar to the test beam are obtained using the existing Monte Carlo simulation package of the ATLAS detector in GEANT3 (ATLSIM) is used. To evaluate the performance in similar circumstances, single pions and muons are generated in a small region around $\eta = 0$. The small (of the order of milli-radians) variation in incidence angles ϕ and θ are chosen in agreement with those observed in the test beam. In the simulation, the transverse momentum of the particles is chosen to be 500 GeV (to be compared with the *infinite* momentum in the beam test. The ATLSIM package includes the

simulation of noise hits. The simulated Equivalent Noise Charge of 1875 electrons is close to what is observed on the irradiated modules.

The simulated events are reconstructed using the xKalman++ algorithm in the ATLAS reconstruction package ATRECON. The PIXEL and TRT data are not reconstructed, but the material of the detectors is included in the simulation.

The efficiency of the simulated stand-alone SCT for isolated muons is found to be 92 %, corresponding to a single-plane efficiency of 99 %. The fake rate is negligible in the absence of pile-up.

In figure 4.21 the residual distributions for the transverse impact parameter d_0 of the track at the point of closest approach to the interaction point are shown. The leftmost histograms shows the result obtained in the beam test using the helix fit algorithm. The filled histogram corresponds to a threshold of 1.0 fC, the empty histogram to 1.2 fC. For the lower threshold the noise occupancy becomes relevant and the probability that a track is *spoilt* by the addition of a noise hit is no longer negligible. This effect is reflected in the slightly broader distribution of the 1.0 fC run. The equivalent results from the simulation of the stand-alone SCT are shown in the rightmost figure.

	TB Tracking		Simulation	
	$1fC$	$1.2fC$	SCT	PT
$\sigma(1/p_T)$ (TeV^{-1})	3.8	3.6	6.0	0.8
$\sigma(\phi)$ (mrad)	1.1	1.0	1.5	0.1
$\sigma(cot\theta)$	0.0053	0.0041	0.0045	0.0007
$\sigma(d_0)$ (cm)	0.022	0.019	0.030	0.001
$\sigma(Z_0)$ (cm)	0.18	0.17	0.18	0.01

Table 4.1: *The resolution of the helix parameter of reconstructed, isolated, high p_T tracks determined in the test beam tracking study and a simulation of the precision tracker (pixel+SCT) and stand-alone SCT*

Both the test beam and the Monte Carlo result show significant non-Gaussian structures. These effects have been discussed in the context of the alignment of the SCT [114] and have been observed in previous beam tests [139]. As discussed before, these are a result of the discrete measurement of silicon strip detectors. Smooth distributions are obtained by the inclusion of extra points (the pixel and TRT detectors) in the helix fit and by considering a larger fraction of the detector.

The resolution of the track parameters are taken to be the Root Mean Square of the distributions of figure 4.21 and similar distributions for the remaining parameters. The beam test results (labeled TB) for two discriminator thresholds corresponding to a noise occupancy of $5 \cdot 10^{-3}$ and $5 \cdot 10^{-4}$ are listed in table 4.1. In the same table the track parameter resolutions obtained from a simulation of the ATLAS precision tracker (labeled PT) consisting of SCT+pixels and a stand-alone SCT are listed for comparison. For the two helix parameters in the non-bending plane, $\cot\theta$ and Z_0, the beam test results agree rather well with the expectation from the simulation. In the bending plane the beam resolutions are consistently better than those obtained from the simulation. At present, there is no good

explanation for this effect. Data from the May 2003 run in a 1.56 T magnetic field, currently being analysed, may shed some light on this apparent discrepancy.

4.7 Summary

Beam tests of recent SCT module prototypes demonstrate that the various geometrical types satisfy the ATLAS efficiency and noise specifications. The measured spatial resolution is in agreement with the $p/\sqrt{12}$ expectation for single strip clusters.

For the reference detector bias voltage of 150 V, the collected charge is within 5 % of the maximum. Modules of the barrel and end-cap types show compatible charge collection results. An analysis of the charge loss mechanisms in the binary readout scheme explains the difference between the measured median *collected* charge and the expectation for the median *deposited* charge. The median signal-to-noise ratio of modules with 12 cm detectors is ~ 14. For the shorter inner modules the better noise performance leads to a $S/N \sim 20$.

Modules irradiated to $3 \times 10^{14} p/cm^2$ collect about 90 % of the deposited charge when biased to 350 V. The noise increases significantly as a result of the irradiation. The median signal-to-noise ratio decreases to values in the range 7-11. The reduced signal-to-noise ratio leaves a rather narrow operating range where the efficiency (> 99 %) and noise occupancy ($< 5 \cdot 10^{-4}$) specifications are met.

The deviation of drifting charge carriers in a magnetic field has been measured on several modules. For a 1.56 T magnetic field and a detector bias voltage of 150 V a Lorentz angle of $3.3^o \pm 0.3^o$ is found. At higher voltage the Lorentz angle decreases significantly: $\theta_L = 2.1^o \pm 0.4^o$. The measurements are in good agreement with the model of reference [58].

The test beam data have been used to reconstruct the pulse shape of the front end amplifier/shaper for a range of different detector bias voltages. Apart from a slight deviation (a *shoulder*) in the shape, the observed bias voltage dependence of the shaper pulse is reproduced rather accurately by a detailed model of the detector signal and front-end response. The simulated peaking time that fits the data best is in agreement with the design peaking time. Large variations (19-24 ns) are observed in the peaking time of different batches of chips.

Irradiated modules show a significantly longer pulse. The rising edge of the pulse in the barrel module can be described fairly well by the simulation with a peaking time of 24 ns, but the longer tail is not reproduced. The effect of the degraded timing performance of the front-end is found to be limited: the inefficiency due to hits spilling over into the next time bin is well below 1 %. The ghost hit probability is approximately 1 % for irradiated modules, yielding a negligible contribution to the occupancy.

A study into the tracking performance of an array of irradiated SCT module prototypes has been performed. The efficiency with which straight tracks are found and the robustness against incorrect reconstructions - fake tracks - have been studied for a range of operating conditions. Track reconstruction efficiencies of over 97 % are obtained using a tracking array consisting of four irradiated modules at a threshold of 1.2 fC and a detector bias voltage of 470 V. The tracking efficiency is accurately predicted by the product of individual plane efficiencies. The four-module array is quite robust against fake tracks: the fake rate

is compatible with 0 for all thresholds that satisfy the noise occupancy specification and increases only slightly for lower thresholds.

Using a helix fit, the fake rate increases for low thresholds, but still vanishes at 1.2 fC. The helix parameter resolutions obtained in the beam test are reproduced qualitatively in a Monte Carlo simulation of a similar setup. The excess noise at low threshold leads to a slight deterioration of the results. This study confirms that an adequate tracking performance is obtained with SCT modules irradiated to the full fluence expected during the operation of ATLAS.

Chapter 5

The ATLAS *b*-tagging performance

The ATLAS inner detector is to perform precise tracking and vertexing of the charged particles that are produced in the collisions. As discussed in chapter 2 the tracking performance is important for many of the key channels of the ATLAS physics programme. Many of the physics processes beyond the standard model show a preference for the heavy quark flavours. A light Standard Model Higgs boson, for example, has a large branching ratio into b-quarks while many super-symmetric signatures involve b-quarks. The $gg \rightarrow t\bar{t}H$ channel may even present a final state with 4 b-jets. Bottom quarks are of course vital in the study of top quark decays and CP violation in the B-sector. Therefore, the capability to efficiently identify b-jets is essential.

Jets originating from a bottom quark can be identified due to the relatively long lifetime of bottom hadrons ($c\tau \sim 460\ \mu m$). Experimental signatures arise from the displaced (secondary) production vertex for the particles originating in the decay of the bottom hadron.

The ATLAS inner tracker design is optimised to provide, among other things, efficient identification (tagging) of b-jets. In this chapter, a study into the b-tagging performance of the ATLAS inner detector is reported. Some of these results reported elsewhere [140, 141]. The b-tagging performance of the complete inner detector is estimated using detailed Monte Carlo simulations of the physical processes and the expected detector response. The simulation tools are briefly outlined in section 5.1. In section 5.2 the lifetime b-tagging method is introduced. The expected b-tagging performance of the ATLAS detector is presented in section 5.3. First of all, the track parameter resolutions are discussed in section 5.3.1. In section 5.3.2 the results of this study are presented. The expected performance of the present ATLAS layout is compared to the expectation for the physics TDR layout. These results show the effect of several recent design changes and provide a more realistic estimate of the ATLAS performance. The effect of different jet reconstruction and b-tag algorithms, additional track quality requirements and the presence of pile-up events is discussed as well. Finally, in section 5.4, the results of this chapter are summarised.

5.1 Monte Carlo simulation

In this section, the tools that are used in studies of the detector performance are briefly outlined. The physics processes in high-energy collisions are described by dedicated packages,

known as *event generators*. The interactions between the produced particles and the detector elements are simulated in programs based on GEANT [80]. Finally, the simulated events are reconstructed using the pattern recognition and reconstruction software developed within the ATLAS collaboration.

5.1.1 Event generation

To study the b-tagging performance large samples of events are generated and simulated. From the large variety of physics processes that involve b-quarks, a benchmark channel is chosen. In the framework of the ATLAS Data Challenges[1] (DC1 phase 1) samples of $WH \rightarrow \mu\nu_\mu q\bar{q}$ events are generated specifically for b-tagging and High Level Trigger studies.

Two Higgs masses are considered: $m_H = 120\ GeV$ and $m_H = 400\ GeV$. The first represents a typical signal from the Standard Model Higgs. The b-jets in this sample have a relatively low transverse momentum of $\sim 60\ GeV$. Jets in the second sample have a much larger transverse momenta, $p_T \sim 200\ GeV$ on average, leading to a different systematics of the b-tagging performance.

For both masses, large statistics of $b\bar{b}$ (20000 events) and reference samples ($u\bar{u}$, $c\bar{c}$, 50000 and 20000 events, respectively) are studied in this analysis[2]. Note that the latter samples do not represent relevant physical processes. Their sole purpose is to provide a reference sample to the $H \rightarrow b\bar{b}$ events. The samples were generated using PYTHIA6.203. Similar samples were generated for the physics TDR in 1999. The main difference is in the mass of the lighter Higgs, which was simulated to be $100\ GeV$.

5.1.2 Detector simulation

The ATLAS data challenges also include the CPU-intensive detector simulation. The response of the ATLAS detector is emulated using the DICE package. Particles from the generator are tracked through the detector in small steps using GEANT3.21 [80]. All relevant energy loss mechanisms are taken into account. The GEANT energy losses are converted into detector digits using a realistic description of the detector Front-End electronics.

The simulation includes a non-uniform magnetic field in the inner detector. The exact position of the collision is varied according to a Gaussian distribution with a width of 15 μm in the transverse directions and 5.6 cm longitudinally.

In DC1 the most recent (2002) ATLAS layout is simulated. In this analysis, the DC1 results are compared to the previous large production of full simulation data, produced in 1999 for the physics TDR [56]. The geometry of the detector has undergone significant changes between both studies. With respect to the b-tagging performance the most important changes are:

- the multi-layer beam pipe design required an increase of the radius of the inner PIXEL layer from 4.3 to 5.05 cm.

[1] The ATLAS data challenge program is intended to develop the distributed computing capacity needed for the analysis of the ATLAS experiment. Detailed information can be found in reference [142]

[2] The gluon jet sample is not considered at this stage.

- the material of the (insertable) PIXEL layout has increased nearly a factor of 1.5.
- the length of the PIXELs in the outer layers increased from 300 to 400 μm.
- a realistic field map of the solenoidal field in the Inner Detector cavity is used in the DC1 simulation.

Throughout this chapter, the results obtained using the DC1 data are referred to as "DC1 geometry", whereas the results obtained using the data sample generated for for the Physics TDR are labeled "TDR geometry". The TDR geometry was simulated using a uniform B-field and an infinitesimal beam spot.

As a result of the high luminosity of the LHC, multiple collisions occur in each bunch crossing. During the initial low-luminosity operation, $\mathcal{L} = 10^{33} cm^{-1} s^{-1}$, on average 2.3 minimum bias events are expected to be superposed on the signal event. The number of minimum bias events increases to 23 during high luminosity operation, $\mathcal{L} = 10^{34} cm^{-1} s^{-1}$.

To take into account *pile-up*, for each of the event samples three simulations are performed in DC1: one where pile-up events are not taken into account, one corresponding to low luminosity and a third corresponding to high luminosity operation. Throughout most of this chapter, the no-pile-up case is considered. In section 5.3.6 the effect of pile-up on the b-tagging is evaluated using the high-luminosity sample.

5.1.3 Track reconstruction

After simulation of the full detector response to the Monte Carlo events, the event is *reconstructed* using the ATLAS pattern recognition and track reconstruction software. The DC1 data are reconstructed using ATRECON[3]. Tracks in the inner detector are reconstructed using xKalman++[4]. The interface to the different sub-detectors is provided by AXXXREC[5]. For data with additional pile-up, the ATRECON version of ATLAS kit 5.3.0 is used for technical reasons. The change of ATRECON version has no significant effect on the performance.

The TDR data, on the other hand, were reconstructed using a FORTRAN version of xKalman. The collision point was smeared at the reconstruction stage to take into account the finite size of the beam spot.

The reconstruction software has evolved over the years. Although both studies are performed using the same pattern recognition approach, the improvements in the software performance may influence the results.

In the dense tracking environment inside a jet, hits cannot always be assigned to a track unambiguously. Moreover, holes in the detector acceptance for low p_T tracks may lead to a loss of hits. To select high-quality tracks the following requirements are applied:

- Number of precision hits (PIXEL + SCT) $N_{pr} \geq 9$ (maximum is usually 11)
- Number of PIXEL hits $N_{pix} \geq 2$ (maximum is usually 3)

[3] as included in ATLAS kit 4.0.1
[4] Version 28 October 2002 for Atlsim and Atrecon frameworks
[5] AXXXREC for DC1 layout 6.09.2002

- A hit in the first pixel layer (B-layer)
- transverse momentum: $p_T > 1\ GeV$
- transverse impact parameter: $d_0 < 1\ mm$

A hit in the B-layer is required as the impact parameter resolution depends critically on the hit closest to the interaction point. The transverse momentum threshold rejects low p_T tracks, where the resolution is deteriorated due to multiple scattering. The last requirement rejects tracks with very large transverse impact parameters. These are mostly due to decays of long-lived particles, conversions and interactions in the detector material and fake tracks. The value of 1 mm is chosen so that virtually no tracks from B-decays are lost.

5.1.4 Jet reconstruction

Jets produced from the fragmentation of a quark or gluon carry energy in many different types of particles: the hadronic energy is largely deposited in the hadronic calorimeter, while photons and electrons are contained in the electromagnetic calorimeter. The momentum measurement for charged particles in the inner detector provides additional information. The muon energy is determined using the muon spectrometer and the inner detector. In order to determine the total energy of the jet, a careful weighing of the different contributions has to be performed to avoid double counting.

For the b-tagging performance, both the jet energy resolution and the precision with which the jet direction can be determined are important. In most b-tagging studies, rather than trying to arrive at a realistic jet reconstruction algorithm on the basis of the detector response, the jets are reconstructed using generator information. A simple cone algorithm is seeded by the direction of the partons from the Higgs decay. The jet transverse energy is determined as the sum of the transverse energies of all observable particles[6] within a cone $\Delta R = \sqrt{(\Delta\eta)^2 + (\Delta\phi)^2} < 0.4$ around the parton direction. The jet direction in η, ϕ is calculated as the mean of the directions of the participating particles weighted by their momenta. Jets based on generator information represent an ideal case since the detector resolution and the effect of the magnetic field are not taken into account. These jets will be labeled KINE jets throughout this chapter.

For the DC1 data, a number of alternative jet reconstruction algorithms are available. Jets reconstructed using ATLFAST are based on generator information, but are smeared using parametrisations of the detector resolution. ATRECON offers *detector jets*, that represent an approximation to the description of the detector response. These jets are used to study the possible deterioration of the b-tagging as a result of fluctuations in the jet energy and direction due to the detector resolution.

Seeding of the jets by the partons from the Higgs decay implicitly rejects jets from gluon radiation off the initial quarks from the sample. Thus, the b-jets are compared to a sample of u- or c-jets under exactly the same conditions. Most importantly the p_T and η distributions of the b- u- and c-jet sample are the same. For jets that are not seeded by the partons (ATLFAST and ATRECON jets) the rejection of gluon radiation jets is achieved by

[6] All stable particles except neutrinos.

requiring the direction of the jet to coincide within $\Delta R < 0.2$ with that of one of the quarks (after Final State Radiation) of the Higgs decay.

For the comparison with TDR results only the jets based on generator information are used. The b-tagging performance using the different jet reconstruction algorithms is studied in section 5.3.4. In all cases a minimum p_T of 15 GeV is required for non-calibrated jets. Jets are reconstructed within the acceptance of the detector, i.e. $|\eta| < 2.5$.

Gluons radiated off u-quarks can split into $b\bar{b}$ or $c\bar{c}$ pairs. *Wrong-flavour* jets (b and c jets in the u-jet sample and light quark jets in the b and c samples) are excluded from the b-tagging analysis. For KINE jets the flavour of the jet is determined from the heaviest quark flavour among the hadrons in the jet. A jet is labeled as a b-jet if at least one charged track originates in the decay of a B-hadron. The ATLFAST jets apply a different definition of b ,c and light jets: the jet is labeled according to the flavour of the heaviest quark after final state radiation with $p_T > 5$ GeV and within $\Delta R < 0.2$ of the jet axis.

5.2 Introduction to *b*-tagging

In this section, some properties of jets originating from the fragmentation of a b-quark are discussed. The experimental observable used in most b-tagging algorithms, the impact parameter, is briefly discussed. Finally, the likelihood b-tagging algorithm is introduced.

5.2.1 Properties of *b*-jets

As explained in section 1.2, jets are formed whenever a quark or gluon appears in the final state of the event. Large fluctuations occur in the number of stable particles formed in the fragmentation and hadronisation of the initial parton. If the initial parton is a bottom quark, one of the hadrons is a B-meson or baryon.

Bottom hadrons have a large number of possible decay channels. A fraction of $\sim 10\%$ of the B-hadrons decays semi-leptonically (for example $\bar{B} \rightarrow D^* l^- \bar{\nu}_l$). Both in semi-leptonic and hadronic decays, charmed hadrons are produced with high probability: the number of charmed particles per B decay is 1.1-1.2. The subsequent decay of the charmed hadron yields a tertiary vertex. The decay chain of B-hadrons yields a relatively large number of decay products.

However, many of the particles are neutral and are not detected by the vertex detector. Also, the fragmentation products tend to have relatively low transverse momentum, which complicates their detection. Detector inefficiencies reduce the number of tracks available for the b-tagging algorithm. Reconstruction of the individual particles in a collimated jet requires a high-granularity detector and sophisticated pattern recognition software.

Figures 5.1 show the charged jet multiplicity after track quality cuts for two samples of jets. For this study, the simple track quality requirements of section 5.1.3 are applied. The first sample (continuous line) corresponds to b-jets formed in the decay of a light Higgs boson ($H \rightarrow b\bar{b}$, $m_H = 120$ GeV). Jets in this sample have an average transverse momentum of about 60 GeV. For the second sample (dashed line) the same process is used, but the Higgs mass is now 400 GeV and the average jet transverse momentum increases to ~ 200 GeV.

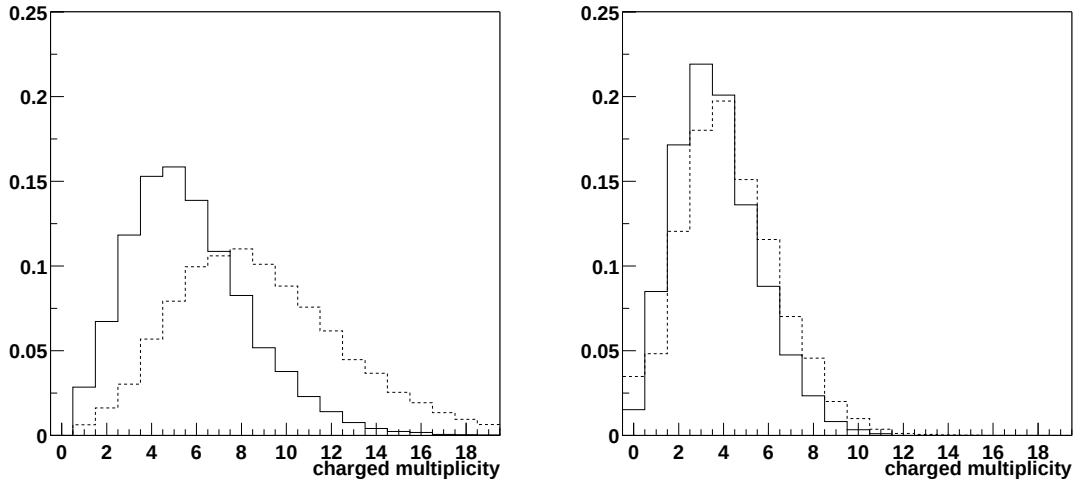

Figure 5.1: *Jet multiplicity distributions for jets from the $m_H = 120$ GeV sample (continuous line) and $m_H = 400$ GeV (dashed line). In the leftmost figure all reconstructed tracks that satisfy the track quality cuts are considered, while in the rightmost figure only tracks that originate in decay of a B hadron are taken into account.*

The leftmost figure shows the number of reconstructed tracks that satisfy the track quality cuts. The mean charged multiplicity in b-jets proceeding from the decay of a 120 GeV Higgs boson is 5.7. For a 400 GeV Higgs boson the number of reconstructed tracks increases considerably (mean charged multiplicity is 8.9).

In the rightmost figure, only those tracks are counted that originate from the decay chain of the B-hadron. For the light Higgs sample, these amount to $\sim$ 65% of the reconstructed tracks (on average 3.7 tracks from the B-decay are reconstructed). Only these tracks originate in the displaced secondary vertex and present measurable signatures to the b-tag algorithm. For the heavy Higgs sample, the fraction of tracks from B-decay after quality cuts decreases to below 50% (the average charged multiplicity from B-decay is 4.3). Thus, the b-tag signature is diluted.

The multiplicity of charged tracks in u-jets is slightly smaller than that in the corresponding b-jet sample, due to differences in the fragmentation of b- and u-jets.

5.2.2 B-lifetimes

The average lifetime of B mesons and baryons is 1.564 ± 0.014 ps [1], corresponding to a proper lifetime in units of length of $c\tau \sim 463 \pm 18$ μm. As expected from the *spectator* model[7], the lifetime varies only slightly between the different B-meson and hadrons. The lifetime of the compound system is determined by the probability for the heavy quark to decay into a charm quark: $b \to cl\nu$.

Due to its large mass, (anti) top quarks predominantly decay weakly into W^+b ($W^-\bar{b}$).

[7] In the spectator model the quarks which accompany the heavy quark in the hadron are assumed to play no significant role in the decay

bottom hadrons		*charmed hadrons*		*others*	
hadron	lifetime (ps)	hadron	lifetime (ps)	hadron	lifetime (ps)
$B^{\pm}$ (ub)	1.65 ± 0.04	$D^{\pm}$ (cd)	1.057 ± 0.015	Λ (uds)	263.2 ± 20
B^0 (ub)	1.56 ± 0.04	D^0 (cu)	0.415 ± 0.004	K_S^0 (ds)	89.34 ± 0.08
B_s^0 (sb)	1.54 ± 0.07	D^0 (cu)	0.415 ± 0.004	$K^{\pm}$ (us)	$1.2 \cdot 10^4$
B baryons	1.20 ± 0.07	Λ_c^+ (udc)	0.206 ± 0.012	Σ^+ (uus)	79.9 ± 0.4

Table 5.1: *Lifetimes of bottom and charm hadrons. In the last column a number of hadrons composed of light quarks, that have long lifetimes are listed. Values from [1]*

The top quark lifetime is very short: $\sim 10^{-25}$ s. It therefore decays before hadronisation can take place. The presence of top quarks in the events has to be inferred from the presence of decay products of the W-bosons and the identification of b-jets in the final state.

The charm quark is relatively light and the approximations in the *spectator* model no longer hold exactly. Therefore, the lifetimes of different charmed hadrons show a larger variation. The average proper lifetime corresponds to approximately $c\tau \sim 60\ \mu m$.

The remaining quarks u,d and s are relatively light. In general *light jets* originate in the interaction point. Only a limited number of combinations of light quarks yields mesons or baryons with long life times. The most notorious are Λ's and kaons.

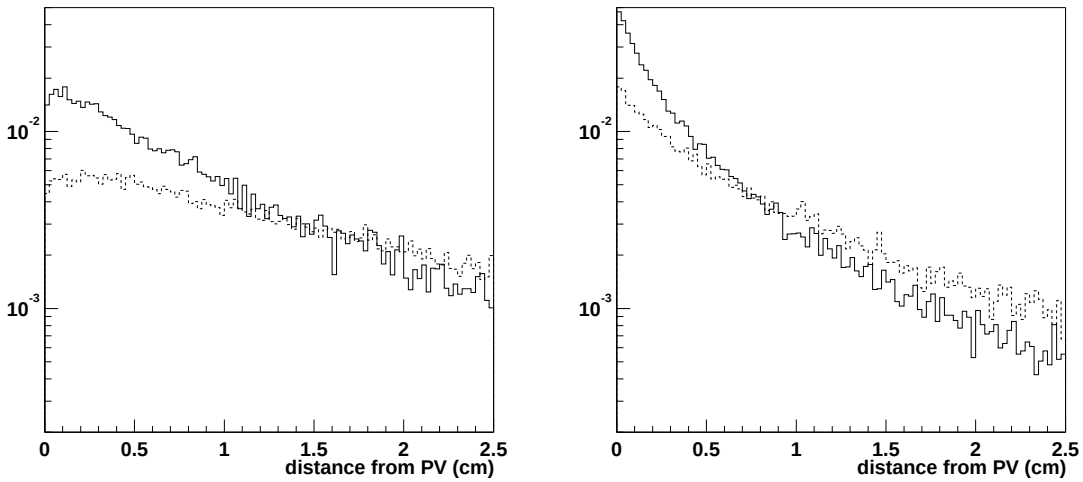

Figure 5.2: *Decay length of jets in the light Higgs sample (continuous line) and the heavy Higgs sample (dashed line). The leftmost figure shows the result for a sample* b*-jets, the rightmost figure for* c*-jets. Jets in the light Higgs sample have an average transverse momentum of* $\sim$ *60 GeV, while for the jets in the heavy Higgs sample* $\langle p_T \rangle \sim 200\ GeV$.

The lifetimes of several bottom and charm hadrons are listed in table 5.1. Some relevant particles made of light quarks are also listed.

The decay length in the laboratory frame depends on the lifetime of the hadron and on the transverse momentum of the B-hadron: $l = \gamma\beta c\tau$, where τ is the lifetime of the

decaying hadron, βc is the velocity of the particle and $\gamma = \sqrt{1-\beta^2}$. For a 20 GeV B-hadron, the γ-factor is approximately 4 and the decay length corresponding to one lifetime is nearly 2 mm. Figure 5.2 shows the absolute decay length (the distance between primary and secondary vertex) for four samples of jets. The leftmost figure shows a sample of b-jets, the rightmost figure is the equivalent result for c-jets. In both cases, the continuous histogram corresponds to jets from the light Higgs sample ($m_H = 120\ GeV$). These jets have a moderate average transverse momentum: $\langle p_T \rangle \sim 60\ GeV$. The dashed line represent the decay length of the energetic jets ($\langle p_T \rangle \sim 200\ GeV$) in the $m_H = 400\ GeV$ sample. The decay length is clearly larger in the heavy Higgs sample.

The detection of the displaced secondary vertex of the B-decay forms the basis of the experimental b-tagging. From a comparison of the two figures in 5.2, it is obvious that charm jets may present experimental signatures similar to those of bottom jets. Separation of b and c-jets is very difficult, even with an excellent vertex resolution. Therefore, in any b-tagging algorithm c-jets form an important source of incorrectly identified jets (mis-tags).

Other sources of mis-tags are related to the amount of material in the detector. Material in the tracking volume leads to a higher probability for conversions of photons ($\gamma \rightarrow e^+e^-$). Also interactions of hadrons with the detector material may mimic tracks with a large impact parameter.

Spoilt and fake tracks arise when one or more hits due to noise or the signal from another particle is erroneously assigned to a track. Their effect is especially significant for collimated highly energetic jets. To maintain a good performance, a high-granularity detector with a good double track resolution is needed.

5.2.3 The impact parameter

Many b-tagging algorithms are based on the track impact parameter, defined as the smallest distance between the helicoidal track fit and the primary vertex. In the schematic representation 5.3 an event is drawn with a B-hadron decaying at some distance from the interaction point. The tracks from the (secondary) B-decay vertex have non-zero impact parameters, while tracks from the primary vertex have impact parameters compatible with 0.

Increasing the momentum of the jet has two effects: the γ factor leads to an increase of the decay length (see figure 5.2) and the boost leads to a collimation of the jet. The rightmost figure of 5.3 shows that the impact parameter is independent of the p_T of the jet in the range between 60 and 200 GeV.

The impact parameters of tracks from the B-decay are typically of the order of 100 μm, within the reach of modern vertexing detectors. The expected impact parameter resolution of the ATLAS inner detector is presented in section 5.3.1.

5.2.4 The likelihood method

The likelihood method provides a means to convert the measured track impact parameter into a discriminating variable for the b-tagging algorithm.

The track significance is defined as the ratio of the impact parameter and its error. Its interpretation is that it represents the significance of the impact parameter measurement

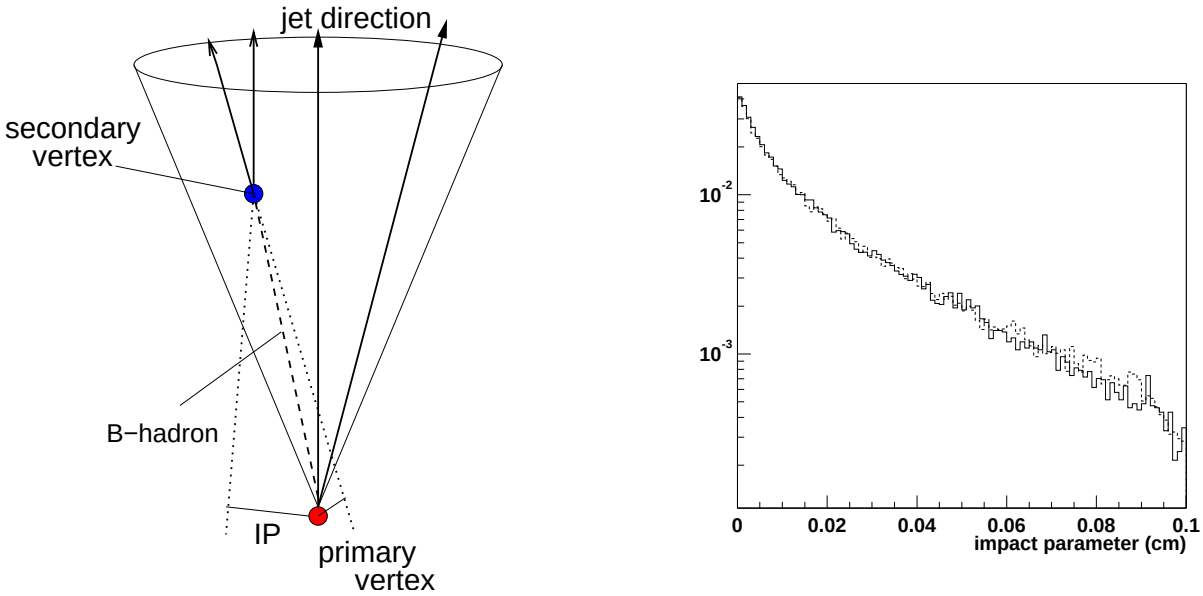

Figure 5.3: *Leftmost figure: schematic drawing of the impact parameter. Tracks from the secondary vertex have large values of the impact parameter. Rightmost figure: impact parameter distribution for B-decay tracks in jets with an average transverse momentum of* $\sim$ *60 GeV (continuous line) and 200 GeV (dashed line).*

with respect to the hypothesis that the track stems from the primary vertex. The sign of the significance is determined from the projection of the impact parameter on the transverse component of the jet direction. For the decay products of particles with a long lifetime, the signed significance is large and positive.

In ATLAS, the longitudinal dimension of the interaction point is much larger than the transverse dimension. Moreover, the resolutions of the sub-detectors in the bending plane of the magnet ($R\phi$) and the Rz plane are very different. Therefore, the impact parameter is separated in a transverse and longitudinal component. The transverse and longitudinal impact parameter are determined as the distance between the track and the primary vertex in the $R\phi$ and Rz-plane, respectively. While the dimension of the beam spot is close to negligible in the transverse direction, the longitudinal impact parameter can only be determined after the reconstruction of the z-coordinate of the primary vertex.

The distributions of the signed significance of the transverse impact parameter for selected tracks in u and b-jets are shown in figure 5.4.

The signed significance distributions for u-jets have a nearly Gaussian shape centered around 0 and with a width of 1. The tails to large values are due to interactions in the inner detector volume (photon conversions and hadronic interactions) and fake and spoilt tracks. The asymmetry (the tail is slightly more pronounced towards positive values) is the result of decays of long-lived particles like Λ or K^0.

The signed significance distributions for b-jets show a pronounced tail towards positive significances due to the long lifetime of the bottom hadrons. The b-sample shows a slight excess over the u-sample towards negative values of the significance. This corresponds to tracks where the sign is determined incorrectly. The effect becomes more pronounced for the

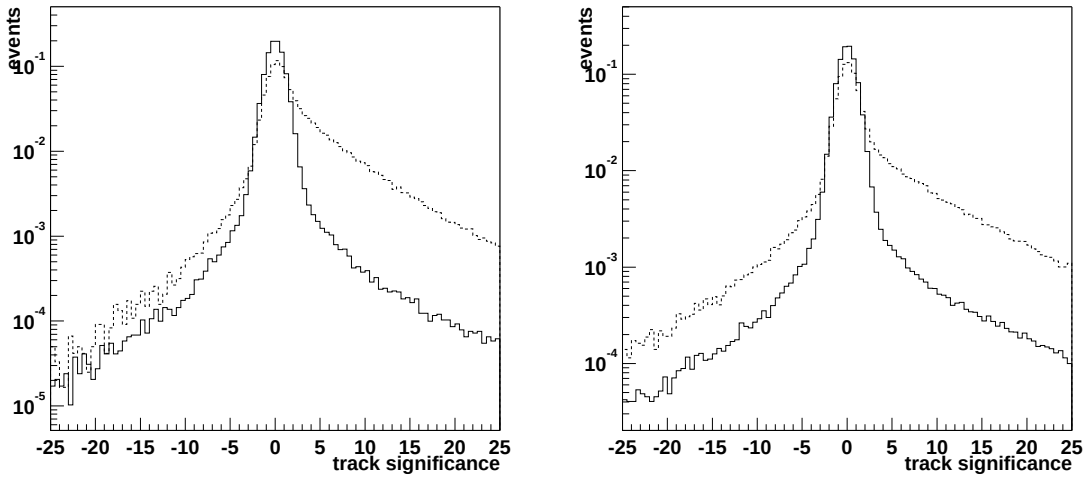

Figure 5.4: *Track significance distributions for u (continuous line) and b jets (dashed line). The leftmost figure corresponds to the $m_H = 120$ GeV sample, the rightmost figure to a 400 GeV Higgs.*

collimated jets of the 400 GeV sample.

The likelihood method takes advantage of the difference between these distributions to identify b-jets. A weight is assigned to each track based on the the signed track significance S_{d_0}. This weight expresses the probability that the track belongs to a b- or light jet. For 2-dimensional (2D) b-tagging only the transverse impact parameter is used:

$$w_{2D}(S_{d_0}) = \log\left[f_b(S_{d_0})/f_u(S_{d_0})\right]$$

where $f_u(S_{d_0})$ is the fraction of tracks in the u-jet sample with track significance S_{d_0}.

The 3-dimensional (3D) b-tagging algorithm combines the information from the transverse and longitudinal impact parameters into a single weight:

$$w_{3D}(S_{d_0}, S_{z_0}) = \log\left[f_b(S_{d_0}, S_{z_0})/f_u(S_{d_0}, S_{z_0})\right]$$

where S_{d_0} and S_{z_0} represent the signed significance of the transverse and longitudinal impact parameter, respectively. In the following, the z-coordenate of the primary vertex is assumed to be determined with a resolution of $\sigma_z^{PV} = 30\ \mu m$ in the absence of pile-up. For events with high-luminosity pile-up a resolution of $\sigma_z^{PV} = 50\ \mu m$ is assumed.

The jet weight is the sum:

$$w_{jet} = \sum w_i$$

where w_i represents the individual track weight i and sums over all tracks in the jet. The jet weight distributions for the $H \to u\bar{u}$ and $H \to b\bar{b}$ quark sample are shown in the leftmost figure 5.5.

For this study, the likelihood weights are extracted from Monte Carlo events. In ATLAS the weights are to be determined from experimental data (with a limited precision). Therefore, the results obtained with these weights represent an ideal case and should be interpreted as an upper limit of the performance.

The track weights are determined on the same sample that is later used to determine the b-tag efficiency. It has been checked that statistical effects do not lead to a significant overestimate of the performance by interchanging the sets of weights for the 120 and 400 GeV samples. The b-tagging performance shows a very small degradation, compatible with statistical errors.

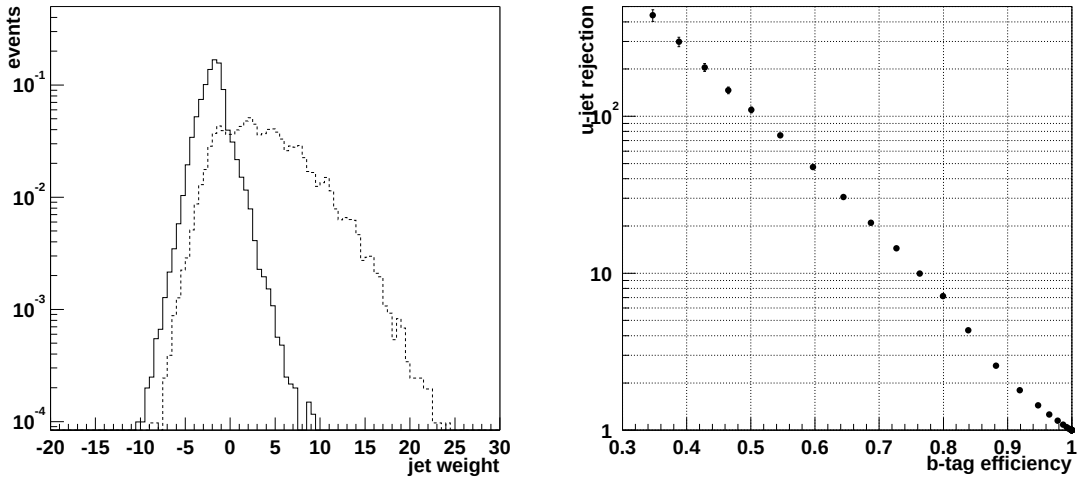

Figure 5.5: *Leftmost figure: typical jet weight distribution. Rightmost figure: the corresponding relation between* u*-rejection vs.* b*-efficiency.*

The relation between the b-jet and u-jet tagging efficiencies are obtained by integrating the normalised jet weight distributions. In the rightmost figure of 5.5 the results are expressed in terms of the b-jet efficiency and the light jet rejection, defined as the inverse of the u-jet efficiency.

The rejection for u-jets, R_u, is a steep function of the b-tagging efficiency. The choice of ϵ_b (and thus R_u) depends on the specific efficiency and purity requirements of every analysis. In the remainder of this chapter results are presented for two values of ϵ_b: 50 % and 60 %. These are the benchmark values used in many analyses.

The rejection for c-jets R_c is determined in the same way using the $H \rightarrow c\bar{c}$ sample. The same set of weights, determined for the u-jet sample, is used for the evaluation of the c-rejection.

In the next chapter, the 2D and 3D likelihood methods are used to predict the ATLAS b-tagging performance under different conditions.

5.3 The ATLAS b-tagging performance

In this section the capability of the ATLAS inner detector to identify b-jets is studied. The performance of the TDR and DC1 geometry is compared in the light of the layout changes.

First, the resolution with which the particle trajectories are reconstructed is discussed. Then, results are presented for the b-tagging performance of the two geometries. The effect

of the use of the longitudinal impact parameter, additional track quality requirements and different jet algorithms are studied. A parametrisation is given for the dependence of the b-tagging performance on the jet transverse momentum and rapidity. Finally, the effect of high-luminosity *pile-up* on the performance is discussed.

5.3.1 Track resolution

For the comparison of the TDR and DC1 data, the track quality cuts listed in section 5.1.3 are used. The cuts are kept as simple as possible to minimise the Monte Carlo dependence.

The track parameter resolutions are most easily studied using a sample of light quark jets. In this case most of the tracks originate from the primary vertex. Remaining tracks with a high value for the transverse impact parameter - secondaries from interactions in the detector volume or tracks originating from hadrons with long lifetimes (K's, Λ's) - are eliminated from the sample. Only tracks within the inner tracker acceptance ($|\eta| < 2.5$) are considered. As the track parameter resolutions depend strongly on the transverse momentum of the track, a minimum p_T of 1 GeV is required.

The essential parameter in the lifetime b-tagging algorithm is the transverse impact parameter. Figure 5.6 shows the resolution of the transverse impact parameter - determined as the width of the residual distribution - versus the transverse momentum of the track. The results obtained using the TDR data and the DC1 data show the same dependence of the impact parameter resolution on the transverse momentum of the track. The deterioration of the resolution towards low transverse momenta is due to multiple scattering. Therefore, the resolution at low momenta depends strongly on the amount of material in the first layer(s) of the detector. At high momenta the resolution reaches a plateau that is determined by the geometry and spatial resolution of the detector. The observed dependence is described by the function: $\sigma(p_T) = a + b/p_T$.

The resolution at low momenta is significantly worse for the DC1 geometry than for the TDR geometry. One can estimate the effect of the increased material and inner radius of the PIXEL b-layer. The typical deflection angle due to multiple scattering is given by:

$$\Delta\theta = 0.015 \frac{\sqrt{L/X_0}}{\beta p_T}$$

where L is the path length through the material, X_0 is the radiation length and β is the particle velocity $\beta = v/c$. The transverse momentum p_T is expressed in GeV. The contribution to the impact parameter resolution due to multiple scattering in the first layer is then given by $\sigma(d_0) = R_1 \Delta\theta$, where R_1 is the radius of the first layer. Thus, the error on the impact parameter at low momenta is expected to increase proportional to the square root of the material and proportional to radius.

For the comparison between TDR and DC1 geometry (with a ~ 50 % material increase in the PIXEL layers and an increase of the radius of the B-layer from 4.3 to 5.05 cm) the p_T dependent term is expected to increase by a factor $\sqrt{1.5} \cdot 5.05/4.3 \sim 1.44$. The result of the simulation, 1.58, is slightly higher.

The transverse momentum of the track is not used directly in the tagging algorithm, but a minimum p_T is required. Therefore, the resolution of the transverse momentum is of some

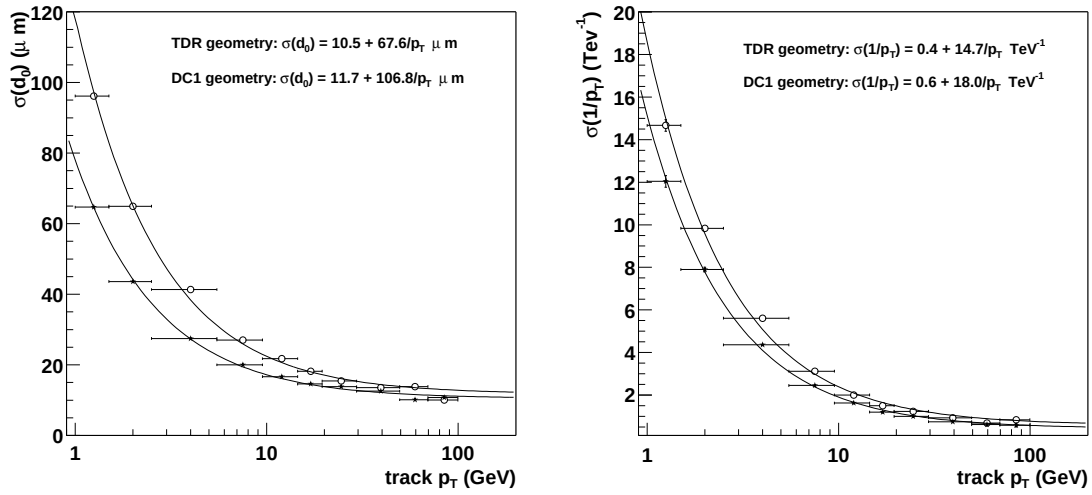

Figure 5.6: *Comparison of the track reconstruction resolution for the TDR (filled markers) and DC1 geometry (open markers). In the leftmost figure the transverse impact parameter resolution is shown versus track momentum. The rightmost figure contains the equivalent result for* $1/p_T$*. Note that the TDR results cannot be compared directly to the parametrisation in section 2.2, as a different function is used.*

interest for the b-tagging performance. The rightmost figure in 5.6 shows the inverse of the of the transverse momentum resolution as a function transverse momentum.

In absence of interactions with detector material, the error on $1/p_T$ does not depend on p_T. Therefore, at high p_T the resolution $\sigma(1/p_T)$ reaches an asymptotic value. At low p_T, multiple scattering leads to a deterioration of the resolution. The p_T-dependent component of the resolution is found to deteriorate by a factor ~ 1.2, in agreement with the $\sqrt{1.5} = 1.22$ expected from the increase in material in the DC1 simulation.

5.3.2 Comparison of the TDR and DC1 geometry

In this section the performance of the likelihood b-tagging algorithm is analysed for a simulation of the TDR and DC1 geometry.

In tables 5.2 and 5.3 R_u and R_c are presented for the light and heavy Higgs samples. For each combination of Higgs mass, quark flavour and b-tag efficiency three results are given; two measurements correspond to the TDR and DC1 geometries, while the third result corresponds to the TDR geometry with an additional smearing of the transverse and longitudinal impact parameters and the transverse momentum to bring these resolutions in agreement with those of the DC1 geometry.

A clear deterioration of the b-tagging performance is observed when comparing the TDR and DC1 geometries. Even after smearing the resolutions of the TDR sample, the DC1 rejections are considerably lower. This indicates that the degradation of the performance cannot be explained entirely by the degradation of the impact parameter resolution. An additional degradation is expected from interactions and photon conversions in detector material.

	2D algorithm			*3D algorithm*		
$R(\epsilon_b)$	*TDR*	*smeared*	*DC1*	*TDR*	*smeared*	*DC1*
$R_u(\epsilon_b = 50\ \%)$	359± 23	197 ± 9	111 ± 7	532± 47	332± 32	222± 9
$R_u(\epsilon_b = 60\ \%)$	130 ± 6	79 ± 3	46 ± 1	184± 11	107 ± 6	87 ± 2
$R_c(\epsilon_b = 50\ \%)$	11.5± 0.4	10.4 ± 0.3	9.9 ± 0.3	12.2± 0.4	12.2 ± 0.5	12.7± 0.2
$R_c(\epsilon_b = 60\ \%)$	6.7± 0.2	6.4 ± 0.2	6.1 ± 0.1	6.9 ± 0.2	7.1 ± 0.3	7.3 ± 0.1

Table 5.2: *2D and 3D (2D+Z)* b-*tagging.* R_u *and* R_c *for* ϵ_b *=50 %, 60 %. All results are obtained using KINE jets of the light Higgs sample (*m_H *= 100 and 120 GeV for TDR and DC1, respectively). The first column corresponds to the results obtained from a reanalysis of the TDR data. In the second column the impact paramater and transverse momentum have been smeared to bring them into agreement with the DC1 resolutions given in figure 5.6. In the third column, the results obtained for the DC1 geometry are listed.*

	2D algorithm			*3D algorithm*		
$R(\epsilon_b)$	*TDR*	*smeared*	*DC1*	*TDR*	*smeared*	*DC1*
$R_u(\epsilon_b = 50\ \%)$	141 ± 9	110 ± 12	62 ± 3	189± 19	125 ± 9	81 ± 2
$R_u(\epsilon_b = 60\ \%)$	69 ± 5	51 ± 3	31 ± 1	82 ± 7	64 ± 4	40 ± 1
$R_c(\epsilon_b = 50\ \%)$	13.6± 0.5	13.0 ± 0.8	10.7± 0.3	13.2± 0.6	13.4 ± 0.6	12.4 ± 0.2
$R_c(\epsilon_b = 60\ \%)$	7.6 ± 0.3	7.1 ± 0.3	6.2± 0.1	7.7± 0.4	7.5 ± 0.3	7.1 ± 0.1

Table 5.3: *2D and 3D (2D+Z)* b-*tagging results:* R_u *and* R_c *for* ϵ_b *=50 %, 60 %. Jets originating from the decay of a 400 GeV Higgs boson.*

The c-rejection is much less sensitive to changes in the layout as it is dominated by the life time ratio of charmed and bottom hadrons.

The combination of the transverse and longitudinal impact parameter in the 3D algorithm yields a significant improvement of the b-tagging performance.

5.3.3 Impact of additional track quality requirements

In this section the effect on the b-tagging performance of additional track quality requirements is studied. A careful optimisation of an extended set of track quality criteria leads to a significant improvement of the b-tagging performance. However, some of the results obtained may depend strongly on the details of the detector description in the Monte Carlo simulation.

In addition to the *standard* track quality cuts, the following requirements are considered here:

- the longitudinal impact parameter: $z_0 < 1.5\ mm$
- the χ^2 of the track fit: $\chi^2 < 3$
- no shared hits in the B-layer
- maximum two shared hits in the precision tracker

The requirement on the longitudinal impact parameter z_0 is useful in rejecting tracks from displaced primary vertices. In the absence of pile-up, the performance is nearly unaffected. The effect of the χ^2 cut is small, within the statistical error.

The last two requirements reject tracks with multiple shared hits in the precision tracker, or a shared hit in the B-layer. Shared hits are space point measurements assigned to multiple tracks by the pattern recognition program. There are several reasons why shared hits occur. Detector inefficiencies may lead to hits from the neighbouring track being assigned to the track to replace the missing hit. For $\gamma \rightarrow e^+e^-$ conversions, the innermost layers have no hits. Again, hits in the innermost layers may be erroneously assigned to the track. In very dense jets, the detector granularity may become insufficient: neighbouring hits can no longer be distinguished experimentally and shared hits are inevitable. Posing a strict maximum on the number of shared hits in the different detector layers effectively reduces the fraction of fake and secondary tracks and thus lead to a significant improvement in the performance.

	120 GeV sample		*400 GeV sample*	
$R(\epsilon_b)$	*2D*	*3D*	*2D*	*3D*
$R_u(\epsilon_b = 50\ \%)$	191 ± 13	383 ± 24	112 ± 4	160 ± 4
$R_u(\epsilon_b = 60\ \%)$	61 ± 3	126 ± 3	43 ± 3	57 ± 2
$R_c(\epsilon_b = 50\ \%)$	10.0 ± 0.2	12.5 ± 0.2	10.2 ± 0.2	12.3 ± 0.2
$R_c(\epsilon_b = 60\ \%)$	6.2 ± 0.1	7.3 ± 0.1	5.9 ± 0.1	6.7 ± 0.1

Table 5.4: *2D and 3D (2D+Z)* b*-tagging results after the application of the additional track quality requirements discussed in the text: R_u and R_c for ϵ_b =50 %, 60 %. These results should be compared to the results of the 2D algorithm listed in the columns labeled* 'DC1' *in tables 5.2 and 5.3.*

The R_u and R_c of the 2- and 3-dimensional b-tagging algorithms obtained with the additional track quality requirements are listed in table 5.4. Compared to the results obtained with the standard cuts (*'DC1'* results of tables 5.2 and 5.3), the R_u performance is significantly improved in both samples and for both algorithms. The c-rejection is nearly unchanged.

In the remainder of this chapter, the additional track quality cuts listed above are applied.

5.3.4 Comparison of jet reconstruction algorithms

For the comparison with the TDR data presented in the previous section, jets based on Monte Carlo truth information are used. A more realistic result is achieved by considering jet reconstruction algorithms that take into account the detector response. In this section, the b-tagging performance is studied using three different jet reconstruction algorithms: KINE jets, ATLFAST jets and ATRECON jets.

ATLFAST jets are reconstructed using the ATLAS fast simulation program [143]. The jets are smeared using a parametrisation of the detector resolution. The ATRECON jets are obtained using a sliding window algorithm on the energy deposited in the calorimeter.

The results for 2D tagging of the b-jets from a 120 GeV Higgs are listed in table 5.5

$R(\epsilon_b)$	*ATLFAST*	*ATRECON*	*KINE*
2D $R_u(\epsilon_b = 50\ \%)$	178 ± 16	219 ± 13	191 ± 13
2D $R_u(\epsilon_b = 60\ \%)$	58± 4	67 ± 3	61 ± 3

Table 5.5: *2D algorithm results on the 120 GeV sample: R_u for ϵ_b =50 % and 60 %. The jet reconstruction algorithms are discussed in the text.*

The ATLFAST and KINE algorithms yield compatible results, i.e. the smearing applied in ATLFAST has a minor effect on the b-tagging performance. The performance obtained using ATRECON jets is slightly better.

Throughout the remainder of this chapter results are given for ATLFAST jets, because of their relevance for physics studies.

5.3.5 p_T and $|\eta|$ dependence

The overall efficiencies and rejections quoted in the previous sections ignore the dependence of the b-tagging performance on the jet momentum and pseudo-rapidity. In this section, the performance is analysed in p_T and $|\eta|$ bins. The 120 GeV and 400 GeV samples are combined into a single data set.

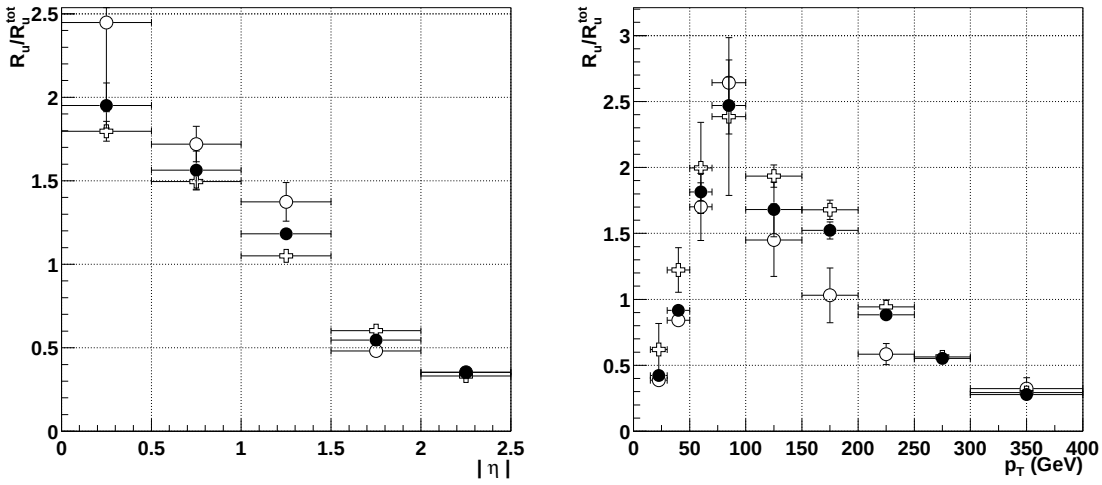

Figure 5.7: *$R_u(\epsilon_b = 60\%)$ for jets from the 120 GeV Higgs sample (open circles), 400 GeV sample (crosses) and the combined sample (filled circles). The result of each sample is divided by the global rejection of the sample. Leftmost figure: R_u versus $|\eta|$. Rightmost figure: R_u versus p_T. All results correspond to the 2D* b*-tag algorithm, ATLFAST jets and the DC1 geometry.*

The overall 2D u-jet rejection determined on the combined sample is:

$$R_u = 150 \pm 2 \qquad \epsilon_b = 50\%$$

$$R_u = 54 \pm 1 \qquad \epsilon_b = 60\%.$$

The c-jet rejection is found to be:

$$R_c = 10.8 \pm 0.1 \qquad \epsilon_b = 50\%$$

$$R_c = 6.2 \pm 0.1 \qquad \epsilon_b = 60\%$$

These results are to be taken as the reference performance throughout this section.

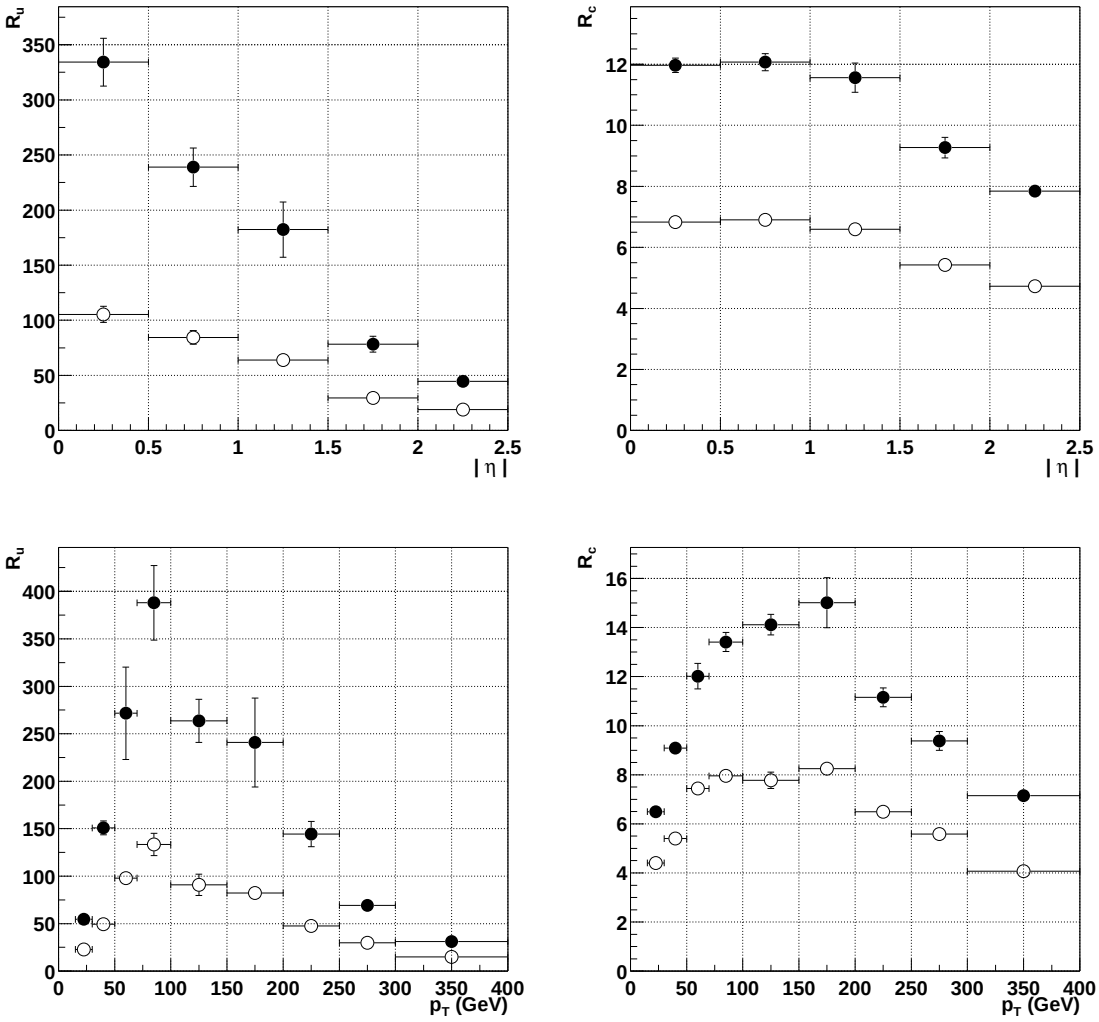

Figure 5.8: *2D algorithm rejections versus jet $|\eta|$ (upper figures) and p_T (bottom two figures). The rejections correspond to* b*-tagging efficiencies of 50 % (filled circles) and 60 % (open circles) for jets from the combined sample. The leftmost figure shows R_u, the rightmost figure R_c. ATLFAST jets, DC1 geometry.*

In figure 5.7 the η and p_T dependence of R_u is shown for the 120 GeV and 400 GeV samples and for the combined sample. To facilitate comparison, for each sample the ratio of R_u of a given rapidity or momentum and the global rejection R_u^{tot} of the sample is drawn. The same set of weights, determined using the full statistics, is used in the three cases.

The η dependence shown in the leftmost figure of 5.7 is similar for the three samples. Also, the p_T dependence of the three samples (each with a different pseudo-rapidity distribution) shown in the rightmost figure of 5.7 is compatible within errors. It is therefore assumed that the effect on the b-tagging performance of η and p_T are not correlated. In the following the dependence is studied independently.

In the upper figures of 5.8, the 2D algorithm results for R_u and R_c are shown as a function of $|\eta|$. The two sets of points correspond to different values of the b-tagging efficiency: 50 % and 60 %. The u-jet rejection depends strongly on the pseudo-rapidity: the lowest and highest bins differ by more than a factor 4. The degraded performance toward large $|\eta|$ is due the extra material in the forward region. The c-rejection is more uniform over the pseudo-rapidity interval: the variation is of the order of 40 %.

In the bottom figures of 5.8 the transverse momentum dependence of R_u and R_c is shown. The largest rejection is obtained in the intermediate momentum range $50 < p_T < 200\ GeV$. For low-p_T jets, the multiplicity and momentum of the tracks become too low to provide a precise measurement of the jet significance. Jets with very high p_T, on the other hand, have a large number of tracks in a very collimated jet cone. Therefore, pattern recognition becomes increasingly difficult. As before, R_c is more uniform over the p_T range: the total variation is roughly a factor 2.

5.3.6 Pile-up

During high luminosity operation of the LHC ($L = 10^{34} cm^{-2} s^{-1}$), on average 23 minimum bias events are superposed in every collision. The effect of *pile-up* on the b-tagging performance is studied in this section.

After applying the standard track quality cuts listed in section 5.1.3, up to 30 % of the tracks in the jet cone is due to pile-up events. As pile-up tracks are from a different interaction their primary vertices are generally displaced by large distances (typically ~ 5.6 cm) in the z-coordinate. This property can be used to reduce the effect of pile-up tracks. The requirement that the longitudinal impact parameter should be less than 1.5 mm, that has a negligible effect in the absence of pile-up, now leads to a very significant improvement of the performance. The use of the longitudinal impact parameter requires the primary vertex of the principal interaction to be precisely reconstructed. In this study a precision of the z-coordinate of the primary vertex of 50 μm is assumed.

u-jet rejection	*with pile-up*	*without pile-up*	*ratio*
2D R_u ($\epsilon_b = 50$ %)	102 ± 8	132± 3	0.77
2D R_u ($\epsilon_b = 60$ %)	40 ± 1	51 ± 1	0.78
3D R_u ($\epsilon_b = 50$ %)	167 ± 8	200 ± 7	0.83
3D R_u ($\epsilon_b = 60$ %)	59 ± 3	71 ± 1	0.83

Table 5.6: *R_u for events with and without pile-up. The number of pile-up events corresponds to the expectation for high luminosity operation of the LHC ($\mathcal{L} = 10^{34} cm^{-2} s^{-1}$). Results are given for the 2D and 3D algorithms on the 400 GeV sample. These results correspond to ATLFAST jets, DC1 geometry.*

c-jet rejection	*with pile-up*	*without pile-up*	*ratio*
2D R_c ($\epsilon_b = 50$ %)	9.8 ± 0.2	11.5± 0.2	0.85
2D R_c ($\epsilon_b = 60$ %)	5.7 ± 0.1	6.4 ± 0.1	0.89
3D R_c ($\epsilon_b = 50$ %)	11.5 ± 0.2	14.8 ± 0.4	0.78
3D R_c ($\epsilon_b = 60$ %)	6.8 ± 0.1	7.8 ± 0.1	0.87

Table 5.7: *R_c for events with and without pile-up. The number of pile-up events corresponds to the expectation for high luminosity operation of the LHC ($\mathcal{L} = 10^{34} cm^{-2} s^{-1}$). Results are given for the 2D and 3D algorithms on the 400 GeV sample. ATLFAST jets, DC1 geometry*

The overall u- and c-jet rejection for the 400 GeV sample[8] are listed in table 5.6 and 5.7 together with the corresponding results without pile-up.

In the presence of high-luminosity pile-up, the performance is significantly degraded. The ratio of R_u with and without pile-up is approximately 0.78. The 3D algorithm seems to be slightly more robust; the ratio between pile-up and no pile-up rejections is approximately 0.83. The effect of pile-up on the c-rejection is of the same order.

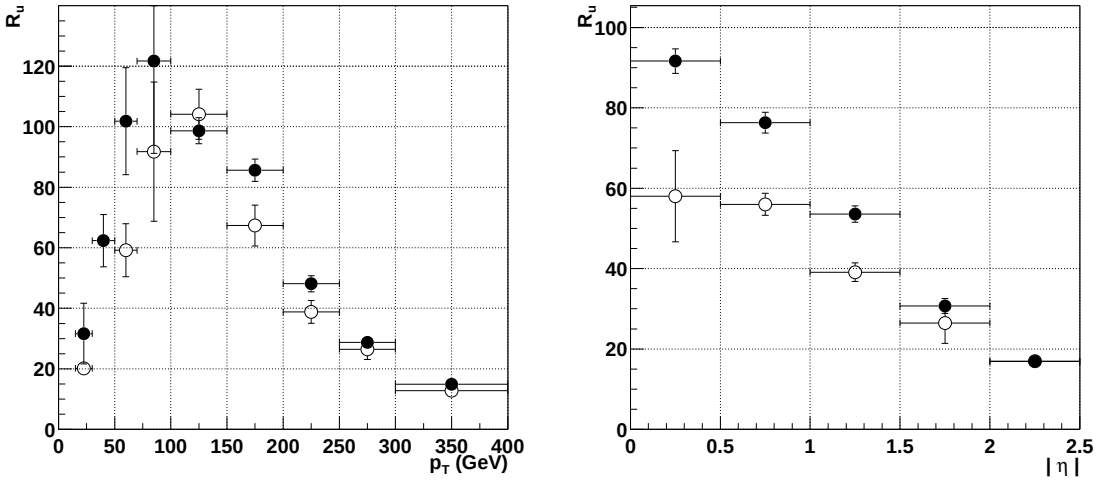

Figure 5.9: *R_u corresponding to* b*-tagging efficiencies of 60 %. Leftmost figure: R_u versus p_T. Rightmost figure: R_u versus $|\eta|$. Jets from the $m_H = 400$ GeV sample without pile-up (filled circles) and with pile-up (open circles) as in high luminosity ($L = 10^{34} cm^{-2} s^{-1}$) operation of the LHC. In all cases the results correspond to ATLFAST jets and the DC1 geometry.*

In figure 5.9 the u-jet rejection results obtained using the 2D algorithm corresponding to a b-tagging efficiency of 60 % are shown for different bins in jet p_T and $|\eta|$. The results without pile-up are shown with black markers, the high-luminosity results with open markers. The leftmost figure shows that the u-jet rejection is equally affected in all momentum bins within statistical errors. Its effect, however, is not uniform over the rapidity range. As can be seen

[8]The 120 GeV pile-up sample is not analysed here.

in the rightmost figure, the performance loss due to pile-up is mostly concentrated in the central rapidity region.

5.3.7 Alternative *b*-tagging algorithms

The likelihood method is entirely based on the large impact parameters of tracks that originate in the decay of a long-lived B-hadron. Additional information may be available in the event that could be taken advantage of to improve the *b*-tagging performance. Two alternative algorithms are discussed here.

The most direct way to use the long lifetime of the B-baryons to tag *b*-jets is through the explicit reconstruction of the event vertices. In that case, a large set of discriminating variables become available:

- the distance between primary and secondary vertex (decay length)
- a comparison of the momentum vector of the secondary vertex (the vectorial sum of the momenta of the tracks in the secondary vertex) with the vector joining the PV and SV (supposedly the flight path of the B-hadron). Secondary vertices due to B-decay show highly correlated directions.
- the invariant mass and transverse momentum at the secondary vertex provides powerful rejection against light Λ and kaons and secondary vertices from conversions.
- the rapidity difference between the jet axis and tracks from the secondary vertex helps to distinguish between D and B decays. The larger mass of the B-hadron leads to slightly larger opening angle.

These Secondary Vertex variables yield a very powerful rejection of non-B vertices. The main limitation to the method is the limited secondary vertex reconstruction efficiency.

Lepton tagging takes advantage of the high probability of *b*-jets, compared to light and *c*-jets, to contain a lepton with relatively high transverse momentum. The method suffers from the low branching ratio for leptonic B-decays. Therefore, the efficiency is limited to some 10 %. The method is interesting as the sign of the lepton allows to distinguish between the B-hadron and its anti-particle.

In many experiments, a combination of the two *b*-tagging techniques described here with a pure impact parameter algorithm, like the likelihood method, is used. Combined algorithms are likely to yield a significant improvement of the performance.

5.3.8 Perspective

The 2D tagging method applied to events with the 100 % efficient detector with 3 PIXEL layers studied here provides a first estimate of the *b*-tagging performance of the ATLAS detector in realistic conditions. In this section, a number of effects are discussed that are likely to affect the ATLAS performance, but have not been (fully) taken into account in the present study.

The performance is likely to be deteriorated by:

- Tracks from pile-up events
- Detector inefficiencies and misalignments
- The ATLAS experiment may start running with an incomplete detector consisting of only 2 PIXEL layers
- The uncertainty in the weights used in the b-tagging algorithm

The effect of pile-up is studied in this work, predicting a degradation of R_u by $15 - 25\%$. Preliminary studies into the effect of small channel and module inefficiencies indicate tolerable losses [144]. The performance of an incomplete geometry (without the intermediate PIXEL layer) at low luminosity is the subject of detailed studies [144]. The extraction of the likelihood weights from the data is being investigated as well.

Fortunately, the expected deterioration of the performance by the effects listed above, may be balanced by improvements of the b-tagging algorithm:

- As reported, the 2D+Z algorithm yields a clear improvement of the performance
- The explicit reconstruction of the secondary vertex provides additional information (invariant mass of the vertex, direction with respect to the jet axis) that can be used to improve the b-tagging performance [145].
- lepton tagging may provide an additional improvement

In view of all this, we estimate that the results of the 2D algorithm on the complete, 100% efficient detector without pile-up can be used as the reference performance in physics analyses.

5.4 Summary

The b-tagging performance of the ATLAS detector is analysed using samples of simulated $WH \to \mu\nu_\mu q\bar{q}$ events, with three quark flavours $q = b, c, u$ and two different Higgs boson masses: $m_H = 120, 400\ GeV$. The events are generated and simulated in the framework of ATLAS Data Challenge 1. The DC1 samples take into account recent changes in the layout: most importantly the new design of the beam pipe and the extra material related to the insertable layout of the pixel detector. Moreover, a realistic field map is used for the inner detector solenoidal. In this chapter, the results for a *complete* inner detector (with 3 PIXEL layers) are compared to a reanalysis of the samples used for the physics TDR.

The impact parameter resolution shows a significant degradation with respect to the results from the TDR sample, confirming the expectation from the layout changes. The TDR and DC1 data are analysed using the standard set of track quality requirements and the likelihood b-tag algorithm. The DC1 rejection for a given b-tag efficiency is significantly deteriorated with respect to the TDR result. The degradation of the impact parameter resolution explains part of the deterioration. Additional effects, like increased interactions with the detector material, are likely to cause the remaining deterioration.

Application of additional track quality requirements, especially those restricting the number of shared hits on the track, lead to a significant improvement of the performance. Assuming that the z-coordenate of the primary vertex can be reconstructed with a precision of 30 μm, the 2D+Z b-tag algorithm yields a significantly better performance. The different jet reconstruction algorithms studied in this chapter show marginally different performance.

Using ATLFAST jets and the extended set of track quality requirements, the overall light and c-jet rejection of the 2D likelihood method on the combined sample of WH events with $m_H = 120\ GeV$ and $m_H = 400\ GeV$ is found to be:

$$R_u = 150 \pm 2, \quad R_c = 10.8 \pm 0.1 \quad \text{for } \epsilon_b = 50\% \tag{5.1}$$

$$R_u = 54 \pm 1, \quad R_c = 6.2 \pm 0.1 \quad \text{for } \epsilon_b = 60\% \tag{5.2}$$

A parametrisation of the b-tagging performance is given in terms of the jet rapidity and momentum. The p_T and η corrections may be assumed to be uncorrelated. Good rejection is obtained in the barrel region for intermediate jet momenta (50-200 GeV). The rejection drops toward the forward regions and for jets with very low or very high p_T.

For the $m_H = 400\ GeV$ sample the effect of pile-up during high-luminosity operation of the LHC ($\mathcal{L} = 10^{34} cm^{-2} s^{-1}$) is analysed. The u-jet rejection deteriorates by approximately 23 % (slightly less for the 3D algorithm). The performance loss is most significant in the central rapidity region.

The use of more sophisticated algorithms is expected to balance the degradation of the performance due to pile-up, detector inefficiencies, imperfect calibration of the likelihood method, etc. Therefore, the 2D results for a 100 % efficient detector without pile-up are proposed as benchmark values for the ATLAS b-tagging performance.

Chapter 6

The detection of light MSSM Higgs bosons

The matter particles and gauge bosons of the Standard Model acquire mass through the Higgs mechanism. The physical expression of the Higgs field, the Higgs boson, provides a testable signature of the mechanism. In common super-symmetric extensions of the Standard Model, a two-doublet Higgs sector arises. The Minimal Super-Symmetric extension of the Standard Model (MSSM) predicts five physical Higgs bosons: three neutral bosons, of which two are scalar (h^0 and H^0) and one is a pseudo-scalar (A^0), and two charged Higgs bosons ($H^\pm$). The phenomenology of the MSSM, i.e. the masses and couplings of the Higgs bosons, depends strongly on a number of parameters that are not predicted by the theory.

For some combinations of MSSM parameters, Higgs boson decay channels that would not be observable in the LHC according to the Standard Model may yield detectable signals. A good example is the strongly enhanced production of neutral Higgs bosons with b-quarks in the MSSM for large values of the ratio of the vacuum expectation values of the two Higgs doublets $\tan\beta$.

In this chapter, the observability in the ATLAS experiment of the two lightest Higgs bosons of the MSSM through their decay to muon pairs is investigated. The results have previously been reported in an ATLAS internal note [146].

In section 6.1 the production of these light Higgs bosons, h^0 and A^0, is discussed together with the most relevant background processes. The calculation of the production cross sections is discussed in this section as well. In section 6.2 the generation of the signal and background samples is discussed. The detector simulation in the ATLAS fast simulation framework is also treated. A method to extract the signal from the background is presented in section 6.3. The expected observability of the signal in the ATLAS detector is discussed. Finally, the results are summarised in a concluding section.

6.1 Signal and backgrounds

In the following sections, the signal and the most important background processes are identified. The expected production rates at the LHC are discussed as well.

6.1.1 Signal and background processes

As discussed in the physics introduction (section 1.3.2) the Yukawa coupling of the Higgs bosons of the MSSM to bottom quarks depends strongly on $\tan\beta$. For large values the associated production of MSSM Higgs bosons with b-quarks is strongly enhanced; it is the dominant mechanism for $\tan\beta > 10$. Moreover, the presence of b-jets in the final state provides an additional signature to experimentally select these events, allowing a substantial reduction of the background. Therefore, this study concentrates on associated production, i.e. on the channel:

$$gg \rightarrow b\bar{b}X, q\bar{q} \rightarrow b\bar{b}X \tag{6.1}$$

where X represents the h^0 or A^0 boson.

In previous studies, reported in the physics section of the ATLAS technical design report [56], encouraging results were reported for the observability of A^0 and the heavier of the two scalar Higgs bosons, H^0, through the $\tau^+\tau^-$ and $\mu^+\mu^-$ decay channels. These studies focus on relatively large values of the A^0 mass: $m_A > 125\ GeV$.

The search for the combined signal from the lighter scalar Higgs boson h^0 with the A^0 boson for $m_A < 125\ GeV$ is more challenging due to the overwhelming background from Z^0 decays in this mass range. The decay to τ-leptons has the advantage of a much larger branching ratio. For the muon decay, the analysis benefits from the very good invariant mass resolution achieved by combining the inner tracker and muon spectrometer measurements. In the presence of a large (partly irreducible) background, the muon decay of the Higgs boson is the most promising channel to extend the analysis to $m_A < 125\ GeV$.

The muon decay has a small branching ratio of the order of $3 \cdot 10^{-4}$, yielding a total rate of $\sigma \cdot B.R. = \mathcal{O}(10^{-1})\ pb$ for $\tan\beta = 15$ and $m_A \sim 100\ GeV$. The production cross section is discussed in detail in section 6.1.2, after a discussion of the most relevant backgrounds. The muon pair in the final state of the event produces a clear experimental signature for the event selection.

Throughout the mass range under study, $70 < m_A < 125\ GeV$, muon pairs are predominantly produced in Z^0/γ^* decays. The Z^0/γ^* interference is produced abundantly in the LHC through direct (Drell-Yan) production ($q\bar{q} \rightarrow Z^0/\gamma^*$). The cross section is much larger than that of the signal: $\sigma \cdot B.R. = 2700\ pb$. This background can, however, efficiently be reduced requiring a tagged b-jet in the final state.

An irreducible background is formed by Z^0/γ^* production in association with b-quarks, i.e. by the process of equation 6.1, where the X represents the Z^0/γ^* interference. The production cross section is of the order of several tens of pb. The final state only differs in the angular distributions of the muon pair due to the different spin of the Z^0 and Higgs bosons. These variables have little discriminating power.

The invariant mass distribution of these muon pairs follows the Z^0/γ^* line-shape: a central Breit-Wigner peak (with $m_Z \sim 91.2\ GeV$, $\Gamma_Z \sim 2.5\ GeV$) and long tails towards higher and lower masses.

An additional source of background is continuum $t\bar{t}$ production. The top quarks decay into W^+b ($W^-\bar{b}$). The subsequent decay of the W bosons into a muon and a neutrino yields the muon pair. The total production of $t\bar{t} \rightarrow b\bar{b}\mu^+\mu^-\nu_\mu\bar{\nu_\mu}$ amounts to a $\sigma \cdot B.R.$ of 5.7 pb. The relatively small production cross section renders this process less harmful: the

$t\bar{t}$ background becomes dominant only for $m_A > 125\ GeV$. The missing energy associated with the neutrinos provides a signature that can be used to distinguish this final state from the signal.

The total irreducible background rate is large compared to that of the signal. A strong enhancement of the Higgs production is needed to achieve a significant signal. The invariant mass resolution of the reconstructed muon pair is crucial to distinguish the signal on top of the background.

6.1.2 Production cross sections

In this section the expectations for the production cross section of bosons in association with bottom quarks are discussed. The discussion is relevant for associated h^0 and A^0 production and the most relevant (irreducible) background: $gg \to b\bar{b}Z^0$. A more detailed discussion can be found in references [147, 148, 149].

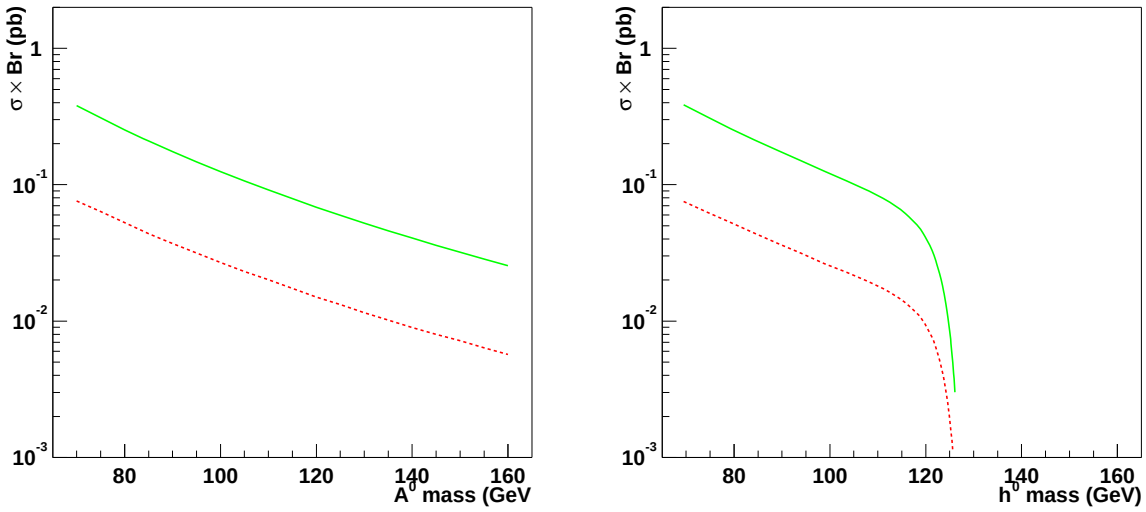

Figure 6.1: *The production cross section times branching ratio into muons of the A^0 (leftmost figure) and h^0 bosons (rightmost figure). The results correspond to* $\tan\beta = 15$. *Increasing (decreasing) the value of* $\tan\beta$ *leads to a strong enhancement (suppression) of the production. The two lines correspond to calculations in two different theoretical approaches: shower (full line) and Matrix Element approach (dashed line).*

The cross section expectation for the associated production of A^0 and h^0 bosons at the LHC is shown in figure 6.1. The two lines represent two different approaches to the cross section calculation: the continuous line corresponds to the *shower approach* [150], the dashed line to the *matrix element approach* [151, 152]. Both approaches yield quite different results for the production cross sections of supersymmetric Higgs bosons with b-quarks. A similar, though slightly smaller, difference is found in the equivalent production mechanism for the Z^0 boson. In the following, possible sources for the apparent incompatibility of both approaches are discussed.

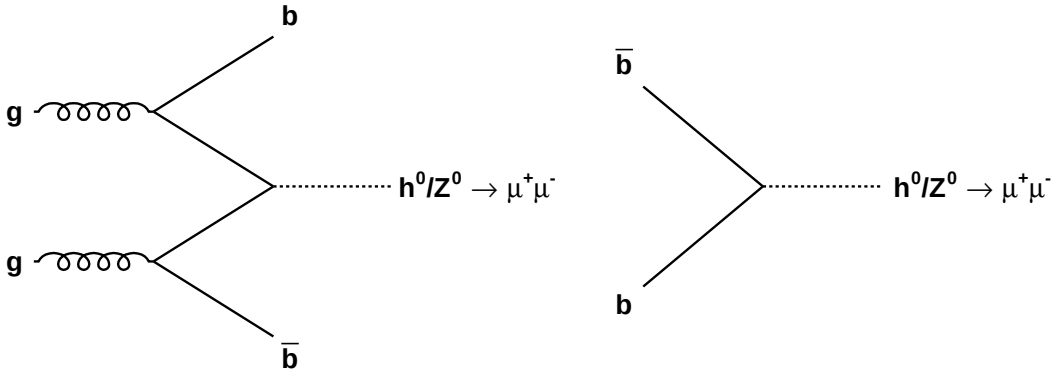

Figure 6.2: *Typical diagrams used in the two calculation schemes. Leftmost figure: Matrix Element approach. Rightmost figure: shower approach.*

In the Matrix Element approach the amplitudes of the process corresponding to the leftmost diagram of figure 6.2 (and similar diagrams, see also equation 6.1) are calculated explicitly. The matrix elements are convoluted with the parton density function that expresses the probability to find a gluon with a fraction x of the proton momentum. The gluon parton density function is quite precisely known: the estimated contribution of the PDF uncertainties to the error on the production rate is of the order of 10 % for the LHC [153].

At the time of this study only the leading order calculation was available. As reference [153] puts it: *"theoretical predictions for cross sections that are based on leading order QCD are notoriously imprecise"*. Moreover, for processes $gg \to Xb\bar{b}$, the correction from higher orders is potentially large through the development of *large logarithms* [149, 154]. For a gluon splitting into a nearly collinear pair of heavy quarks, a factor of the form $\ln(q^2/{m_Q}^2)$ appears from the integration over the phase phase of the external quark. The scale q is normally taken to be the mass m_X of the produced boson. For top quarks ($t\bar{t}X$ production) the perturbation series in $\alpha_s \ln(q^2/{m_Q}^2)$ converges quite well. However, for the relatively light b-quarks the convergence is deteriorated.

In the shower approach [150] the cross section for associated production of Higgs and Z^0 bosons is calculated using the rightmost diagram of figure 6.2. The leading order process in this case is:

$$b\bar{b} \to X \tag{6.2}$$

where X may represent the Z^0 boson or one of the neutral MSSM Higgs bosons.

The bottom content of the proton is taken from the b-quark parton density function. The associated b-jets in the final state are obtained in parton shower-based event generators (such as PYTHIA) by the backward evolution of the b-quark to its parent gluon.

The central point in the shower approach is the factorisation of the vertex where the gluon splits into a $b\bar{b}$ pair into a b-density of the proton. The *large logarithms* that develop in the matrix element approach are resummed and absorbed in the PDF. This procedure

greatly facilitates the calculations.

In the shower approach, NLO (and even NNLO) corrections to the cross section can be calculated. The process of equation 6.1 and $gb \to bA^0/h^0$ are corrections to the leading order process of equation 6.2. However, as logarithmic terms $\ln[{m_H}^2/{m_b}^2]$ from the higher order contributions have already been resummed into the bottom quark density, the higher order corrections cannot simply be summed. A careful subtraction of terms is needed to avoid double counting. The NNLO order calculations have recently become available [155, 156], yielding a small correction to the NLO result.

The use of b-densities implies an approximation to the kinematics of the hard process: the b-quarks are assumed to be massless and to have negligible transverse momentum. There is considerable discussion among theorists about the interpretation of the bottom quark density function. The validity of the approximations in factorisation (inherent to the shower approach) depend on the mass of the "heavy" quark and the center-of-mass energy of the collider. While for light quarks, PDFs are thought to be valid even at low energies, for top quarks an explicit calculation of the gluon splitting is preferred. Whether the intermediate mass of the bottom quark should be classified as light or heavy is an issue of debate. According to reference [149]: *"$b\bar{b}\phi$ production at the LHC develops sizeable bottom mass effects, so that the use of bottom densities in the process $b\bar{b}\phi$ may lead to an overestimate of the correct theoretical result due to too crude approximation in the kinematics of the hard process".*

In addition to the interpretation of the b-densities, the use of b-quark PDFs introduces a significant numerical uncertainty. The b-quark content of the proton has not been measured directly, but is inferred from the gluon density function.

Thus, both approaches are prone to large uncertainties. In the leading-order Matrix Element calculation potentially large corrections of the form $\ln[{m_b}^2/{m_H}^2]$ develop at higher orders. In the shower approach calculation on the order hand, a possibly large error is due to the approximation of the kinematics of the hard process.

As seen in section 1.2.2 the result of a finite-order calculation depends on the renormalisation scale μ_R. Factorisation of the parton content of the proton into parton density functions gives rise to a second scale, the factorisation scale μ_F. The dependence of the result under variation of the scales over a given interval is known as the scale dependence. It is an indication of the stability of the result, i.e. it provides an estimate of the relative size of the higher order corrections not taken into account in the calculation.

In figure 6.3 the scale dependence of the cross section calculations in the shower and matrix element approaches are compared. Two processes are considered: the associated production of the h^0 boson with b-quarks is shown in the leftmost figure, the equivalent process for the Z^0 boson is shown in the rightmost figure. In both cases, the renormalisation and factorisation scale are identified: $Q_R = Q_F = Q$, and varied from a quarter of the mass of the heavy boson produced to four times that mass. For the shower approach, the full scale dependence stems from factorisation. In the Matrix Element approach the factorisation scale has a small effect and the bulk of the dependence stems from the dependence on the renormalisation scale.

The variation of the cross section has a similar shape in the $h^0b\bar{b}$ and $Z^0b\bar{b}$ processes. For both approaches the scale dependence is quite strong: variation of the scale from $2m_X$ to $m_X/2$ leads to a factor of approximately 2 in the cross section result. The sign of the depen-

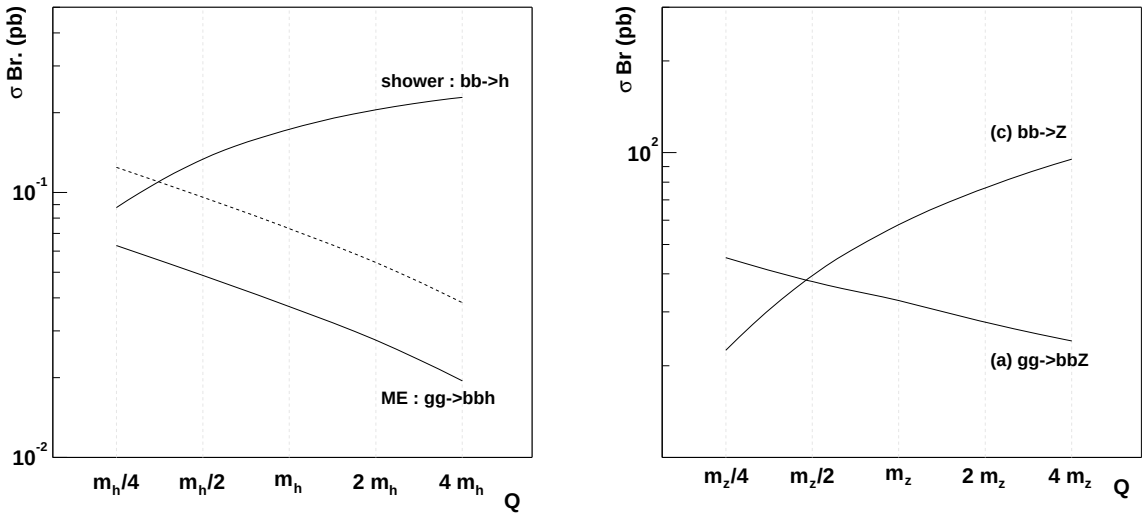

Figure 6.3: *The scale dependence of the cross section calculation in the shower and matrix element approach. Leftmost figure: production of a 90 GeV h boson in association with b quarks. The dashed line represents the Matrix Element cross section evaluated using the running* b*-quark mass in the phase space integration. Rightmost figure: the equivalent cross section for* Z^0 *boson production.*

dence is opposite for both approaches: where the shower approach cross section decreases towards lower scales, the matrix element result increases. The results from both approaches match at some scale $Q^2 < {m_H}^2$.

Given the scale dependence observed in figure 6.3 it seems reasonable to conclude that the uncertainty in both approaches is of the same order. Taking into account these uncertainties, the cross section predictions of the shower and matrix element approach for the LHC are not mutually exclusive.

The range of validity for both approaches may be clarified by NLO Matrix Element calculations. The recent publication of NLO order corrections for the associated Higgs boson production with top quarks [154, 152, 153, 157, 158] is an important step. Preliminary results for the $hb\bar{b}$ process indicate that the K-factor of the matrix element calculations (the ratio of NLO and LO cross section results) is indeed quite large (around 1.6 for $m_H \sim 100\ GeV$, increasing to around 2.2 for higher masses [159]). With this new result and an appropriate choice of the renormalisation and factorisation scale, the results are brought into agreement.

A number of additional sources of uncertainty exist that are common to both approaches. Like for the Standard Model Higgs boson, the Yukawa coupling between the Higgs and quarks depends quadratically on the quark mass. There seems to be a general consensus, followed by this analysis, that for the determination of the Yukawa coupling the running quark mass at the Z^0-scale ($m_b(m_Z) \sim 2.91 \pm 0.10\ GeV$) should be used. The uncertainty in the (running) b-quark mass affects the result of the calculation.

The production rate of the MSSM Higgs bosons depends strongly on the MSSM parameters. The variation of the cross section with the A^0 mass is shown in figure 6.1. The production decreases by a factor 4 from the lowest (70 GeV) to the highest mass (125 GeV)

considered here. Even more important is the dependence on $\tan\beta$. The coupling of the A^0 (h^0) boson to b-quarks is proportional to $\tan\beta$ ($\sin\alpha/\cos\beta$). The cross section is therefore enhanced by several orders of magnitude for large values of $\tan\beta$.

Finally, it should be kept in mind that the luminosity scenarios for the accelerator are an important source of uncertainty as well.

To study the observability in the presence of a large uncertainty in the event rates, the analysis is performed separately for the two approaches of the cross-section calculation. The first analysis is performed following the shower approach prescription. The corresponding results for the Matrix Element approach are estimated by rescaling the signal and background production rates. The difference between the outcomes of both analyses is an indication of the uncertainty inherent to this study. Since the dominant uncertainty equally affects the signal and the irreducible background, the significance, that depends on the signal *and* background, may be expected to less sensitive than each of the individual rates.

The cross section of the Matrix Element cross sections for associated production of MSSM Higgs boson with b-quarks are calculated using the HQQ program [160]. The equivalent process of the Z^0 boson is available in PYTHIA [31] as an external process [161]. The branching ratios of Higgs and Z^0 bosons to muons for different values of m_A and $\tan\beta$ have been calculated using HDECAY [162] and PYTHIA, respectively.

6.2 Generation & simulation

In this section the simulation chain is outlined. First, the generation of events is discussed, followed by a discussion of the simulation of the detector response. Finally, a set of kinematical cuts are applied to emulate the detector and trigger acceptance.

6.2.1 Event generation

To study of the observability of the combined A^0/h^0 signal a large sample of signal and background events is generated using Monte Carlo techniques. Dedicated programs, *event generators*, are used to produce large samples of events, varying the kinematical properties over the available *phase space*. For this study samples of signal and background events are generated using PYTHIA6.157. The events contain information on the energy-momentum four-vectors of all generated particles. For unstable particles with short lifetimes the decay is treated in the same package. For quarks and gluons a parton evolution algorithm is used to produce jets of particles.

In the shower approach the b-jets associated with Z^0/γ^* or Higgs bosons are generated through the backward evolution of the parton shower. The initial low p_T of the b-quarks receives corrections due to final-state-radiation. To improve the soft p_T distribution, Matrix Element corrections are implemented in PYTHIA according to the scheme of reference [163, 164]. This generator mode is selected setting switch MSTP(68)=1. For the associated production of the MSSM Higgs bosons, Matrix Element corrections are not available; the non-default setting of MSTP(68)=2 is used for MSSM Higgs production.

The p_T distributions of the b-jets associated with Higgs boson (Z^0/γ^*) production returned by PYTHIA for Matrix Element and shower approach are compared in the leftmost

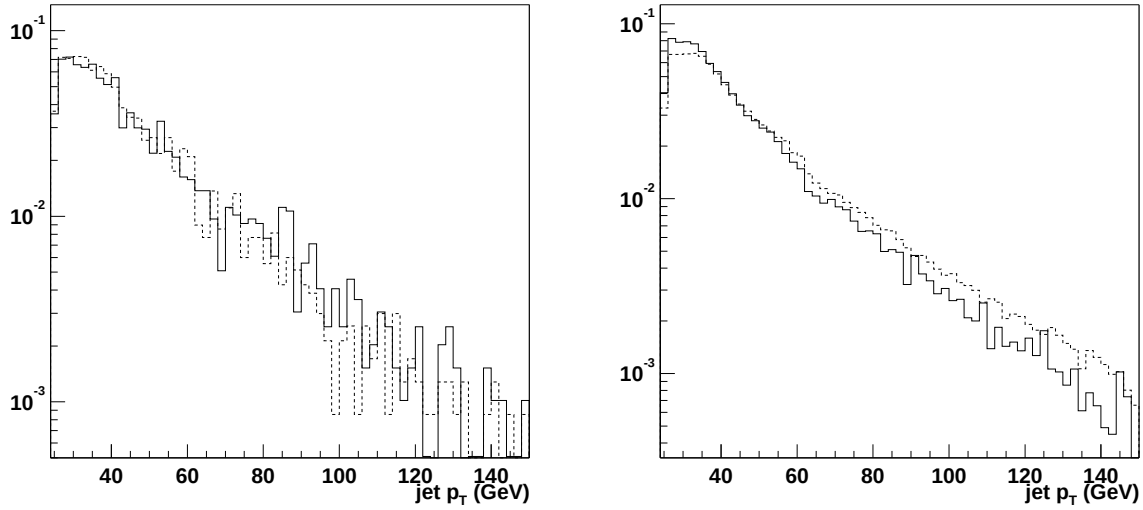

Figure 6.4: *Kinematical distribution of* b*-jets in the shower (continous line) and matrix element approach (dashed line). Leftmost figure: p_T distribution of* b*-quarks associated with A^0 production. Rightmost figure: The corresponding distributions for $Z^0 b\bar{b}$ production. The $b\bar{b} \to Z^0$ events are generated with PYTHIA option MSTP(68)=1. The $b\bar{b} \to A^0$ events have MSTP(68)=2. The MSSM parameters are chosen to be $m_A = 120\ GeV$,* $\tan\beta = 15$

(rightmost) figure of 6.4. Small differences in the distribution persist after correction; the p_T spectrum obtained for the shower approach is slightly softer. The description of the p_T distributions affect the total observable signal, as the experiment is only sensitive to b-jets with relatively high p_T. Small differences in the p_T distributions of matrix element and shower approach tend to bring the predictions for the partial cross section with $p_T(jet) > 25\ GeV$ of both methods in better agreement. See reference [147] for a detailed discussion.

The jets associated with Higgs production are predominantly produced in the central rapidity region. The kinematical distributions of the final state particles affect the observability of the signal, as the ATLAS precision measurements are limited to a rapidity acceptance $|\eta| < 2.5$. Moreover, the b-tagging performance is a steep function of rapidity. The kinematical cuts are discussed in more detail in the next section.

6.2.2 Detector simulation

To simulate the detector response, the ATLAS fast simulation (ATLFAST 00-02-21 [143]) is used. This package is intended to provide a fast simulation of the detector response, reproducing the expected resolution of the various sub-detectors as closely as possible. To reduce the execution speed, detector effects are simulated by smearing the particle properties using parametrisations of the detector performance as a function of particle type, momentum and rapidity.

The applicability of the package depends heavily on comparisons with *full* simulation studies, in which the particles are explicitly tracked through the detector volume using

specialised packages like GEANT [80]. The expected detector and reconstruction efficiencies are taken into account by applying efficiency factors off-line.

The intrinsic invariant mass resolution for muon pairs combining the inner detector and the muon system is expected to be 1.3 GeV at a mass of $\sim$ 90 GeV [143]. Muons with a transverse momentum larger than 6 GeV are expected to be identified with a an efficiency of over 90 % (see figure 2.10 or reference [56]).

Two possibilities exist to take advantage of the muons in the event to create a trigger. A trigger menu for pairs of isolated muons with $p_T > 6$ GeV is likely to be present in the ATLAS trigger. For a single-muon trigger, a much larger p_T is required. The muons originating in the decay of the Higgs have a rather large transverse momentum, on average $\sim$ 40-60 GeV, and a more stringent muon momentum cut has a small effect on the signal rate. Therefore, in this analysis, at least one of the muons is required to have a transverse momentum > 20 GeV.

The only signature in final state that allows a significant reduction of the background are the associated b-jets. In this analysis, one or more tagged b-jets are required in the final state. This leads to a reduction of the Drell-Yan background over more than an order of magnitude, while retaining more than half of the signal events.

The background could be reduced further by requiring both b-jets to be reconstructed and tagged. However, requiring a *double tag* leads to a quite severe degradation of the signal due to tagging inefficiencies and geometrical acceptance (often jets are lost in the beam-pipe). Given that the background is dominated by the irreducible associated production $gg \rightarrow Z^0/\gamma^* b\bar{b}$, the single tag yields a better significance. The effect of a double tag is studied in detail in reference [165], reaching the same conclusion.

The b-tagging efficiency has been studied in detail in the previous chapter. To facilitate the comparison between different physics analyses, benchmark values for the rejections of light and c-jets are used. For b-jets with $p_T > 25$ GeV the tagging efficiency is taken to be 50 % at high luminosity. The corresponding rejections are taken to be 100 for light (u,d,s and gluon) jets and 10 for c-jets.

These values should be compared to the rejection achieved with the 2D likelihood method reported in the previous chapter (see equations 5.1). The benchmark values used for this analysis represent a conservative estimate of the ATLAS b-tagging performance. In this case, the rejection is sufficient so that a *single tag* maintains the Drell-Yan background well below the irreducible $Z^0 b\bar{b}$ background. Therefore, the use of more ambitious rejection rates does not lead to a significant improvement of the discovery potential in this channel.

Jets are reconstructed by ATLFAST on the basis of smeared generator information. A simplified cone algorithm is used to determine the jet energy and direction, as discussed in chapter 5. A flavour tag is assigned to the jets according to the heaviest quark in the parton shower with p_T ¿ 5 GeV within the jet cone.

The reconstruction efficiency for jets with low transverse momenta is likely to be degraded during high-luminosity operation. Therefore jets with a calibrated p_T below 25 GeV are not considered in this analysis.

An additional small rejection of the $t\bar{t}$ background without much loss of the signal is achieved by requiring the total missing transverse energy in the event to be less than 40 GeV. As the $t\bar{t}$ background is not dominant anywhere in the mass range under study,

loosening this cut to $E_T^{miss} < 100$ does not have a significant effect on the final results.

The geometrical acceptance of the tracker and muon chambers are taken into account by requiring $|\eta| < 2.5$. A mass window of $\pm$ 4 GeV around the Higgs mass is selected to determine the number of signal and background events. For the results reported in section 6.3.2 the signal is extracted from the background explicitly and the latter cut is no longer relevant.

The selection requirements can be summarised as follows:

- a muon pair with an invariant mass in $m_A - 4GeV < M_{\mu\mu} < m_A + 4GeV$
- at least one isolated muon with $p_T > 20$ GeV
- $p_T > 6$ GeV for the second muon
- the missing transverse energy of the event $E_T^{miss} < 40$ GeV
- at least one tagged b-jet with $p_T > 25$ GeV

Signal and background process are listed in table 6.1. For each production mechanism the cross section, multiplied by the branching ratio, is given. The cross section for A^0 production in association with b-quarks is given for both approaches to the calculation discussed in section 6.1.2. Values are given for $\tan\beta = 15$ and two Higgs masses: $m_A = 90$ GeV and 120 GeV.

Signal and background processes				
	$m_A = 90$ GeV		$m_A = 120$ GeV	
process	$\sigma \cdot BR(pb)$	*events*	$\sigma \cdot BR(pb)$	*events*
$b\bar{b} \to A^0$ (shower)	0.17	2600	0.08	1500
$gg \to A^0 b\bar{b}$ (ME)	0.037	670	0.015	330
reducible Z^0 + jets (shower)	2700	320 000	2700	2100
irreducible $b\bar{b} \to Z^0$ (shower)	58	810 000	58	3 900
irreducible $Z^0 b\bar{b}$ (ME)	23	340 000	23	1500
$t\bar{t} \to b\bar{b}\mu^+\mu^-\nu_\mu\bar{\nu_\mu}$	5.7	5 600	5.7	3 900

Table 6.1: *A list of the most relevant signal and background processes. For each process the cross section is given for two A^0 masses. The adjacent columns list the number of events expected after kinematical cuts in a mass window is $\pm$ 4 GeV around the A^0 mass, for an integrated luminosity of 300 fb^{-1} and* $\tan\beta = 15$.

The expected number of signal and background events to be recorded in ATLAS are determined from the simulation. To this end the kinematical requirements described above are applied to the generated event samples. The reconstruction efficiency is taken into account using the efficiency factors discussed above. The results in table 6.1 correspond to an integrated luminosity of 300 fb^{-1}, expected to be accumulated in 3 years of high-luminosity running of the LHC.

For a 90 GeV Higgs the mass window falls right on the Z^0 peak and the contribution to the background from $Z^0 b\bar{b}$ is very large. For a relatively heavy Higgs boson, $m_A = 120$ GeV,

the Z^0 background is two orders of magnitude lower. The $t\bar{t}$ background becomes relevant for this relatively high mass. Over the full mass range the contribution to the background from Drell-Yan production is well below the irreducible background.

6.3 Signal extraction

In the mass range $m_A \sim m_h < 125\ GeV$ the $Z^0 b\bar{b}$ background cannot be significantly reduced. However, the good invariant mass resolution for the muon pair allows to distinguish a narrow signal peak on top of the well-known background. In this section, a method to extract the Higgs signal from the background is presented.

6.3.1 Method

The signal extraction method studied here is based on the use of a reference sample to determine the background shape. A data set is generated that contains the contributions from the Z^0/γ^* and $t\bar{t}$ backgrounds and the combined signal from the h^0 and A^0 bosons. The number of events again corresponds to three years of high luminosity running. The signal sample is obtained by applying the kinematical cuts listed above. The reference sample consists of all events that satisfy the remaining cuts, but failed to meet the b-tag requirement.

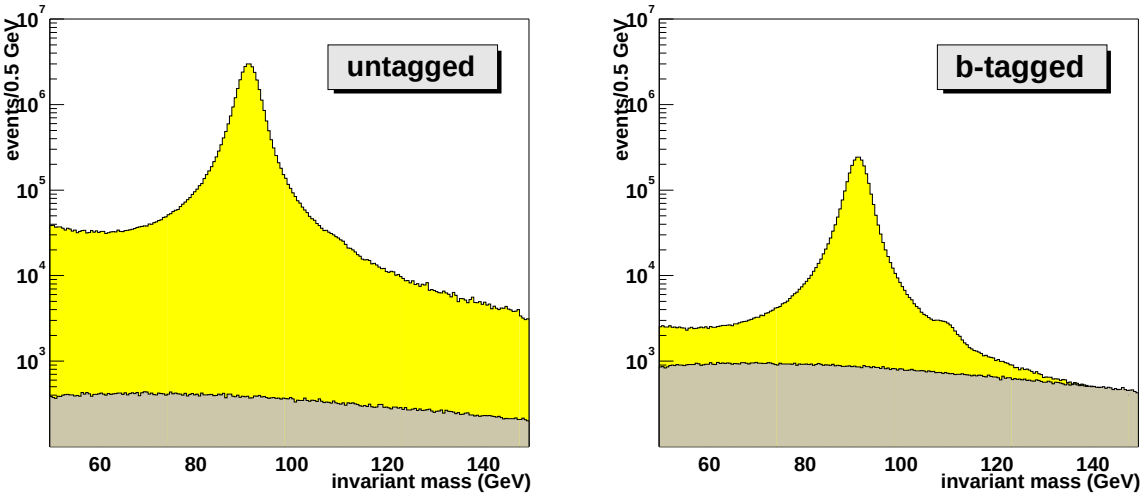

Figure 6.5: *Combined A^0 and h^0 signal superimposed on the background for $m_A = 110\ GeV$, $\tan\beta = 20$. The rightmost figure shows the sample with at least one detected light (non-b) jet, while in the rightmost figure at least one tagged* b*-jet is required. The darker fill area represents the $t\bar{t}$ background.*

In figure 6.5 the invariant mass distribution of muon pairs in both samples are shown for the case $m_A = 110$,$\tan\beta = 20$. As expected, muon pairs from Z^0/γ^* decay clearly dominate both samples. The reference sample receives an important contribution from the Drell-Yan

process. The number of events is an order of magnitude larger than in the b-tagged sample. The Higgs signal, that is present in both samples, is rendered insignificant in the reference sample. Thus, the untagged sample provides an opportunity to determine the properties of the Z^0/γ^* lineshape. This measurement is then used to constrain the background in the signal sample. A slightly different approach, taking advantage of the $Z^0 \to e^+e^-$ sample, is reported in reference [165].

To describe the combined background, a fit function is constructed:

$$f(x) = N_1 \cdot f_V(x; \gamma_L, \gamma_G, m_Z) \cdot \left(\frac{m_Z}{x}\right)^n + \frac{N_2}{x^3} + N_3 \cdot p_3(x) \tag{6.3}$$

where f_V is a pseudo-Voigtian function[1], used to describe the Z^0 line shape. Apart from the normalisation, the pseudo-Voigtian has three free parameters corresponding to the Z^0 mass and natural width and the muon pair invariant mass resolution. The Z^0 shape is tilted slightly by the $\left(\frac{m_Z}{x}\right)^n$ factor to account for the luminosity function - the convolution of the parton density functions of both quarks $f_q(x_1, Q^2) f_q(x_2, Q^2) dx_1 dx_2$. The exponent n is set to 0.9 for light quarks and 1.2 for b-quarks, parametrising the CTEQ5L result of the luminosity function for uds and b-quarks, respectively. The γ^* and interference term are accounted for by the second term. The $t\bar{t}$ background is rather flat and is parametrised by a third degree polynomial. In these last two terms the only free parameter is the normalisation, giving a total of six free parameters.

The signal extraction proceeds as follows:

- The function is fitted to the light jet sample of the leftmost figure of 6.5 with all six parameters free.
- The Z^0-mass, width and detector resolution are fixed to the obtained values, leaving only the three normalisation values to vary freely.
- Then, the function is fitted to the signal sample of the leftmost figure of 6.5 with the three remaining free parameters. For both samples deviations from the fit with respect to the data of up to ~ 5 % remain.
- These deviations can be removed to a large extent by dividing the fit/data result from the b-jet sample by the equivalent histogram for the light jet sample.

Figure 6.6 shows the invariant mass distribution of the signal extracted from the rightmost figure of 6.5. The signal clearly stands out over a flat background.

For the signal of single Higgs boson or the superposition of degenerate A^0 and h^0, a Gaussian is an adequate description for the signal shape. After the fit of the extracted signal, the obtained mass and width are stored. The significance of the signal is estimated from the fit as the normalisation of the function divided by the uncertainty in the normalisation, i.e. $h/\Delta h$.

The procedure - generation of the signal, signal extraction, fitting of the signal shape - is repeated for a mesh of points in parameter space in the range $70 \leq m_A \leq 130$ and $1 \leq \tan\beta \leq 50$.

[1] Approximation to the convolution of a Breit-Wigner and Gaussian, see [166]

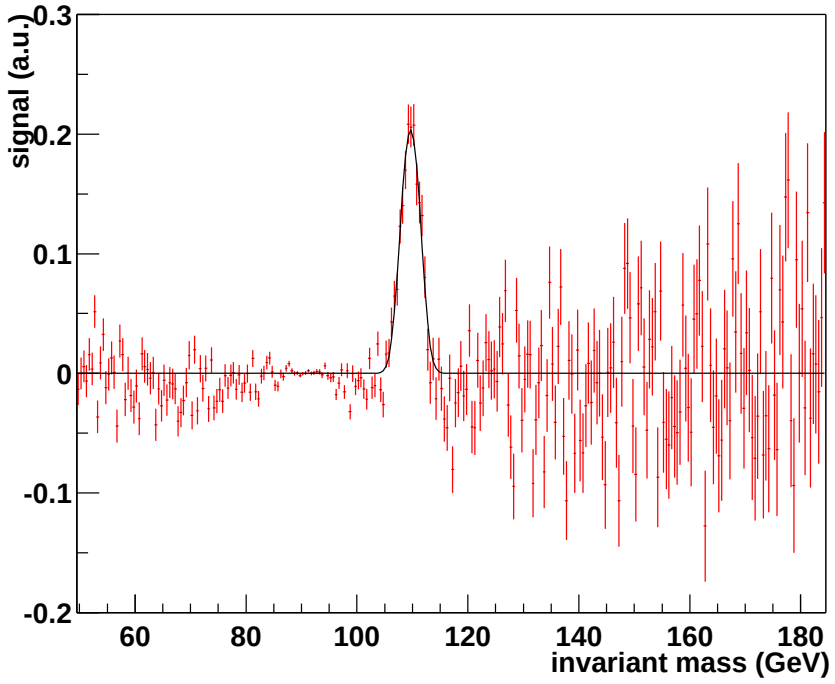

Figure 6.6: *Extracted signal of A^0 and h^0 bosons ($m_A = 110$ GeV, $\tan\beta = 20$). The extraction procedure is described in detail in the text.*

6.3.2 Results

Using the method described in the previous section the signal may be extracted from the background. The ratio of the height of the Gaussian fit to the signal and its error is a measure of the significance of the combined h^0/A^0 signal after three years of high-luminosity running. By explicitly scanning the m_A, $\tan\beta$ space, the ATLAS discovery potential for this channel is determined.

This study is performed entirely within the maximal mixing benchmark scenario. The minimal mixing scenario, with minimal mixing in the top sector and therefore a much lower value for the upper limit on the h^0 mass, is nearly completely excluded by the LEP results. However, it should be noted that other combinations of the MSSM parameters are possible, see [49] for a detailed discussion.

In figures 6.7 the significance of the combined h^0/A^0 signal is estimated using the cross section prediction from the shower approach. An integrated luminosity of 300 fb^{-1} is assumed. The results are shown as contours on the m_A, $\tan\beta$-space in the leftmost figure of 6.7. The same results in terms of m_h are shown in the rightmost figure.

Three significance contours are drawn: the continuous line maps out the combinations of m_A and $\tan\beta$ where $h/\delta h$ is equal to 5. The discovery region, with a confidence level of 5σ or more, is indicated with grey shading. The dashed and dotted lines correspond to $h/\delta h = 10$ and $h/\delta h = 15$, respectively.

A second shaded area shows the region excluded by LEP under the assumption of maximal

mixing. The global lower limit of $\sim 88\ GeV$ for the h^0 and A^0 masses stems from large values of $\tan\beta$. For lower values of $\tan\beta$ the lower limit grows rapidly. In the mass region considered here, values of $\tan\beta$ below $\sim$8 are disfavoured.

Given the shower approach cross-sections and an integrated luminosity of 300 fb^{-1}, the combined h^0/A^0 signal is expected to yield a 5σ discovery only for enhanced Higgs-to-b-quark coupling, i.e. at large $\tan\beta$. The combined h^0/A^0 signal yields a 5 σ discovery limit at a moderate value of $\tan\beta > 10$, whenever m_A is in the range from 105 to 125 GeV. For lower mass values the Z^0 background becomes prohibitive; on the steep slopes of the central Z^0 peak the signal cannot be distinguished. The upper limit on the mass is the result of the MSSM properties; the h^0 and A^0 decouple in this mass limit.

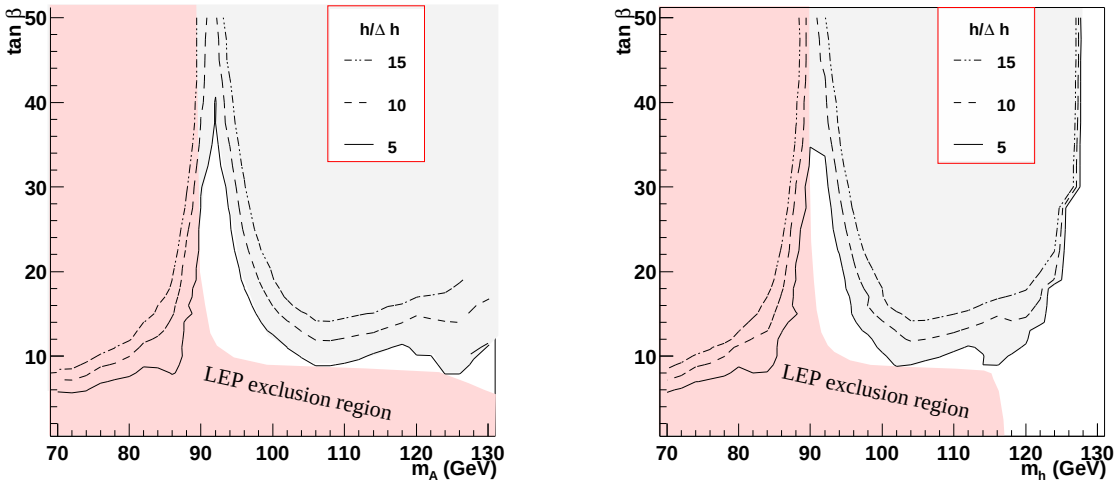

Figure 6.7: *Fit results: the h^0/A^0 significance for an integrated luminosity of 300 fb^{-1}. The shower approach cross-sections are used. In the leftmost figure the contours are shown on m_A, $\tan\beta$ space. In the rightmost figure, the same results are drawn on m_h, $\tan\beta$ space.*

The uncertainty in the production rates has a considerable effect on the outcome of this study. Using the Matrix Element approach (see equation 6.1) to calculate the Z^0 and h^0/A^0 cross sections the predicted significance for an integrated luminosity of 300 fb^{-1} decreases, as shown in figures 6.8. The minimum $\tan\beta$ to yield a 5σ discovery for $105 < m_A < 125$ is thus raised to about 14.

Note that even though matrix element cross sections are used, the efficiencies of the kinematical cuts are taken from the events generated in the shower approach. The softer p_T spectrum in the shower approach leads to a slight underestimate of the event rates for both signal and background. The result given here is therefore somewhat conservative. In reference [165] the same channel is studied entirely in the matrix element framework, with a different approach to the signal extraction. The results for the discovery region are in agreement with the estimate in figure 6.8.

The difference between the results obtained with the shower and matrix element approach is an indication of the systematic uncertainty due to the cross section calculation.

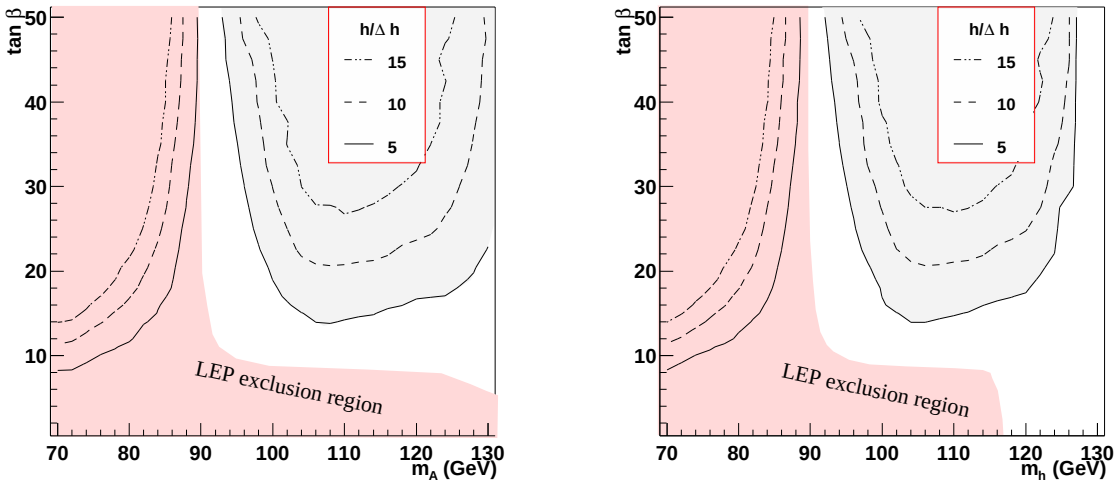

Figure 6.8: *Fit results: the h^0/A^0 significance for an integrated luminosity of 300 fb^{-1}. The Matrix Element approach cross-sections are used. In the leftmost figure the contours are shown on m_A, $\tan\beta$ space. In the rightmost figure, the same results are drawn on m_h, $\tan\beta$ space.*

In either approach, the muonic decay of the lightest MSSM Higgs bosons is expected to yield a significant signal for a low A^0 mass of just over 105 GeV and moderate and large values of $\tan\beta$. This region is favoured by the LEP results. Moreover, the lightest Higgs boson is not visible in any other channel in this region. Thus, the $h^0/A^0 \to \mu^+\mu^-$ can make an important contribution to the coverage of the ATLAS detector for this important region in m_A, $\tan\beta$ space

A narrow band of m_A values between the LEP lower limit of 88 GeV and $\sim$ 105 GeV remains problematic; in this region the minimum value of $\tan\beta$ to yield a 5σ discovery increases rapidly due to the large, steep $Z^0 \to \mu^+\mu^-$ background. For $m_A = m_Z$ a value of $\tan\beta$ as large as 35-40 is needed for a 5 σ discovery (shower approach cross-sections). Assuming the Matrix Element production rates, there is even a narrow region around m_Z where the h^0 cannot be discovered for $\tan\beta < 50$.

6.3.3 Determination of the MSSM parameters

As seen in the previous sections, the $A^0/h^0 \to \mu^+\mu^-$ channel covers a small, but important region of m_A, $\tan\beta$ space. Moreover, the good mass resolution of the di-muon channel could provide valuable information to constrain on the MSSM parameters. In this section the prospect of this channel for a determination of the properties of the Higgs sector are discussed.

Throughout nearly all of the discovery region, the two Higgs boson masses, m_h and m_A are experimentally indistinguishable, see figure 1.5. The observation of two separate signal peaks for the A^0 and h^0 is therefore improbable for $m_A < 125\ GeV$.

The channel studied here is complemented by many other production and decay channels. A relatively large integrated luminosity and/or large value of $\tan\beta$ are needed to discover a

significant signal in the $h^0 \to \mu^+\mu^-$ channel. As far as the lightest Higgs boson is concerned, good coverage of a large fraction of parameter space is provided by Higgs production with associated top quarks in the decay channel to b-quarks. From $m_A \sim 120\ GeV$ upward, the $t\bar{t}h^0 \to t\bar{t}b\bar{b}$ channel is predicted to yield a detectable signal, irrespective of the value of $\tan\beta$, with a luminosity as low as 30 fb^{-1}, see reference [167].

The heavier H^0, on the other hand, could well be observed separately. The $H^0 \to \tau^+\tau^-$ and $H^0 \to \mu^+\mu^-$ decays are expected to provide a significant signal for $\tan\beta > 10\ GeV$ with a relatively small integrated luminosity $\mathcal{O}(30fb^{-1})$, see for example reference [56]. Another possibility is the detection of a charged Higgs boson. For $m_A < 130\ GeV$ and moderate or large values of $\tan\beta$ the $t \to bH^+ \to b\tau^+\nu_\tau$ is likely to be discovered with only 30 fb^{-1} [167].

Thus, the ATLAS detector is expected to discover at least one MSSM Higgs boson irrespective of the values of the MSSM parameters. Moreover, in a large fraction of parameter space, the signal from more than one Higgs boson would be visible [167]. This discovery should provide conclusive evidence to rule out the Standard Model Higgs mechanism. In that case, precision measurements of the Higgs properties are needed to disentangle the possible supersymmetric models and determine their free parameters.

Whenever the h^0 and A^0 masses are degenerate, the center of the combined peak itself forms a measurement of m_A. Provided the signal is significant and the signal does not overlap with the center of the Z^0 peak, neither the signal extraction method nor the mass difference of h^0 and A^0 signals introduce significant systematic offsets in the mass measurement. Thus, the standalone muon channel may be used to determine m_A with a precision well below 1 GeV. The final precision to be achieved depends strongly on the signal rate.

The Higgs-to-b-quark coupling depends strongly on $\tan\beta$. Therefore, the event rate in the associated channel can in principle provide a rather sensitive measurement of $\tan\beta$. However, the interpretation of the rate is prone to systematic errors due to uncertainties in the cross section calculation. Given the uncertainty in the production cross sections of shower and ME approach, discussed in section 6.1.2, an improved theoretical understanding is needed to use the event rate to obtain a precise measurement of $\tan\beta$.

From figure 1.5 the width of the Higgs bosons is seen to become significantly larger than the experimental resolution for values of $\tan\beta > 20$. In this region, the width of the signal peak therefore yields a stringent constraint on $\tan\beta$.

In case the signal from several Higgs bosons is observed, the relation between the Higgs masses is a very strong constraint on the MSSM parameters.

Thus, if the MSSM turns out to be correct, the data from the full 10 years of operation of the ATLAS detector will allow a large number of observables to be measured. The precise determination of the masses and widths of several Higgs bosons will provide severe constraints on the model. On the other hand, the MSSM has a large number of theoretically unconstrained parameters. This situation will require a complex multi-parameter fit to take full advantage of the experimental results. The h^0/A^0 signal height and shape may provide valuable input to such a fit.

6.3.4 Significance estimators

As explained in the previous section, the significance of an A^0/h^0 signal is estimated for a mesh of points in the m_A, $\tan\beta$ plane. In this section, the significance result is compared to more conventional estimators. In many ATLAS physics studies, two estimators are used to determine the significance of a signal in the presence of background:

- For relatively small numbers of signal and noise events, the significance is normally estimated as $S/\sqrt{B}$.
- For very large numbers of background events a second criterium is often added, requiring the S/B ratio to be superior to 1% to account for the uncertainty in the background description.

In figure 6.9 the contours of $S/\sqrt{B}$, S/B and the $h/\Delta h$ from the two fits in m_A, $\tan\beta$ space are compared.

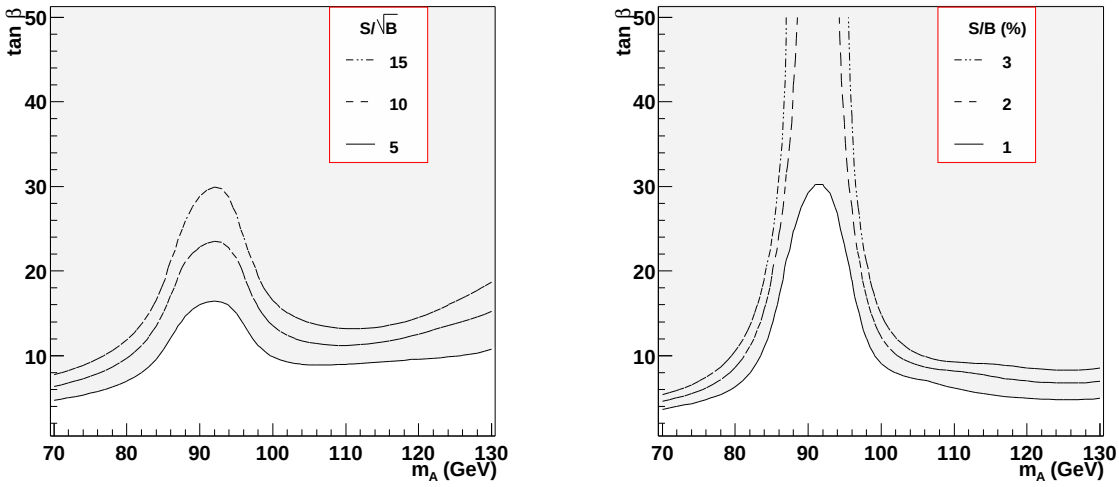

Figure 6.9: *Contours of two conventional significance estimators in m_A, $\tan\beta$ space. In the leftmost figure: $S/\sqrt{B}$, in the rightmost figure: S/B. The shower approach cross-section are used. The integrated luminositity is 300 fb^{-1}. The discovery region in these figures should be compared to figure 6.7*

The significance estimated as $h/\Delta h$, in figure 6.7 coincides with the estimate from $S/\sqrt{B}$ provided that the signal to background ratio is not deteriorated too much, i.e. for m_A not too close to m_Z. In the region around $m_A = m_Z$, where the signal to background ratio falls below 2 %, the $S/\sqrt{B}$ prediction is more optimistic than the explicit fit result. A combined requirement that $S/\sqrt{B} > 5$ and that the signal is at least 2 % of the background gives rather good agreement with $h/\Delta h > 5$.

Thus, the explicit determination of the significance forms an important cross-check of the many ATLAS significance studies based on simple significances ($S/\sqrt{B}$). An additional requirement on the signal-to-background ratio ($S/B > 2\%$) is needed to reproduce the discovery regions obtained by an explicit signal extraction.

6.4 Summary

In a maximal mixing MSSM scenario with values of m_A below 125 GeV, the two lightest Higgs bosons - h^0 and A^0 - are nearly degenerate in mass. Due to the enhanced coupling to b-quarks at large $\tan\beta$ the decay of both Higgs bosons to muons, that is not expected to be observed if the Standard Model is correct, may yield a significant signal.

Two approaches to the cross-section calculation of associated production with b-quarks have been discussed. An explicit calculation of the leading order matrix elements is prone to potentially large higher order corrections (*large logarithms*). An alternative approach factorising the $g \to b\bar{b}$ splitting in the bottom density of the proton and then calculates the cross section for $b\bar{b} \to X$. For the latter approach NLO and even NNLO calculations are available. Its weakness resides in the simplification of the kinematics of the hard process.

Both approaches yield rather distinct cross-section predictions. However, both show a large scale dependence, indicating that higher order corrections are likely to be large. Taking into account the large uncertainty of both predictions, the results are compatible within errors. To study the observability of the $h^0/A^0 \to \mu^+\mu^-$ channel, the cross-section predictions from both approaches are used. The difference between both predictions should be interpreted as the uncertainty on the final result.

A first attempt to extract the signal from the overwhelming Z^0 background is presented. Taking advantage of the similarity of a reference sample, large systematic deviations in the description of the background can be avoided.

With an integrated luminosity of 300 fb^{-1} the combined h^0/A^0 signal is observable only for enhanced Higgs to b-quark coupling, i.e. at large $\tan\beta$. Using the shower approach predictions for the cross section, the combined h^0/A^0 signal would yield a 5 σ discovery whenever m_A is in the range from 105 to 125 GeV and $\tan\beta > 10$. Calculating the cross sections in the Matrix Element approach the predicted minimum $\tan\beta$ increases to 14.

In a narrow region between the LEP lower limit ($\sim$ 88 GeV) and $\sim$105 GeV the minimum value of $\tan\beta$ to yield a 5σ discovery increases rapidly due to the large $Z^0 \to \mu^+\mu^-$ background. For $m_A = m_Z$ a value for $\tan\beta$ as large as 35-40 is needed for a 5 σ discovery (shower approach cross-sections). Assuming the Matrix Element production rates, there is even a narrow region around m_Z where the h^0 cannot be discovered for $\tan\beta < 50$.

The significance found as the $h/\delta h$ of a fit of the signal after signal extraction agrees with the conventional $S/\sqrt{B}$ estimate provided the signal to background ratio does not become too low ($S/B > 2\%$).

If discovered, the excellent di-muon invariant mass resolution provides a stand-alone precision measurements of m_A. This channel is sensitive to the value of $tg\beta$ for large values: $\tan\beta > 20$. More generally, the channel provides important input to a global MSSM fit.

Summary

The Large Hadron Collider (LHC), currently under construction at CERN, will collide two 7 TeV proton beams at a frequency of 40 MHz. Moreover, it is designed to reach a luminosity of $10^{34} cm^{-2} s^{-1}$. The unprecedented beam energy and event rate allow to explore a new regime in high energy physics.

The ATLAS collaboration has designed one of the four experiments to be installed at the interaction points of the LHC. The ATLAS physics program includes any signatures of *new physics* that appear below a scale of several TeV. Focal points of the program are the detection of the Higgs boson and the discovery of supersymmetry. The ATLAS detector will consist of an inner tracker, electromagnetic and hadronic calorimetry and a muon spectrometer.

The Semi-Conductor Tracker (SCT) is to occupy the intermediate radii of the ATLAS tracker. Its goal is to precisely reconstruct the trajectories of the charged particles formed in the collisions. To this end several planes of silicon micro-strip detectors are to accurately measure the 3D position of the particles. Within the SCT collaboration, detectors have been developed to meet the stringent requirements of the ATLAS physics program. A special challenge for the detector is the severe radiation environment in the inner tracker cavity.

Beam tests of prototype microstrip detectors allow to determine the tracking performance of individual detectors. The SCT modules with binary readout are found to satisfy the ATLAS specifications for tracking efficiency and spatial resolution. The dependence of the performance on detector bias voltage, incidence angle and magnetic field is characterized. The (bias voltage-dependent) Lorentz angle is found to agree with model calculations.

To ensure that the lifetime of the detector exceeds the envisaged 10 year operation of the LHC, prototype modules are irradiated to the expected dose. Tests on irradiated module prototypes indicate that an adequate performance is maintained after the flux of radiation expected during the 10 years of operation of ATLAS. The statistical reconstruction of the shaper pulse shows a loss of speed of the front-end. The effect on the ATLAS performance, however, is negligible. The tracking performance of a mini-tracker made up of irradiated final-design SCT modules has been studied. The results confirm that an adequate tracking performance is obtained with SCT modules irradiated to the full fluence expected during 10 years of ATLAS operation.

The performance of the complete inner detector is predicted from single module performance using a detailed Monte Carlo simulation of the physics processes and the layout. In this work the capability of the ATLAS detector to identify jets originating from bottom quarks is studied using samples of $WH \rightarrow q\bar{q}\mu^+\mu^-$ events for two Higgs masses: 120 GeV and 400 GeV.

A significant degradation of the track resolution is found when comparing a recent layout (DC1 geometry) of the detector to the envisaged geometry in 1999. The degradation can be understood from several layout changes that are the result of the new beam pipe design and the insertable layout of the PIXEL detector.

The b-tagging performance of the 2-dimensional likelihood method is severely degraded by these changes. The global rejection of u and c-jets is given by:

$$R_u = 150 \pm 2, \;\; R_c = 10.8 \pm 0.1 \quad \text{for } \epsilon_b = 50\%$$

$$R_u = 54 \pm 1, \;\; R_c = 6.2 \pm 0.1 \quad \text{for } \epsilon_b = 60\%$$

The performance is found to depend strongly on the jet transverse momentum and rapidity. A parametrisation of the dependence is derived.

The effect of *pile-up* during the high-luminosity operation of the LHC is a deterioration of the rejection by ~20 %. A further degradation is expected from channel and module inefficiencies and the uncertainty on the likelihood weights. On the other hand, a significant improvement can be achieved through the application of more sophisticated track quality requirements. Provided the primary vertex can be reconstructed accurately, the 3-dimensional likelihood method offers additional improvement. The expected improvements and deteriorations of the performance are estimated to approximately cancel. Therefore, the results of the 2-dimensional likelihood method are proposed as benchmark values for ATLAS physics studies.

The potential of the ATLAS detector for the discovery of *new* physics is evaluated using Monte Carlo event generators. The response of the detector is taken into account by a *fast* simulation based on a parametrisation of the full detector simulation results.

The minimal supersymmetric extension of the standard model (MSSM) predicts superpartners for all existing particles. Moreover, a Higgs sector consisting of two doublet is expected to exist, giving rise to five physical Higgs bosons. Assuming maximal mixing in the top-sector, the upper limit on the mass of the lightest Higgs boson is 130 GeV.

At high values of the ratio of the vacuum expectation values of the Higgs doublets, the production of the two lightest Higgs boson in association with b-quarks ($gg \to b\bar{b}A^0/h^0$) is strongly enhanced. Thus, decay channels that are not accessible in the Standard Model may yield a detectable signal in the MSSM.

The cross section for Higgs (or Z) production associated with b-jets is highly uncertain. The leading order matrix element calculation suffers from potentially large higher-order corrections. An alternative, the shower approach, uses b-quark densities to calculate the cross section. The kinematical assumptions this implies may lead to an overestimate of the result. The large scale dependence of both calculations confirms this argument.

In this work, the muonic decay channel of light, neutral supersymmetric Higgs bosons is studied. This allows to take advantage of the excellent invariant mass resolution of the muon pair. The ($Z \to \mu^+\mu^-$) background is effectively reduced requiring at least one tagged b-jet. An irreducible background due to $gg \to b\bar{b}Z$ production remains.

A method has been developed to explicitly extract the signal from the irreducible background using the similarity of the Z-lineshape of the tagged and untagged samples. After an integrated luminosity of 300 fb^{-1} the combined signal of the A^0 and h^0 boson yields a significant (5σ) signal in the mass range m_A = 105-125 GeV provided $\tan\beta$ is larger than ~10

($\sim$14 using the matrix element cross sections). Thus, the muon decay covers an important region of m_A, $\tan\beta$ space.

The discovery of several Higgs bosons should be possible throughout a large portion of MSSM parameter space, thus ruling out the standard model Higgs mechanism. If the h^0/A^0 boson signal is discovered in this channel, the excellent di-muon invariant mass resolution can contribute to precise measurement of m_A. A measurement of the width of the signal peak is sensitive to $\tan\beta$, provided its value is larger than 20.

Bibliography

[1] K. Hagiwara et al. (the particle data group). *Review of particle physics. Phys.Rev.* **D 66** (2002).

[2] M.J. Costa Mezquita. *Determination of the* b *quark mass at the M_Z scale with the DELPHI detector at LEP.* PhD thesis, University of Valencia, Spain, 2003.

[3] S. Fukuda et al. (the Super-Kamiokande Collaboration). Deterimination of solar neutrino oscillation parameters using 1496 days of Super-Kamiokande data. *Phys.Lett.* **B 539** (2002) 179–187.

[4] Q.R. Ahmad et al (the SNO collaboration). Direct evidence for neutrino flavor transformation from neutral current interactions in the Sudbury Neutrino Observatory. *Phys.Rev.Lett.* **89** (2002).

[5] M.C. Gonzalez-Garcia et al. Global three neutrino oscillation analysis of neutrino data. *Phys.Rev.* **D 63** (2001).

[6] D. Decamp et al. (the ALEPH collaboration). A precise determination of the number of families with light neutrinos and of the Z boson partial widths. *Phys.Lett.* **B 235** (1990) 399.

[7] B. Adeva et al. (the L3 collaboration). A direct determination of the number of light neutrino families from $e^+e^- \rightarrow$ neutrino anti-neutrino gamma at LEP. *Phys.Lett.* **B 275** (1992) 209–221.

[8] M. Chemarin. Number of neutrino families from LEP1 measurements. *Nucl.Phys.Proc.Suppl.* **85** (2000) 67–71.

[9] P.W. Higgs. Broken symmetries and the masses of gauge bosons. *Phys.Rev.Lett.* **13** (1964) 321.

[10] G. Kane. *Perspectives on Higgs physics.* Advanced series on directions in high energy physics, 2000.

[11] H.B. Thacker B.W. Lee, C. Quigg. Weak interactions at very high-energies: the role of the Higgs boson mass. *Phys.Rev.* **D 16** (1977) 1519.

[12] D.V. Nanopoulos J. R. Ellis, M. K. Gaillard. A phenomenological profile of the Higgs boson. *Nucl.Phys.* **B 106** (1976) 292.

[13] H.B. Thacker B.W. Lee, C. Quigg. The strength of weak interactions at very high-energies and the Higgs boson mass. *Phys.Rev.Lett.* **38** (1977) 883.

[14] Y Shen J. Kuti, L. Lin. Upper bound on the Higgs boson mass in the standard model. *Phys.Rev.Lett.* **61** (1988) 678.

[15] The LEP and SLD electroweak working groups. A combination of preliminary electroweak measurements and constraints on the standard model. (hep-ex/0212036)

[16] The LEP Higgs working group. Search for the standard model Higgs boson at LEP. Submitted to Phys.Lett. **B** (2003).

[17] M. Spira et al. Higgs boson production at the LHC. *Nucl.Phys.* **B 453** (1995) 17–82.

[18] W.J. Stirling R.K. Ellis, B.R. Webber. *QCD and collider physics.* Cambridge University press, 1996.

[19] A. Pich. Aspects of quantum chromodynamics. *Presented at ICTP Summer School in Particle Physics, Trieste, Italy, 7 Jun - 9 Jul, 1999.* (hep-ph/0001118)

[20] G. Altarelli, G. Parisi. Asymptotic freedom in parton language. *Nucl.Phys.* **B 126** (1977) 297.

[21] M. Botje. A QCD analysis of HERA and fixed target structure function data. *Eur.Phys.J.* **C 14** (2000) 285–297.

[22] C. Paus (for the CDF collaboration). Heavy quark production at CDF. *Presented at 31st International Conference on High Energy Physics, Amsterdam, The Netherlands, 24-31 Jul, 2002.* (Fermilab-Conf-02-276-E)

[23] M. Bishai (for the CDF II collaboration). Heavy quark production at CDF. *Presented at 14th Topical Conference on Hadron Collider Physics, Karlsruhe, Germany, 29 Sep - 4 Oct, 2002.* (Fermilab-Conf-02-315-E)

[24] F. Olness. PDF's: what do we need to know? *Presented at the APS / DPF / DPB Summer Study on the Future of Particle Physics (Snowmass 2001), Snowmass, Colorado, 30 Jun - 21 Jul, 2001.* (hep-ph/0112307)

[25] W. Beenakker et al. QCD corrections to heavy quark production in p anti-p collisions. *Phys.Rev.* **D 40** (1989) 54–82.

[26] R. Demina et al. Heavy quark production and PDF's subgroup report. *Presented at the Physics at Run II: QCD and Weak Boson Physics Workshop: 2nd General Meeting, Batavia, Illinois, June, 1999. hep-ph/0005112.*

[27] R. Brock et al. (the CTEQ Collaboration). Handbook of perturbative QCD. *Rev.Mod.Phys.* **67** (1995) 157–248.

[28] H.L. Lai et al. (the CTEQ Collaboration). Global QCD analysis of parton structure of the nucleon: CTEQ5 parton distributions. *Eur.Phys.J.* C12:375–392, 2000.

[29] R.S. Thorne et al. (the MRST collaboration). Update of MRST parton distributions. *Acta Phys.Polon.* **B 33** (2002) 2927–2932.

[30] H. Plothow-Besch. PDFLIB: a library of all available parton density functions of the nucleon, the pion and the photon and the corresponding alpha-s calculations. *Comput.Phys.Commun.* **75** (1993) 396–416.

[31] T. Sjöstrand et al. High-energy physics event generation with PYTHIA 6.1. *Comput.Phys.Commun.* **135** (2001) 238–259.

[32] HERWIG 6: an event generator for hadron emission reactions with interfering gluons (including supersymmetric processes). G. Corcella et al. *JHEP* **0101** (2001). and references therein, especially: B. R. Webber, *Ann.Rev.Nucl.Part.Sci.* **B 238** (1986) 253.

[33] G. Kane. *Supersymmetry.* Perseus Publishing, 1997.

[34] J. Wess, J. Bagger. *Supersymmetry and supergravity.* Princeton series in physics, 1992.

[35] S. Ferrara. *Supersymmetry.* World Scientific, 1987.

[36] J. Mandula, S. R. Coleman. All possible symmetries of the S matrix. *Phys.Rev.* **159** (1967) 1251–1256.

[37] N. De Filippis (for the LEP collaborations). Search for supersymmetry at LEP. *Acta Phys.Polon.* **B 33** (2002) 3881–3886.

[38] S. Ask. A review of the supersymmetry searches at LEP. *Presented at the 38th Rencontres de Moriond on Electroweak Interactions and Unified Theories, Les Arcs, France, 15-22 March, 2003.* (hep-ex/0305007)

[39] G. Sguazzoni. SUSY particles searches at LEP and interpretations within the MSSM. *Presented at the 31st International Conference on High Energy Physics, Amsterdam, The Netherlands, 24-31 July, 2002.* (hep-ex/0210022)

[40] R. Haas (for the CDF Collaboration). Search for SUSY with missing transverse energy and jets at CDF. *Int.J.Mod.Phys.* **A16S1B** (2001) 793–796.

[41] J.F. Gunion, H. E. Haber. Higgs bosons in supersymmetric models. *Nucl.Phys.* **B 272** (1986) Erratum-ibid. **B 402** (1993) 567-569.

[42] E. Richter-Waş et al. Minimal supersymmetric standard model Higgs rates and backgrounds in ATLAS. *ATLAS internal note*, ATL-PHYS-96-74.

[43] Z. Kunszt, F. Zwirner. Testing the Higgs sector of the minimal supersymmetric standard model at large hadron colliders. *Nucl.Phys.* **B 385** (1992) 3–75.

[44] J. D. Wells G. L. Kane, C. F. Kolda. Calculable upper limit on the mass of the lightest Higgs boson in any perturbatively valid supersymmetric theory. *Phys.Rev.Lett.* **70** (1993) 2686–2689.

[45] Ralf Hempfling Howard E. Haber. Can the mass of the lightest Higgs boson of the minimal supersymmetric model be larger than M_z? *Phys.Rev.Lett.* **66** (1991) 1815–1818.

[46] M. Carena et al. Analytical expressions for radiatively corrected Higgs masses and couplings in the MSSM. *Phys.Lett.* **B 355** (1995) 209–221.

[47] M. Carena et al. Reconciling the two loop diagrammatic and effective field theory computations of the mass of the lightest CP-even Higgs boson in the MSSM. *Nucl.Phys.* **B 580** (2000) 29–57.

[48] M. Carena et al. Suggestions for improved benchmark scenarios for Higgs-boson searches at LEP2. *Presented at the Workshop on New Theoretical Developments for Higgs Physics, Geneva, Switzerland, 27 Oct, 1999.* (hep-ph/9912223)

[49] M. Carena et al. Suggestions for benchmark scenarios for MSSM Higgs-boson searches at hadron colliders. *Eur.Phys.J.* **C 26** (2003) 601–607.

[50] The LEP Higgs working group. Searches for the neutral Higgs bosons of the MSSM: preliminary combined results using LEP data collected at energies up to 209 GeV. (hep-ex/0107030)

[51] A. Heister et al. (the ALEPH collaboration). Final results of the searches for neutral Higgs bosons in e^+e^- collisions at $\sqrt{s}$ up to 209 GeV. *Phys.Lett.* **B 526** (2002) 191–205.

[52] J. Abdallah et al. (the DELPHI collaboration). Searches for neutral Higgs bosons in e^+e^- collisions from $\sqrt{s} = 191.6$ to 201.7 GeV. *Eur.Phys.J.* **C 23** (2002) 409–435.

[53] J. G. Wacker. Little Higgs models: new approaches to the hierarchy problem. *Presented at the 31st International Conference on High Energy Physics, Amsterdam, The Netherlands, 24-31 Jul, 2002.* (hep-ph/0208235).

[54] I. Hinchliffe L. Vacavant. Model independent extra dimension signatures with ATLAS. *ATLAS internal note*, ATL-PHYS-2000-016, 2000.

[55] I. Hinchliffe L. Vacavant. Signals of models with large extra dimensions in ATLAS. *ATLAS internal communication*, ATL-COM-PHYS-2001-006, also published as*J. Phys.* **G 27** (2001) 1839-50.

[56] The ATLAS Collaboration. ATLAS detector and physics performance technical design report. Technical report, CERN, 1999.

[57] T. Lari. Study of silicon pixel sensors for the ATLAS detector PhD thesis, University of Milan, Italy, 2001.

[58] T. Lari et. al. Lorentz angle variation with electric field for ATLAS silicon detectors. *ATLAS internal note*, ATL-INDET-2001-004.

[59] I. Gorelov et al. Electrical characteristics of silicon pixel sensors. *ATLAS internal note*, ATL-INDET-2001-011.

[60] The ATLAS collaboration. ATLAS inner detector technical design report. Technical report, CERN, 1997.

[61] T. Akesson et. al. (the TRT collaboration). Tracking performance of the transition radiation tracker prototype for the ATLAS experiment. *Nucl.Instr.Meth.* **A 485** (2002) 298–310.

[62] T. Akesson et. al. (the TRT collaboration). Electron identification with a prototype of the transition radiation tracker for the ATLAS experiment. *Nucl.Instr.Meth.* **A 412** (1998) 200–215.

[63] The ATLAS collaboration. Technical proposal for a general purpose pp experiment at the large hadron collider at CERN. Technical report, CERN, 1994.

[64] The ATLAS collaboration. ATLAS liquid argon calorimeter technical design report. Technical report, CERN, 1996.

[65] The ATLAS collaboration. ATLAS calorimeter performance technical design report. Technical report, CERN, 1996.

[66] A.L. Maslennikov. Test beam results of the ATLAS electromagnetic calorimeter prototype modules. *Nucl.Instr.Meth.* **A 494** (2002) 346–354.

[67] The ATLAS collaboration. ATLAS tile calorimeter technical design report. Technical report, CERN, 1996.

[68] B. Dowler et al. Performance of the ATLAS hadronic end-cap calorimeter in beam tests. *Nucl.Instr.Meth.* **A 482** (2002) 94–124.

[69] J. Budagov et al. Electron and pion calibration of the atlas tilecal modules (september 2001 testbeam). *ATLAS internal note*, ATL-TILECAL-2003-005.

[70] The ATLAS collaboration. ATLAS muon spectrometer technical design report. Technical report, CERN, 1997. updated version under: /afs/cern.ch/atlas/www/GROUPS/MUON/newTDR/version_0.

[71] G. Avolio et. al. First results of the 2001 MDT chambers beam test. *ATLAS internal note*, ATL-MUON-2003-001.

[72] The ATLAS collaboration. ATLAS HLT, DAQ and DCS technical proposal. Technical report, CERN, 2000.

[73] The ATLAS collaboration. ATLAS level 1 trigger technical design report. Technical report, CERN, 1998.

[74] The ATLAS collaboration. ATLAS trigger performance status report. Technical report, CERN, 1998.

[75] The ATLAS collaboration. ATLAS DAQ, EF,LVLE2 and DCS technical progress report. Technical report, CERN, 1998.

[76] S. George for the ATLAS collaboration. Design and expected performance of the ATLAS trigger and event selection. *Eur. Phys. J. direct* **C4S1** (2002).

[77] Gerold W.Neudeck. *The PN Junction Diode*, volume II. Addison-Wesley Publishing Company.

[78] W.R. Leo. *Techniques for nuclear and particle physics.* Springer, 1987.

[79] L. Landau. *J. Phys. (USSR)*, **201** (1944).

[80] M. Hansroul et al., GEANT: Simulation program for particle physics experiments. User guide and reference manual. *CERN internal note*, CERN-DD-78-2-REV, 1978.

[81] G. Hall. Ionisation energy losses of highly relativistic charged particles in thin silicon layers. *Nucl.Instr.Methods* **220** (1984) 356–362.

[82] K. Lassila-Perini, L. Urban. Energy loss in thin layers in GEANT. *Nucl.Instr.Meth.* **A 362** (1995) 416-422.

[83] S.Agostinelli et. al. GEANT4 collaboration. GEANT4: a simulation toolkit. *CERN internal note*, CERN-IT-2002-003, 2002.

[84] E. Belau et. al. Charge collection in silicon strip detectors. *Nucl.Instr.Meth.* **214** (1983) 253.

[85] G. Lindstrom F. Lemeilleur, S. Watts. Third RD48 status report. (CERN-LHCC-2000-009).

[86] G. Lindstrom et al. Developments for radiation hard silicon detectors by defect engineering - results by the CERN RD48 (ROSE) collaboration. *Nucl.Instr.Meth.* **A 465** (2000) 60–69.

[87] K. Gill et al. Radiation damage by neutrons and photons to silicon detectors. *Nucl.Instr.Meth.* **A 322** (1992) 177–188.

[88] J.A.J. Matthews et. al. Bulk radiation damage in silicon detectors and implications for ATLAS SCT. *ATLAS internal note*, ATL-INDET-95-118.

[89] T. Kohriki et al. First observation of thermal runaway in the radiation damaged silicon detector. *IEEE Trans.Nucl.Sci.* **43** (1996) 1200.

[90] S. Marti i Garcia et al. A model of charge collection for irradiated p^+n detectors. *Nucl.Instr.Meth.* **A 473** (2001) 128-135.

[91] G. Casse et. al. Comparison between ATLAS forward microstrip detectors made on 6" $\langle 100 \rangle$ and 4" $\langle 111 \rangle$ crystal oriented silicon wafers. *Nuovo Cim.* **112A** (1999) 1253-1259.

[92] T.Akimoto et al. Characteristics of irradiated silicon microstrip detectors with ⟨100⟩ and ⟨111⟩ substrates. *Nucl.Instr.Meth.* **A 466** (2001) 354–358.

[93] T.J. Brodbeck et. al. Carrier mobilities in irradiated silicon. *Presented at the5th Conference on Position Sensitive Detectors, London, September, 1999.* (ROSE/TN/2000-09).

[94] D. Robinson et al. Comparison of signals obtained from oxygenated and non-oxygenated silicon microstrip detectors after irradiation to 3 x 10**14-p/cm**2. *Nucl.Instr.Meth.* **A 461** (2001) 226–228.

[95] A. Seiden J. Leslie, Y. Unno. Signal simulation for double-sided silicon strip detectors. (SCIPP 92/61).

[96] R. Muller, T. Kamins. Device electronics for integrated circuits. *Wiley*, 1986.

[97] S. Ramo. Currents induced by electron motion. *Proc. IRE*, **27(9)** (1939) 584.

[98] M. Dentan et al. A mixed analog digital radiation hard technology for high- energy physics electronics: DMILL (durci mixte sur isolant logico-lineaire): R & D proposal. (CERN-DRDC-92-31).

[99] P. Borgeaud et al. DMILL: A mixed analog - digital radiation hard technology for high-energy physics electronics: Status report project RD29. (CERN-DRDC-93-45, CERN/LHCC 97-15).

[100] M. Dentan et al. DMILL (durci mixte sur isolant logico-lineaire): A mixed analog-digital radiation hard technology for high energy physics electronics. *Nucl.Phys.Proc.Suppl.* **32** (1998) 530–534.

[101] Y. Hu, A. Loge, W. Dulinski. A low noise, low power biCMOS preamplifier-shaper for microstrip detectors using DMILL process and irradiation measurements. *Nucl.Instr.Meth.* **A 423** (1999) 272–281.

[102] F. Anghinolfi et al. Development of front-end electronics for silicon strip detectors using the DMILL bicCMOS rad-hard process. *Presented at the 2nd Workshop on Electronics for LHC Experiments, Balatonfured, Hungary, 23-27 Sep, 1996.*

[103] J. Kaplon et al. DMILL implementation of the analogue readout architecture for position sensitive detectors at LHC experiments. *Presented at the 4th Workshop on Electronics for LHC Experiments, Rome, Italy, 21-25 Sep, 1998.*

[104] *ABCD3T ASIC Project Specification Version 1.1.*

[105] W. Dabrowski et al. A single chip implementation of the binary readout architecture for silicon strip detectors in the ATLAS silicon tracker. *Presented at the 3rd Workshop on Electronics for LHC Experiments, London, England, 22-26 Sep, 1997.*

[106] W. Dabrowski et. al. Progress in development of the readout chip for the ATLAS semiconductor tracker. *Presented at the 6th Workshop on Electronics for LHC Experiments, Cracow, Poland, 11-15 Sep, 2000.*

[107] W. Dabrowski et al. Design and performance of the abcd chip for the binary readout of silicon strip detectors in the ATLAS semiconductor tracker. *IEEE Trans.Nucl.Sci.* **47** (2000) 1843–1850.

[108] W. Dabrowski et. al. Radiation hardness of the ABCD chip for the binary readout of silicon strip detectors in the ATLAS semiconductor tracker. *Presented at the 5th Workshop on Electronics for the LHC Experiments, Snowmass, Colorado, 20-24 Sep, 1999.*

[109] W. Dabrowski. Readout electronics for the ATLAS semiconductor tracker. *Nucl.Instr.Meth.* **A 386** (1997) 117–121.

[110] F. Anghinolfi et.al. SCTA - a rad-hard biCMOS analogue readout ASIC for the ATLAS semiconductor tracker. IEEE Trans.Nucl.Sci. **44** (1997) 298–302.

[111] T. Ohsugi et. al. Microdischarges of AC coupled silicon strip sensors. *Nucl.Instr.Methods* **A 342** (1994) 22–24.

[112] J. Bernabeu et. al. Measurements of the temperature dependence of the calibration circuit and input noise. private communication.

[113] The SCT end-cap collaboration. Final design report of the end-cap module. *ATLAS internal report* (ATL-IS-EN-009)

[114] S.J.M Peeters. Alignment of the ATLAS precision tracker using tracks. *ATLAS internal communication*, ATL-COM-INDET-99-007.

[115] A. Clark et al. Thermal performance of the ATLAS SCT forward modules. *ATLAS internal communication*, ATL-COM-INDET-2003-010.

[116] M.Vos et. al. A study of the tracking performance of irradiated SCT prototypes using beam test data. *ATLAS internal note*, ATL-INDET-2003-003.

[117] M.Vos et. al. Charge collection with binary readout from a test beam perspective. *ATLAS internal note*, ATL-INDET-2003-011.

[118] A. Barr et. al. Beamtests of ATLAS SCT modules in august and october 2001. *ATLAS internal note*, ATL-INDET-2002-024, 2002.

[119] Y. Unno et. al. Beamtest of non-irradiated and irradiated ATLAS SCT microstrip modules at KEK. *IEEE Trans.Nucl.Sci.* **49** (2002) 1868-1875.

[120] J. Bernabeu et. al. Beam study of irradiated ATLAS-SCT module prototypes. *Nucl.Instr.Meth.* **A 485** (2002) 67-72

[121] A. Barr et. al. Beamtests of ATLAS SCT modules in june and august 2000. *ATLAS internal note*, ATL-INDET-2002-005, 2002.

[122] J. Bernabeu et. al. Results of the 1999 H8 beam tests of ATLAS-SCT prototypes. *ATLAS internal note*, ATL-INDET-2000-004, 2000.

[123] J. Bernabeu et. al. Results of the 1999 H8 beam tests of ATLAS-SCT prototypes.

[124] F. Albiol et al. Beam test of the ATLAS silicon detector modules. *Nucl.Instr.Meth.* **A 409** (1998) 236–239.

[125] F. Albiol et al. Beam test of the ATLAS silicon detector modules with binary readout in the CERN H8 beam in 1996. *ATLAS internal note*, ATL-INDET-96-153.

[126] F. Albiol et al. Beam test results on a prototype SCT module using CSEM detectors. *ATLAS internal note*, ATL-INDET-97-175.

[127] J. deWitt et al. Beam test of the binary silicon system in H8 in september 1995. *ATLAS internal note*, ATL-INDET-96-135.

[128] F. Albiol et al. Performance of the ATLAS silicon strip detector modules *Nucl.Instr.Meth.Phys.* **A 403** (1998) 247–255.

[129] H. F. W. Sadrozinski et al. Monitoring the performance of silicon detectors with binary readout in the ATLAS beam test. *Nucl.Instr.Meth.* **A 383** (1996) 245–251.

[130] J. Morris. SCT barrel test box. http://hepwww.ph.qmw.ac.uk/ morris/qmweng.html.

[131] L. Sospedra. SCT forward test box. http://ific.uv.es/.

[132] J.E. Garcia Navarro et. al. Beamtests of ATLAS SCT modules in 2002. *ATLAS internal note in preparation*

[133] C. Leroy et. al. Charge transport in non-irradiated and irradiated silicon detectors. at the IEEE Nuclear Science Symposium and Medical Imaging Conference, Toronto, Ontario, Canada, 8-14 Nov 1998. (CERN-OPEN-99-007)

[134] L.J. Beattie et. al. The electric field in irradiated silicon detectors. *Nucl.Instr.Meth.* **A 418** (1998) 314–321.

[135] V. Bartsch et. al. An algorithm for calculating the Lorentz angle in silicon detectors. *CMS internal note*, CMS IN-2001/027.

[136] V. Eremin, Z. li. Carrier drift mobility study in neutron irradiated high purity silicon. *Nucl.Inst.Meth.* **A 362** (1995) 338–43.

[137] S. Gadomski. Model of the SCT detectors and electronics for the ATLAS simulation using GEANT4. *ATLAS internal note*, ATL-SOFT-2001-005, 2001.

[138] P. Reznicek. *Test of semiconductor microstrip detectors of ATLAS detector.* PhD thesis, Charles University of Prague, 2003.

[139] A. Barr et. al. Results from an LHC structured beam test on SCT module prototypes. *ATLAS internal note*, ATL-INDET-2002-025.

[140] R. Hawkings The ATLAS inner detector and flavour tagging performance. *ATLAS scientific note*, SN-ATLAS-2003-026

[141] S. Gonzalez de la Hoz, E. Ros, M. Vos. A comparative study of the ATLAS b-tagging performance between the Physics TDR layout and the DC1 layout using WH events. *ATLAS internal note in preparation.*

[142] N.A. mcCubbin. Data challenges. ATL-ENEWS-2001-094.

[143] D. Froidevaux E. Richter-Waş, L. Poggioli. ATLFAST: 2.0 a fast simulation package for ATLAS. *ATLAS internal note*, ATL-PHYS-98-131.

[144] J.B. de Vivie. private communication.

[145] V. Kostiouchine. private communication.

[146] E. Ros S. Gonzalez, M. Vos. Analysis of the process pp $\rightarrow$ bbh/A $\rightarrow$ bbmumu in the MSSM with mA $<$ 125 GeV *ATLAS internal note*, ATL-PHYS-2002-021.

[147] E. Ros S. Gonzalez, M. Vos. On the simulation of $Zb\bar{b}$ and $Hb\bar{b}$ events at LHC. *ATLAS internal note*, ATL-PHYS-2002-028.

[148] M. Carena et al. Report of the tevatron Higgs working group. (hep-ph/0010338).

[149] D. Cavalli et al. The Higgs working group: summary report. *Presented at the Workshop on Physics at TeV Colliders, Les Houches, France, 21 May - 1 Jun, 2001.* (hep-ph/0203056).

[150] D. Dicus et al. Higgs-boson production in association with bottom quarks at next-to-leading order. *Phys.Rev.* D59, 1999.

[151] R. Kleiss B. van Eijk. On the calculation of the exact g g $\rightarrow$ Z b anti-b cross-section including Z decay and b quark mass effects. *Presented at the Large Hadron Collider workshop, Aachen, Germany, July, 1991.* (CERN-90-10-B)

[152] W. Beenakker et al. NLO QCD corrections to t anti-t h production in hadron collisions. *Nucl.Phys.* **B 653** (2003) 151–203.

[153] W. Beenakker et al. Higgs radiation off top quarks at the tevatron and the LHC. *Phys.Rev.Lett.* **87** (2001).

[154] B. Plumper. *NLO QCD corrections to Higgs radiation of heavy quarks.* PhD thesis, Hamburg University, 2001.

[155] W.B. Kilgore R.V. Harlander. Techniques for NNLO Higgs production in the standard model and the MSSM. *Presented at 38th Rencontres de Moriond on QCD and High-Energy Hadronic Interactions, Les Arcs, Savoie, France, 22-29 Mar, 2003.* (hep-ph/0305204).

[156] W.B. Kilgore R.V. Harlander. Higgs boson production in bottom quark fusion at next-to-next-to leading order. (hep-ph/0304035).

[157] L. Wackeroth L. Reina, S. Dawson. Associated Higgs boson production with heavy quarks at hadron collider: impact of NLO results. *Presented at the APS / DPF / DPB Summer Study on the Future of Particle Physics (Snowmass 2001), Snowmass, Colorado, 30 Jun - 21 Jul, 2001.* (hep-ph/0110299).

[158] S. Dawson et al. NLO QCD predictions for associated t anti-t h production in hadronic collisions. *Phys.Rev.* D67 ,2003.

[159] M. Krämer. Associated Higgs production at hadron colliders. *Presented at the 2003 Les Houches workshop, France, 2003.*

[160] M. Spira et al. The HQQ code for the calculation of the matrix element for $gg \to hqq$.

[161] B.P. Kersevan, E. Richter-Waş. The $gg, q\bar{q} \to z/\gamma^*(\to ll)b\bar{b}$ processes: matrix element implementation to pythia 6.1. *ATLAS internal note*, ATL-PHYS-2001-021.

[162] A. Djouadi et al. HDECAY: a program for Higgs boson decays in the standard model and its supersymmetric extension. *Comput.Phys.Commun.* **108** (1998) 56–74. (hep-ph/9704448).

[163] T. Sjostrand G. Miu. W production in an improved parton shower approach. *Phys.Lett.* **B 449** (1999) 313–320.

[164] G. Miu. A matrix element based modification of the parton shower. (hep-ph9804317).

[165] P. Violini S. Gentile, M. Paniccia. Search for supersymmetric neutral Higgs h in the decay $\to mu^+mu^-$ in ATLAS detector at LHC. *ATLAS internal note*, ATL-PHYS-2003-013.

[166] D.E. Cox P. Thomson, J.B. Hastings. *J.Appl.Cryst.* **20**, 1987.

[167] F. Gianotti. Higgs physics at LHC. *Presented to the LHCC, july, 2000.*

Samenvatting

De *Large Hadron Collider* (LHC), die op dit moment gebouwd wordt in het CERN, zal twee bundels van 7 TeV protonen met elkaar in botsing brengen. Botsingen zullen elke 25 ns plaatsvinden, zodat een totale luminositeit van $10^{34} cm^{-2} s^{-1}$ bereikt kan worden. Met deze ongekende botsingsenergie en luminositeit verkent de LHC een nieuw gebied in de hoge-energie-fysica.

In de interactiepunten van de LHC zullen vier experimenten geïnstalleerd worden. Een van de twee polyvalente detectoren is ontworpen door de ATLAS collaboratie. Het experimentele programma bestrijkt het energie gebied tot enkele TeV. Speciale aandacht gaat uit naar de detectie van het Higgs boson en de ontdekking van supersymmetrie. De ATLAS detector bestaat uit een sporen- en vertex detector (de *inner tracker*), electromagnetische en hadronische calorimeters en een muon spectrometer.

De SemiConductor Tracker (SCT) vormt de middelste laag van de ATLAS *inner tracker*. Het doel van de SCT is de reconstructie van de sporen van de geladen deeltjes die worden gevormd in de botsingen. Het gebruik van meerdere lagen silicium micro-strip detectoren geeft verscheidene precisie 3D positiemetingen langs het spoor van het deeltje. Binnen de SCT collaboratie zijn detectoren ontwikkeld die voldoen aan de strenge eisen die volgen uit het ATLAS fysica programma. Het detector-ontwerp moet bestand zijn tegen de hoge stralingsniveaus in het volume van de tracker.

Prototypes van micro-strip detectoren zijn getest in een deeltjesbundel uit een versneller om de spoor-reconstructie capaciteit vast te stellen. Metingen aan SCT modulen met binaire uitlezing geven aan dat dit ontwerp aan de ATLAS specificaties voor efficiëntie en positie resolutie voldoet. De afhankelijkheid van de spoor-reconstructie capaciteit van de detector voedingsspanning, de invalshoek en het magnetische veld is in detail bestudeerd. De gemeten (spannings-afhankelijkheid van de) Lorentz hoek komt overeen met model-berekeningen.

Tests van bestraalde prototypen laten zien dat een adequate werking behouden blijft, zelfs na een dosis zoals die verwacht wordt tijdens de 10 jaar dat ATLAS operationeel zal zijn. De statistische reconstructie van het signaal na versterking laat zien dat de *front-end* trager wordt na bestraling. Het effect op de track reconstructie in ATLAS is echter verwaarloosbaar. Een studie van een mini-tracker, bestaande uit vier bestraalde SCT modulen, laat zien dat efficiënte spoor-reconstructie mogelijk is.

Voorspellingen over de werking van de volledige sporen-detector worden geëxtrapoleerd uit de werking van enkele modulen middels een gedetailleerde Monte Carlo simulatie van de fysische processen in de detector en de detector-geometrie. In dit proefschrift wordt de capaciteit van de ATLAS detector om *jets* die van *bottom quarks* stammen te identificeren bestudeerd (b-selectie) voor gesimuleerde $WH \rightarrow q\bar{q}\mu^+\mu^-$ *events*.

De spoor-resolutie van het huidige ontwerp (DC1 geometrie) is achteruit gegaan in vergelijking met de oorspronkelijk voorziene geometrie (ten tijde van de physics TDR in 1999). De achteruitgang kan worden verklaard uit de veranderingen in het detector ontwerp, met name het nieuwe ontwerp van de bundelpijp en de PIXEL detector.

De b-identificatie capaciteit met een 2-dimensionale *likelihood* methode is aanzienlijk verminderd in het nieuwe ontwerp. De globale onderdrukking van u en c-jets wordt gegeven:

$$R_u = 150 \pm 2, \;\; R_c = 10.8 \pm 0.1 \quad \text{voor } \epsilon_b = 50\%$$

$$R_u = 54 \pm 1, \;\; R_c = 6.2 \pm 0.1 \quad \text{voor } \epsilon_b = 60\%$$

De prestaties van de detector zijn sterk afhankelijk van de transverse impuls en de rapiditeit van de *jet*. Een parametrisatie van de gevonden afhankelijkheid is bepaald.

Het effect van *pile-up* vanwege de hoge luminositeit in de LHC leidt tot een vermindering van de discriminatie van u,d,s-jets met $\sim$20 %. De prestaties zullen verder worden aangetast door inefficiënte kanalen en modulen en de onzekerheid in de gewichten van de *likelihood* methode. Aan de andere kant wordt een aanzienlijke verbetering van de b-selectie verkregen door het toepassen van meer geavanceerde spoor-selectie criteria. Indien het botsingspunt van de bundels precies gereconstrueerd kan worden, kan de 3-dimensionale b-selectie methode gebruikt worden, hetgeen leidt tot een extra verbetering. De verwachte verbeteringen en verslechteringen van de b-tag capaciteit ten opzichte van de 2D methode op de perfecte detector simulatie heffen elkaar ongeveer op. Daarom wordt voorgesteld deze resultaten te gebruiken als *benchmark* waarden in ATLAS studies.

Het potentieel van de ATLAS detector om *nieuwe* fysica te ontdekken wordt bestudeerd door middel van Monte Carlo *event* generatoren. De respons van de detector wordt hier in aanmerking genomen middels een parametrisatie (*fast simulation*) van de gedetailleerde simulatie (*full simulation*) van de detector.

De minimale supersymmetrische uitbreiding van het standaard model (MSSM) voorspelt het bestaan van superpartners voor alle bestaande deeltjes. Bovendien voorspelt het model een Higgs sector met twee doubletten, wat leidt tot vijf fysieke Higgs bosonen. Onder de aanname dat de menging in de top-sector maximaal is, is de bovengrens voor de massa van het lichtste Higgs boson 130 GeV.

Grote waarden van de verhouding van de vacuumverwachtingswaarden van de Higgs doubletten leiden tot een sterke toename van de productie van de twee lichtste Higgs bosonen samen met bottom quarks ($gg \rightarrow b\bar{b}A/h$). Zodoende kunnen kanalen, die niet of moelijk te detecteren zijn in het standaard model, in het MSSM een significant signaal opleveren.

De werkzame doorsnede voor Higgs of Z productie met b-jets is hoogst onzeker. De eerste-orde matrix element berekening heeft te leiden onder potentieel grote hogere-orde correcties. Een alternatieve aanpak, de zogenaamde *shower* berekening, gebruikt de b-quark dichtheid om de werkzame doorsnede te berekenen. De kinematische aanname impliciet in deze aanpak kan mogelijk leiden tot een overschatting van het resultaat. De sterke schaalafhankelijkheid van beide berekeningen levert een bevestiging voor dit argument.

In dit proefschrift wordt het muon-verval van lichte, neutrale, super-symmetrische Higgs bosonen bestudeerd. Dit kanaal benut de uitstekende invariante massa resolutie van de ATLAS detector voor muon-paren. De $Z \rightarrow \mu^+\mu^-$ achtergrond wordt aanzienlijk gereduceerd

door minstens één b-tag in de eindtoestand van de botsing te eisen. Een onreduceerbare achtergrond ten gevolge van $gg \to b\bar{b}Z$ productie blijft echter bestaan.

Een methode is ontwikkeld waarmee het Higgs signaal expliciet wordt geextraheerd uit de achtergrond. De verzameling *gebeurtenissen* zonder geselecteerde b-jet wordt gebruikt om de vorm van de achtergrond te bepalen. Met een geintegreerde luminositeit van 300 fb^{-1} geeft een combinatie van h^0 en A^0 gebeurtenissen een significant (5σ) signaal in het massa interval van $m_A = 105$ - $125\ GeV$ indien $\tan\beta$ groter is dan $\sim$10 ($\sim$14 indien matrix element werkzame doorsneden gebruikt worden).

De ontdekking van meer dan één Higgs boson is mogelijk in een groot deel van de MSSM parameter ruimte. Deze meting zou aantonen dat het standaard model Higgs mechanisme niet compleet is. Als het h/A boson in dit kanaal gevonden wordt, kan de uitstekende dimuon resolutie bijdragen aan een preciese bepaling van m_A. De meting van de breedte van het Higgs signaal is gevoelig voor $\tan\beta$, indien deze een waarde groter dan 20 heeft.

Acknowledgements

Many people have in some way or other contributed to the realization of this thesis.

First, I have to thank my supervisors. Juan Fuster offered me the opportunity to carry out the research that has gone into this thesis. He has known how to leave to work freely, without ever feeling lost or on my own. Bob van Eijk accepted to be my thesis supervisor. He has been very efficient in proof-reading the first (sometimes very rough) versions and catching loose ends.

Eduardo Ros has guided my first steps in the marvellous world of b-tagging and supersymmetric Higgs physics (chapters 5 and 6 are dedicated to him). Elzbieta Richter-Was, as convenor of the Higgs working group, has been the driving force behind the Higgs analysis.

In the beam tests, I've worked together with a great group of people: the SCT TB team. Gareth Moorhead has been a very easy-going test beam coordinator. Not only has he inspired the TB team during working hours, but he has also been able to organize the world-famous test beam outings. Javier Sanchez was my first test beam mentor. Jose Enrique Garcia probably suffered me most. Gabriela Llosa has had her share of test beam work and I hope Sergio Gonzalez will be able to continue. Monica D'Onofrio has been very good at pointing out errors in my offline, analysis, notes etc., and has helped to keep the test beams exciting these last years. Lars Eklund and Alan Barr have been a lot of fun to be around. I would like to thank the Czechs (Zdenek, Peter K., Pavel) for a very nice collaboration.

I would like to thank the people at IFIC Valencia who have helped me along the way. A few of them, I will name personally: Pepe Bernabeu has been very patient in explaining the SCT electronics. The mechanics department (Luis, Pablo, Jose-Vicente) have always been very willing to explain module assembly or design a test box. Juanba has helped a lot finding my lost pointers in the first years. Santi has been a great help with my first steps at PYTHIA and launching jobs in the Valencia PC farm. Emiliano was always willing to explain new linux or ROOT tricks. Paco has tried to explain jet reconstruction. The secretaries (Tere (2x), Asun, Paqui) have done their best to make the inevitable paperwork as pleasant as possible. Maria-Jose Costa has been mentoring very nearly everything, from the rent contract of my appartment to the quark masses, and, with even more merit, has been able to cope with my presence for more than 5 years.

For the cover of this little book I would like to thank Jurjen Hoogland. And, of course, many thanks to my "paranimfen" during the ceremony, Tjan en Tommie.

Of course, not all is work. The people surrounding me have played an important role offering support and distraction.

My little family has had to endure quite a lot during the last months of thesis writing. Annemarie has accepted to move to Spain and now on to Italy (our own little travelling

circus). Vincent has shown me that a cardboard box can be more interesting than a thesis on high energy physics. I hope in the future I will be home earlier.

I would like to thank my parents for everything. And I would also like to mention here my two extra parents, Egbert and Helena. And not to forget my brothers Vincent and Frank. And our Dutch friends that haven't forgotten us, even though we've visited them far too little.

A todos los amigos en Valencia: muchas gracias por cinco años inolvidables. Llevaremos un recuerdo (Vincent) a todas partes y prometemos volver pronto. Ya sabeis que nuestra casita en Pisa siempre esta abierta.